INVESTIGATION ON SYNTHESIS, MECHANISM OF FORMATION AND CATALYTIC APPLICATION OF METAL NANOPARTICLES IN NANOSCALE CONFINEMENT OF POLYMER MATRICES

By
SABYASACHI PATRA
CHEM01201204007

Bhabha Atomic Research Centre, Mumbai

A thesis submitted to the
Board of Studies in Chemical Sciences
In partial fulfillment of requirements
for the Degree of
DOCTOR OF PHILOSOPHY
of
HOMI BHABHA NATIONAL INSTITUTE

September, 2016

Homi Bhabha National Institute

Recommendations of the Viva Voce Committee

As members of the Viva Voce Committee, we certify that we have read the dissertation prepared by **Mr. Sabyasachi Patra** entitled **"Investigation on synthesis, mechanism of formation and catalytic application of metal nanoparticles in nanoscale confinement of polymer matrices"** and recommend that it may be accepted as fulfilling the thesis requirement for the award of Degree of Doctor of Philosophy.

Chairman – Prof. Sudhir Kapoor Sudhir Kapoor **Date:** 16/09/2016

Guide / Convener – Prof. Asok Goswami Goswami **Date:** 16/09/2016

Examiner – Prof. Tarasankar Pal **Date:** 16/09/2016

Member 1- Prof. Pradeep K. Pujari **Date:** 16/9/16

Member 2- Dr. Ashok K. Pandey Pandey **Date:** 22/9/16

Member 3- Dr. Debasis Sen Debasis Sen **Date:** 16.09.2016

Final approval and acceptance of this thesis is contingent upon the candidate's submission of the final copies of the thesis to HBNI.

I/We hereby certify that I/we have read this thesis prepared under my/our direction and recommend that it may be accepted as fulfilling the thesis requirement.

Date: 16/9/2016

Place: BARC, MUMBAI

Goswami
(Signature)
Guide

STATEMENT BY AUTHOR

This dissertation has been submitted in partial fulfillment of requirements for an advanced degree at Homi Bhabha National Institute (HBNI) and is deposited in the Library to be made available to borrowers under rules of the HBNI.

Brief quotations from this dissertation are allowable without special permission, provided that accurate acknowledgement of source is made. Requests for permission for extended quotation from or reproduction of this manuscript in whole or in part may be granted by the Competent Authority of HBNI when in his or her judgment the proposed use of the material is in the interests of scholarship. In all other instances, however, permission must be obtained from the author.

Sabyasachi Patra

DECLARATION

I, hereby declare that the investigation presented in the thesis has been carried out by me. The work is original and has not been submitted earlier as a whole or in part for a degree / diploma at this or any other Institution / University.

Sabyasachi Patra

List of Publications arising from the thesis

Journal

1. Local conditions influencing in situ formation of different shaped silver nanostructures and subsequent reorganizations in ionomer membrane. **S. Patra**, D. Sen, A.K. Pandey, C. Agarwal, S.V. Ramagiri, J.R. Bellare, S. Mazumder, A. Goswami, *J. Phys. Chem. C* **2013**, *17*, 12026–12037.
2. Synthesis, characterisation and counterion dependent mesoscopic modifications of ionomer nanocomposites having different dimensional silver nanostructures. **S. Patra**, D. Sen, C. Agarwal, A.K. Pandey, S. Mazumder, A. Goswami, *AIP Conf. Proc.* **2013**, *1512*, 230-231.
3. Time resolved growth of membrane stabilized silver NPs and their catalytic activity. **S. Patra**, D. Sen, A.K. Pandey, J. Bahadur, S. Mazumder, S.V. Ramagiri, J.R. Bellare, S.V. Roth, G. Santoro, S. Yu, A. Goswami, *RSC Advances* **2014**, *4*, 59379–59386.
4. Redox decomposition of silver citrate complex in nanoscale confinement: an unusual mechanism of formation and growth of silver nanoparticles. **S. Patra**, A.K. Pandey, D. Sen, S.V. Ramagiri, J.R. Bellare, S. Mazumder, A. Goswami, *Langmuir* **2014**, *30*, 2460−2469.
5. Wonderful nanoconfinement effect on redox reaction equilibrium. **S. Patra**, A.K. Pandey, S.K. Sarkar, A. Goswami, *RSC Advances Communication* **2014**, *4*, 33366-33369.
6. Silver Nanoparticles Stabilized in Porous Polymer Support: A Highly Active Catalytic Nanoreactor. **S. Patra**, A.N. Naik, A.K. Pandey, D. Sen, S. Mazumder, A. Goswami, *Applied Catalyis A: General* **2016**, *524*, 214-222.

Symposia

1. Novel synthesis of silver nanoparticles in ionomer matrix by citrate reduction. **S. Patra**, A.K. Pandey, A. Goswami, ANBRE13 Congress at Seoul, Korea during August 25-28, 2013.
2. Mechanism of citrate synthesis of silver nanoparticles within ionomer matrix by radiotracer study. **S. Patra**, A.K. Pandey, A. Goswami, DAE-BRNS Symposium on Nuclear and Radiochemistry at Govt. Model Science College, R. D. University, Jabalpur, Madhya Pradesh, India, during February 19-23, 2013. Page: 563-564.
3. A highly recyclable silver nanoparticles based solid phase catalyst for reduction of aromatic nitro groups. **S. Patra**, A.N. Naik, A.K. Pandey, A. Goswami, DAE-BRNS symposium ISMC, at Mumbai, India during December 09-13, 2014.
4. Synthesis of silver nanocatalysts in anion-exchange membrane for catalytic reduction of 4-nitrophenol. **S. Patra**, A.K. Pandey, A. Goswami, DAE-BRNS symposium Organic Devices, at Mumbai during March 03-06, 2014.
5. Study on size dependence of the catalytic activity of anion exchange membrane hosted silver nanoparticles using SAXS and ^{110m}Ag radiotracer. **S. Patra**, A.N. Naik, A.K. Pandey, D. Sen. A. Goswami, DAE-BRNS symposium NUCAR, at Mumbai during February 09-13, 2015, page 478-479.

Other

1. Redox reactions in nanoscale confinement, Radiochemistry & Isotope Group, *BARC Newsletter*, Issue No. 337, March-April, **2014**.

Sabyasachi Patra

To my mother

ACKNOWLEDGEMENTS

I express my profound gratitude to my Ph.D supervisor, **Prof. Asok Goswami**. From finding an appropriate research problem to the process of writing thesis, Prof. Goswami offered his unreserved help, guidance and supports but for which I could not complete my thesis. With his enthusiasm, inspiration, and great efforts to explain things clearly and simply, learning chemistry became a fun for me. He inspired me to become an independent researcher and helped me realize the power of critical analysis based on basic scientific knowledge.

I am thankful to **Dr. K.L. Ramakumar**, Director, Radiochemistry & Isotope Group, BARC for permitting me to registrar for my Ph.D. My sincere thanks must go to the members of my Ph.D committee: **Dr. S. Kapoor** (Chairman), **Dr. P.K. Pujari**, **Dr. A.K. Pandey** and **Dr. D. Sen** for their valuable comments and suggestions. **Dr. A.K. Pandey** of Radiochemistry Division and **Dr. D. Sen** of Solid State Physics Division deserve a special mention for their help in carrying out the present work, and constant supports. I learned a lot from them.

I would like to thank all my teachers who taught me chemistry and deeply motivated me to do research. I express special gratitude to my M.Sc. Project supervisor **Prof. S.P. Moulik**, Emeritus Professor, Centre for Surface Science, Jadavpur University, who first introduced me to the world of scientific research. His wide knowledge and way of living a purposeful life has been a constant source of inspiration for me.

I express my sincere thanks to **Dr. H. Naik** and my fellow labmates**: Dr. C. Agarwal, Dr. S. Chaudhury, Mr. A.M. Mhatre, Dr. V.R. Chavan, Ms. A.N. Naik, Mr. S. Chappa and Mr. P. Rathod** for providing a stimulating academic environment to learn and grow. I am indebted to many of my colleagues at Radiochemistry Division: **Dr. A.**

Bhattacharyaa, Dr. D. Dutta, Dr. K. Sudarsan, Dr. R. Tripathi, Dr. S. Sodaye, Dr. S. Mukherjee, Dr. P. Maheswari, Dr. S. Ansari, Dr. R. Gujar, Mr. A. Kanekar, Dr. D. Rout, Dr. A. Sengupta, Dr. S.K. Gupta, Mr. P.K. Verma, Mr. N. Pathak, and Mr. T.N. Nag for their continuous help and supports during the course of the present work.

I express my sincere thanks to my collaborators, who have contributed significantly to make my work complete in all respect. I am especially grateful to **Prof. J.R. Bellare** and **Mrs. S.V. Ramagiri** of IIT Bombay, Mumbai, **Dr. S.V. Roth, Dr. G. Santoro, and Dr. S. Yu** of DESY, Hamburg, Germany, and **Mr. S.K. Sarkar** of GAMD, BARC for their help. I am also thankful to the operating personnel of Sophisticated Analytical Instrumentation Facility (**SAIF**), IIT Bombay, Mumbai for providing FE-SEM facility on chargeable basis.

I am deeply grateful to my **parents** for their love, care and support. They raised me, taught me and gave me strength to pursue my dreams. I express my gratitude to my dearest uncle **Mr. A.K. Patra** for his endless love and support. I thank my loving sisters **Sathi, Mala,** and **Mukul** who have been supportive all the time. I sincerely acknowledge the love and supports given to me by my **parent-in-laws**. I have no word to thank my wife, **Manideepa** for her patience, care and constant encouragement during the course of this work. She has tried her best to keep me cheerful during all these days. She also stood by me through my weal and woe. I am indeed blessed to have her in my life. During the course of my work, I received help from many, whose name I could not mention. I thank all of them.

Sabyasachi Patra

CONTENTS

Page No.

SYNOPSIS i
LIST OF FIGURES xvii
LIST OF SCHEMES xxxi
LIST OF TABLES xxxiii
ABBREVIATIONS xxxv

Chapter 1 **Introduction** 1

1. Nanochemistry: the Chemistry of Small 2
    - 1.1. Nanomaterials 3
        - 1.1.1. Effect of Surface: From Bulk to Nanoscale 5
        - 1.1.2. Quantum Effect: Change in Electronic States 7
    - 1.2. Synthesis and Stabilization of Nanomaterials 8
        - 1.2.1. Bottom up Techniques 9
        - 1.2.2. Top down Techniques 10
        - 1.2.3. Stabilization of Nanomaterials 11
    - 1.3. Thermodynamics and Kinetics of formation of Nanoparticles 15
        - 1.3.1. Thermodynamics of Nanoparticles Stability: Classical Nucleation Theory 15
        - 1.3.2. Mechanism of Formation of Metal Nanoparticles: Journey from a Molecular Precursor to Metal Nanoparticles 18
    - 1.4. Metal Nanoparticles as Catalyst 21
    - 1.5. Nanostructured Materials as Hosts for Metal Nanoparticles 25
        - 1.5.1. Polymer Membranes 25

1.5.2. Mesoporous Silica and Polymer Resins 26
1.6. Chemical Reactions in Nanoscale Confinement 26
2. Scope of the Thesis 28

Chapter 2 **Experimental Methods** 33
1. Synthesis of Nanoparticles 34
2. Characterization of Nanoparticles 35
2.1. Small Angle X-ray Scattering (SAXS) 36
2.1.1. Principle of SAXS 36
2.1.2. Laboratory Based SAXS Instrument 37
2.1.3. Synchrotron Radiation Based SAXS Instrument 41
2.2. Dynamic Light Scattering (DLS) 43
2.3. Electron Microscopy 44
2.3.1. Transmission Electron Microscopy (TEM) 45
2.3.2. Field-Emission Scanning Electron Microscopy (FE-SEM) 47
2.4. Applications of Radiotracers as an Analytical Tool 49
2.4.1. Choice of Radiotracer 50
2.4.2. Production of Radiotracer 50
2.4.3. Units of Radioactivity 52
2.4.4. Operational Safety with Radiotracer 52
2.4.5. Measurement of Radiation 52
2.4.6. Application of ^{110m}Ag Radiotracer in Silver Nanoparticle Characterization 54
2.5. Inductively Coupled Plasma Atomic Emission Spectroscopy (ICP-AES) 55

3. Application of Nanoparticles for Catalysis 56

3.1. Choice of Model Reaction 56

3.1.1. Reduction of p-Nitrophenol (PNP) 57

3.1.2. Reduction of Methylene Blue (MB) 58

3.2. Monitoring of the Progress of Catalytic Reaction 59

3.2.1. Ultraviolet-visible (UV-VIS) spectroscopy 59

Chapter 3 **Formation of Silver Nanoparticles in Cation Exchange Membrane by in-situ Reduction Method: Effect of Local Environment on Morphology of Nanoparticles** 65

1. Introduction 66

1.1. Morphology of Nafion Membrane 66

1.2. Nafion Membrane as a Host for Nanoparticles 68

2. Experimental Section 70

2.1. Materials and Reagents 70

2.2. Membrane Sample Preparation 71

2.2.1. Reduction of Ag^+ Loaded Membrane with Formamide 71

2.2.2. Reduction of Ag^+ Loaded Membrane with Ascorbic Acid 71

2.3. Characterization 73

2.3.1. Transmission Electron Microscopy 73

2.3.2. Small Angle X-ray Scattering 73

3. Results and Discussion 76

3.1. Chemical Reactions Involved in the Reduction of Silver Ions 77

3.1.1. Reduction of Ag^+ by Formamide 77

3.1.2. Reduction of Ag^+ by Ascorbic Acid 78

3.2. Shapes and Spatial Distributions of Nanostructures 80

3.2.1. Formamide Reduced Samples (AFT65, AFT50, AFT40) 80

3.2.2. Ascorbic Acid Reduced Samples (A1, A2 & A3) 85

4. Conclusions 94

Chapter 4 **Mechanism of Growth of Silver Nanoparticles by Ascorbic Acid Reduction in Cation-exchange Membrane with Subsecond Time Resolution** 96

1. Introduction 97

2. Experimental Section 99

2.1. Materials and Methods 99

2.2. Nanoparticle Synthesis 100

2.2.1. TEM Characterization 100

2.2.2. Temporal Evolution of AgNPs: In-situ Time Resolved SAXS Study using Synchrotron Radiation 101

3. Results and Discussion 103

4. Conclusions 111

Chapter 5 **Synthesis and Mechanism of Formation of Silver Nanoparticles by Redox Decomposition of Silver Citrate Complex in Nanoscale Confinement** 113

1. Introduction 114

2. Experimental Section 116

2.1. Materials and Methods 116

2.1.1. Description of Host Matrices 116

2.1.2. Nanoparticle Synthesis 118

2.2. Nanoparticle Characterization 119

2.2.1. Microscopy 119

2.2.2. Small Angle X-ray Scattering 120

2.3. Radiotracer Technique 121

3. Results and Discussion 123

3.1. Formation of Nanoparticles in Anion Exchange Membrane 126

3.2. Formation of Nanoparticles in Cation Exchange Membrane 130

3.3. Mechanism of Formation of Nanoparticles in Ion-Exchange Membranes 135

3.3.1. Mechanism of Nucleation 137

3.3.2. Mechanism of Growth 139

3.4. Formation of AgNPs in Neutral Nanoporous Beads 143

3.5. Formation of AgNPs in Silica Gel Particles 147

4. Conclusions 148

Chapter 6 **Synthesis of Noble Metal Nanoparticles by Polyol Reduction: Role of Nanoconfinement in Softening the Reaction Conditions** 149

1. Introduction 150

2. Experimental Section 151

2.1. Materials and Methods 151

2.1.1. Synthesis of Metal Nanoparticles at Ambient Conditions 152

2.1.1.1. Reduction of Noble Metal Ions with Ethylene Glycol (EG) at Ambient Temperature 152

2.1.2.2. Reduction of $PtCl_6^{2-}$ with Sodium Borohydride 152

2.2. Characterization of Nanoparticles 153

2.2.1. Field Emission Scanning Electron Microscopy 153

3. Results and Discussion 153

4. Conclusions 158

Chapter 7 **Catalytic Performances of Silver Nanoparticles in Nanoscale Confinement** 159

1. Introduction 160

2. Experimental 162

    2.1. Materials and Reagents 162

    2.2. Preparation of catalytic Nanoreactor 163

        2.2.1. Synthesis of Anion Exchange Membrane (AEM) 163

        2.2.2. Synthesis of Silver Nanoparticles of Different Sizes in the AEM 163

    2.3. Characterization of the Nanoreactor 164

        2.3.1. Filled Emission Scanning Electron Microscopy and Energy Dispersive X-ray Spectroscopy 164

        2.3.2. Small Angle X-ray Scattering 164

        2.3.3. Quantification of Silver Host Matrices in the Polymer Host Matrices 165

            2.3.3.1. Radiotracer Technique 165

            2.3.3.2. Inductively Coupled Plasma Atomic Emission Spectroscopy Technique 166

    2.4. Catalytic Study 167

        2.4.1. Reduction of Methylene Blue (MB) 168

        2.4.2. Reduction of Para Nitrophenol 168

3. Results and Discussion 168

    3.1. Catalytic Activity of Silver Nanoparticles Hosted in Nafion 117 Membrane 169

    3.2. Catalytic Activity of Silver Nanoparticles Hosted in XAD-4 Resin Beads 172

3.3. Catalytic Activity of Silver Nanoparticles Hosted in Pore Filled Tailor-made Anion Exchange Membrane (AEM) 175

3.3.1. Synthesis and Characterization of Silver Nanoparticles in AEM 175

3.3.2. Catalytic Activity of Silver Nanoparticles (Ag@AEM) for Borohydride Reduction of Para Nitrophenol 181

3.4. Comparison of Catalytic Activity of Spatially Confined Silver Nanoparticles with Unconfined Silver Nanoparticles 185

3.5. Possible Origin of the “Lag Phase” 186

3.6. Catalytic Activity of XAD-4 Beads and AEM without Metal Nanoparticles: Evidence of Pure Nanoconfinement Effect 187

4. Conclusions 190

Chapter 8 **Effect of Nanoscale confinement on Chemical Reactions: Entropic Origin of Nanoconfinement Effect** 191

1. Introduction 192

2. Experimental 194

2.1. Materials and Reagents 194

2.2. Catalytic Study 195

3. Results and Discussion 197

4. Conclusions 202

Chapter 9 **Summary and Future Scopes** 204

1. Summary of the Present Study and Major Conclusions 205

2. Future Scopes 209

Bibliography 210

Synopsis

Nanochemistry has seen a tremendous growth over a period of last two decades. Current research in nanochemistry mostly includes synthesis of nanopartclies with better control of shape and size, synthesis of self assembled nanostructures (mesoporous materials), and applications of such nanomaterials. Particularly metal nanoparticles have drawn considerable research interest during the last decade because of their special optical, electrical, and catalytic properties compared to the bulk metal. For example, gold has been considered to be catalytically inactive for long time (till 1980). Pioneering work by Parravano group and Haruta et al. showed that nanogold can be used as a catalyst for various reactions [Cha and Parravano 1970.; Galvagno and Parravano 1978.; Schwank et al. 1980.; Haruta et al. 1987.; Haruta et al. 1989.; Haruta et al. 1997]. Since then extensive work has been carried out in preparing metal nanoparticle (Au, Ag, Pt, Pd etc) based active catalysts for various types of reactions like C-C coupling, hydrogenation, CO oxidation etc [Jana et al. 2008.; Makosch 2012.; Lopez and Nørskov 2002]. Apart from catalysis there are other areas of technological importance like chemical platforms, sensorics, optoelectronics etc. where metal nanoparticles find considerable applications.

One major limitation of the use of nanoparticles is their tendency to agglomerate. Various approaches have been evolved with time to prevent self-aggregations of colloidal nanoparticles by surface modification. These include steric stabilization (by the use of capping agents), electrostatic stabilization (by the use of electrolytes), and a combination of two. Porous material supported nanoparticles have drawn considerable research interest due to their high stability, long self-life (less corrosion), and appreciable reactivity (due to absence of capping agents on the surfaces). Also, the use of such matrix supported nanoparticles is advantageous as they can be easily handled for a particular application on demand. Various structured mesoporous materials like molecular sieves, layered solids, carbon nanotubes, polymer membranes and resins etc. have been used as support for nanoparticles [Lithikar et al. 2007.; Papp et al. 2001.; Shchukin and Sukhorukov 2004.; Mohan et al. 2006.; Jeon et al. 2011.; Simo et al. 2012.; Zhu et al. 2013.; Rollins et al. 2000.; Sun 2000.; Sun et al. 2004.; Jana et al. 2006.; Takahashi et al. 2008.; Shah and Kaur 2014].

Ion-exchange membranes are ion containing polymers having fixed charge groups and mobile counter ions. They swell in water forming a gel like structure and the hydrophilic water channels contain the ion-exchange groups and counter ions. Metal nanoparticles can be produced in these membranes by choosing suitable counter ions and in-situ reduction of the counter ions with a suitable reductant. Various reducing agents like borohydride, formamide, ascorbic acid have been extensively used over the years for the synthesis of metal nanoparticles in ion-exchange matrices [Sun et al. 2004, Hasegawa et al. 2012, Rollins et al. 2000, Sachdeva et al. 2006, Kumar et al. 2010]. The nanoparticles/clusters so formed are stabilized by the polymer matrix of the membrane and can be used for various applications without loss of integrity. These metal polymer nanocomposites can have potential applications in catalysis, sensorics, optoelectronics, electrochemical studies and artificial muscles [Sanchez et al. 2005, Corma and Garcia 2008, Wang et al. 2003, Selvaraju and Ramaraj 2005, Ramaraj 2006, Alonso et al. 2012, Xing et al. 2011, Hirano et al. 2011]. Practical applications of nanoparticles demand a well-defined particle size and size distribution, requiring synthetic routes having better control over the growth of nanoparticles. The size controlled synthesis of metal nanoparticles for any kind of metal-polymer system has not been attempted up to now. The knowledge of the growth kinetics and mechanism is a prerequisite for size controlled synthesis of metal nanoparticles in ion-exchange membrane matrices. This requires real time experimental information about the particle size and concentration during the course of synthesis. In addition to membranes, polymer resins (both ionic and neutral) have also got significant importance as a host for metal nanoparticles [Jana et al. 2006.; Takahashi et al. 2008.; Shah and Kaur 2014].

Noble metal nanoparticles (Ag, Au, Pt, Pd) act as catalysts for many electron transfer reactions due to their increased Fermi potential at nanoscale [Pradhan et al. 2001, Jana and Pal 1999, Jana et al. 1999, Sau et al. 2001, Jana et al. 2000, Ghosh et al. 2002, Ghosh et al. 2004, Colby et al. 2008, Hall et al. 2012, Iwahori and Yamashita 2007, Behrens et al. 2004, Vijayaraghavan and Nalini 2010, Esumi et al. 2002, Hayakawa et al. 2003, Esumi et al. 2004, Baruah et al. 2013]. Solid matrix supported metal nanoparticles are promising materials for heterogeneous catalysis because of their high stability, appreciable reactivity and less chance of contaminating the product [Zhu et al. 2013]. Finding new routes of synthesis of such matrix supported nanoparticles involving softer reaction conditions is important. Various researchers have studied different types of chemical reactions both theoretically and experimentally under nanoscale spatial confinement of solid matrices, and have shown that the reactions gets significantly facilitated in nanospaces in comparison to bulk under identical reaction conditions. Possible explanations for such extraordinary effect have been put forward in the literature which includes surface effect, increased density of the pore phase, suitable orientation of molecules near the pore walls, different diffusion rates, high pressure effect due to geometrical constraints, shift of equilibrium towards product side because of reaction-product reduced mixing, system size dependent entropy variation etc [Turner et al. 2001, Turner et al. 2002, Santiso et al. 2005, Thomas et al. 2003, Shon and Cohen 2012, Polak and Rubinovich 2008, Polak and Rubinovich 2011, Rubinovich and Polak 2013, Nielsen et al. 2010,Thompson 2002, Li and Thompson 2005, Hill 2001]. The role of nanoscale confinement on a redox reaction has never been studied, and therefore of potential interest from the point of synthesis of nanoparticles as well as their redox catalytic applications.

The work presented in this thesis is mainly focused on the study of synthesis, mechanistic aspects of formation and catalytic applications of noble metal nanoparticles (silver nanoparticles in particular) stabilized in the confined nanodomains of various ion-exchange membranes and nanoporous polymer resins. Experiments have been carried out to find out novel routes for synthesis of metal nanoparticles under mild reaction conditions. In order to understand the growth mechanism, kinetics of growth of metal nanoparticles in host matrices have been studied by various techniques like small angle X-ray scattering (SAXS), transmission electron microscopy (TEM), and Field emission scanning electron microscopy (FE-SEM). In addition, ^{110m}Ag radiotracer has been used for quantification of time dependent loading of silver nanoparticles in the matrices, which is important for understanding the mechanism of nanoparticles growth and also to obtain the mass normalised rate of catalysis. The catalytic activity of such matrix supported nanoparticles has also been studied with some model catalytic reduction reactions. The unique morphology of the membranes as well as the resins have been shown to offer remarkable “Nanoconfinement Effect” which favours the synthesis of nanoparticle under mild reaction conditions, and enhances the catalytic activity of embedded nanoparticles. Experiment has been carried out to understand the origin of such effect. Plausible explanation of nanoconfinement effect has been given in terms of shifting of equilibrium due to reduced molecular mixing of the reactant and product in confined nanospace. The thesis is divided into nine chapters. The content of the chapters is briefly described in the following.

Chapter 1: Introduction

This chapter describes the basic introduction to the chemistry of nanoscale materials and their size dependent properties. The general methods of synthesis of metal nanoparticles and various approaches for stabilizing the nanoparticles have been discussed briefly. Properties of various host matrices like ion-exchange membranes and porous polymer resins used in the present work have been listed. General introduction on metal nanoparticle mediated catalysis has also been given in this chapter. The current literature status on studying the role of nanoscale confinement on different types of chemical reactions and the concept of nanochemical equilibrium has been briefly discussed. At the end the scope of the present thesis has been outlined.

Chapter 2: Experimental Procedures

The instrumental and experimental details of the various characterization techniques used during the course of present work have been discussed briefly in this chapter. The techniques include Small angle X-ray scattering (SAXS), Transmission electron microscopy (TEM), Field emission scanning electron microscopy (FE-SEM), Inductively coupled plasma atomic emission spectroscopy (ICP-AES), and UV-Vis spectrophotometry. The advantages of using radiotracer in physicochemical study and also the production route of the radiotracers are discussed. Emphasis has been given on the choice of radiotracer and the operational safety of radiotracers. Brief description has been given on the radiation measurement procedures using radiation detectors. Various radiotracer used in this work and their nuclear properties have been given.

Chapter 3: Formation of Silver Nanoparticles in Cation-exchange Membrane by In-situ Reduction Method: Effect of Local Environment on Morphology of Nanoparticles

In this chapter the chemical synthesis of different shaped silver nanoparticles in Nafion-117, a commercially available cation exchange membrane, has been described. The general steps for synthesis of metal nanoparticles in an ion-exchange membrane are: (i) loading of precursor metal ions through ion-exchange and (ii) subsequent reduction of the metal ions with a suitable reducing agent. The effect of ionic and non ionic reductant on the formation of silver nanoparticles in Nafion membrane has been studied earlier [Kumar et al, 2010]. The two different reductants change the local environment of the metal ions in the membrane. However the role of local environment of the membrane on the formation of different dimensional silver nanoparticles is not properly understood. In this chapter, study on the synthesis of silver nanoparticles in the confined nanodomains of Nafion-117 under various local environments of the membrane has been reported. The local environment has been varied by altering the membrane morphology with carefully selected reductants, varying temperature and extent of precursor loading in the membrane. Formamide, a non ionic reductant, and ascorbic acid, an ionic reductant, have been used as reducing agents. Combined small angle X-ray scattering (SAXS) and transmission electron microscopy (TEM) have been used for morphological characterization of the nanocomposite membranes in different counterionic forms. Homogeneously distributed spherical silver nanostructures (~10 nm diameter) with significant size dispersion have been formed by formamide reduction. However bigger nanostructures have been produced in the membrane by ascorbic acid reduction. Under specific conditions (25 % of the ion-exchange sites are loaded with Ag^+), silver nanorods having ~8 nm mean diameter and ~40 nm length have been formed using ascorbic acid as reductant. At lower loading of precursor ions in the membrane (for the cases where 10 % and 2% of the ion exchange sites are loaded with Ag^+), silver nanosponge and nanoclusters have been formed. These results show the change of local environment of the membrane by varying the nature of reductant, concentration of precursor ions in the membrane, as well as temperature significantly alters the morphology of the nanoparticles.

Chapter 4: Mechanism of Growth of Silver Nanoparticles by Ascorbic Acid Reduction in Cation-exchange Membrane with Subsecond Time Resolution

Ascorbic acid has been selectively chosen as reducing agent for this work because of its interesting role as a weak reductant for the growth of metal nanoparticles with various aspect ratios [Suber and Plunkett 2010]. However, formation of silver nanoparticles by ascorbic acid reduction is almost instantaneous and hence it is difficult to study the mechanism of growth of the nanoparticles. This requires an in-situ characterization technique which can capture the growth of the nanoparticles in subsecond time scale. Synchrotron based small angle X-ray scattering (SAXS) is ideal tool for such study. In this chapter, experiments on the real time in-situ characterization of growth of silver nanoparticles during ascorbic acid reduction in the confined nanodomains of Nafion membrane using synchrotron radiation based SAXS has been described. The SAXS analyses, corroborated by transmission electron microscopy (TEM), have shown that the sizes of nanoparticles increase rapidly along with their number density until they attain size that could be accommodated in the ~5 nm water-sulfonate ionic clusters of Nafion. Further growth takes place either by self-agglomeration of the particles ejected out from the water-sulfonic acid clusters or by continuous reduction of metal ions on the existing nanoparticle surfaces (uniformly or at some specific facet) leading to formation of bigger nanostructures with various aspect ratios. The time resolved information on growth of nanoparticle provides an opportunity for the controlled synthesis of metal nanoparticles with definite size, shape and size distribution for a specific application.

Chapter 5: Synthesis and Mechanism of Formation of Silver Nanoparticles by Redox Decomposition of Silver Citrate Complex in Nanoscale Confinement.

Chapter 3 and chapter 4 deal with the synthesis of silver nanoparticles in the nanoscale confinement of Nafion membrane. No special attention has been paid on the role of nanodomain of the membrane on such reduction reactions. The focus of this chapter is to study the intrinsic role of nanoconfinement in facilitating the chemical reduction of metal ion precursors for the synthesis of metal nanoparticles. The citrate reduction of silver ions has been studied under the unusual condition of $[\text{citrate}]/[\text{Ag}^+] \gg 1$. It has been observed that the silver citrate complex, stable in bulk aqueous solution, decomposes readily in confined nanodomains of charged and neutral matrices (ion-exchange membranes and nanoporous polystyrene beads), leading to the formation of silver nanoparticles. This is the first report of a reduction reaction occurring in the confined nanodomain of polymer matrix which otherwise does not occur in the bulk. This shows the nanoconfinement plays distinct role in the progress of such reaction. The kinetics and mechanism of growth of silver nanoparticles in the ion-exchange membranes has been studied using a combination of ^{110m}Ag radiotracer, small-angle X-ray scattering (SAXS) experiments, and transmission electron microscopy (TEM). Due to the slower reduction rate, it has been possible to study the kinetics with laboratory based SAXS instrument. The redox decomposition of silver citrate complex in nanoconfined space of the matrices has been found to be responsible for the formation of Ag seeds, which thereafter catalyze oxidation of citrate and act as electron sink for subsequent reduction of silver ions. Because of these parallel processes, the particle sizes have been found to be in bimodal distribution at some stages of the reaction. A continuous seeding with parallel growth mechanism has been observed. Based on the SAXS data and radiotracer study, the growth mechanism has been elucidated as a combination of continuous autoreduction of silver ions on the nanoparticle surfaces and a sudden coalescence of nanoparticles at a critical number density. However, for a fixed period of reduction, the size, size distribution, and number density of thus-formed silver nanoparticles have been found to be dependent on physical architecture and chemical composition of the matrix. In order to study the matrix dependence of nanoconfinement effect, the method of auto-reduction of silver-citrate complex has been extended further in the nanoconfinement of amberlite XAD-4 neutral resin beads having 10 nm pores and silica gel particles having 4 nm pores. Silver nanoparticles have been formed by nanoconfinement facilitated autoreduction of silver citrate complex in nanopores of the XAD-4 beads and silica gel particles, which shows that the nanoconfinement effect is matrix independent. Because of sufficiently slow kinetics of the nanoparticles growth, the present method can be used to control the size of the silver nanoparticles by carrying out reduction for different time periods.

Chapter 6: Synthesis of Noble Metal Nanoparticles by Polyol Reduction: Role of Nanoconfinement in Softening the Reaction Conditions.

The effect of nanoconfinement on the reaction rate has been studied further in the synthesis of noble metal nanoparticles by polyol reduction route. Polyol reduction of noble metal ions is not feasible under ambient condition. In this work, nanoporous amberlite polystyrene XAD-4 resin beads (average pore diameter of 10 nm) have been used as matrix for nanoconfinement. Neutral polymeric beads have been chosen over ion-exchange membranes to avoid the effect of charged species on the reaction. Field Emission - Scanning Electron Microscopy (FE-SEM) characterization of the beads clearly shows that the clusters of nanoparticles have been formed near the nanoscale crevices in the matrix. This suggests that nanoconfinement facilitates the polyol reduction process at room temperature that is not observed in bulk solution under the same reaction condition. They have been observed with appreciable rate in nanoconfined spaces of solid matrices for the first time. The results are interesting from the point of view of exploring new green synthetic routes for other reactions under softer conditions.

Chapter 7: Catalytic Performances of Silver Nanoparticles in Nanoscale Confinement.

The role of nanoscale confinement of solid matrices (ion-exchange membranes, and XAD-4 resin beads) in altering the course of a chemical reaction for the synthesis of metal nanoparticles in energy efficient route and the role of such matrices in providing excellent stability to the formed nanoparticles have been discussed in the earlier chapters. The overall catalytic performances of the nanoparticles stabilized in nanoconfined solid supports have been investigated and the results have been discussed in this chapter. It has been demonstrated that the catalytic performances of silver nanoparticles are improved significantly in a nanoconfined environment in comparison to unconfined bare nanoparticles. The nanoparticles used in the present work have been synthesised with proper size control in commercially available Nafion-117 membrane (by ascorbic acid reduction as discussed in chapter 4), in a tailor-made anion exchange membrane (by citrate reduction route as discussed in Chapter 5) and in Amberlite XAD-4 resin beads (by polyol process as discussed in Chapter 6). The catalytic activities of silver nanoparticles formed in the cation-exchange membrane (Nafion-117) have been examined using borohydride reduction of a model cationic dye methylene blue (MB). It has been observed that smaller silver nanoparticles with a mean diameter ~ 3 nm, confined in the hydrophilic clusters of the Nafion matrix, have good catalytic activity. Borohydride reduction of para nitrophenol to para aminophenol has been used as a model reaction to study the catalytic activity of silver nanoparticles hosted in an anion exchange membrane and in Amberlite XAD-4 beads. Progress of the catalytic reactions has been monitored by time resolved UV-Vis spectrometry. The successive decrease in intensity of the absorption maximum of the substrate and appearance of a new absorption maximum due to the formation of product in the UV-Vis spectra gives the rate of catalysis. Effect of nanoscale confinement provided by the host matrix on the rate of catalytic reaction has been explored. The activity parameters ($s^{-1}g^{-1}$) of the catalytic reactions using present catalysts have been found to be remarkably high in comparison to unconfined bare nanoparticles. The origin of such a high catalytic activity has been attributed to the effect of membrane nanoconfinement which accelerates the electron transfer process during catalytic reduction. The anion-exchange membrane confined silver nanoparticles have been found to be highly reusable. It has been shown for the first time that a pure physical confinement is enough to catalyse the borohydride reduction of para nitrophenol, which is otherwise impossible in absence of a catalyst. This confirms the intrinsic role of physical confinement on facilitating chemical reactions.

Chapter 8: Effect of Nanoscale confinement on Chemical Reactions: Entropic Origin of Nanoconfinement Effect

As described in the previous chapters, the experimental observations on synthesis and catalytic activity of nanoparticles in the confined spaces of a solid matrices clearly show that physical compartmentalization of the reactants alters the course of a chemical reaction. Various researchers have studied different types of chemical reactions both theoretically and experimentally under nanoscale spatial confinement, and proposed possible origins of such extraordinary effect. However, proper understanding of such effect is still limited. In this chapter the concept of "nanoconfinement effect" has been introduced in detail based on the theoretical and experimental data available from current literature. The effect of average pore occupancy on the kinetics of catalytic reaction has been studied. Silver nanoparticles loaded XAD-4 nanoporous beads have been used as catalyst. The average pore diameter in XAD-4 beads is 10 nm. The average pore occupancy has been varied by varying the bulk reactant concentration. Bulk concentration has been varied to reach the average occupancy much less than one (assuming ideal compartmentalization when pores are not connected). The result shows the reaction rate constant increases significantly with decrease in the average pore occupancy of the reactant molecules, the effect being more prominent when the average pore occupancy is much less than one. This has been attributed to the fact that, at lower value of average pore occupancy, the average distance between the reactant molecules are very large in the porous network. Thus the molecular diffusion of reactants from the neighboring pores can't alter the average occupancy of a pore during the chemical reaction. So the condition of "single molecule" experiment (perfect compartmentalization) is achieved. Therefore the system contains either reactant or product molecule at a particular time under the condition of single molecule occupancy of a pore. In such a situation, equilibrium is highly shifted toward the product side because of absence of reactant product mixed microstate. This essentially enhances the rate constant for the reaction. At higher reactant concentration, each pore will contain larger number of reactant molecules, thereby making the situation similar to that exists in bulk when both reactant and product molecules are homogeneously distributed. Thus it is concluded that the nanoconfinement effect would be pronounced below a certain bulk concentration range of the reactant molecules.

Chapter 9: Summary and Future Scopes

The conclusions drawn from the work carried out have been described in the last chapter of the thesis. The future scopes of research in this rapidly growing area have also been highlighted. The major conclusions of the present thesis work are:

(a) Local conditions during reduction and subsequent reorganizations of matrix influence the shape, size dispersion, and distribution of Ag nanostructures formed in nanoconfined domains of Nafion membrane. The water cluster network in the matrix is modified significantly after incorporation of bigger Ag nanoparticles and nanorods.

(b) Real time *in-situ* SAXS with millisecond time resolution shows that the early growth of spherical Ag nanoparticles of the size of ~ 3nm in the nanoscale confinement (water sulfonate clusters) of Nafion membrane by room temperature ascorbic acid reduction is a three stages process. Further growth by sacrificial self-agglomeration takes place after ejection of nanoparticles from water-sulfonate clusters leading to formation of rod-like nanostructures with bigger sizes. This study demonstrated the possibility for controlled synthesis of AgNPs in Nafion membranes with different shapes and sizes.

(c) The confined nanospace in a solid matrix has been found to facilitate the citrate reduction of Ag^+ ions for the formation of SNPs, which otherwise does not take place in bulk solution. Silver citrate complex has been found to be a promising substrate for selectively incorporating silver nanostructures in ion-exchange membranes as well as in neutral nanoporous beads by way of its diffusion into the matrix, resulting in the slower kinetics of nanoparticle growth. This provides better control in tuning the size of the nanoparticles by carrying out reaction efficiently for a desired time period. The growth of nanoparticles in the present case has been assisted by both autocatalytic reductions of Ag^+ ions on the nanoparticle surface by thermal oxidation of citrate and the interparticle coalescence. There is a critical size (~5 nm) and a critical relative number density of the nanoparticles in the matrices, beyond which they suddenly collapse into bigger nanoparticles, resulting in rapid rise in the diameter of the particles. The synthetic method developed in the present work is very general for all kinds of matrices having confined nanospaces (confined water domain, nanopores etc.).

(d) The chemical reduction of noble metal ions in nanoconfined spaces provides a soft synthetic route for preparing a variety of noble metal nanoparticles stabilized in inorganic or polymer matrices using an appropriate combination of reductant and precursor ions.

(e) The rate of a catalytic reaction using silver nanoparticles as catalyst has been found to be significantly enhanced in nanoconfined environment in comparison to the unconfined case. It has been found that the enhancement is more in slit like nanopores in a XAD-4 bead in comparison to nanodomains of membranes. However, in both the cases the activity parameters are much more in comparison to the bare nanoparticles of identical dimensions. Observation of PNP reduction by borohydride in presence of XAD-4 resin beads without any catalyst clearly shows the effect of nanoconfinement in facilitating chemical reaction.

(f) The reaction equilibrium has been found to be highly dependent on the pore loading or occupancy. At lower pore occupancy the chemical equilibrium is highly shifted toward the product side because of absence of reactant product mixed microstate. This essentially enhances the rate constant for the reaction.

The chapter is concluded by outlining the directions for future research related to the topic of the thesis.

List of Figures

Chapter 1

Figure 1.1. The 4th century Roman Lycurgus cup (a), Centuries ago decoration of stained glass with gold nanoparticles in Europe (b), and Cranberry glass bowl prepared by adding a gold salt (probably gold chloride) to molten glass (c).

Figure 1.2. Variation of the dispersion (F) as a function of n for cubic clusters up to n = 100 ($N = 10^6$). The structure of the first four clusters is shown.

Figure 1.3. Density of states (DOS) diagram for valence band structures of bulk, nanoparticles, clusters, and atoms.

Figure 1.4. The use of bottom-up and top-down techniques in nanomanufacturing.

Figure 1.5. Schematic representation of electrostatic stabilization of colloidal metal nanoparticles.

Figure 1.6. Schematic representation of steric stabilization of colloidal metal nanoparticles.

Figure 1.7. Variation of surface and volume contribution to the total free energy with nanoparticle growth. ΔG_{tot} reaches a maximum at a critical radius r_c.

Figure 1.8. Schematic representation of variation of monomer concentration with time during particle nucleation and growth from solution in the classical LaMer mechanism. The blue arrows define the nucleation period (zone II). The red arrow defines the growth period (zone III).

Figure 1.9. Schematic illustration of Ostwald ripening process.

Figure 1.10. Scatter plot of the d-band centre of the metal surface versus the adsorption strength of para nitrophenol.

Figure 1.11. Nanostructure of ion-exchange membrane.

Chapter 2

Figure 2.1. Schematic representation of the experimental setup for a SAXS experiment and representation of the scattering vector (q) on the detector surface.

Figure 2.2. A schematic of typical SAXS instrument is shown.

Figure 2.3. Detector response for the SAXS measurement of a silver nanoparticles embedded Nafion 117 membrane after data acquisition for 10 minutes (a) and the corresponding radial averaged SAXS profile.

Figure 2.4. The new high brilliance 3rd Generation Synchrotron radiation Source at DESY: PETRA III (a) and the fourteen available beamlines at PETRA III (b).

Figure 2.5. Schematic set-up of dynamic light scattering experiment.

Figure 2.6. Representative TEM image of silver nanoparticles hosted in Nafion 117 membrane.

Figure 2.7. A representative FE-SEM image of silver nanoparticles in XAD-4 resin beads.

Figure 2.8. Schematic comparison of optical/light microscope (LM), transmission electron microscope (TEM), and scanning electron microscope (SEM).

Figure 2.9. Schematic representation of energy bands in a NaI(Tl) crystal.

Figure 2.10. Block diagram of a NaI(Tl) detector.

Figure 2.11. Schematic representation of an ICP-AES instrument.

Figure 2.12. Reduction reaction of PNP to PAP.

Figure 2.13. Chemical structure of methylene blue in its oxidized and reduced form.

Figure 2.14. Possible electronic transitions in UV-VIS spectroscopy.

Figure 2.15. Schematic representation of a typical UV-VIS spectrophotometer.

Figure 2.16. Time resolved UV-VIS spectrum during the reduction of p-nitrophenol by sodium borohydride in presence of silver nanoparticles.

Chapter 3

Figure 3.1. Structural formula of the monomer unit of Nafion-117 and the cluster-network model of Nafion-117 membrane as proposed by Hsu and Gierke.

Figure 3.2. Schematic representation of Polymeric bundle model (a), Parallel cylinder model (b), and Bicontinuous network model (c) of Nafion 117 membrane.

Figure 3.3. Variation of Ag^+ ions in ion-exchange sites (mol %) in a Nafion-117 membrane sample (2 cm x 2 cm) as a function of equilibration time in $NaNO_3$ (0.25 mol L^{-1}) under stirring condition.

Figure 3.4. SAXS profiles of (a) formamide (65 ^{o}C) and (b) ascorbic acid (27 ^{o}C) treated Nafion 117 samples.

Figure 3.5. Representative TEM image of cross-section of membrane showing spatial distribution of silver nanospheres produced in sample AFT65 after post reduction neutralization with Na^+ ions (a), and corresponding size distribution histogram (b).

Figure 3.6. SAXS profiles for formamide reduced samples in Na^+ (a) and Cs^+ (b) counterionic forms, obtained after post reduction neutralization.

Figure 3.7. Size distributions of spherical Ag nanoparticles in formamide reduced Nafion samples obtained from analyses of SAXS profiles in Na^+ and Cs^+ post reduction neutralized forms.

Figure 3.8. Water cluster size distribution plots for formamide reduced samples followed by post reduction neutralization with Na^+ ions (a) and Cs^+ ions (b).

Figure 3.9. TEM images showing shapes and spatial distributions of Ag nano-cylinders near surface (a), and nano-rods across thickness (b) of the ionomer nanocomposite prepared by ascorbic acid reduction of the ionomer sample loaded with 25% of Ag^+ ions.

Figure 3.10. TEM images of cross-section of ionomer nanocomposite (A2) showing clustering of nanoparticles to nanosponge like big nanostructures at surface (a) as well as interior matrix (b-d). The samples were prepared by ascorbic acid reduction of the ionomer sample loaded with 10% of Ag^+ ions followed by neutralization with Na^+ ions. The length of the scale bars as shown in the images is 100 nm.

Figure 3.11. TEM images of cross-section of nanocomposite (A3) showing formation of nanoparticle clusters in ionomer matrix. The nanocomposite samples were prepared by ascorbic acid reduction of ionomer sample loaded with 2% of Ag^+ ions followed by neutralization with Na^+ ions. The scale bars as shown in the images are 100 nm (a) and 50 nm (b).

Figure 3.12. SAXS profiles for ascorbic acid reduced samples after post reduction neutralization with Na^+ (a) and Cs^+ (b) ions.

Figure 3.13. Comparison of diameter and length distributions of nanorods in A1 samples obtained by SAXS analyses (a) with TEM histograms (b).

Figure 3.14. Comparison of experimental SAXS profile of sample A1 (in Na^+ form) with that fitted with form factor of cylinder (a), and diameter distributions of nanorods in membrane samples having Na^+ and Cs^+ ionic forms.

Figure 3.15. Ag nanostructures size distributions of the ascorbic acid reduced samples A2 (a) and A3 (b) obtained by SAXS analyses. The samples were converted to Na^+ and Cs^+ ionic forms after reduction.

Figure 3.16. Water cluster size distribution plots for ascorbic acid reduced samples in Na^+ (a) and Cs^+ (b) ionic forms.

Chapter 4

Figure 4.1. Schematic diagram of the experimental setup for in situ SAXS experiment.

Figure 4.2. In-situ time resolved SAXS profiles during the formation and growth of silver nanoparticles by ascorbic acid reduction in Nafion-117 membrane (a), and corresponding evolution of median diameter of silver nanoparticles (b) as a function of reduction time.

Figure 4.3. Temporal evolution of AgNPs size distributions deduced from SAXS profiles.

Figure 4.4. Time dependence of the number density (particles cm^{-3}) of AgNPs during in situ reduction.

Figure 4.5. TEM image of cross section of Ag^+ loaded Nafion-117 membrane subjected to reduction with L-ascorbic acid for 60 s in bulk (a) and in surface (b) and size distribution histogram of silver nanoparticles as obtained from the TEM images analysis (c).

Figure 4.6. TEM image showing the spatial distribution of silver nanorods across thickness of the membrane subjected to reduction with ascorbic acid for 5 min.

Chapter 5

Figure 5.1. Possible arrangement of functional groups in Selemion AMV ionomer.

Figure 5.2. Chemical structure of amberlite XAD-4 resin.

Figure 5.3. Schematic representation of the experimental set-up for the synthesis of AgNPs in ion-exchange membranes.

Figure 5.4. Time profile of Ag activity in Nafion matrix during the chemical reduction process at 75 °C. The solid line through the points is an eye guide.

Figure 5.5. TEM images along the thickness of the Selemion AMV membrane and respective size distribution profiles of formed nanoparticles after 10 min (a), 20 min (b), 40 min (c) and 80 min (d) of reduction.

Figure 5.6. Radial averaged SAXS profiles at different reduction time (a), the size distribution of the nanoparticles obtained from SAXS analyses (b) and the time dependence of the peak diameter and the relative number density (n_t/n_5) (c) in Selemion AMV matrix. The term 'n_t' and 'n_5' represents the number density of the nanoparticles at time t and 5 min respectively. Solid lines through the points are eye guide.

Figure 5.7. TEM images along the thickness of the Nafion 177 membrane and respective size distribution profiles of formed nanoparticles after 45 min (a), 90 min (b), 180 min (c) and 300 min (d) of reaction.

Figure 5.8. Radial averaged SAXS profiles at different reduction time (a), the size distribution of the growing nanoparticles obtained from SAXS analyses (b) and the time dependence of the peak diameter and the relative number density (n_t/n_{30}) (c) in Nafion 117 matrix. The term 'n_t' and 'n_{30}' represents the number density of the nanoparticles at time t and 30 min respectively. Solid lines through the points are eye guide.

Figure 5.9. Time dependence of the silver loading per unit area of (a) Selemion AMV membrane and (b) Nafion 117 membrane with and without silver seeds during the synthesis as obtained from radiotracer experiment. For pre-seeded Nafion membrane, mass given excludes the mass of pre-loaded silver seeds.

Figure 5.10. Digital photograph of the XAD-4 beads before and after treatment with [Ag-citrate] solution at 75 ^{O}C for 210 min.

Figure 5.11. FE-SEM images of the surface of a AgNP incorporated XAD-4 bead in secondary electrons imaging mode for surface topography (a) and backscattered electron imaging mode for elemental mapping (b). White dots represent the silver nanoparticles.

Figure 5.12. FE-SEM images of the interior of a AgNP incorporated XAD-4 bead in secondary electrons imaging mode for surface topography. White dots represent the silver nanoparticles (AgNPs).

Figure 5.13. FE-SEM image showing distribution of Ag nanoparticles (brighter spots) in nanoporous silica matrix.

Chapter 6

Figure 6.1. Pore size distribution of Amberlite XAD-4 beads as obtained from FE-SEM images.

Figure 6.2. Digital photograph of blank XAD-4 beads (a), XAD-4 beads equilibrated with aqueous solution of $HAuCl_4$ and EG for 48 h, the colour in the beads is due to formation of AuNPs (b), XAD-4 beads containing AgNPs (c), XAD-4 beads containing AuNPs (d).

Figure 6.3. FE-SEM image of the surface of the XAD-4 bead showing blank matrix.

Figure 6.4. FE-SEM images (secondary electrons mode) at different magnifications of the surface of a XAD-4 bead after treating with an aqueous solution of EG and $AgNO_3$ (a and b), EG and $AuCl_4^-$ (c and d), EG and $PtCl_6^{2-}$ (e and f). Clusters of bright spherical objects near the nanoscale crevices represent the respective metal nanoparticles as produced.

Figure 6.5. FE-SEM images showing distributions of Pt nanoparticles in XAD-4 beads after nanoconfined reduction of $PtCl_6^{2-}$ ions with EG at 25 ^oC (a), EG at 80 ^oC, (b) and BH_4^- at 80 ^oC (c).

Chapter 7

Figure 7.1 Digital photograph of the portable UV-VIS spectrometer system (K-MAC, Korea) used in the present study.

Figure 7.2. TEM images showing spatial distribution of AgNPs across thickness of the membrane subjected to reduction with ascorbic acid for 1 min (a) and 5 min (b).

Figure 7.3. Successive UV-VIS spectra of catalytic reduction of MB by $NaBH_4$ in the presence of silver nanosphere (1 min reduction) embedded Nafion-117 membrane (a), and variation of logarithm of A_t/A_0 as a function of reduction time in the presence of AgNPs loaded membrane samples formed by ascorbic acid reduction for 1 min (Δ) and 5 min (O) (b). The dashed line plot (X) shows the variation of A_t/A_0 with time in absence of the reducing agents (only because of diffusion of MB through AgNPs (1 min) embedded Nafion). A_t and A_0 represent absorbance of 665 nm at time t and initial time, respectively.

Figure 7.4. UV-Vis spectra obtained as a function of time during reduction of para-nitrophenolate anions (PNP) to para-aminophenol (PAP) with BH_4^- ions in presence of XAD-4 beads containing silver nanoparticles.

Figure 7.5. Variation of logarithm of A_t/A_0 as a function of time during reduction of PNP to PAP in presence of poly(styrene) beads containing Ag nanoparticles formed by nanoconfined reduction with EG. A_t and A_o represents absorbance of 400 nm at time t and initial, respectively.

Figure 7.6. FE-SEM image of the surface of a pristine polypropylene membrane (a), the pore filled AEM with dense surface and fibrous interior (b), EDS mapping showing the spatial distribution of (3-acryloxy propyl) trimethoxy silane (c), (3-acrylamido propyl) trimethyl ammonium iodide (d), and combined distribution of both Si and I (e) across the membrane thickness. Red dots and green dots represent Si and I respectively.

Figure 7.7. FE-SEM images of surface (a) and interior (b) of Ag@AEM composite membrane after 20 min of reduction.

Figure 7.8. Radial averaged SAXS profiles at different reduction time (a), the size distribution of the nanoparticles obtained from SAXS analyses (b), and the time dependence of the peak diameter and the relative number density (n_t/n_5) of the nanoparticles(c). n_t and n_5 represent the number density of the particles at time t and 5 min, respectively. Solid lines connecting the points are eye guide.

Figure 7.9. FE-SEM images of Ag@AEM composite after 20 min reduction (a), 40 min reduction (b), 60 min reduction (c) and respective size distribution profile of the nanoparticles (d).

Figure 7.10. Time dependent profile of silver loading per unit area of AEM (mg cm^{-2}) during redox decomposition of silver-citrate complex.

Figure 7.11. Time resolved UV-VIS absorption spectra for the catalytic reduction of para nitrophenol (PNP) with four different catalyst membrane containing AgNPs of median diameter (SAXS data) 17 nm (a), 20 nm (b), 30 nm (c) and 61 nm (d).

Figure 7.12. Variation of logarithm of (A_t/A_0) with time during the catalytic reduction of para nitrophenol (PNP) with four different catalyst membrane containing AgNPs of median diameter (SAXS data) 17 nm (a), 20 nm (b), 30 nm (c) and 61 nm (d).

Figure 7.13. The plot of logarithm of activity parameter with inverse of diameter (a), and the variation of activity parameter ($s^{-1}g^{-1}$) with number of catalytic cycle for four different catalyst membranes (b).

Figure 7.14. Time resolved UV-Vis absorption spectra during the room temperature BH_4^- reduction of para nitrophenol (PNP) to para aminophenol (PAP) in presence of blank nanoporous XAD-4 beads (a) and blank AEM (b) without nanoparticles. Inset in Figure 7.14a shows the digital photograph of the cuvette at start (yellow solution of PNP) and at end (colourless solution of PAP) of the reaction.

Figure 7.15. The UV-Vis absorption spectra of PNP in solution containing excess of $NaBH_4$ at different time period.

Chapter 8

Figure 8.1. UV-Vis absorption spectrum of SDS and PVP stabilized unconfined silver nanoparticles prepared by BH_4^- reduction.

Figure 8.2. Size distribution of PVP stabilized unconfined silver nanoparticles prepared by BH_4^- reduction as obtained from DLS study.

Figure 8.3. FESEM image of the Ag@XAD nanoreactor. White spots represent silver nanoparticles.

Figure 8.4. Variation of logarithm of (A_t/A_0) with time at $\lambda = 400$ nm during catalytic reduction of para nitrophenol (PNP) with variable initial concentration of PNP using AgNPs@XAD-4 catalyst. Solid lines connecting the points are eye guide.

Figure 8.5. Variation of normalized rate constant (sec^{-1}) with bulk PNP concentration (mM) during room temperature BH_4^- reduction of PNP using PVP and SDS stabilized bare AgNPs (control experiment) and spatially confined AgNPs in XAD-4 beads as catalyst. Solid lines connecting the points are eye guide.

List of Schemes

Chapter 3

Scheme 3.1. Chemical reactions involved during the reduction of silver ions with formamide.

Scheme 3.2. Resonance structures in the conjugate bases of L-ascorbic acid. H_2A, HA^- and A^{2-} represents the neutral, mono-protonated and deprotonated form of ascorbic acid.

Scheme 3.3. Stoichiometric equation for the reduction of silver ions by L-ascorbic acid.

Chapter 5

Scheme 5.1. Proposed mechanism of redox decomposition of silver citrate complex in the nanoconfinement of ionomer matrices at 75 ^{O}C.

Scheme 5.2. Mechanism of the thermal oxidation of citrate on AgNP and the autoreduction of Ag^+ on AgNP surface at high temperature.

Scheme 5.3. Proposed mechanism of nanoparticles growth in both Selemion and Nafion membrane by citrate complex route. The bimodal particle distribution has been schematized in a combination of yellow (silver seeds) and green (silver particles) spheres for clarity.

Chapter 6

Scheme 6.1. Chemical reactions involved for the ethylene glycol reduction of metal ions.

List of Tables

Chapter 2

Table 2.1. Routes of synthesis of metal nanoparticles as carried out during the present study.

Table 2.2. Commonly used radiotracers, their production routes and decay characteristics.

Chapter 5

Table 5.1. Peak diameter of the growing AgNPs in different matrices and their relative number density.

Chapter 7

Table 7.1. Comparison of rate constant (k) and activity parameter (κ) of different AgNPs catalysts during reduction of PNP with $NaBH_4$ at room temperature.

Abbreviations

2θ : scattering angle

AEM : Anion exchange membrane

AEM : Anion exchange membrane

AFM : Atomic force microscopy

AFM : Atomic force microscopy

AgNP : Silver nanoparticle

APMC : (3-acrylamido propyl) trimethyl ammonium chloride

APTMS : (3-acryloxy propyl) trimethoxy silane

BEP : Brønsted−Evans−Polanyi

Bq : Becquerel

Ci : Curie

CTAB : Cetyl tri-methyl ammonium bromide

DESY : Deutsches Elektronen-Synchrotron

DLS : Dynamic light scattering

DLVO : Derjaguin-Landau-Verwey-Overbeek

DMF : Dimethyl formamide

DMPA : α-α’-dimethoxy-α-phenyl acetophenone

DOS : Density of states

EDGM : Ethylene glycol dimethacrylate

EG : Ethylene glycol

FE-SEM : Field-emission scanning electron microscopy

h : Plank constant

ICP-AES : Inductively coupled plasma atomic emission spectroscopy

ICP-OES	: Inductively coupled plasma optical emission spectrometry
IES	: Ion-exchange sites
MB	: Methylene Blue
MCA	: Multichannel analyzer
NMR	: Nuclear magnetic resonance
PAP	: Para aminophenol
PMO	: Periodic mesoporous organosilica
PMT	: Photomultiplier tube
PNP	: Para nitrophenol
PTFE	: Polytetrafluoro ethylene
PVC	: poly vinyl chloride
PVP	: Poly vinyl pyrrolidone
SANS	: Small angle neutron scattering
SAXS	: Small angle X-ray scattering
SDS	: Sodium dodecyl sulfate
SEM	: Scanning electron microscopy
SPM	: Scanning probe microscopy
STM	: Scanning tunneling microscopy
TEM	: Transmission electron microscopy
UV-VIS	: Ultraviolet visible
WAXS	: Wide angle X-ray scattering
XAFS	: X-ray absorption fine structure

Chapter 1

Introduction

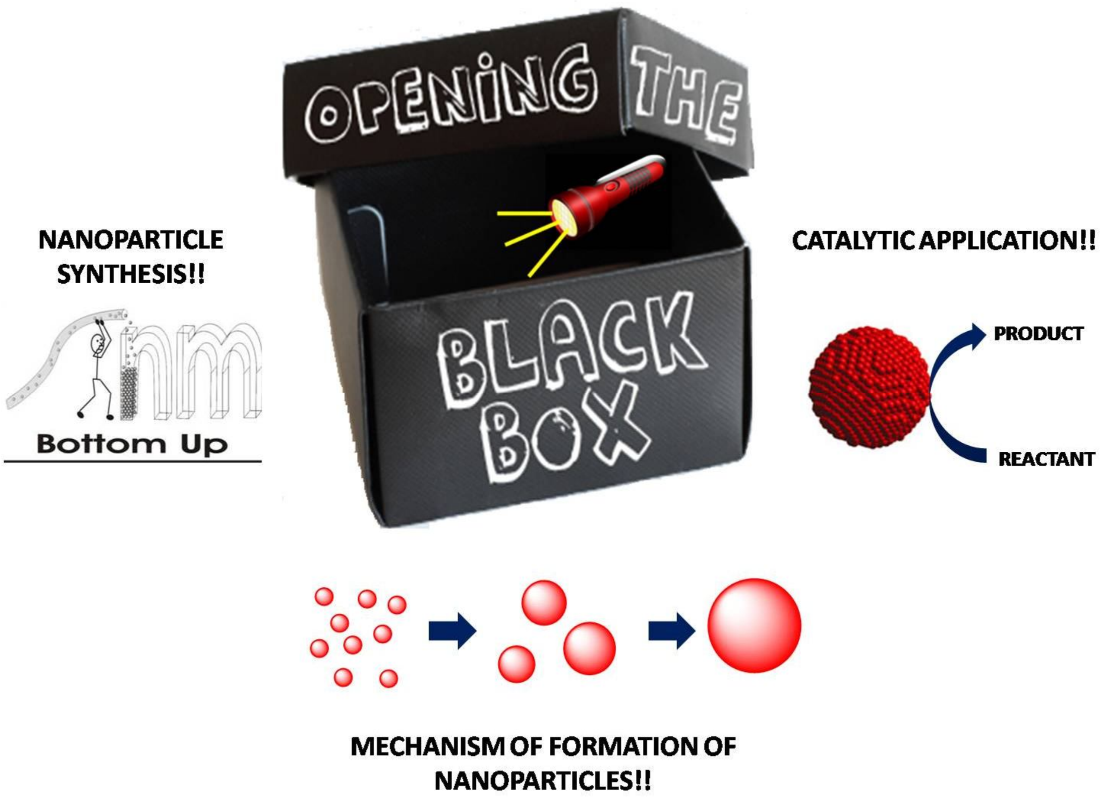

1. Nanochemistry: the Chemistry of Small

The area of nanoscale science and technology has grown rapidly in recent years and is expected to make a paradigm shift in the history of science. Nanotechnology is not just a tool to get a better answer to a problem in a smarter way, but a new approach to tackle a problem with a new set of game rules [Cademartiri and Ozin 2009]. Nanochemistry, in specific, provides a unique approach to build devices with a molecular-scale precision. The full utilization of nanochemistry in building today's technology needs detailed understanding of the system which lies at the threshold between classical and quantum laws of physical science [Díaz and Bohn 2004]. The concept of nanoscience was first propounded about 55 years ago, by the famous physicist Richard Feynman when on December, 1959 he asked at an American Physical Society meeting at Caltech, "What would happen if we could arrange the atoms one by one the way we want them?" [Clinton 2000]. Feynman highlighted the possibility of direct manipulation of atoms as a more promising form of synthetic chemistry. Unfortunately the talk was unnoticed for long time and it didn't boost the conceptual growth of the subject. The field started developing with a rapid pace after the development of many advanced instruments necessary for studying the nanoworld [Díaz and Bohn 2004]. These include the atomic force microscope (AFM), scanning tunneling microscope (STM), high resolution scanning and transmission electron microscopies (SEM and TEM), X- rays, ion and electron beam probes etc.

Nanochemistry is a new area of chemistry within the broad field of nanoscience and nanotechnology, where chemistry enters the nanodomain [Tersoff 2001, Ball 2000, Sohn 1998]. It should be noted that the basic concept of nanochemistry, nanophysics, nanobiology and nanoengineering are same. The difference is only in the way of using the concepts to solve a problem. The prefix nano- was born from the early surprising observation that materials exhibited unusual properties when their size lay in the nanometer scale. Nanochemistry was then defined as the science of synthesising nanoscale materials showing size dependent effects. Later on it has been realized that nanochemistry is not only just a method to prepare nanostructures [Ozin 1992, Whitesides 1998], but it also deals with extraordinary size-dependent effects emerging from confined states of all matter [Ozin et al. 1998, Thomas et al. 2003]. A spatial confinement of different length scale can influence the properties of matter differently. Larger size confinement (2-50 nm) can be used for the preparation of colloidal nanostructures by way of restricting the uncontrolled growth. However, at spatial confinement of smaller sizes (1-10 nm), molecular events such as the outcome of a chemical reaction might be influenced [Thomas et al. 2003].

1.1. Nanomaterials

Materials confined to nanosizes exhibit different behaviour in comparison to their bulk state. The optical, electronic, mechanical, thermal and catalytic properties of materials are significantly modified in nanoscale. Although nanochemistry research has picked up momentum in the past few years, nanoscale materials are being used since ancient age. Figure 1.1 shows some centuries old artifacts, where colour is attributed to gold nanoparticles.

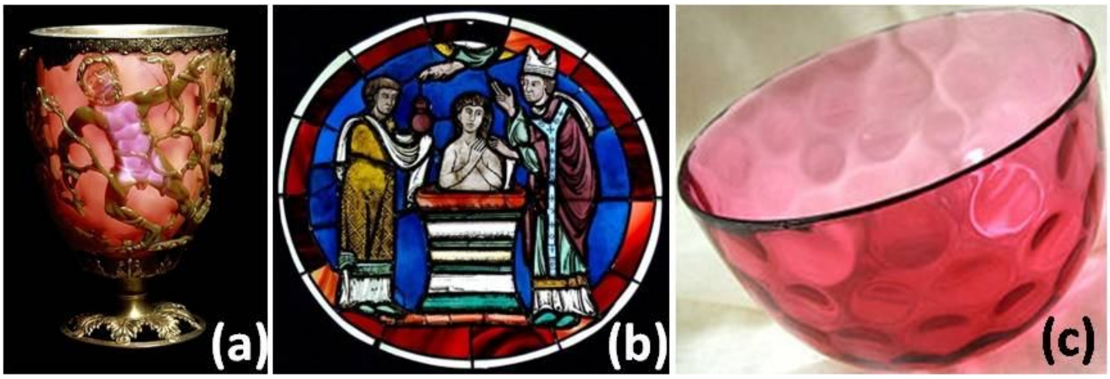

Figure 1.1. The 4th century Roman Lycurgus cup (a), Centuries ago decoration of stained glass with gold nanoparticles in Europe (b), and Cranberry glass bowl prepared by adding a gold salt to molten glass (c).

Attention is now focused on synthesising nanostructured materials by direct manipulation of atoms or clusters. The question that is frequently asked: "How small or big are nanomaterials?". One simple answer is that nanomaterials are intermediate in size between isolated atoms or molecules, and bulk materials. By definition nanoscale materials are identified as materials having length between 1 to 100 nm atleast in one dimension. They contain approximately 1-10000 atoms. The nanomaterials can be broadly classified into two types: (i) nanoparticles and (ii) materials with nanoscale morphology (e.g, nanoporous materials). Nanochemistry is fast evolving as a new branch of chemistry. Nanochemists manipulate materials at nanoscale by chemical means. Chemists have successfully made use of their knowledge to synthesize not only nanostructured materials having desired size and shape, but also engineered bulk scale materials with unique properties by self-assembly of nanostructured materials. The power of chemistry has been remarkably enhanced because of the possibility of manipulating the size of nanomaterials to fine tune their physical and chemical properties.

It is known since long time that diamond and graphite are different allotropic forms of carbon which highly differs in their structures, bonding and different physical and chemical characteristics. However, some new forms of carbon like fullerenes (C60, C70, and others) and carbon nanotubes have been discovered recently showing wonderful properties. The nature of chemical bonding in a nanomaterial is different from that in bulk. Also, the property of the atom at the surface of a material is entirely different than the property of an atom at bulk.

Though the unusual properties of nanomaterials have been witnessed since ancient time, only in the last one or two decades, chemists are synthesizing nanomaterials in controlled and reproducible manner and investigating their unique properties. These developments have become possible due to advancement of characterization techniques like electron microscopy and X-ray based scattering techniques. There are mainly two types of size-dependent effects observed in nanomaterials: (i) variation of fraction of total number of atoms at the surface, and (ii) quantum confinement effects [Roduner, 2006].

1.1.1. Effect of Surface: From Bulk to Nanoscale

The surface area of a spherical object is directly proportional to the square of its radius, whereas its volume is directly proportional to the cube of its radius. Also, the total number of atoms (N) in a spherical object is directly proportional to its volume. Therefore the fraction of surface atoms is directly proportional to the surface area divided by the volume, i.e. with the inverse radius or diameter of the object. Therefore, the fraction of surface atoms, also called the dispersion is directly proportional to $N^{-1/3}$. Figure 1.2 gives the evolution of the dispersion as a function of $N^{1/3}$ for cubic clusters.

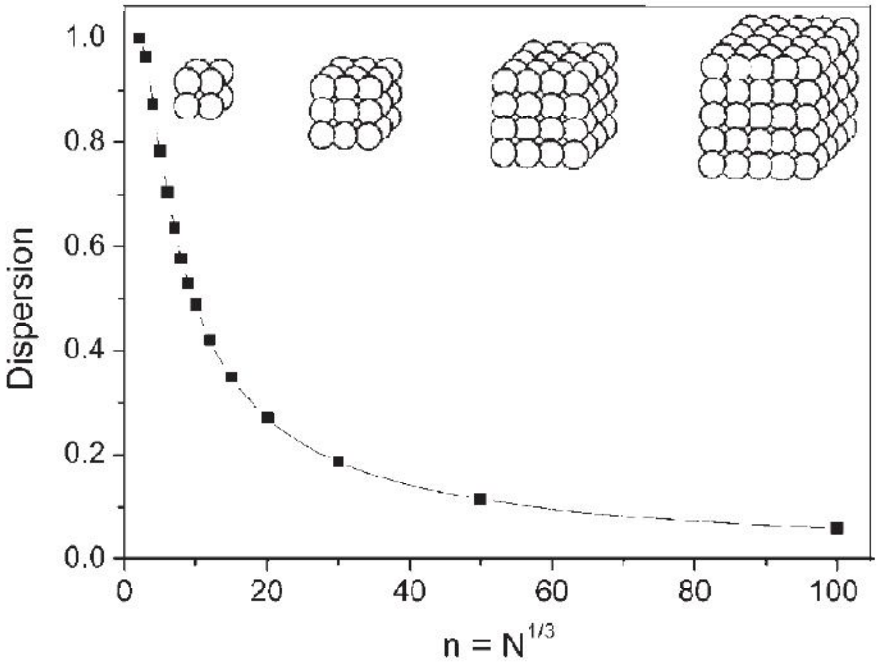

Figure 1.2. Variation of the dispersion (F) as a function of n for cubic clusters up to n = 100 (N = 10^6). The structure of the first four clusters is shown. [Roduner, 2005]

The sharp change in dispersion at $n \leq 20$ i.e., $N \leq 8000$ atoms shows that the extraordinary nano effect appears in nanoparticles with this range of number of atoms. The nanoparticles are having a lower mean coordination number and high surface energy in comparison to bulk materials. The cohesive energy (binding energy per atom) also varies in the same manner from bulk to nano materials as the coordination number [Roduner, 2006]. Because the surface atoms or edge atoms are poorly coordinated than the bulk atoms in a nanoparticle, they have very high affinity for binding the adsorbate molecules. For a non spherical particle, the affinity is highest for corner atoms (least coordinated) followed by edge atoms (moderately coordinated) followed by bulk interior atoms (highest coordinated). Because of their low mean coordination number and low mean cohesive energy, nanomaterials exhibit unusual properties such as lower melting temperature in comparison to bulk phase melting temperature of the same material [Roduner, 2006.; Unruh et al, 1993].

1.1.2. Quantum Effect: Change in Electronic States

As the sizes of the nanomaterials are closer to single atoms or molecules in comparison to bulk materials, quantum size effect starts appearing. The solution of Schrödinger wave equation for an electron and hole in a 3D, 2D or 1D box gives the individual energy states of the materials. The band structure of solid is modified from bulk to nano materials. Set of discrete energy levels appears and their energy separations display an analytic dependence on the spatial dimension of the material [Ozin and Arsenault, 2008]. This results in modification of optical, magnetic and catalytic behavior.

The change in the structure of energy levels can be explained in terms of density of states (DOS). The size dependence of density of states (DOS) is not continuous like the surface effect. This discontinuity in the energy levels density comes from the basic approximation of “particle in a box”, where the size of the box is assumed to be the size of the particle. Figure 1.3 gives the density of states (DOS) diagram at different cluster sizes. The discretization of the electronic states (which are continuous in bulk materials) and a bandgap widening makes some nanoparticles strongly fluorescent (for example CdS, PbS etc.). The magnetic properties of a material are also expected to be modified at nanoscale. Catalytic behavior is also altered in nanoparticles of dimension $\leq$ 10 nm due to this quantum effect.

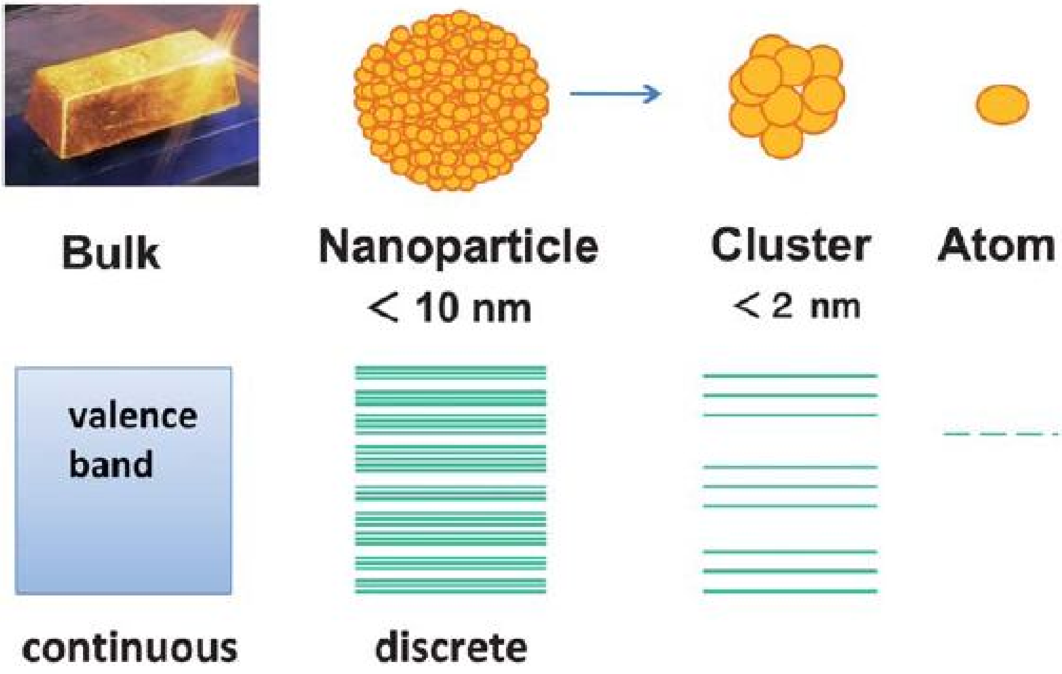

Figure 1.3. Density of states (DOS) diagram for valence band structures of bulk, nanoparticles, clusters, and atoms. [Haruta 2011]

1.2. Synthesis and Stabilization of Nanomaterials

Nanomaterials can be broadly classified into two types: (i) nanoparticles and (ii) materials with nanoscale morphology (e.g, nanoporous materials). Wide variety of methods is used prepare nanomaterials with various morphologies. These methods falls under two basic categories: (i) bottom up and (ii) top down. Each approach has its own limitation in terms of feature size and quality of the nanomaterials produced. Figure 1.4 gives the schematic chart of different bottom up and top down techniques available for the synthesis of different types of nanomaterials and products.

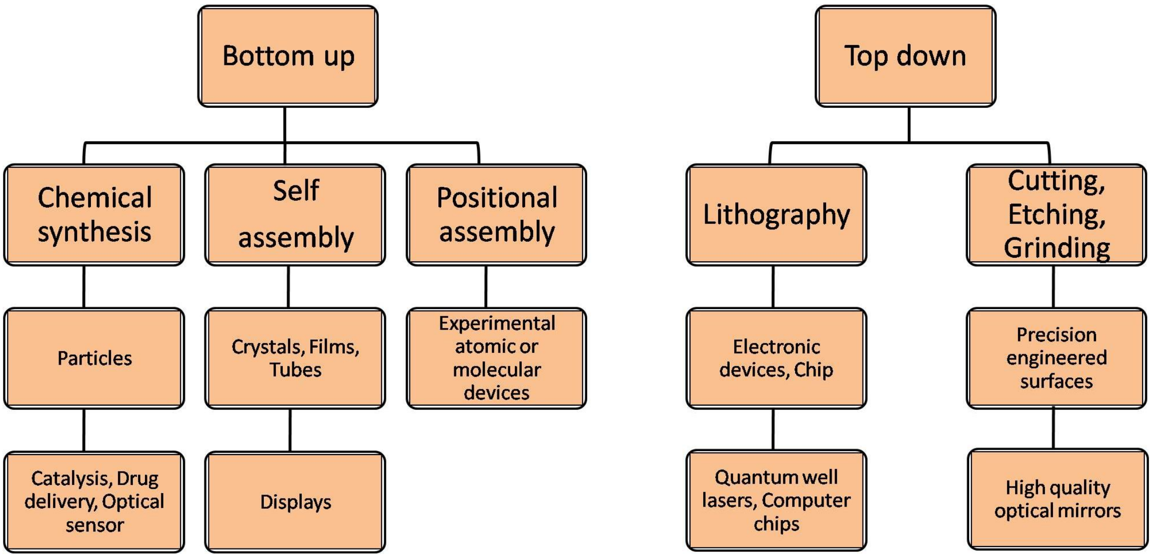

Figure 1.4. The use of bottom-up and top-down techniques in nanomanufacturing.

1.2.1. Bottom up Techniques

Bottom up approaches of nanomaterials synthesis involves the preparation of nanostructures by atom-by-atom or molecule-by-molecule manipulation. This approach can be split into three categories: chemical synthesis, self-assembly, and positional assembly.

(i) Chemical Synthesis: A well described chemical reaction is performed to generate nanoparticles of the desired material. Chemical synthesis of nanomaterials provides opportunity for preparing raw materials such as nanoparticles, which can be further used directly in products or as the building block materials for the preparation of other advanced materials. The chemical synthesis of nanomaterials begins from a precursor phase, where the materials can be in any physical state.

(ii) Self Assembly: Self-assembly is the bottom up method of preparing ordered nanoscale structures where atoms or molecules arrange themselves by physical or chemical interactions between the small nanoscale units. In chemistry the most common example of self assembly process is the formation of salt crystals. In nature self assembly is a common process. However, the commercial use of such process in industry is relatively recent. There is a serious need of economically cheaper and also environmentally benign methods for nanomaterial synthesis or nanomanufacturing. Self-assembly processes generate less waste and also require minimum energy, but till now are applicable only to the preparation of rudimentary systems. Recent advances in the characterization techniques and improved computer modeling has helped in understanding the thermodynamics and kinetics at nanoscale. This holds promises for further development of more complex nanoscale systems. In industry, directed self assembly is much adopted technique. Directed self assembly is an advanced self-assembly technique, where an external electric/magnetic field is applied in order to accelerate the self assembly process.

(iii) Positional Assembly: In this method of nanomaterial synthesis, the atoms, molecules or clusters are directly manipulated and positioned one-by-one. Scanning probe microscopy (SPM) and optical tweezers based techniques are generally used for nanomanufacturing on the surface and in free space respectively. However, being extremely laborious technique, this method is not much adopted as an atomic-scale industrial process.

1.2.2. Top down Techniques

In the top down methods, the nanomanufacturing process begins with a large piece of material and reach to a nanostructured material by the way of etching, milling or machining, producing more waste than bottom up methods. This approach can be split into the categories: Precision engineering and lithography. One important example of nanostructured material formed by top down method is the production of computer chips, where the bottom up synthesis is not yet possible.

1.2.3. Stabilization of Nanomaterials

Because of high surface energy, nanomaterials are unstable and tend to agglomerate into bigger particles in order to reduce the surface energy. As a result of agglomeration, the properties associated with the colloidal state of these particles are lost. For example catalytic activity of smaller colloidal particles is significantly lost when they coagulate into bigger particles during catalysis. Thus long term stabilization of colloidal nanomaterials in their finely dispersed state is a challenge during nanomaterials synthesis. When the interparticle distance between two nanoparticles is short, the particles experience attractive van der Waals forces to each other. The extent of van der Waals force varies inversely as the sixth power of the distance between the surfaces of two adjacent particles. Thus in order to stabilize the nanoparticles from agglomeration, a repulsive force opposed to the van der Waals forces is needed. External stabilizing agents are used in order to induce a repulsive force between the nanoparticles. The mechanism of stabilization of colloidal nanomaterials has been described in Derjaguin-Landau-Verwey-Overbeek (DLVO) theory [Evans and Wennerstrom 1999]. Nanocluster stabilization can be primarily categorized in two types: (i) charge stabilization and (ii) steric stabilization. Based on the types of stabilizing agent used, it can be further distinguished into five kinds of stabilization procedures: (i) electrostatic stabilization with the adsorbed anions on surfaces, (ii) steric stabilization with the presence of bulky groups, (iii) electrosteric stabilization (combination of these two kinds of stabilization) with the presence of surfactants, (iv) stabilization with a ligand or solvent, and finally (v) stabilization in structured media such as glasses, polymers, molecular sieves etc.

(i) Electrostatic Stabilization: Electrostatic stabilization can be induced in aqueous colloidal solution by dissolving ionic compounds such as halides, carboxylates, or polyoxoanions. An electrical double layer is formed around the particles by the adsorption of these species on the surface of colloidal metal nanoparticles, which results in a repulsive coulombic interaction between the particles (Figure 1.5). When this repulsive interaction overcomes the van der Waals attractive forces, the particles agglomeration is prevented.

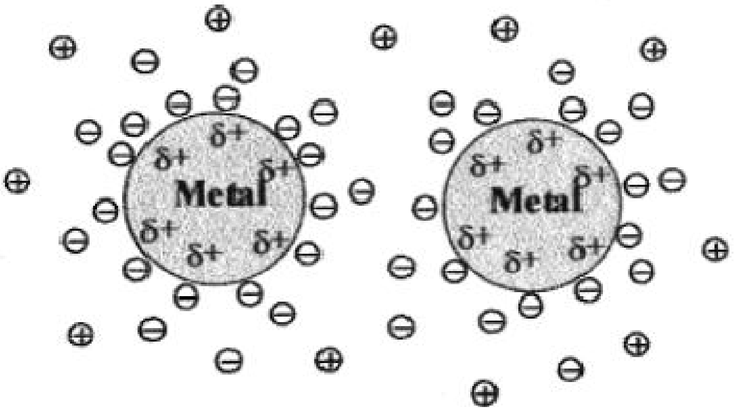

Figure 1.5. Schematic representation of electrostatic stabilization of colloidal metal nanoparticles. [Roucoux et al. 2002]

(ii) Steric Stabilization: Adsorption of macromolecules at the surface of the nanoparticles provides a protective layer and prevents nanoparticles agglomeration [Hunter 1987.; Napper 1983]. The restrictions in motion of the adsorbed macromolecules in the interparticle space lead to decrease in entropy and thus increase in free energy. Also, due to increase in local concentration of the adsorbed macromolecules in the interparticle space results in osmotic repulsion between the two adjacent particles in order to reestablish the equilibrium by diluting the macromolecules and thus separating the nanoparticles (Figure 1.6). Examples of different aqueous and non-aqueous steric stabilizers are poly(acrylamide), poly (vinyl pyrrolidone), poly (vinyl methyl ether), polystyrene, poly (lauryl methacrylate) etc.

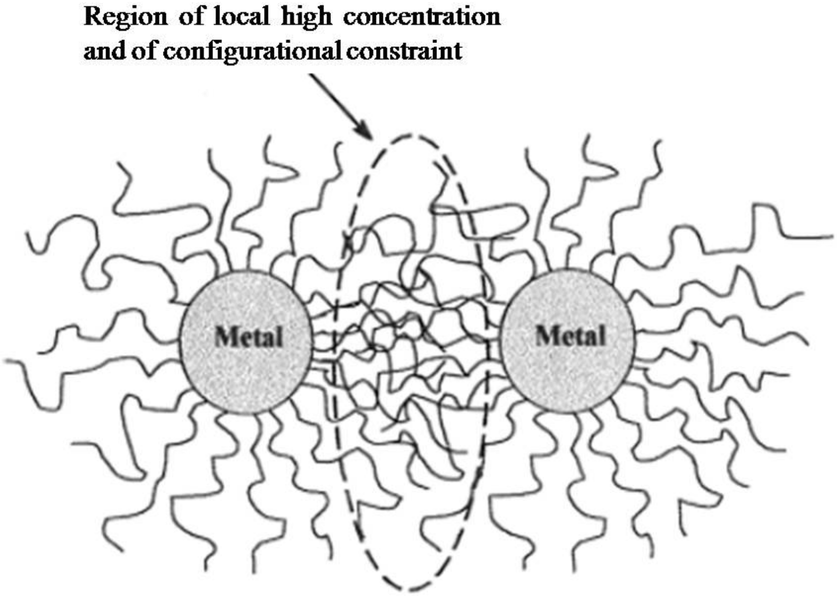

Figure 1.6. Schematic representation of steric stabilization of colloidal metal nanoparticles. [Roucoux et al. 2002]

(iii) Electrosteric Stabilization: This kind of stabilization is usually induced by ionic surfactants, where the electrostatic and steric stabilization are combindly effective [Aiken et al. 1996.; Lin and Finke 1994]. Being amphiphilic in nature, these surfactants contain a polar head group and a non polar hydrophobic tail. The head part generates the electrostatic repulsion by generating an electrical double layer and the tail part provides the steric repulsion. Typical examples are sodium dodecyl sulphate (SDS), cetyl trimethyl ammonium bromide (CTAB) etc.

(iv) Stabilization with a Ligand or Solvent: Stabilization of colloidal nanoparticles with traditional ligands occurs by the coordination of nanoparticles with specific ligands such as thiols [Dassenoy et al 1998.; Chen and Kimura 2001], phosphines [Schmid et al. 1981.; Amiens et al. 1993.; Duteil et al. 1995], amines [Schmid et al. 1989.; Schmid et al. 1996.; Schmid et al. 1996] or carbon monoxide [Rodriguez et al. 1996]. Some solvents like tetrahydrofuran, thioethers, etc. also provide stability to colloids without adding any steric or electrostatic stabilizers.

(v) Stabilization in Solid Confined Media: Stabilization of nanoparticles in solid matrices has been regarded as one of the best ways to overcome the problem of self-agglomeration. Various structured media like layered solids, molecular sieves, micelles/microemulsions, gels, polymers, and glasses have drawn considerable attention as the media for nanoparticle synthesis [Lithikar et al. 2007.; Papp et al. 2001.; Shchukin and Sukhorukov 2004.; Mohan et al. 2006.; Jeon et al. 2011.; Simo et al. 2012].These media can influence the growth kinetics by imposing constraints in the form of confinement in nanopores or nanochannels. Such composites are promising materials for heterogeneous catalysis because of their high stability, and appreciable reactivity. There are other substrates with high surface area and good stability like metal oxide, active carbon, carbon nanotubes, graphene oxide, carbon nanofibres, magnetic nanoparticles, mesoporous silica, hybrid periodic mesoporous organosilica (PMO) yolk-shell structures, halloysite nanotube, mesoporous g-C_3N_4 nanorods, hydrogels, resin beads, which have been used as metal nanoparticle support over the years [Zhu et al. 2013].

Ion-exchange membranes (ion containing polymer) provide superior platform for the synthesis of metal nanoparticles because of their homogeneity, transparency and imparting excellent stability to the metal nanoparticles and smaller clusters. The unique bicontinuous morphology of ion-exchange membranes in a combination of hydrophilic and hydrophobic nanodomains makes such materials as nanoreactors. These composites may have wide range of potential applications in catalysis, sensorics, optoelectronics, electrochemical studies and artificial muscles [Sanchez et al. 2005.; Corma et al. 2008.; Wang et al. 2003.; Selvaraju and Ramaraj 2005.; Ramaraj 2006.; Selvaraju et al. 2008.; Xing et al. 2011.; Hirano et al. 2011.; Shahinpore et al. 1998.; Kim and Shahinpore 2003.; Shahinpore and Kim 2005]. Metal nanoparticles hosted in ion-exchange membranes are good candidates for use in heterogeneous catalysis because of high thermal, chemical and mechanical stability and good contact of the reactants with the nanoparticle surfaces by the way of diffusion through hydrophilic channels. Also the membrane based catalyst can be easily separated from the reaction media after the completion of the reaction. Apart from ion-exchange membranes, there are other mesoporous substrates like nanoporous polymer resin beads (for example Amberlite XAD-4), nanoporous silica gel particles also provide excellent stability to the nanoparticles. Detailed discussion on various types of mesoporous host materials is given in Section 1.4.

1.3. Thermodynamics and Kinetics of Formation of Nanoparticles

1.3.1. Thermodynamics of Nanoparticles Stability: Classical Nucleation Theory

Nucleation is the first step during the formation of a new thermodynamic phase or a new structure via self-assembly or self-organization. Nucleation is typically defined as the process that determines the rate at which the nuclei of new phase or self-organized structure appears. Classical nucleation theory is the most fundamental theoretical model which explains the origin of different nucleation time for different cases (subseconds or minutes or hours or years or sometimes never happen).

The classical theory assumes that the ΔG_{tot} of forming the nucleus of a spherical crystal of radius r in a liquid is the sum of bulk volume (ΔG_v) and surface (ΔG_s) free energy terms.

$$\Delta G_{tot} = \Delta G_v + \Delta G_s = \frac{4\pi r^3 \rho \Delta\mu}{3} + 4\pi r^2 \gamma \qquad (1)$$

The first term is proportional to volume of the nucleus, while the second term is proportional to the surface area of the nucleus. The term r denotes the radius of nucleus (considering spherical shape of the nucleus). ρ denotes the density of the bulk phase and $\Delta\mu$ denotes the difference in chemical potential between the thermodynamic phase nucleation is occurring in, and the phase that is nucleating [Nielsen et al, 1993]. $\Delta\mu$ is always negative. γ denotes the surface tension of the nucleus, which is always positive.

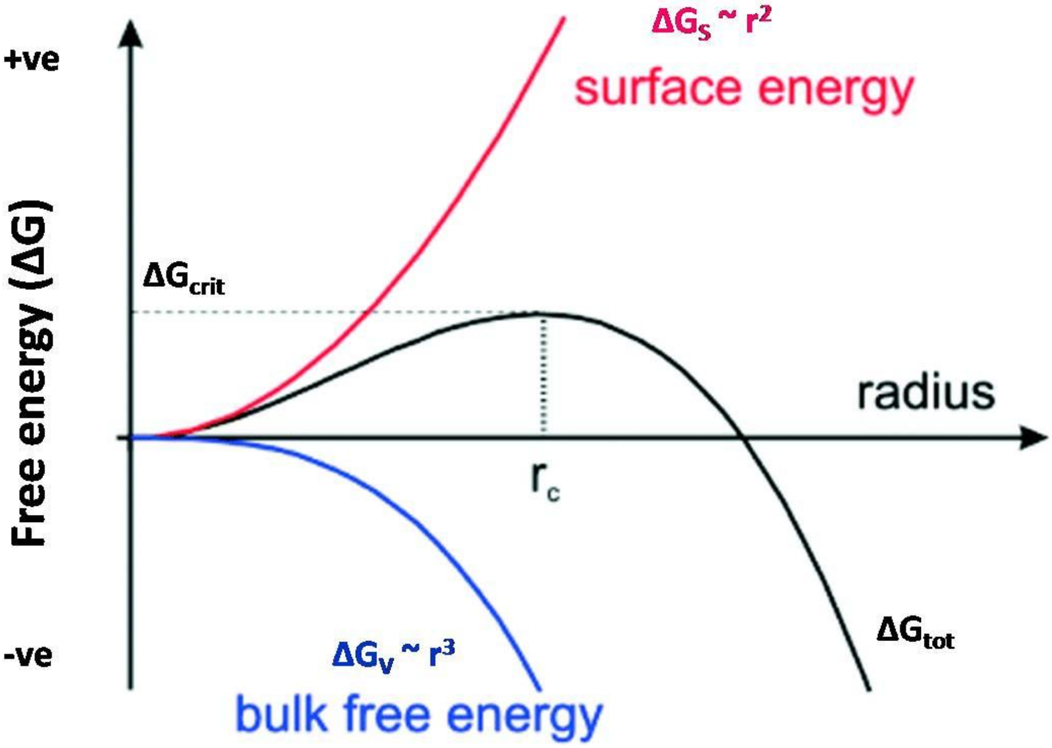

Figure 1.7. Variation of surface and volume contribution to the total free energy with nanoparticle growth. ΔG_{tot} reaches a maximum at a critical radius r_c.

The first term is negative and decreases as r^3 while the second term is positive and increases as r^2. Thus ΔG passes through a maximum as shown schematically in Figure 1.7. The maximum value of ΔG (ΔG_{crit}) is called activation barrier for nucleation. The corresponding value of r (r_c) is called critical radius for nucleation. This critical radius corresponds to the minimum size at which a nucleus can survive in solution without being redissolved [Thanh et al. 2014]. Therefore, if a nucleus crosses this barrier during the stage of nucleation, it will grow in size to form nanoparticle, otherwise it will redissolve. The value of ΔG_{crit} and r_c is governed by $\Delta \mu$ and γ, and is characteristic of the crystals. Further addition of new atoms to nuclei larger than this critical radius decreases the free energy, so these nuclei are more probable. According to transition state theory, the rate of nucleation will be governed by the activation barrier (ΔG_{crit}) and temperature.

1.3.2. Mechanism of Formation of Metal Nanoparticles: Journey from a Molecular Precursor to Metal Nanoparticles

Size control of metal nanoparticles provides an effective key to an accurate adjustment of their properties. The most common approach to control the size is testing different sets of synthesis parameters via trial and error. However the actual particle growth mechanisms, and in particular the influences of synthesis parameters on the nanoparticle growth process, remain a black box till today, making the precise size control of nanoparticles difficult [Wuithschick et al. 2013]. The mechanistic knowledge of metal nanoparticle synthesis is prerequisite for controlling the size and shape of nanoparticles.

The current state of understanding of nanoparticle synthesis can be compared with the organic synthesis over a century ago, when synthesis in organic chemistry was an empirical venture guided largely by chance experimentation, which had resulted in a catalog of useful but poorly understood procedures [Wang et al. 2014]. Empirical procedures have been developed over the years for the synthesis of a wide class of metal and semiconductor nanoparticles. In most of the cases, the synthetic procedures have been optimized to prepare nanoparticles of narrow size distributions and with better control over mean sizes. However, such approaches are more empirical art than science. Today's nanoparticle synthesis is not far ahead of trial and error stage. Without giving proper evidence, the mechanisms are sometimes invoked. Apart from the classical LaMer mechanism and Ostwald ripening, there exist no established growth mechanisms which can provide guidance for nanoparticle synthesis [Wang et al. 2014].

The processes of nucleation and growth of nanoparticles have been described by the LaMer burst nucleation model for many decades [LaMer and Dinegar 1950.; LaMer 1952]. Figure 1.8 gives the classical picture of homogeneous nucleation and growth based on LaMer model. Based on LaMer mechanism the process of nucleation and growth can be divided into three phases (i) production of monomers by a chemical reaction such that the concentration of free monomers in solution increase rapididly, (ii) the monomers undergo “burst nucleation” which significantly reduces the concentration of free monomers in solution. The nucleation rate is described as “effectively infinite” and after this point, the concentration of free monomers becomes too low in the solution that further nucleation is ceased; (iii) growth of the nanoparticles takes place by controlled diffusion of the monomers through the solution. The change in particle size during its formation has been also been described by Ostwald ripening model [Ostwald 1900], which was originally introduced by Reiss [1951] with an accepted model being developed by Lifshitz, Slyozov and Wagner [Lifshitz and Slyozov 1961.; Wagner 1961]. This is known as the Lifshitz-Slyozov-Wagner or LSW Theory of Ostwald ripening. Later Watzky and Finke [1997] proposed an approach of slow nucleation followed by autocatalytic growth. Ostwald ripening is a nanoparticle growth mechanism which describes the change of an inhomogeneous structure over time, i.e., small crystals or sol particles dissolve, and redeposit onto larger crystals or sol particles. Figure 1.9 gives the schematic representation of Ostwald ripening process.

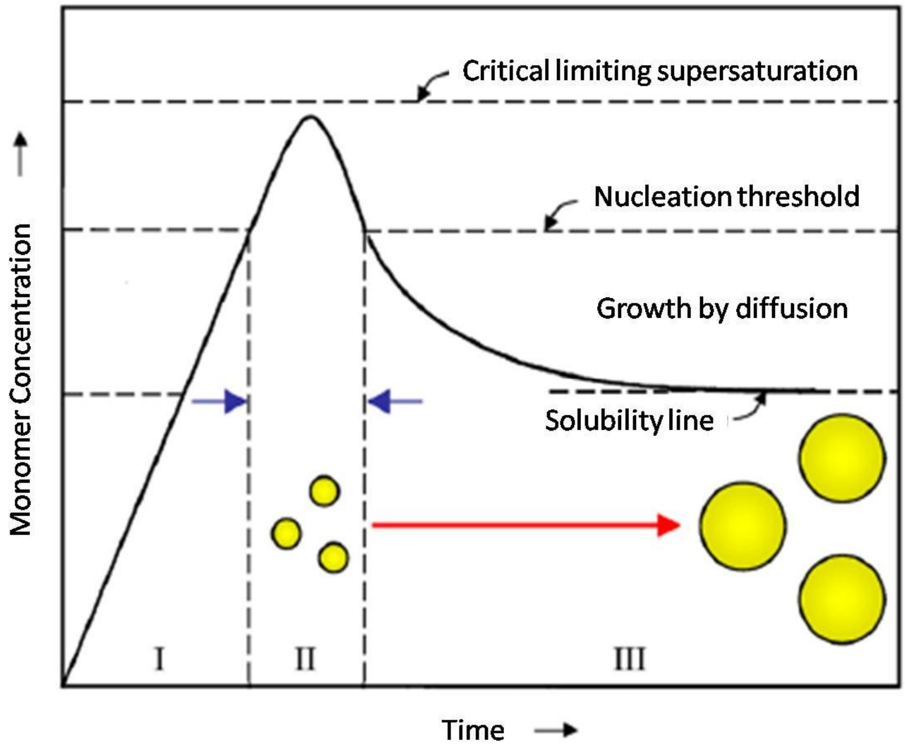

Figure 1.8. Schematic representation of variation of monomer concentration with time during particle nucleation and growth from solution in the classical LaMer mechanism. The blue arrows defines the nucleation period (zone II). The red arrow defines the growth period (zone III) [Wang et al. 2014].

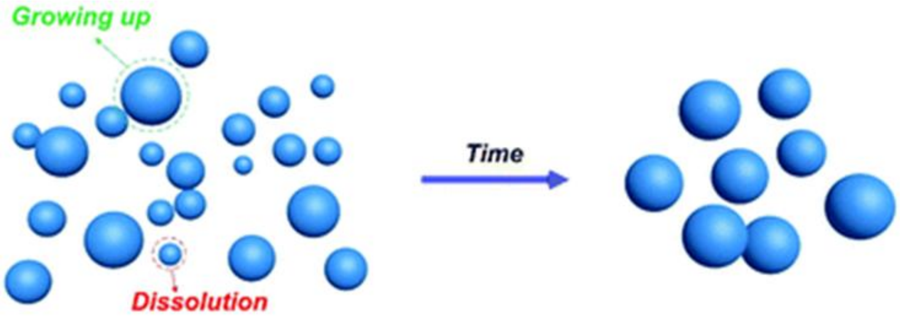

Figure 1.9. Schematic illustration of Ostwald ripening process [Wu et al. 2016].

Recently with the advancement of sophisticated characterization techniques, many research groups are performing experiments to understand the mechanism deeply. Ultraviolet-visible spectroscopy and small angle X-ray scattering (SAXS) are the two most commonly used techniques for time resolved mechanistic investigation [Rechards et al. 2010.; Polte et al. 2010.; Polte et al. 2010.; Takesue et al. 2011.; Harada et al. 2011.; Polte et al. 2012.; Sabir et al. 2012.; Sabir et al. 2013.; Chen et al. 2015.; Wuithschick et al. 2013.; Wang et al. 2014.; Simo et al. 2012.; Perala and Kumar 2013]. The application of some other technique like X-ray absorption fine structure (XAFS) spectroscopy in mechanistic investigation has recently been reviewed by Tanakaa et al [2012]. Thanh et al. [2014] has recently reviewed the nucleation and growth mechanism of noble metals, quantum dots and magnetic nanoparticles in solution. Though some literature exists on the mechanism of growth of nanoparticles in solution, there is limited study on nanoparticle growth mechanism in polymer matrices or in any other solid host matrices. There is lack of understanding about the parameters that control the nucleation and growth in both in solution as well as in solid matrices. A strong mechanistic basis for size controlled synthesis of nanoparticles will provide true control on the nucleation and growth stages.

1.4. Metal Nanoparticles as Catalyst

Metal nanoparticles form the basis for heterogeneous catalysis and electrocatalysis for future energy and fuel technology applications. Significant progress has being made in preparation of metal nanoparticles of different sizes and shapes during the last few decades. There has been a rapid progress in basic understanding of the particle size and shape effects, selectivity, and long-term stability of metal nanoparticle based catalysts [Xia et al. 2013]. Nanoparticle catalysts are superior in comparison to the bulk single crystals in terms of their activity due to enhanced number of dangling bonds per unit area compared to bulk crystals. This excess surface energy helps adsorbing reactant molecules on its surface providing an alternative reaction pathway with lower activation barrier. Additionally, the irregular surface of a nanoparticle provides a suitable environment with variety of defects, where catalytic reactions can take place. Also, because of sufficient flexibility of the surface atoms of small clusters, the nanoparticles surface can easily restructure as required during the catalysis process. However such restructuring is difficult in a bulk single crystal. Finally, because of increased Fermi energy level (the energy of the frontier orbitals) the availability of electrons for a redox process and for the formation of chemical bonds with the adsorbate molecules is more in a nanoparticle in comparison to a single crystal [Roduner 2005].

The interaction between an adsorbate and a metal catalyst can be explained based on molecular orbital (MO) theory. Both the noble metals and the transition metals are known for their superior homogeneous and heterogeneous catalytic activity. Nanoparticles based catalysis involves the formation of bonds between reactant molecules and the surface atoms of the nanoparticles. This essentially increases the concentration of the reactant molecules at the catalyst surface and also makes the bonds in the reacting molecules weaker. This results in the lowering of activation barrier. The geometry and electronic structure is an important consideration in metal nanoparticles catalysis. Newns [1969] modeled the role of electronic structure in metals, specifically the d-band center for the first time. Later Hammer and Nørskov (1995) expanded it with further first principles calculations. The reaction rate depends linearly with the absorption energy for first order surface reactions, which are of utmost importance in metal nanoparticle mediated catalysis.

This has been first predicted from the Brønsted−Evans−Polanyi (BEP) relation that strong adsorption energies result in faster reaction rates for first-order surface reactions. The turnover frequency of a catalyst is not favorable in both the weak binding and strong binding cases. In the case of strong binding, the BEP relation shows the smallest reaction barriers, and thus the catalytic performance is limited by the desorption of products. However, in the case of weak binding, the reaction rate is limited by the large activation energies as predicted by BEP. Therefore for better performance of a catalyst, there should be an optimum binding energy such that the barriers are low enough to be overcome and that the adsorbed molecules may diffuse and desorbs from the catalytic surface easily [Pozun et al. 2013].

Pozun et al. [2013] have recently studied the catalytic performances of monometallic and bimetallic metal nanoparticles for the reduction of para nitrophenol (PNP). Using BEP relation they have shown that the rate of PNP reduction can be predicted from the binding energy of adsorption. The reduction of PNP with excess of sodium borohydride ($NaBH_4$) follows pseudo-first-order kinetics in presence of metal nanoparticle catalysts and depends only upon the concentration of PNP in solution. The metallic catalyst binds the PNP molecules through the two oxygens of the nitro group. Therefore, the rate constant for the catalytic reaction can be easily correlated to the initial adsorption of the PNP molecule to the nanoparticle surface. Binding of different organic molecules to metal surfaces has been thoroughly studied and modeled by various researchers [Newns 1969.; Hammer and Nørskov 1995.; Hammer and Nørskov 1995.; Hammer et al. 1996.; Hammer and Nørskov 1996.; Hammer 2006]. According to the Hammer−Nørskov model, the center of the d-band of the metal surface is the primary controlling factor for the strength of chemisorption. Upon interacting with the metal d-band, the adsorbate state overlaps with the metal states and is split off into bonding and antibonding interactions. When the d-band shifted farther below the Fermi energy level, the antibonding states are increasingly populated, and the strength of chemisorption weakens [Pozun et al. 2013]. Figure 1.10 gives the scatter plot of the d-band centre of the metal surface versus the absorption strength of para nitrophenol. From Figure 1.10 it can be seen that, the adsorption strength increases with a d-band centre closer to the Fermi energy. The d-band of noble metals is nearly filled and thus many antibonding states are populated. As one moves down a column in periodic table, the repulsive interaction between bonding and antibonding states population increases which finally increases the orbital size. This accounts for the weaker adsorption onto Pt and Pd rather than Cu, despite the differences in d-band centers [Pozun et al. 2013].

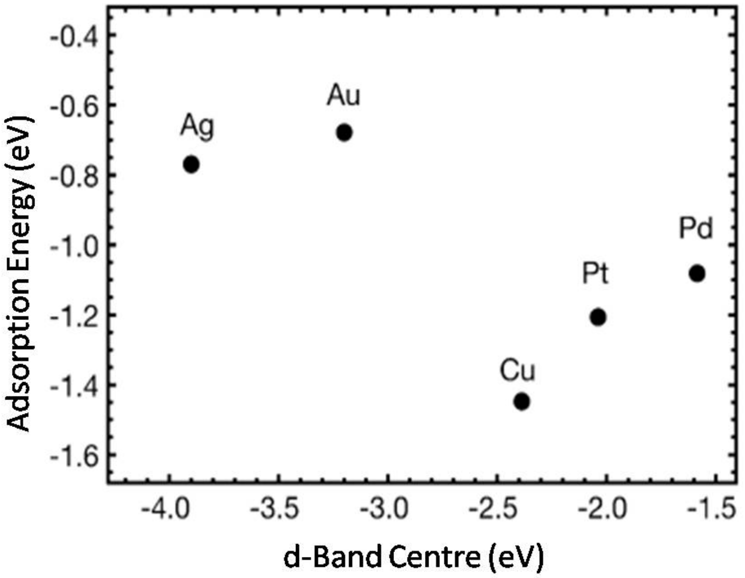

Figure 1.10. Scatter plot of the d-band centre of the metal surface versus the adsorption strength of para nitrophenol [Pozun et al. 2013].

1.5. Nanostructured Materials as Hosts for Metal Nanoparticles

Nanostructured materials that are widely used as a support for nanoparticle synthesis are generally neither small (microscopic, < 1nm) nor large (macroscopic, >50 nm). This class of nanostructured materials is generally termed as mesoscale materials or mesomaterials.

1.5.1. Polymer Membranes

Polymer matrices with nanostructured morphology provide superior platform for the synthesis of metal nanoparticles because of their homogeneity, transparency and ability to provide excellent stability to the metal nanoparticles and smaller clusters. Ion-exchange membranes are having unique morphology in a combination of hydrophilic and hydrophobic nanodomain as shown in Figure 1.11. The hydrophilic domain serves as very good template for the synthesis of nanoparticles [Tant 1997.; Jana et al. 2006.; Takahashi et al. 2008.; Shah and Kaur 2014].

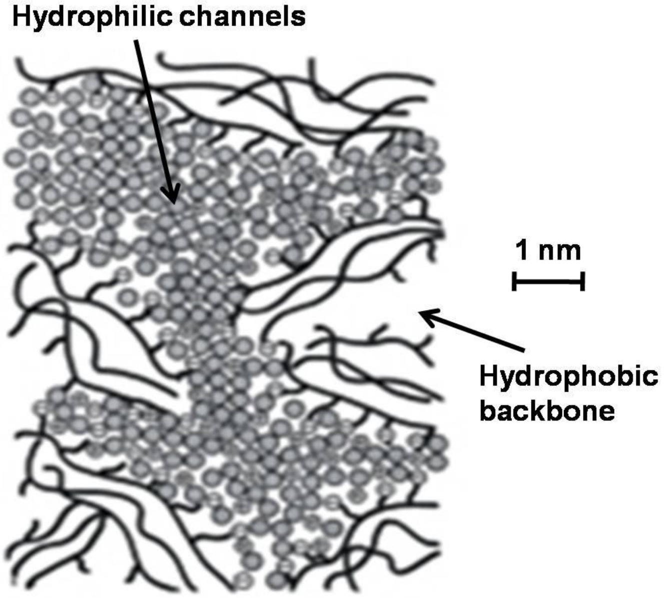

Figure 1.11. Nanostructure of ion-exchange membrane. [Taken from Kreuer. 2001]

1.5.2. Mesoporous Silica and Polymer Resins

Pioneering development of silica based mesostructured materials (with finely tuned void spaces between 1 and 10 nm) by Kresge et al [Kresge et al. 1992] have been a big step forward in the nanochemistry research. Mesoporous silica materials, for example silica gel paticles, MCM-41 (acts as molecular sieves) are well suited for the synthesis of a diverse range of nanomaterials with at least two dimensions between 2-10 nm because of their large adsorption capacity, high surface area, tailorable channel diameters and control over morphology [Ozin et al. 1998]. Many polymer resin beads (ion-exchange or neutral) can also serve as templates for nanoparticle synthesis due to their nanoporous morphology.

1.6. Chemical Reactions in Nanoscale Confinement

Apart from the synthesis of nanomaterials of various shapes and sizes, the current interest in nanochemistry research is to study various chemical reactions in the confined nanodomains of mesostructured materials. The confinement of a molecule in a pore as small as a few billionth of a meter can be compared with the situation of an imprisoned person, whose life is changed due to restricted freedom. It has been observed by various researchers that, when atoms or molecules are confined in a nanospace, their reactivity enhances significantly. Spatially confined chemical reactions are ubiquitous in nature, as for instance in enzymatic reactions, reactions in micelles, catalysis in microporous zeolites etc. Spatial confinement can be simply described as the division of a given volume into many small compartments of molecular dimensions by adiabatic walls, i.e, by nanoscale spatial confinement the reaction equilibrium switches to microcanonical ensemble situation from the classical canonical ensemble situation, such as a reaction in a bulk solution. Spatially confined chemical reaction at nanoscale is thus equivalent to carrying out reaction in a nanoflask. The outcome of many reactions has been found to be significantly influenced by spatial restrictions in a confined environment in comparison to that in bulk. Pioneering work by Turner *et al.* and Santiso *et al.* based on molecular simulation of some chemical reactions in carbon micropores shows the possibility of reaction rate enhancement in the porous medium due to enhanced energetics [Turner et al. 2001.; Turner et al. 2002.; Santiso et al. 2005]. The reason for this extraordinary phenomenon has been attributed to increased density of the pore phase, adsorption of some species, suitable orientation of molecules near the walls, different diffusion rates, etc in the porous medium. Nanoscale confinement is also known to affect the catalytic behaviour of mesoporous materials [Goettmanna and Sanchez 2007]. Thompson has demonstrated that the solvent nanoconfinement mostly affects the chemical reactions that are strongly coupled to the solvent, typically electron and proton transfer reactions [Thompson 2002]. Polak and Rubinovich have predicted that a reaction involving a small number of molecules in an entirely segregated nanoscale domain can lead to shift in equilibrium toward products side via reactant-product reduced mixing [Polak and Rubinovich 2008.; Polak and Rubinovich 2011]. Recently the same group has demonstrated that the DNA hybridization in nanoconfinement is significantly favored over the same reaction occurring in bulk media with the same reactant concentrations [Rubinovich and Polak 2013]. Though there is a lack of clear understanding, several explanations have been put forward in the literature for the nanoconfinement effect [Turner et al. 2001.; Turner et al. 2002.; Thomas et al. 2003.; Santiso et al. 2005.; Shon and Cohen 2012.; Polak and Rubinovich 2008.; Polak and Rubinovich 2011.; Rubinovich and Polak 2013.; Nielsen et al. 2010.; Thompson 2002.; Li and Thompson 2005.; Hill 2001]. These include surface effect, change in solvent structure in nanodomain, pore size selectivity, reactant product reduced mixing, system size dependent entropy variation etc.

Lorenz *et al* have also reported the electron transfer rate enhancement of metal complexes confined in a nanoscale reverse micellar waterpool [Lorenge 2014]. Many organic reactions like borohydride reduction of esters, organic coupling reactions, etc have been studied in reverse micelles, and in organic supramolecules having nanocavities [Das et al. 2004, Padma et al. 2013, Masson et al. 2012, Assaf and Nau 2015]. It is of general interest to explore different nanoconfinement driven reactions. Relatively fewer inorganic oxidation reduction reactions have been studied so far under nanoconfinement conditions and there is a need of detailed investigation on the effect of confinement on redox reactions.

2. Scope of the Thesis

The present thesis is mainly focused on studying synthesis, mechanism of formation and catalytic application of noble metal nanoparticles in confined nanodomains of solid matrices. Different mesoporous materials like ion-exchange membrane, porous polystyrene beads, and silica gel particles have been used throughout the course of the work. Three different types of ion-exchange membrane have been used: (i) commercially available cation exchange membrane Nafion-117, (ii) commercially available anion exchange membrane Selemion AMV, and (iii) a tailor made pore filled anion exchange membrane. Silver nanoparticles have been prepared in the confined nanospaces of Nafion-117 membrane by conventional route. The role of local environment in a membrane on the nanoparticle morphology has been investigated [Patra et al. 2013]. The local environment has been varied by altering the membrane morphology with carefully selected reductants, varying temperature and extent of precursor loading in the membrane. Formamide and ascorbic acid has been chosen as reducing agents because the membrane (Nafion-117) swells in different extent in these two reductants. The early growth kinetics of silver nanoparticles in the nanoscale ionic cavities of Nafion-117 membrane has been followed with small angle X-ray scattering (SAXS) experiment with millisecond time resolution using synchrotron radiation source [Patra et al. 2014]

The role of nanoconfinement in facilitating chemical reduction of metal ion precursors with a suitable reductant for the synthesis of metal nanoparticles has been studied. It has been shown that the highly stable silver citrate complex (under the condition of [citrate]/[Ag^+]>>1) decomposes readily in confined nanodomains of charged and neutral matrices (ion-exchange film, nanoporous polystyrene beads and nanoporous silica gel particles) leading to the formation of silver nanoparticles. The mechanism of growth of silver nanoparticles in the ion-exchange membranes has been studied using a combination of ^{110m}Ag radiotracer, small angle X-ray scattering (SAXS) experiments, and transmission electron microscopy (TEM). It has been demonstrated that the nanoconfined redox decomposition of silver citrate complex is responsible for the formation of Ag seeds, which thereafter catalyze oxidation of citrate and act as electron sink for subsequent reduction of silver ions. Based on the SAXS data and radiotracer kinetics, the growth mechanism has been elucidated as a combination of continuous auto-reduction of silver ions on the nanoparticle surfaces and a sudden coalescence of nanoparticles at a critical number density.

The role of nanoconfinement in significantly softening the reaction condition has been studied taking the case of polyol reduction of noble metal (Ag, Au and Pt) ions for the formation of noble metal nanoparticles. It has been seen that in presence of nanoporous amberlite XAD-4 resin beads, the polyol reduction takes place at ambient condition (room temperature and pressure) which otherwise requires vigorous condition. The formation of noble metal nanoparticles clusters has been clearly seen near the nanoscale crevices in the matrix by field emission-scanning electron microscopy (FE-SEM) characterization of the beads. This has confirmed the role of nanoconfinement on significantly softening the reaction condition.

Finally, the catalytic performances of metal nanoparticles hosted in different mesoporous supports have been studied. It has been demonstrated that the metal nanoparticles, hosted in nanoconfined matrices exhibit superior catalytic performances in comparison to unconfined bare nanoparticles. The catalytic activities of silver nanoparticles formed in the cation-exchange membrane (Nafion-117) have been studied using borohydride reduction of a model cationic dye methylene blue (MB). Borohydride reduction of para nitrophenol to para aminophenol has been chosen as a model reaction in order to study the catalytic activity vis-à-vis the effect of nanoconfinement on the rate of catalysis using silver nanoparticles hosted in an anion exchange membrane and in Amberlite XAD-4 beads. The origin of remarkably high catalytic activity of mesoporous matrix supported nanoparticles has been attributed to the effect of nanoconfinement which accelerates the electron transfer process during catalytic reduction. The dependence of catalytic activity on the size of metal nanoparticles has also been studied. It has been demonstrated for the first time that the borohydride reduction of para nitrophenol takes place in a pure nanoscale physical confinement, which is otherwise impossible in absence of a catalyst. This confirms the role of nanoconfinement on facilitating a chemical reaction. It has been shown that the reaction equilibrium depends on the pore loading or occupancy significantly. The compartmentalization of the reactant molecules in nanodomains of solid matrices essentially favours the forward reaction because of reduced molecular mixing of reactant and product. At lower occupancy, the condition for "single molecule" experiment is achieved, which shifts the equilibrium towards product side, resulting in remarkably high rate constant (s^{-1})/activity parameter ($s^{-1}g^{-1}$).

This thesis interpolates material from six papers by the author published in different international journals [Patra et al. *J. Phys. Chem. C* **2013**, *17*, 12026–12037.; Patra et al. *AIP Conf. Proc.* **2013**, *1512*, 230-231.; Patra et al. *RSC Advances* **2014**, *4*, 59379–59386.; Patra et al. *Langmuir* **2014**, *30*, 2460−2469.; Patra et al. *RSC Advances* **2014**, *4*, 33366-33369.; Patra et al. *Applied Catalysis A: General* **2016**, *524*, 214-222]. Chapter 3 uses material from *J. Phys. Chem. C* **2013**, *17*, 12026–12037 and *AIP Conf. Proc.* **2013**, *1512*, 230-231, both coauthored with D. Sen, A.K. Pandey, C. Agarwal, S.V. Ramagiri, J.R. Bellare, S. Mazumder, and A. Goswami. Chapter 4 is based on *RSC Advances* **2014**, *4*, 59379–59386 coauthored with D. Sen, A.K. Pandey, J. Bahadur, S. Mazumder, S.V. Ramagiri, J.R. Bellare, S.V. Roth, G. Santoro, S. Yu, and A. Goswami. Chapter 5 is written mostly based on *Langmuir* **2014**, *30*, 2460−2469 coauthored with A.K. Pandey, D.Sen, S.V. Ramagiri, J.R. Bellare, S. Mazumder, and A. Goswami, and a small fraction of *RSC Advances* **2014**, *4*, 33366-33369 coauthored with A.K. Pandey, S.K. sarkar, and A. Goswami. Chapter 6 includes the materials from *RSC Advances* **2014**, *4*, 33366-33369. Chapter 7 is based on the materials of *RSC Advances* **2014**, *4*, 59379–59386., *RSC Advances* **2014**, *4*, 33366-33369 and *Applied Catalysis A: General* **2016**, *524*, 214-222 coauthored with A.N. Naik, A.K. Pandey, D. Sen, S. Mazumder and A. Goswami. Finally, Chapter 8 is also based on *Applied Catalysis A: General* **2016**, *524*, 214-222. Some material from each of these papers has also been used in this introduction Chapter.

Chapter 2

Experimental methods

1. Synthesis of Nanoparticles

Bottom up chemical approach of metal nanoparticle synthesis in polymer matrices has been adopted in the present work for the synthesis of noble metal nanoparticles. The general stages during the bottom up synthesis of noble metal nanoparticles include (i) precursor, (ii) nucleation, and (iii) growth. Size and shape of the metal nanoparticles depends on the type of reducing agent, experimental conditions, and the nature of stabilizer. Ion-exchange membranes have been extensively used as a host matrix as well as stabilizing media throughout the study. The general methodology for the synthesis of metal nanoparticles in ion-exchange membrane includes: (i) Loading of the desired metal ions in the membrane through ion-exchange and (ii) subsequent reduction with a suitable reducing agent. The size, shape, and the number density of nanoparticles are controlled by varying the concentration of precursor in the membrane, reduction time, and temperature etc. Apart from the conventional routes, another new approach has been adopted for the first time in the present work, whereby nanoparticles have been synthesized by reduction of metal ions in ion-exchange membrane or nanoporous polystyrene resin beads, facilitated by nanoconfinement effect. This approach is described as “nanoconfinement driven chemical synthesis of metal nanoparticles”. Table 2.1 summarizes the combination of different metal ions and reducing agents used throughout the course of the present work for the synthesis of metal nanoparticles in polymer matrices.

Table 2.1. Routes of synthesis of metal nanoparticles as carried out during the present study.

Route of synthesis	Metal ion	Reducing agent	Host matrix	Nanoparticles	Source
Conventional route of synthesis	Ag^+	Formamide	Nafion 117	AgNPs (nanosphere)	Chapter 3
	Ag^+	Ascorbic acid	Nafion 117	AgNPs (nanorods, nanosponge, nanospheres)	Chapter 3 & Chapter 4
Nanoconfinement driven synthesis	Ag^+	Citrate	Selemion AMV membrane, Nafion 117 membrane, XAD-4 resin beads, silica gel particles, Pore filled anion exchange membrane (AEM)	AgNPs (nanosphere)	Chapter 5 & Chapter 7
	Ag^+, $AuCl_4^-$, $PtCl_6^{2-}$	Ethylene glycol	XAD-4 resin beads	AgNPs, AuNPs, PtNPs (nanosphere)	Chapter 6
	$PtCl_6^{2-}$	$NaBH_4$	XAD-4 resin beads	PtNPs (nanosphere)	Chapter 6

2. Characterization of Nanoparticles

Characterization of nanoparticles includes: (i) chemical characterization, and (ii) physical characterization. Chemical characterization includes chemical composition, surface composition, electrochemistry and oxidation state [Gilham and Brown 2010]. Physical characterization includes particle size, number density, surface area, particle morphology and optical properties [Gilham and Brown 2010]. Several characterization techniques like small angle X-ray scattering (SAXS), transmission electron microscopy (TEM), field-emission scanning electron microscopy (FE-SEM), radiotracer techniques, and inductively coupled atomic emission spectroscopy (ICP-AES) have been extensively used throughout the study. The principals and technical details of the individual techniques are described as follows:

2.1. Small Angle X-ray Scattering (SAXS)

Small-angle X-ray scattering (SAXS) is a technique to probe micro-inhomogeneity (in the nanometer range) in a sample matrix. It involves measurement of elastically scattered X-rays (wavelength 0.1 - 0.2 nm) at very small angles (typically 0.1 - 10°) [Glatter and Kratky 1982.; Guinier et al. 1955.; Porod 1982]. This is a nondestructive technique which provides information about the shape and size of different nanostructured materials (particles, lamellae, fractals etc.), distances between scatterers in partially ordered materials, pore sizes etc. The technique requires only a minimum of sample preparation. It can be broadly used for the characterization of metals, colloids, oil, polymers, cement, plastics, proteins, foods and pharmaceuticals in fundamental research as well as in quality control. The SAXS experiment can be performed using a laboratory X-ray source or synchrotron light source (higher X-ray flux). Advantages of synchrotron source are its monochromaticity and high intensity, allowing rapid experiment and use of weakly scattering sample.

2.1.1. Principle of SAXS

When a collimated beam of monochromatic radiation is incident on an object, part of it undergoes elastic scattering, which changes the direction of incident radiation. The scattering intensity (or amplitude) is a function of scattering angle (2θ) or scattering vector (q). The scattering vector is defined as the difference between the incident and scattered wave vector K_i and K_s. As the wave vectors K_i and K_s are proportional to the linear momentum of the scattered and incident photon respectively (p=hK, h denotes the Plank constant), the scattering vector $q=K_s - K_i$ denotes the momentum transfer vector. Figure 2.1 is a schematic representation of a SAXS experimental setup. The scattering vector can be described as $q = |\mathbf{q}| = 4\pi \sin(\theta)/\lambda$, 2θ is the scattering angle.

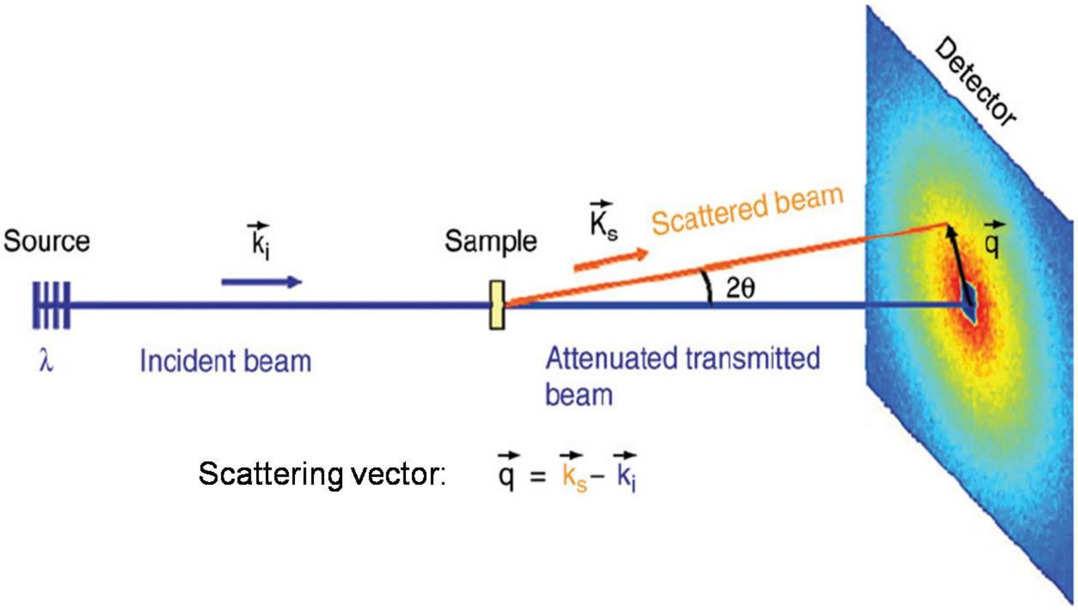

Figure 2.1. Schematic representation of the experimental setup for a SAXS experiment and representation of the scattering vector (q) on the detector surface.

2.1.2. Laboratory Based SAXS Instrument

A typical laboratory based SAXS experimental setup consists of: X-ray source, monochromator, collimator, and detector. Because 2θ is small, large sample to detector distance is maintained to improve angular resolution. In SAXS, the non-scattered beam that merely travels through the sample must be blocked without blocking the closely adjacent scattered radiation. Most available X-ray sources produce divergent beams and this compounds the problem. In principle, the problem could be overcome by making beam parallel by a multilayer parabolic mirror (Gobble mirror) in conjunction with slit collimation. A schematic of typical laboratory based SAXS instrument is shown in Figure 2.2. Laboratory SAXS instruments can be divided into two main groups based on collimator design:

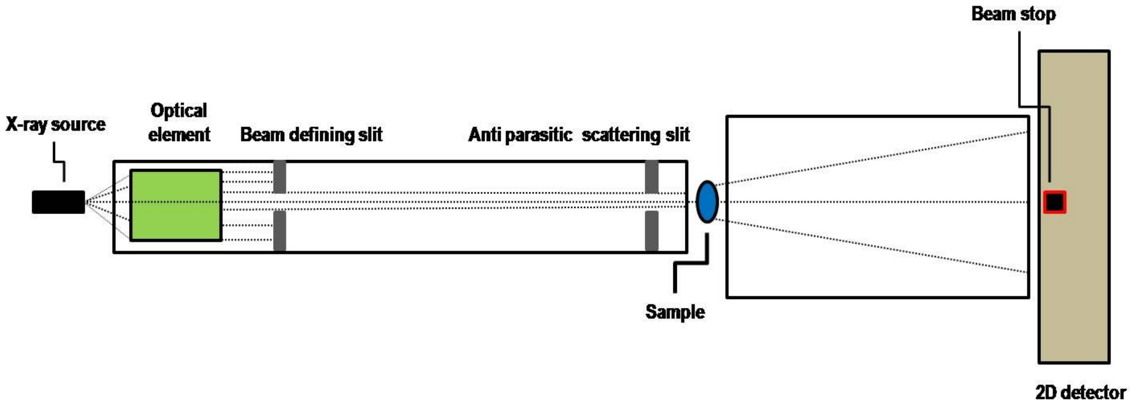

Figure 2.2. A schematic of typical SAXS instrument is shown.

(i) Point Collimation Instruments: Point collimation instruments have pinholes that shape the X-ray beam to a small circular or elliptical spot that illuminates the sample. Thus, the scattering is centro-symmetric about the primary X-ray beam and the scattering pattern in the detection plane consists of circles around the primary beam. Owing to the small illuminated sample volume and the loss of incident beam intensity in the collimation process, the scattered intensity is small and therefore the measurement time is in the order of hours or days in case of very weak scatterers. If focusing optics like bent mirrors or bent monochromatic crystals or collimating and monochromating optics like multilayers are used, measurement time can be greatly reduced. Point collimation geometry allows one to investigate non-isotropic systems such as fibers, sheared liquids.

(ii) Line Collimation Instrument: Line collimation instruments confine the beam only in one dimension so that the beam profile is a long but narrow line. The illuminated sample volume is much larger compared to that in point-collimation and the scattered intensity at the same flux density is proportionally larger. Thus measurement time with line-collimation SAXS instruments is much shorter compared to point-collimation and in the range of minutes. A disadvantage is that the recorded pattern is essentially an integrated superposition (a self-convolution) of many pinhole patterns. The resulting smearing can be easily removed using model-free algorithms or deconvolution methods based on Fourier transformation, but only if the system is isotropic. Line collimation is of great benefit for any isotropic nanostructured materials, e.g., proteins, surfactants, particle dispersion and emulsions. Figure 2.3 shows from the present work a typical detector response (a) and radial averaged SAXS profile (b) of a silver nanoparticle hosted Nafion membrane. The peak at high q is due to scattering from water cluster. The region due to scattering from nanoparticles is also marked in the figure.

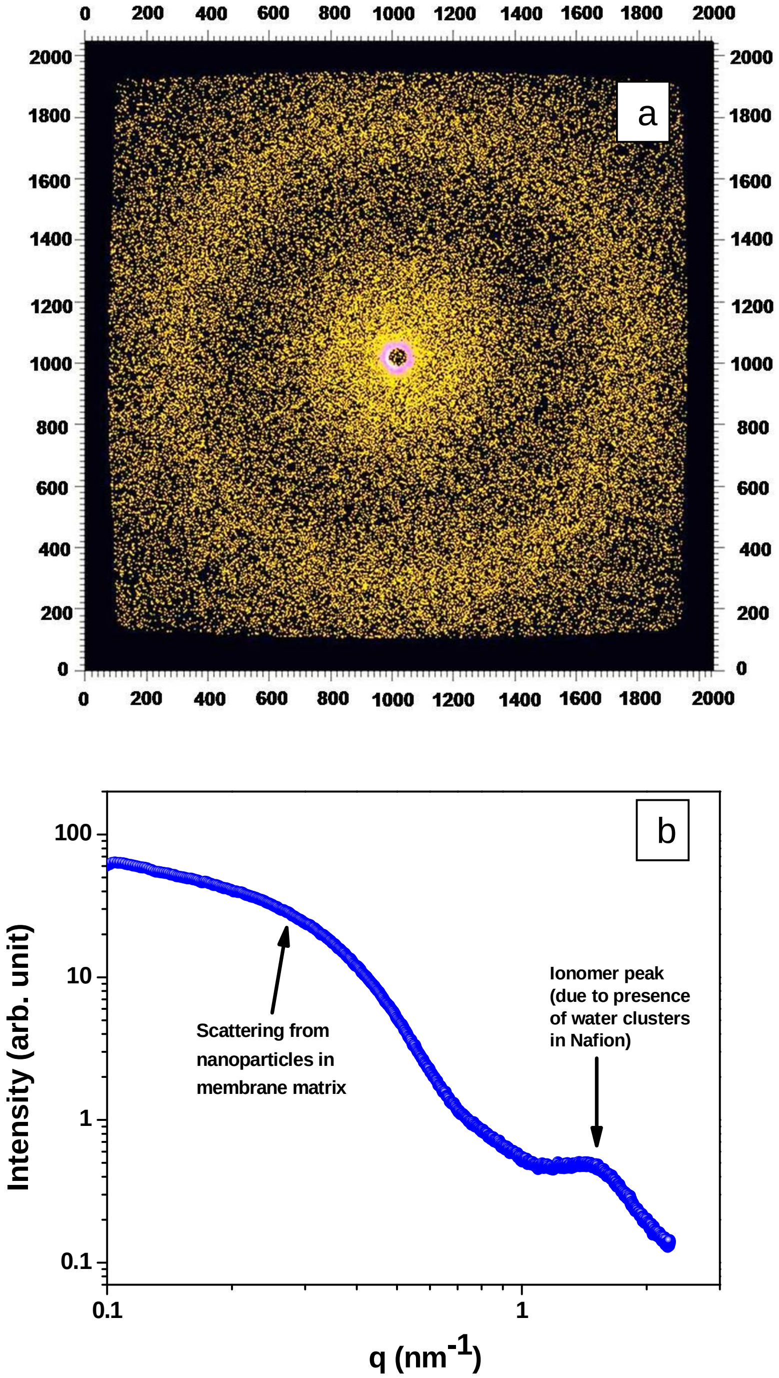

Figure 2.3. Detector response for the SAXS measurement of a silver nanoparticles embedded Nafion 117 membrane after data acquisition for 10 minutes (a) and the corresponding radial averaged SAXS profile.

2.1.3. Synchrotron Radiation Based SAXS Instrument

Synchrotron radiation is the electromagnetic radiation emitted when ultrarelativistic electrons are accelerated radially through magnetic fields. Synchrotron has been first introduced by Veksler and McMillan as a new successful accelerator for the acceleration of both electrons and protons. The 6.5-GeV accelerator at DESY (Deutsches Elektronen Synchrotron), Hamburg, Germany and a 12-GeV accelerator at Cornell University are among the highest-energy alternating-gradient electron synchrotrons built [Friedlander et al. 1981]. When relativistic electrons are bent in a magnetic field, continuous spectrum of electromagnetic radiation is emitted tangentially in the plane of the electron orbit. The energy loss from the circular electron accelerators in the form of radiation, known as synchrotron radiation, has become an important research tool for the present century. Thus the synchrotron radiation facilities are now being built to serve as dedicated photon sources throughout the globe.

The present experiments have been carried out at PETRA III, DESY, Hamburg, Germany using P03 beamline. P03 is the microfocus small- and wide-angle X-ray scattering μSAXS/WAXS beamline at PETRA III. With a circumference of 2.3 km PETRA III is the biggest and most brilliant storage ring light source in the world. This beamline provides micro- and nanofocused beams with ultra-high intensity and resolution in real and reciprocal space. The energy range of the beamline is 8 - 23 keV. For nanofocusing of the beam several optical components are used which include waveguides, Fresnel-zone plates, Beryllium compound refractive lenses and planar Silicon refractive lenses. Dedicated micro- and nano-focus endstations exists for transmission as well as grazing incidence experiments. The beam dimensions of the microfocus end station are 42 x 20 μm^2 and 22 x 13 μm^2.

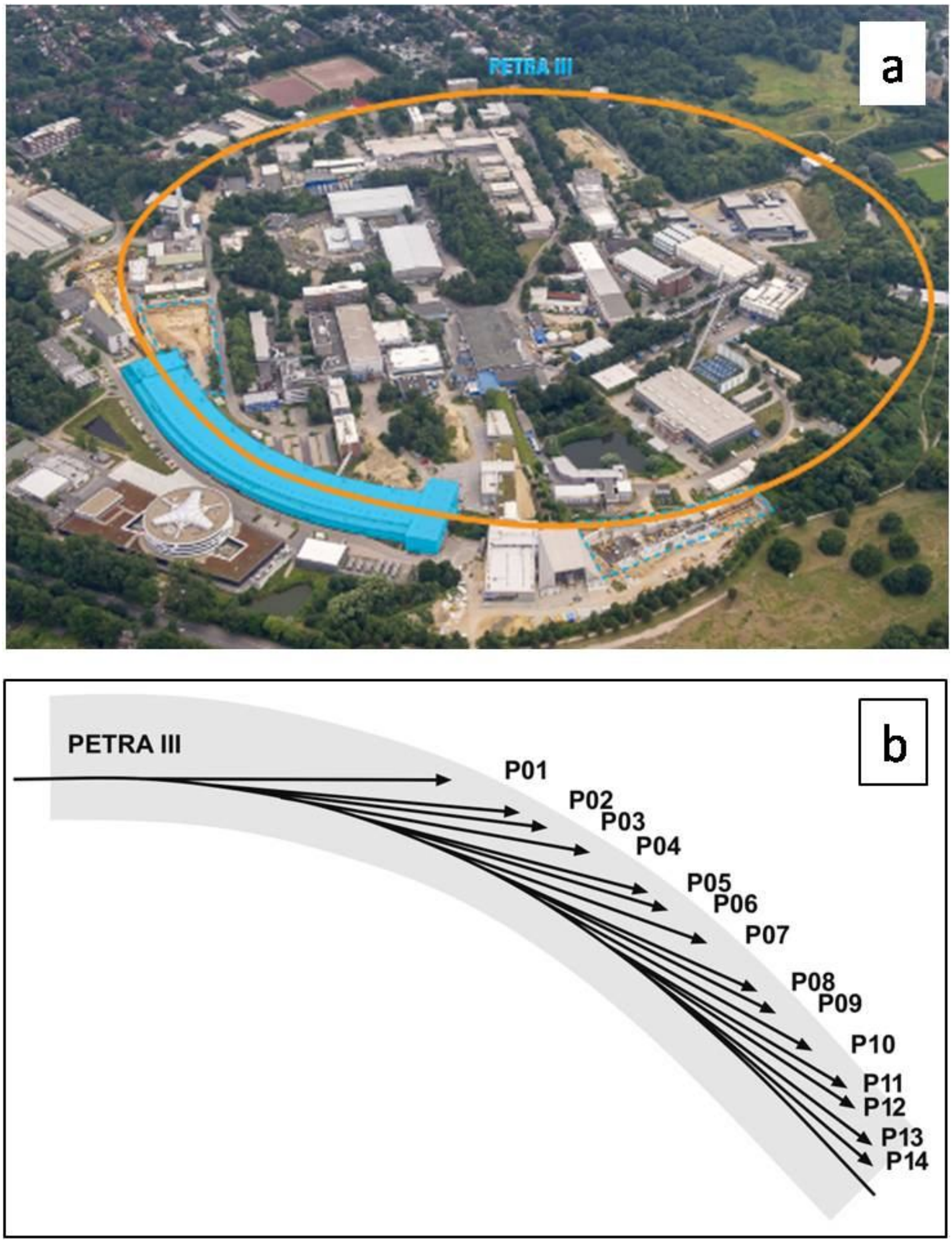

Figure 2.4. The new high brilliance 3rd Generation Synchrotron radiation Source at DESY: PETRA III (a) and the fourteen available beamlines at PETRA III (b).

2.2. Dynamic Light Scattering (DLS)

Dynamic Light Scattering (DLS), also known as Photon Correlation Spectroscopy or Quasi-Elastic Light Scattering is a non-invasive, well-established technique for measuring the size and size distribution of molecules and particles typically in the submicron region and with the latest technology lower than 1 nm [Berne and Pecora 2000]. In this technique the sample is illuminated by a laser beam and the fluctuations of the scattered light are detected at a given scattering angle θ by a fast photon detector. The Brownian motion of particles or molecules in suspension causes laser light to be scattered at different intensities. Analysis of these intensity fluctuations yields the mobility of the Brownian motion and hence the particle size using the Stokes-Einstein relationship. Equation 1 gives the Stokes-Einstein relation between diffusion coefficient and particle size.

$$D_h = \frac{k_B T}{3\pi\eta D_t} \tag{1}$$

Where D_h is the hydrodynamic diameter (measure of particle size), D_t is the translational diffusion coefficient, k_B is Boltzmann's constant, T is thermodynamic temperature, η is dynamic viscosity. The calculations are handled by instrument software. The particle size determined by dynamic light scattering is the hydrodynamic size. That is, the determined particle size is the size of a sphere that diffuses the way as the particle. Figure 2.5 gives the schematic set up of the dynamic light scattering (DLS) experiment.

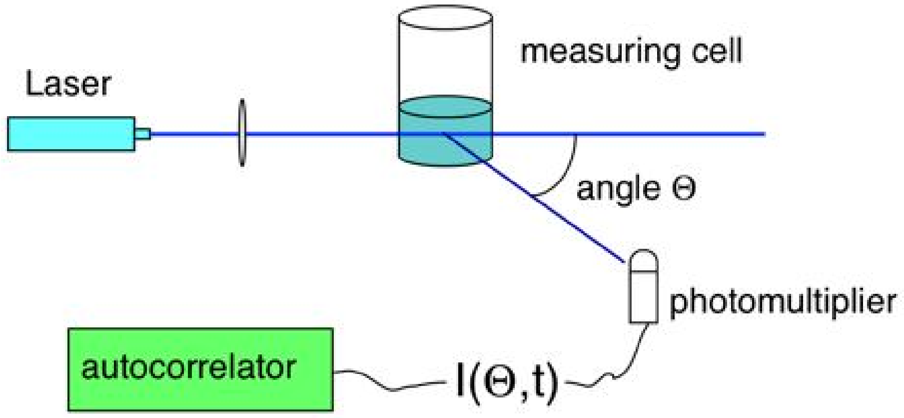

Figure 2.5. Schematic set-up of dynamic light scattering experiment.

2.3. Electron Microscopy

Electron microscopy is a technique that uses a beam of accelerated electrons as a source of illumination [Skoog et al. 2006.; Kuo 2007]. The resolution of an optical microscope is limited by the wavelength of light. Electrons are used as “light source” in electron microscopes and their much lower de Broglie wavelength makes it possible to get a spatial resolution a thousand times better than with a light microscope. Therefore it is possible to see objects at size of the order of a few angstrom (10^{-10} m). Thus the examination of the finer detail of as small as single atoms is possible in electron microscopes, which is impossible with optical microscope. In electron microscopes, electrons are generated by heating of a tungsten filament by means of a current to a temperature of about 2800°C. Sometimes a crystal of lanthanum hexaboride (LaB_6) mounted on a tungsten filament is used to produce electrons. This modification produces a higher electron density in the beam and results in an improved resolution than with the conventional device. In a field emission (FE) electron gun, a so-called "cold" source is used. An extremely thin and sharp tungsten needle with typical tip diameter of $10^{-7} – 10^{-8}$ m functions as a cathode in front of a primary and secondary anode with a voltage between cathode and anode at the order of 0.5 to 30 KV. Because the electron beam produced by the FE source is about 1000 times smaller than in a standard electron microscope, the image quality is significantly better. A field emission tip last theoretically for a lifetime in contrast to a conventional tungsten filament provided the vacuum is maintained. Two types of electron microscopes are commonly used to probe nanoscale objects. They are: (i) transmission electron microscopes (TEM), and (ii) scanning electron microscopes (SEM). The principle of the techniques is described in the following.

2.3.1. Transmission Electron Microscopy (TEM)

Transmission electron microscopy (TEM) is a microscopy technique in which an electron beam is transmitted through an ultra-thin sample specimen, interacting with the sample matrix as it passes through [Reimer and Kohl 2008]. The interaction of the electrons with the specimen generates an image which is magnified and focused onto an imaging device, such as a fluorescent screen, or a layer of photographic film, or a sensor such as a CCD camera. The basic principles of transmission electron microscope (TEM) are same as the optical microscope but uses electrons instead of light. Because of higher magnification, TEM has wide applications in materials, biological and medical research. TEM instrument was built for the first time by Max Knoll and Ruska in the year 1931.

A "light source" situated at the top of the microscope emits the electrons that travel through vacuum in the column of the instrument. Instead of optical lenses focusing the light in the optical microscope, electromagnetic lenses are used in TEM to focus the electrons into a narrow beam, which then travels through the sample specimen. Some of the electrons are scattered and disappear from its path depending on the density of the material it passes through. The unscattered transmitted electrons hit a fluorescent screen placed at the bottom of the microscope. This gives rise to a "shadow image" of the sample specimen with its different parts displayed in varied darkness according to their density. The image can be studied directly by the operator or captured in a camera. A representative TEM image of silver nanoparticles hosted in Nafion 117 membrane from the present work is shown in Figure 2.6.

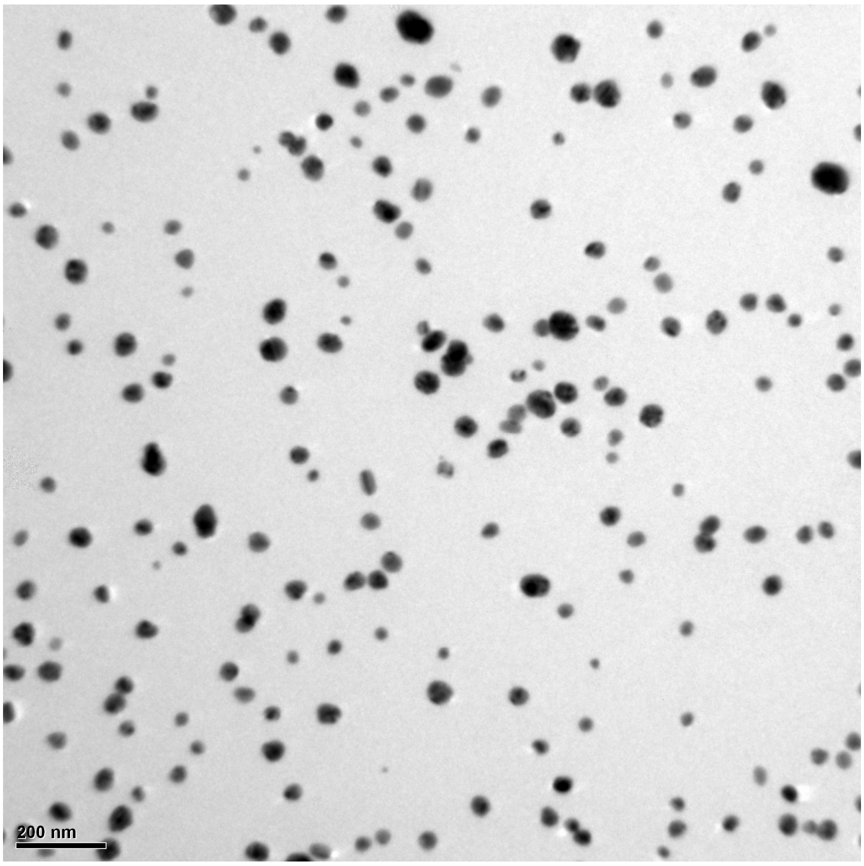

Figure 2.6. Representative TEM image of silver nanoparticles hosted in Nafion 117 membrane.

2.3.2. Field-Emission Scanning Electron Microscopy (FE-SEM)

Field emission scanning electron microscopy (FE-SEM) is used to visualize ultrasmall topographic details (as small as 1 nanometer) on the surface of an object [Goldstein et al. 2003]. This technique is popular among researchers in biology, chemistry and physics. In this technique, electrons are generated from a field emission source and accelerated in a high electrical field gradient. These primary electrons are focused and deflected within the high vacuum column by electronic lenses to produce a narrow scan beam that bombards the object, resulting in emission of secondary electrons from each spot on the object. The angle and velocity of these secondary electrons are correlated with the surface structure of the object. The secondary electrons are captured by a detector, producing an electronic signal. This signal is amplified and transformed to a video scan-image or to a digital image.

For scanning electron microscopy of insulators like polymers, the samples are first made conductive for current. This is done by an extremely thin layer coating (1.5 - 3.0 nm) of gold or gold palladium. Also, the samples must be able to sustain the high vacuum and should not alter the vacuum conditions, for example by losing water molecules or gasses. Samples of metals, polymers and crystals are usually less problematic and retain their structure during the SEM. However, biological material needs a prefixation, e.g. with cold slush nitrogen (cryo-fixation) or with chemical compounds. Chemically fixed material requires washing and drying below the critical point to avoid damage of the fine structures due to surface tension. Coating is then done in a separate device. A typical FESEM image of silver nanoparticles hosted in XAD-4 resin beads obtained in the present work is given in Figure 2.7. Figure 2.8 gives the schematic comparison of optical microscope, transmission electron microscope and scanning electron microscope instruments.

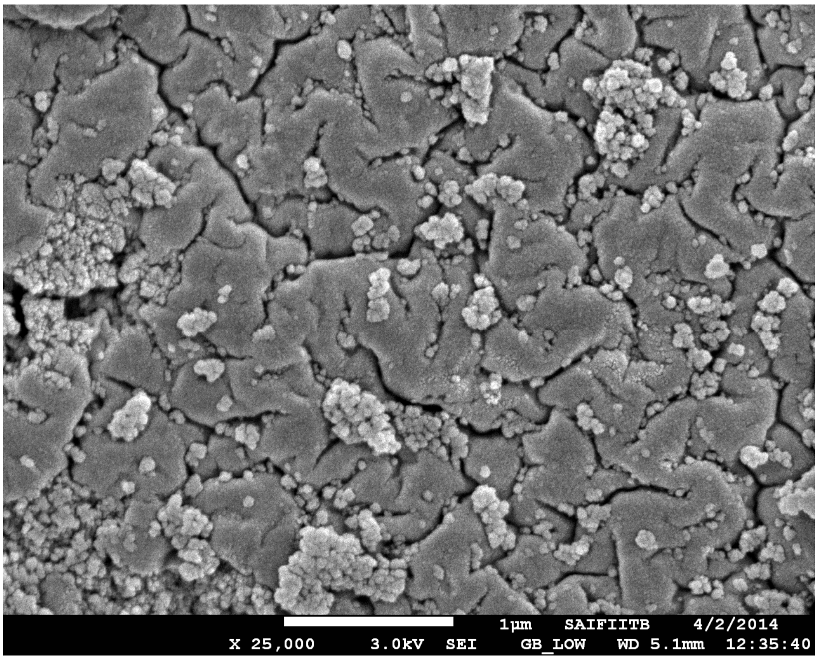

Figure 2.7. A representative FE-SEM image of silver nanoparticles in XAD-4 resin beads.

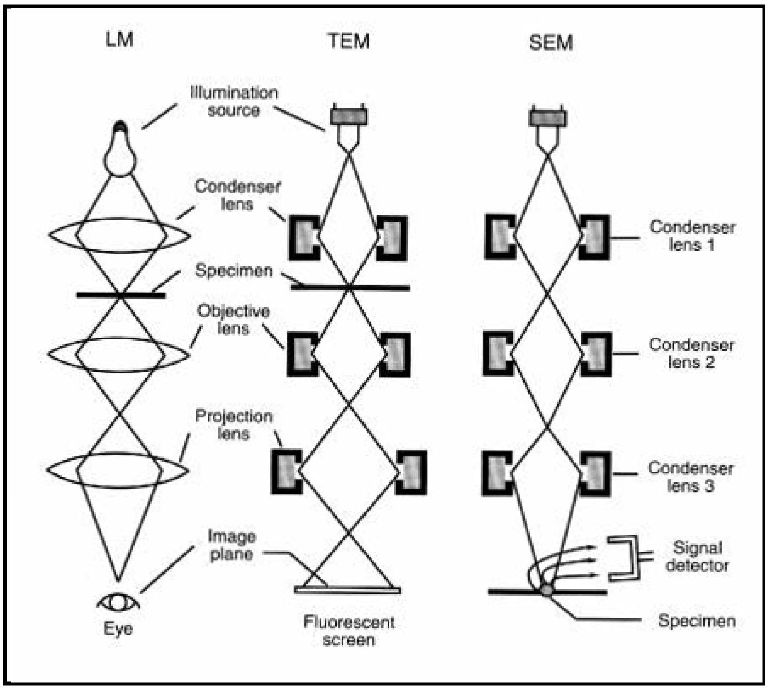

Figure 2.8. Schematic comparison of optical/light microscope (LM), transmission electron microscope (TEM), and scanning electron microscope (SEM).

2.4. Applications of Radiotracers as an Analytical Tool

A radiotracer is the radioactive isotope of an element, which acts as a marker to follow the course of chemical, biological or physical processes. Its applications stem from the fact that the chemical properties of a radioisotope are same as that of the inactive isotopes of the element. When the atom of an element in a compound is replaced by its radiotracer, the subsequent fate of the atom during a chemical or physical change can be tracked by measurement of radioactivity. Almost all elements in the periodic table have radioactive isotopes which may be naturally occurring or can be produced artificially. Since their discovery, radiotracers have been used as analytical tool. The basic criteria for a radionuclide to act as a tracer or label are [Ruth 2009]:

(i) The presence of radionuclides should not affect the system under study, and

(ii) The radionuclide concentration should be easily measured.

Conventional chemical analysis allow detection of a substance typically in the range of ng to µg, which means 10^{13}-10^{16} analyte atoms are needed to get an analytical response. However, it is possible to detect the disintegration corresponding to a single radioactive atom. Routine radioanalytical techniques allow detection of quantities that are ~10^5 times smaller than those required for chemical analysis. Radiotracer based techniques are highly sensitive, simple, and comparatively less expensive compared to other techniques such as mass spectrometry or atomic spectroscopy. Also, the interference from other species that may be present within the system is not important in radiotracer based methods, which is the major source of error in conventional chemical analysis. Thus the radiotracer based analytical techniques provide deeper insight of a reaction mechanism. Areas where radiotracers find considerable applications are [Arnikar 1989]:

(i) Analytical applications

(ii) Chemical and physicochemical investigations

  (a) Study of reaction mechanism

  (b) Measurement of equilibrium constants (thermodynamic study)

  (c) Measurement of rate constants (kinetic study)

  (d) Study of diffusion

(iii) Medical and agricultural applications

2.4.1. Choice of Radiotracer

The choice of a radiotracer for a particular application is based on the following criteria:

(i) Good compatibility with the system under study.

(ii) High specific activity (radioactivity per unit mass of the radionuclide)

(iii) Optimum half-life (not too short or long). Very short half-life leads to fast decay of the radionuclides, which is not suitable for the use of the tracer over a period of time. However, very long half-life results in poor specific activity, problem of waste-management, and high dose in the case of in-vitro studies.

(iv) Type of the radiation emitted by the radionuclide, and availability of detection systems in the experimental condition.

(v) Availability and the cost of the radionuclide.

2.4.2. Production of Radiotracer

Radioisotopes are usually produced in nuclear reaction, by bombardment of stable target with a projectile. The projectile can be neutral particle like neutron or charged particle like proton, deuteron and alpha. Typical examples of some reactions to produce radioisotope are: $^{59}Co(n,\gamma)^{60}Co$, $^{109}Ag(n,\gamma)^{110m}Ag$, $^{14}N(n,p)^{14}C$, $^{24}Mg(d,\alpha)^{22}Na$, $^{13}C(p,n)^{13}N$,

$^{17}O(\alpha,n)^{20}Ne$. Radionuclides are usually produced in three general routes: (i) neutron induced reactions in a nuclear reactor (R) such as (n,γ) or (n,p) or (n,α) reactions, (ii) charged particle induced reactions using a cyclotron (C) such as (p,n), (α,n) reaction, and (iii) as a fission product (F), obtained by chemical separation from irradiated uranium. Reactors are generally used for the production of neutron rich nuclide, while the proton rich nuclides are produced at cyclotrons. Table 2.2 gives a list of some commonly used radiotracers and their decay characteristics.

Table 2.2. Commonly used radiotracers, their production routes and decay characteristics.

Radionuclide	Production route*	Half-life (yr)	Decay characteristics/ Energy (keV)
^{3}H	R	12.33	β^- 18
^{14}C	R	5730	β^- 156
^{22}Na	C	2.60	β^+, γ 1274
^{24}Na	R	1.75×10^{-3}	γ 1369
^{32}P	R	39.1×10^{-3}	β^- 1710
^{33}P	R	69.3×10^{-3}	β^- 249
^{35}S	R	23.9×10^{-2}	β^- 167
^{36}Cl	R	3.0×10^{5}	β^- 710
^{45}Ca	R	44.5×10^{-2}	β^- 257
^{47}Ca	R	12.4×10^{-3}	β^- 1990; γ 1297
^{51}Cr	R	75.9×10^{-3}	γ 320
^{54}Mn	R	85.5×10^{-2}	γ 835
^{55}Fe	R	2.73	EC
^{59}Fe	R	12.2×10^{-2}	γ 1292, 1099
^{57}Co	C	74.4×10^{-2}	γ 122
^{60}Co	R	5.27	γ 1173, 1332
^{63}Ni	R	100.1	β^- 67
^{65}Zn	C,R	66.9×10^{-2}	γ 1116
^{75}Se	R	32.8×10^{-2}	γ 265, 136
^{86}Rb	R	50.9×10^{-3}	β^- 1770
^{85}Sr	R,C	17.7×10^{-2}	γ 514
$^{99}Mo/^{99m}Tc$	F	7.5×10^{-3} / 6.86×10^{-4}	γ 143
^{106}Ru	F	1.02	β^- 39
^{110m}Ag	R	68.4×10^{-2}	β^- 3000, γ 658
^{109}Cd	C	1.26	γ 88
^{111}In	C	7.6×10^{-3}	γ 171
^{125}I	R	16.2×10^{-2}	γ 35
^{131}I	R	21.9×10^{-3}	β^- 606, γ 365
^{137}Cs	F	30.1	γ 662
^{153}Gd	R	65.8×10^{-2}	γ 103
^{201}Tl	C	8.3×10^{-3}	γ 167
^{210}Pb	R	22.3	β^- 17, 64

*R ≡ Reactor, C ≡ Cyclotron, F ≡ Fission product

2.4.3. Units of Radioactivity

The commonly used unit of radioactivity is curie (Ci), which corresponds to activity of 1g of ^{226}Ra. It is defined as:

1 curie = 3.7x10^{10} radioactive decays per second.

In SI unit, the curie has been replaced by the becquerel (Bq), where

1 becquerel = 1 radioactive decay per second = 2.703x10^{-11} Ci.

2.4.4. Operational Safety with Radiotracer

Safety should be an important consideration during the handling of radiotracers. The experiments with radiotracers need a proper radiochemistry laboratory. The laboratory is generally kept at slight underpressure (~ 3 mbar). The experiments should be performed in fume hoods with good ventilation (closed circuit) and with necessary protective clothing. Handling of highly active radiotracers must be done inside glove box. A special container for collecting radioactive waste must be there in the laboratory. It is necessary to have some approximate knowledge of activity of the sample during experiment. The radiotracer experiments are generally carried out with micro Curie (μCi) to milli Curie (mCi) level of activity with a γ-dose of few mR/hour (milli Roentgens per hour) at about 1 ft distance from the radioactive sample. Instruments for regular checking of radioactivity contamination must be installed for monitoring of hands after the experiment is over.

2.4.5. Measurement of Radiation

Radiotracers used in common applications can be α or β particle emitters or γ-ray emitters. Since the mechanism of interactions of radiations with matter vary depending upon the nature of the radiation, different types of detectors are used for detection and measurement of different types of radiation [L'Annunziata 2003, Knoll 1979]. The high-energy radiations/particles are produced by nuclear decay, cosmic radiation, or reactions in a particle accelerator. Due to their long range in matter, gamma-emitting radioisotopes provide the in-situ information of a chemical process. Usually two types of detectors are used for the measurement of γ radiation. They are scintillation detector and semiconductor detector. In the work presented in this thesis, NaI(Tl) scintillation detector attached to a 4K multichannel analyser has been used for the measurement of gamma radiation. A brief description of the detector system is given below:

NaI(Tl) detector system: Crystals of sodium iodide (NaI) doped with trace quantity of Tl is used as radiation detector because of its scintillation property. The crystal emits light when gamma rays interact with it. The intensity of the light is proportional to the energy deposited in the crystal by the gamma radiation. The light is then converted into electrical signals in a photomultiplier tube attached to the crystal. The NaI(Tl) crystal is encased in aluminium coverings because it is hygroscopic.

Gap between the valence and conduction band in a pure NaI crystal is ~5 eV [Knoll 1979]. When electromagnetic radiation interacts with a scintilator crystal, it excites electrons from valence band to conduction band. When the excited electrons return to the valence band, photons are emitted. In a pure NaI crystal, the reverse transition of electron from conduction band to the valence band with emission of a photon is not an efficient process. Due to the high band gap in a pure NaI crystal, the energy of the emitted photon lies in the ultraviolet range. Such photons are incompatible with the photomultiplier tubes. This problem is overcome by modifying the band structure of the crystal by doping Thallium (Tl) into the pure NaI crystal. The Tl acts as activator which creates new levels (activator levels) within the band gap as shown in Figure 2.9. The electronic transitions from the conduction band to the activator levels produce light in the visible region, which is easily detectable by photomultiplier tube. Figure 2.10 gives the block diagram of a NaI(Tl) detector.

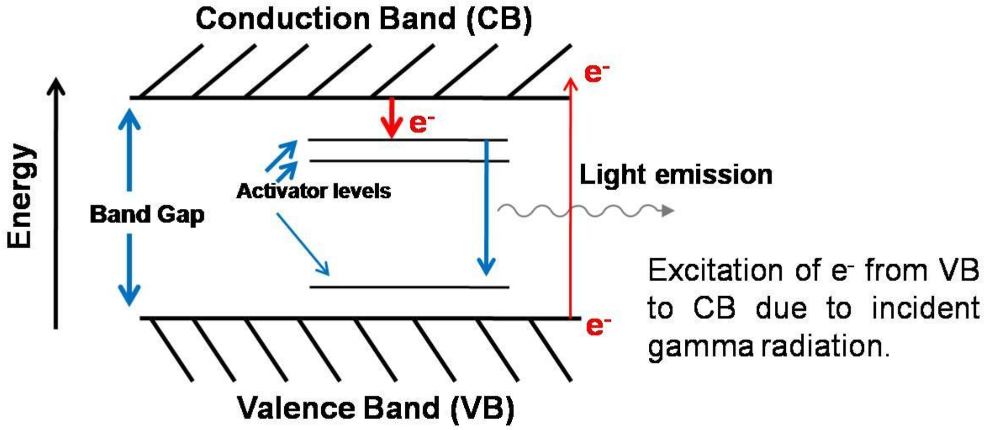

Figure 2.9. Schematic representation of energy bands in a NaI(Tl) crystal.

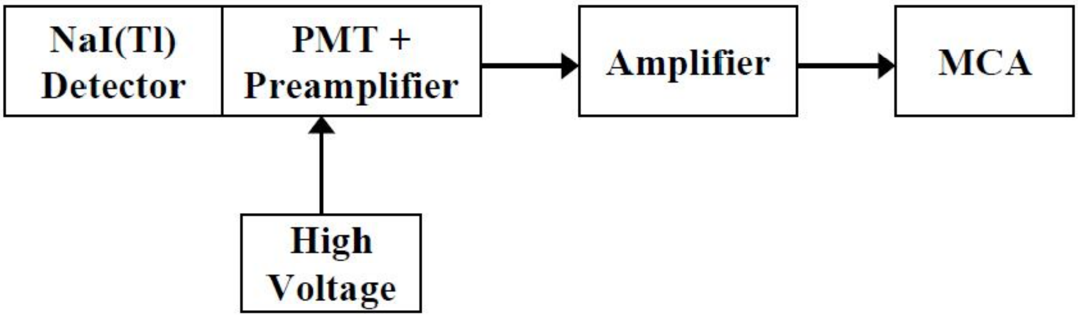

Figure 2.10. Block diagram of a NaI(Tl) detector.

2.4.6. Application of ^{110m}Ag Radiotracer in Silver Nanoparticle Characterization

The present work involves the synthesis of mostly silver nanoparticles in different polymer matrices. Therefore ^{110m}Ag has been used as a radiotracer for understanding the mechanism of growth of silver nanoparticles vis-à-vis for the in-situ quantification of silver amount in the host matrices in the form of silver nanoparticles. The technique is direct, nondestructive, and therefore provides exact information under the experimental condition. This is the first report showing the possible application of radiotracer based techniques in nanochemistry research. In this method, the known quantity of silver nitrate solution used as precursor for nanoparticle synthesis is tagged with measured activity of radiosilver (^{110m}Ag). Following reduction, this radioactive silver is accumulated in the polymer matrix (membrane) in the form of AgNPs. The rate of accumulation has been studied to obtain information about the mechanism of formation of nanoparticles. A NaI(Tl) detector coupled with a 4K multichannel counter has been used for the measurement of gamma-ray of ^{110m}Ag. The gamma-ray line with highest intensity (657.7 keV with intensity 94 %) has been monitrored. The region of interest (ROI) has been kept unaltered during the measurement.

2.5. Inductively Coupled Plasma Atomic Emission Spectroscopy (ICP-AES)

Atomic emission spectroscopy AES) is a an analytical technique for the elemental analysis in a sample using flame, plasma, arc, or spark as excitation source. The elements are identified from the characteristic wavelength of the atomic emission line. The intensity of the emitted light is proportional to the concentration of the element within the sample. Inductively coupled plasma atomic emission spectroscopy (ICP-AES), also referred to as inductively coupled plasma optical emission spectrometry (ICP-OES), is a type of emission spectroscopy that uses the inductively coupled plasma to produce excited atoms and ions. The flame temperature in ICP-AES is in a range from 6000 to 10000 K.

The ICP-AES instrument is mainly made of two parts: the plasma (ICP) generator and the optical spectrometer. When the ICP torch is turned on, an intense electromagnetic field is created within the coil. An aqueous or organic sample is delivered into an analytical nebulizer using a peristaltic pump where it is changed into mist and introduced directly inside the plasma flame. The sample is immediately broken down into charged ions by collision with the electrons and charged ions in the plasma. The analyte molecules break up into their respective atoms which lose electrons and recombine repeatedly in the plasma. As a result radiation of characteristic wavelengths of the elements is emitted. Figure 2.11 gives the schematic representation of the different components of an ICP-AES instrument.

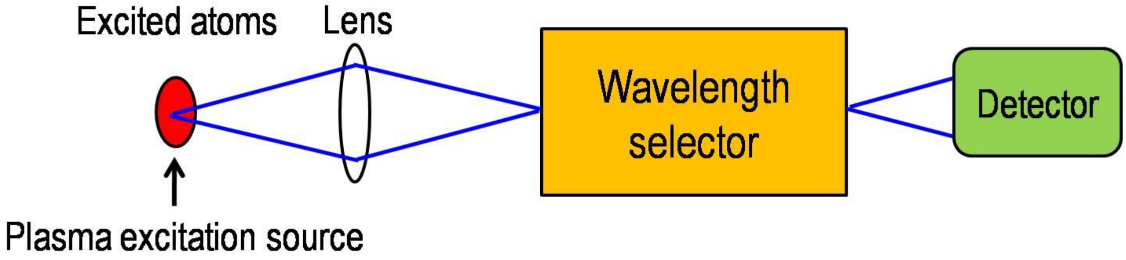

Figure 2.11. Schematic representation of an ICP-AES instrument.

3. Application of Nanoparticles for Catalysis

3.1. Choice of Model Reaction

Selection of an appropriate model reaction is necessary to determine the catalytic activity of different types of metal nanoparticles. It is preferred that the model reaction proceeds only in the presence of nanoparticle catalyst and does not occur without the catalyst. Also a simple technique should be available to follow the change in concentration of reactant/product with time. A relatively slow reaction is preferred. A simple visual clue can be used in some cases to determine a reaction rate. Thus, if one of the reactants is colored but the products are colorless, the rate of the reaction can be easily followed by measuring the time it takes for the color to disappear. It is most important that the reaction should take place under mild reaction conditions, so that any degradation or transformation of the nanoparticles does not occur during the study.

3.1.1. Reduction of *p*-Nitrophenol (PNP)

The reduction of *p*-nitrophenol by sodium borohydride in the presence of metal nanoparticles catalyst has been widely used as a model reaction for catalysis over last decade. Pioneering work by Pradhan *et al.* [2002] and Esumi *et al.* [2002] has made this reaction as a benchmark reaction for studying the activity of metal nanoparticle catalysts. One major reason for such a high popularity of this reaction is the ease of monitoring the reaction by UV-VIS spectroscopy. *p*-nitrophenol (PNP) exhibits a distinct absorption peak at 317 nm, which shifts to 400 nm when the solution is made alkaline. The product p-aminophenol (PAP) shows a weak absorption peak at 300 nm. Thus the rate of the catalytic reduction can be easily obtained by measuring the gradual decrease in absorbance at 400 nm using a UV-VIS spectrophotometer. In presence of excess of borohydride, a pseudo first order reaction is assumed [Ghosh et al. 2004.; Hayakawa et al. 2003]. It is important to mention that the reduction of *p*-nitrophenol does not take place without catalyst [Shine and Mallory 1962]. Figure 2.12 gives the reduction reaction scheme of PNP to PAP.

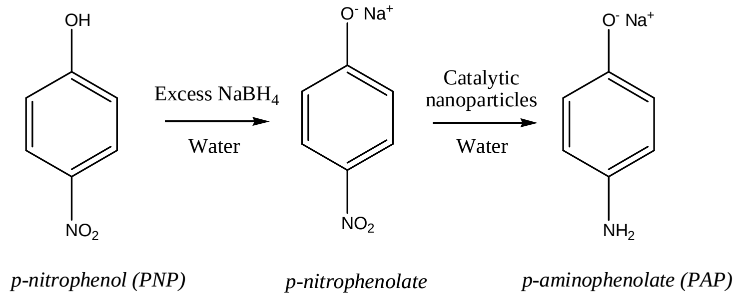

Figure 2.12. Reduction reaction of PNP to PAP.

3.1.2. Reduction of Methylene Blue (MB)

Reductive degradation of various organic dyes in presence of metal nanoparticle catalyst is another popular model reaction for catalysis study [Jana et al. 2000.; Panáček et al. 2014]. Methylene blue in particular is a cationic dye which undergoes slow reduction in the presence of $NaBH_4$. In presence of metal nanoparticle catalyst, the reduction gets significantly accelerated [Ghosh et al. 2002]. This is a convenient model reaction to study catalytic activity of metal nanoparticles. Methylene blue (MB) exists in two different forms, a reduced form and an oxidized form, that shows different colors. The oxidized form of MB is blue while the reduced form is colorless. MB can be reduced by sodium borohydride in presence of metal nanoparticle catalysts. The reduced form in turn can be converted back to the oxidized form by simply shaking it with oxygen in air. The reactions involving the two forms of methylene blue are sometimes termed as clock reactions, because they involve a quick color change that is easy to monitor. Figure 2.13 gives the chemical structure of the oxidized and reduced form of MB.

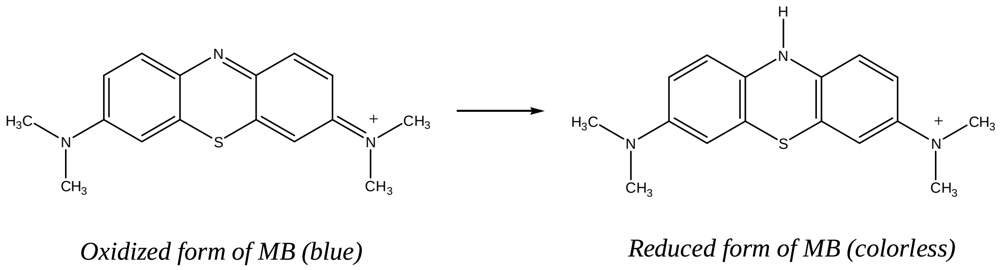

Figure 2.13. Chemical structure of methylene blue in its oxidized and reduced form.

3.2. Monitoring of the Progress of Catalytic Reaction

3.2.1. Ultraviolet-visible (UV-VIS) spectroscopy

Ultraviolet–visible spectroscopy or ultraviolet-visible spectrophotometry (UV-VIS) is a spectroscopic technique based on absorption or reflectance of light in the ultraviolet-visible spectral region. The absorption or reflectance in the visible range dictates the color of the chemical compound involved. Molecules undergo electronic transitions by absorption or emission of radiation in this region of electromagnetic spectrum. This analytical technique is complementary to the fluorescence spectroscopy. The electronic transitions from the excited states to the ground state of an analyte molecule are used in fluorescence spectroscopy, while the absorption spectroscopy measures the transitions from the ground state to the excited states.

When ultraviolet-visible light passes through a solution, a portion of it is absorbed by the molecules present in the solution. The absorption is accompanied by the excitation of the electrons of the absorbing molecule from ground state to excited states. Since electronic transition is accompanied by rotational and vibrational transition, absorption occurs over a wide range of wavelength. Thus UV-VIS absorption spectra appear as band. The wavelength at which maximum absorption occurs is called λ_{max} and the intensity of absorption is determined by molar extinction co-efficient which is a property of the absorbing molecule. The degree of absorption at each wavelength is recorded in an optical spectrometer. The resulting spectrum is presented as a graph of absorbance (A) versus wavelength. Valence electrons in a molecule are present in one of the following types of molecular orbitals:

a) σ (bonding orbitals)
b) π (bonding orbitals)
c) non-bonding orbitals (lone pair electrons)

Generally energy of the sigma bonding orbitals are lower than π bonding orbitals, which in turn are lower in energy than non-bonding orbitals. When an electromagnetic radiation of matched frequency is absorbed, a transition takes place from one of these orbitals to an antibonding empty orbital, σ* or π*. Figure 2.14 shows the possible electronic transition in UV-VIS spectroscopy.

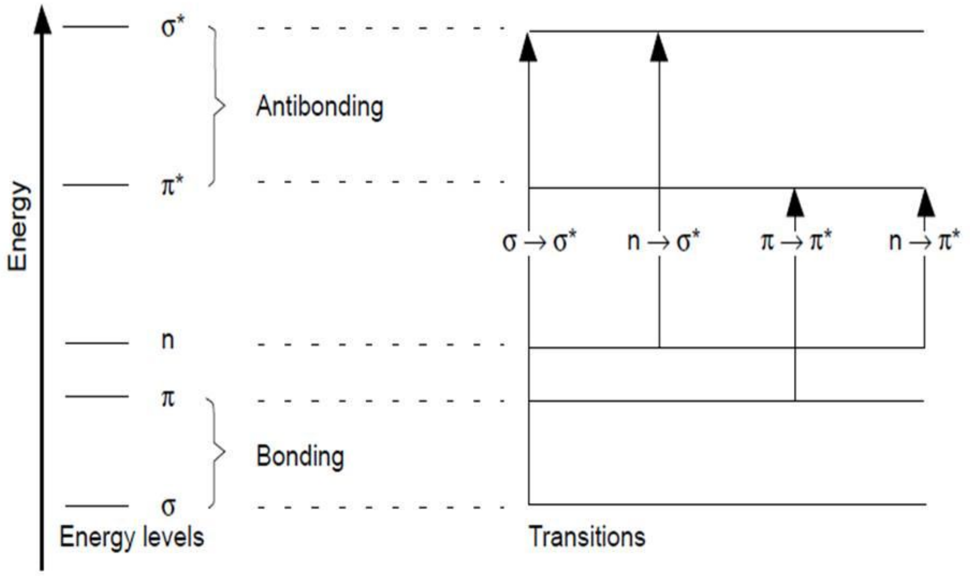

Figure 2.14. Possible electronic transitions in UV-VIS spectroscopy.

In UV-VIS spectroscopy, absorptions occur due to π→π*, n→σ* and n→π* transitions. σ→σ* transitions are difficult to observe due to very high frequency (too short a wavelength) of absorption.

For UV-VIS measurement the sample solution is taken in a quartz cell. Ideally the solvent should not have any absorption in the ultraviolet-visible range. However in real situation this is rarely the case. Thus transmittance of the incident radiation through the sample solution is always measured relative to the transmittance of the solvent, kept in another quartz cell of same dimension. The incident beams is split into two parallel beam, one passes through the sample cell, and the other passing through the reference cell. Figure 2.15 gives the schematic representation of a typical spectrophotometer set up.

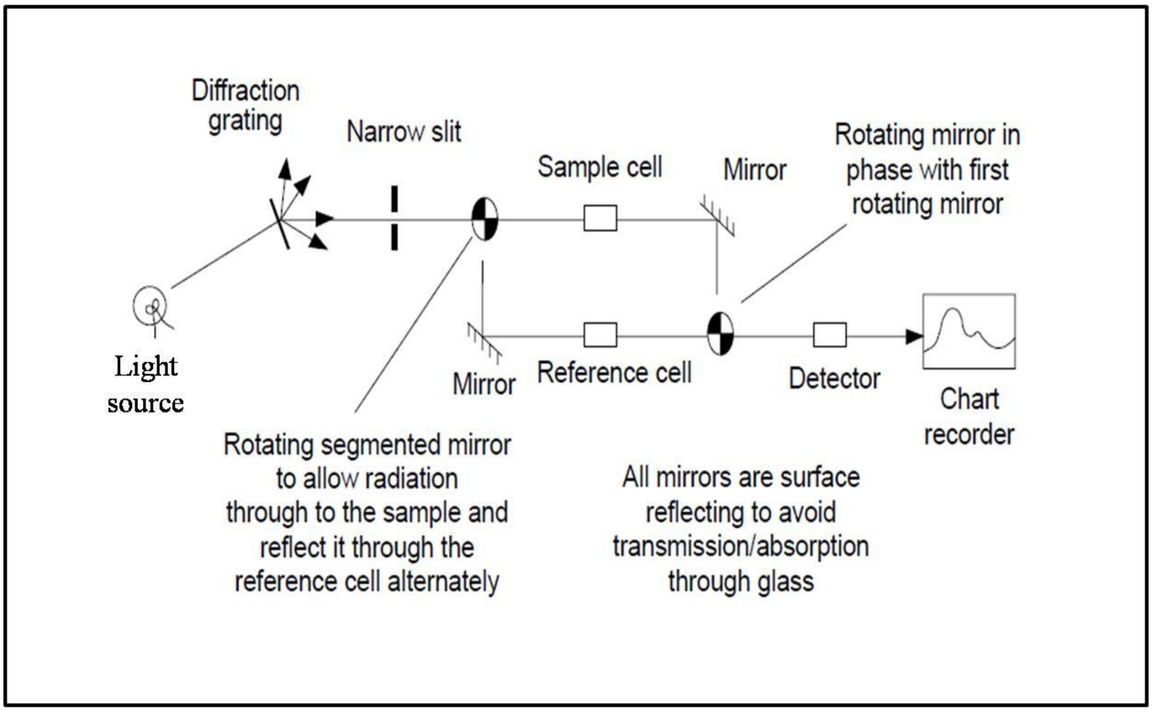

Figure 2.15. Schematic representation of a typical UV-VIS spectrophotometer.

The absorption phenomenon in UV-VIS spectroscopy follows Beer-Lambert law. According to Beer's law the absorption is proportional to the concentration of the absorbing molecules, and according to Lambert's law, the fraction of radiation absorbed is independent of the intensity of the incident radiation. Combination of the two laws give the Beer-Lambert Law as:

$$\log_{10}\left(\frac{I_0}{I}\right) = \varepsilon c l \qquad (1)$$

where I_0 = the intensity of the incident radiation, I = the intensity of the transmitted radiation, ε = molar absorption coefficient mol^{-1} dm^{3} cm^{-1}) c = the concentration of the absorbing species mol dm^{-3}), and l = the path length of the absorbing solution cm). The term $\log_{10}\left(\frac{I_0}{I}\right)$ is known as the absorbance of the solution, and is obtained directly from the spectrometer output in a recording device, often as ‘absorbance units’. The wavelength at which maximum absorption occurs (λ_{max}) is another important parameter, characteristic of absorbing molecule. Therefore for a known value of ε, λ_{max} and l, the concentration of a solution can be obtained from Beer-Lambert law. The values of both ε and λ_{max} are strongly influenced by the nature of the solvent, and for organic compounds, by the degree of conjugation and substitution.

Application of ultraviolet-visible spectroscopy in the study of reaction kinetics: UV-VIS spectroscopy has been successfully applied to investigate the kinetics of a chemical reaction. The method is based on measuring the change in absorbance due to change in reactant or product concentration.

The method can be explained taking an example of a first order reaction. For a first order reaction, the rate equation can be written as:

$$r = -\frac{dC}{dt} = k.C \tag{2}$$

$$\ln C = \ln C_0 - kt \tag{3}$$

where, r = rate of the reaction, C = concentration of reactant, t = time, *k* = rate constant.

Since absorbance of the absorbing species (reactant or product) is proportional to its concentration (equation 1), as such the absorbance (A) can be used in the rate expression instead of concentration.

$$\log_{10}\left(\frac{I_0}{I}\right) = A = \varepsilon cl \tag{4}$$

$$\ln(A_t - A_\infty) = \ln(A_0 - A_\infty) - kt \tag{5}$$

Where, A_t = absorbance at time t, A_0 = absorbance at the beginning of reaction, A_∞ = absorbance at completion of reaction.

One can consider A_∞ to be of the same value as the absorbance of the reference sample ($A_\infty = A_{ref} = 0$). Thus, the equation (5) can be rewritten as follows:

$$\ln\left(\frac{A_t}{A_0}\right) = -kt \tag{6}$$

The slope of the $\ln\left(\frac{A_t}{A_0}\right)$ vs. t curve gives the rate constant of a reaction.

Figure 2.16 gives a typical time resolved UV-VIS spectra of the PNP reduction from the present study. Appearance of several isobestic points in the spectra confirms the absence of any side reactions and the formation of single species as product.

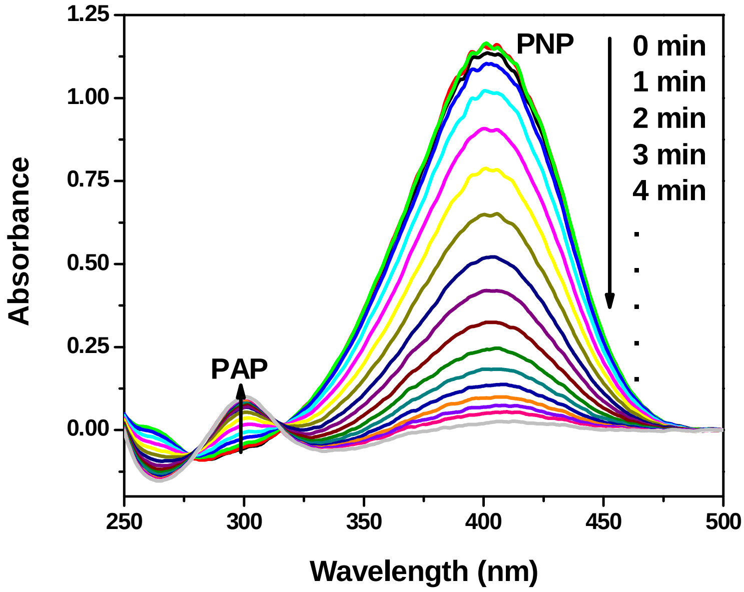

Figure 2.16. Time resolved UV-VIS spectrum during the reduction of p-nitrophenol by sodium borohydride in presence of silver nanoparticles.

Chapter 3

Formation of Silver Nanoparticles in Cation Exchange Membrane by in-situ Reduction Method: Effect of Local Environment on Morphology of Nanoparticles

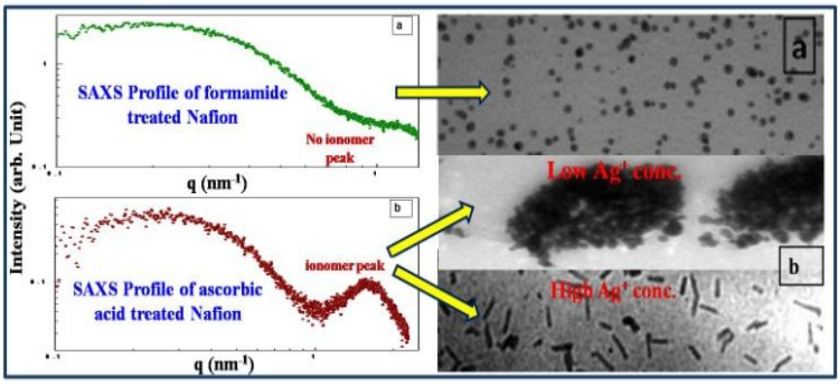

1. Introduction

Ion-exchange membranes [Tant 1997] due to their unique morphology having bicontinuous domain of water and polymer matrix serve as platform for in situ synthesis of metal nanoparticles using appropriate precursor metal ions. Nafion 117 is a commercially available cation exchange membrane consisting of polytetrafluoroethylene (PTFE) backbone and randomly spaced long perfluorovinyl ether side chains terminated by sulfonate ionic group [Gierke et al. 1981].

1.1. Morphology of Nafion Membrane

Morphology of Nafion under different environment has been studied using several experimental techniques like small angle X-ray scattering (SAXS), wide angle X-ray scattering (WAXS), small angle neutron scattering (SANS), atomic force microscopy (AFM), transmission electron microscopy (TEM) and nuclear magnetic resonance (NMR) spectroscopy [Hsu and Gierke 1982.; Hsu and Gierke 1983.; Gierke et al. 1982.; Lee et al. 1992.; Rollet et al. 2001.; Rollet et al. 2002.; Lehmani et al. 1998.; Xue et al. 1989.; MacMillan et al. 1999.; McLean et al. 2000]. Based on these studies, different models describing the self-assembling morphology of Nafion under different physico-chemical environments have been proposed [Mauritz and Moore 2004.; Elliott et al. 2011.; Beers et al. 2011.; Kusoglu et al. 2012.; Mistry et al. 2010.; Gebel and Moore 2010.; MacKnight et al. 1974.; Roche et al. 1980.; Schmidt-Rohr and Chen 2008.; Rubatat et al. 2002.; Rollet et al. 2004.; Rubatat et al. 2004.; Haubold et al. 2001.; Starkweather 1982.; Heitner-Wirguin 1996.; Fujimura et al. 1981.; Fujimura et al. 1982.; Gebel 2000].

The first important morphological description of Nafion is based on "Cluster-channel network model" proposed by Hsu and Gierke [1982, 1983]. This model qualitatively explains the origin of ionomer peak in SAXS profile (due to water clusters), high permselectivity and ionic conductivity of Nafion membrane. Figure 3.1 gives the structural formula of the monomer unit of Nafion-117 and the schematic diagram of cluster channel network model as proposed by Hsu and Gierke. This model has been found to be quantitatively inconsistent with data over a wide range of scattering angles and from membranes oriented by tensile draw. Also the connecting cylindrical nanochannels proposed in this model have never been directly evidenced by scattering techniques and microscopy.

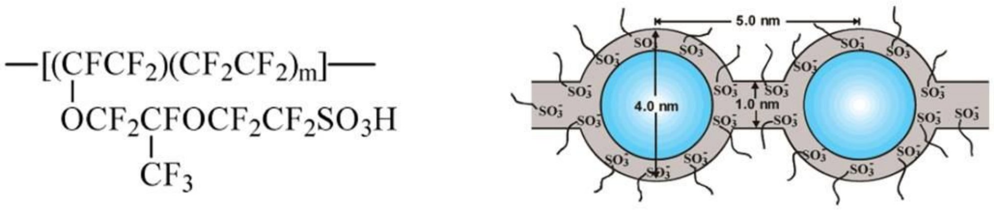

$$\begin{array}{l} -[(\mathrm{CFCF_2})(\mathrm{CF_2CF_2})_m]- \\ \quad | \\ \quad \mathrm{OCF_2CFOCF_2CF_2SO_3H} \\ \qquad\quad | \\ \qquad\quad \mathrm{CF_3} \end{array}$$

Figure 3.1. Structural formula of the monomer unit of Nafion-117 and the cluster-network model of Nafion-117 membrane as proposed by Hsu and Gierke [1982, 1983].

Rubatat et al. suggested the “Polymeric bundle model” consisting of fluorocarbon chains surrounded by ionic groups and water [Rubatat et al. 2002.; Rubatat et al. 2004]. From their recent studies, Schmidt-Rohr and Chen have quantitatively simulated previously published small-angle scattering data of hydrated Nafion and have proposed the “Parallel cylinder model” [Schmidt-Rohr and Chen 2008]. They described the characteristic ‘ionomer peak’ to be arising from long parallel but otherwise randomly packed water channels surrounded by partially hydrophilic side branches, forming inverted-micelle cylinders. More recently, a unified morphological description of organization of water swollen Nafion has been proposed [Elliott et al. 2011]. This model is based on both statistical (Maximum Entropy approach) and thermodynamic (Dissipative Particle Dynamics) descriptions, and suggests a bicontinuous network of ionic clusters embedded in a matrix of fluorocarbon chains. This model accepts the existence of ionic clusters network without need of extended parallel channels. Figure 3.2 gives the schematic representation of the morphological models as discussed above.

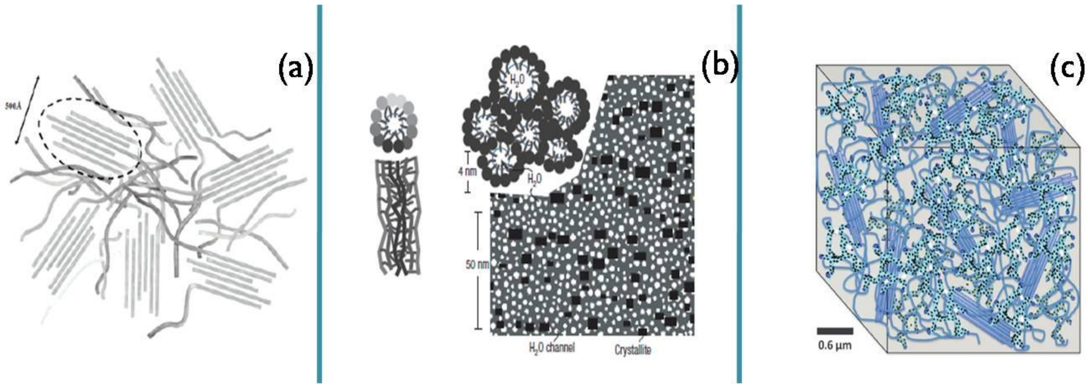

Figure 3.2. Schematic representation of Polymeric bundle model (a) (Rubatat et al [2002, 2004]), Parallel cylinder model (b) (Schnidt-Rohr and Chen [2008]), and Bicontinuous network model (c) (Elliott et al. [2011]) of Nafion 117 membrane.

1.2. Nafion Membrane as a Host for Nanoparticles

The presence of self-assembled water-sulfonate clusters in Nafion 117 has prompted many researchers to use them as nanoreactors for synthesis of nanosized metal and ceramic particles [Shahinpore et al. 1998.; Kim and Shahinpore 2003.; Shahinpore and Kim 2005.; Sachdeva et al. 2006.; Kumar et al. 2010.; Sun et al. 2004.; Hasegawa et al. 2012.; Rollins et al. 2000.; Domenech et al. 2014]. In most of these studies, the spherical nanoparticles having size much bigger than 4-5 nm size of the water clusters have been formed. This suggests that the formation of nanoparticles in Nafion membrane is a multi-steps process that may be controlled by unknown matrix parameters and nature of reductants. The understanding of these parameters is important to incorporate desirable nanostructures having appropriate shape and size for a given application. Though Nafion 117 membranes have been used as a template for the synthesis of metal nanostructures, the role of local environment prevailing in the membrane matrix in the process of formation of different dimensional metal nanostructures is not clearly known.

Water clusters in Nafion membrane contain fixed ionic groups with mobile counter ion in a reverse micellar structure which can act as template for nanoparticles synthesis. The morphology of Nafion membrane can be altered by swelling the membrane in organic solvent which destroys the reverse micellar structure and hence the templating structure. In the present work silver nanostructures of different shapes and sizes have been synthesized in Nafion-117 membrane by manipulating local environment in the membrane using carefully selected reductants, varying temperature and controlled loading of Ag^+ ions in the matrix by ion-exchange process. Transmission electron microscopy (TEM) and small angle X-ray scattering (SAXS) technique have been used to study the morphology of membrane, and size, shape and spatial distribution of AgNPs in the membrane. It has been observed that the reduction of Ag^+ ions with BH_4^- ions occurs at the surface of Nafion membrane [Sachdeva et al. 2006]. This is attributed to fact that anions are excluded from cation-exchange matrix due to Donnan exclusion. During reduction with BH_4^-, Na^+ ions displace Ag^+ ions from ion-exchange sites and thus reduction occurs at the membrane interface. Nonionic reductants like formamide ($HCONH_2$), and dimethyl formamide ($HCON(CH_3)_2$) have been used to form Ag nanoparticles uniformly distributed in the Nafion matrix [Kumar et al. 2010]. However, these non-ionic reductants swell Nafion matrix and destroy original physical architecture of the membrane during reduction. The choice of reductant with suitable reactivity is therefore important to prepare AgNPs of different size, shape and spatial distribution in the membrane. Ascorbic acid has been used in the present work which is well known chemical reductant for nanoparticle synthesis [Qin et al. 2010.; Lu et al. 2006.; Singha et al. 2014.; Chekin and Ghasemi 2014.; Sun et al. 2009.; Steinigeweg and Schlucker 2012.; Jana et al. 2001] and it does not affect the water clusters network in the membrane. In order to study the formation of nanoparticles in Nafion without water clusters, formamide has also been used as reductant as it swells Nafion matrix resulting in destruction of the water clusters network, and altering the local environment. The role of the membrane morphology and nature of the reductant in controlling sizes and shapes of the nanostructures has been investigated. The modifications in self-assembling morphology of the membrane in different solvent/reductant have been studied by SAXS. The size, size dispersion and spatial distribution of AgNPs under different reduction condition have been studied by combined SAXS and TEM. The results have been discussed.

2. Experimental Section

2.1. Materials and Reagents

Nafion-117 ionomer membrane with an equivalent weight of 1100 g/SO_3H was purchased from Ion Power Inc. Analytical Reagent grade chemicals $AgNO_3$, CsCl, NaCl, $NaNO_3$, formamide and ascorbic acid were purchased from BDH (Poole, England). De-ionised water (18 MΩ/cm) purified by model Quantum^{TM} from Millipore (Mumbai, India) were used throughout the experiments.

2.2. Membrane Sample Preparation

Nafion-117 membrane was cut into a few 2 cm x 2 cm pieces, and conditioned by conventional treatments described elsewhere [Goswami et al. 2001]. The conditioned pieces of Nafion membrane in Na^+ counterionic form were equilibrated with freshly prepared 0.25 mol L^{-1} $AgNO_3$ solution for 30 min under stirring condition, ensuring complete exchange of Na^+ ions by Ag^+ ions. These Ag^+ loaded membrane samples were subjected to chemical reduction for the formation of silver nanoparticles in the membrane. Post reduction, the nanocomposite membranes were converted to Na^+ and Cs^+ ionic forms by immersing the membrane pieces into 25 mL of 0.5 mol L^{-1} NaCl and 0.5 mol L^{-1} CsCl solutions, respectively, for about 24 h. The conditions used for conversion of one ionic form to another ionic form of the membrane sample under stirring conditions are based on our previous work [Sodaye 2008].

2.2.1. Reduction of Ag^+ Loaded Membrane with Formamide

The membrane samples fully loaded with Ag^+ ions were chemically reduced with formamide at 40, 50 and 65 ^oC. A water bath was used to maintain the constant temperature during reduction process. Reduction was carried out for 30 min for each of the samples. The samples were named as AFT40, AFT50 and AFT65 for identification of the formamide reduced samples at 40, 50 and 65 ^oC, respectively. The membrane samples were finally equilibrated with 0.25 mol L^{-1} $NaNO_3$ to remove any unreduced Ag^+ ions.

2.2.2. Reduction Ag^+ Loaded Membrane with Ascorbic Acid

Ag^+-loaded membrane samples were immersed in 0.25 mol L^{-1} $NaNO_3$ solution under stirring condition for 30, 45 and 60 s to prepare the membrane samples having 25%, 10% and 2 % of ion-exchange sites occupied by Ag^+ ion. The time required for preparing membranes having desired extent of loading of Ag^+ ions were fixed based on experimental information given in the paper by Sachdeva et al. [2006]. Figure 3.3 gives the plot reproduced from Sachdeva et al. [2006], showing the variation of Ag^+ ions in ion-exchange sites (mol %) in a Nafion-117 membrane sample (2 x 2 cm^2) as a function of equilibration time in $NaNO_3$ (0.25 mol L^{-1}) under stirring condition. The membrane samples were then reduced with 0.1 mol L^{-1} ascorbic acid solution for 5 min at room temperature under stirring condition. A thin metallic layer was formed on the membrane surface which was removed by gentle scratching of membrane surfaces with wet adsorbent paper. The samples were named as A1, A2 and A3 for identification of ascorbic acid reduced samples containing 25%, 10% and 2 % of Ag^+ ions occupying the ion-exchange sites. Finally, the membranes were equilibrated with 0.25 mol L^{-1} $NaNO_3$ to remove any unreduced Ag^+ ions.

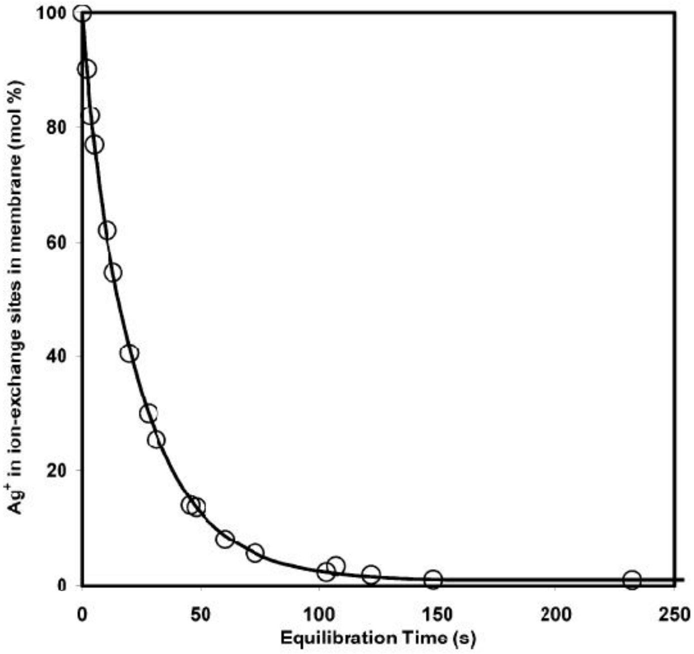

Figure 3.3. Variation of Ag^+ ions in ion-exchange sites (mol %) in a Nafion-117 membrane sample (2 cm x 2 cm) as a function of equilibration time in $NaNO_3$ (0.25 mol L^{-1}) under stirring condition. [Sachdeva et al. 2006]

2.3. Characterization

2.3.1. Transmission Electron Microscopy

Post reductions, the AgNPs containing membranes were equilibrated with $NaNO_3$ solution to convert them into Na^+ form. TEM of the cross-section across the thickness of these membrane samples been carried out. The membrane samples were sectioned under cryogenic environment in Leica ultramicrotome to 70 nm thickness. The sections were picked on 200 mesh formvar and carbon coated Cu grids. The grids were examined in an FEI Technai G2 electron microscope at IIT Mumbai at 120 keV without any external treatment.

2.3.2. Small Angle X-ray Scattering

Water soaked nanocomposite membrane pieces (2 cm x 2 cm) were subjected for SAXS experiment. The experiments were carried out using a laboratory based SAXS instrument with CuK_α as probing radiation. Radial averaged scattering intensity (I(q)) was obtained within a wave vector transfer ($q=4\pi \sin(\theta)/\lambda$, where λ is the wavelength and 2θ is the scattering angle) range of ~0.1 nm^{-1} to 2.5 nm^{-1}.

Analyses of SAXS data: Due to the existence of water-sulfonate clusters as well as silver nanostructures, the whole scattering profile was broadly subdivided into two zones i.e. water clusters and Ag nanostructures embedded in fluorocarbon matrix. The hydrophobic fluorocarbon structures and the silver nanostructures were not considered separately for simplicity. In the entire analysis and discussion, the silver nanostructures profile therefore indicates the profile due to nanostructures in hydrophobic fluorocarbon matrix. As the scattering space and the real space are connected by Fourier transform, the information about the smaller length scale (water cluster in this case) is primarily manifested at relatively higher q region. Similarly, the scattering signal at lower q region is primarily due the nanoparticles and their agglomerated structures. The following model was used for analysis of the scattering profiles.

Total scattering intensity at a given scattering vector [I(q)] may be represented as sum of two components:

$$I(q) = C_I I_1(q) + C_2 I_2(q) \tag{1}$$

In equation 1, the first and second terms on the RHS correspond to scattering from Ag nanostructures and water clusters, respectively. C_1 and C_2 are proportional to respective number densities.

(i) Polydisperse spherical particle model: For such a case, $I_1(q)$ may be approximated as:

$$I_1(q) = I_{NS}(q) = \left(\int_0^\infty P_{NS}(q,R) R^6 D_{NS}(R) dR \right) \tag{2}$$

where, $P_{NS}(q,R)$ represents the form factor of a nanostructure. For spherical nanostructures of radius R, it is given by:

$$P_{NS}(q,R) = 9 \frac{(\sin(qR) - qR\cos(qR))^2}{(qR)^6} \tag{3}$$

$D_{NS}(R)$ represents the nanostructure size distribution, i.e., $D_{NS}(R)dR$ indicates the probability of having size between R and R+dR. In the present case, standard log normal distribution of following type

$$D_{NS}(R) = \frac{1}{\sqrt{2\pi\sigma^2 R^2}} \exp\left[-\frac{\left[\ln(R/R_0)^2\right]}{2\sigma^2} \right] \tag{4}$$

was considered. R_0 represents the mean radius and σ represents the variance of the distribution being obtained by fitting the SAXS profiles.

(ii) Local monodisperse spherical particle model: The second term ($I_2(q)$) of the eq 1 under local monodisperse approximation is expressed as

$$I_2(q) = I_{WC}(q) = \left(\int_0^{\infty} P_{WC}(q,R) R^6 D_{WC}(R) S_{WC}(q,R) dR \right) \tag{5}$$

where, $P_{WC}(q,R)$ represents the form factor of a water cluster. $D_{WC}(R)$ represents the water cluster size distribution and defined in the same manner as $D_{NS}(R)$. $S_{WC}(q,R)$ is the structure factor which represents the presence of water cluster in the membrane. The peak at higher q in the scattering profile appears due to such correlation between the water clusters. A hard sphere type interaction potential was considered in the present case between the water clusters [Pedersen 1994].

In some samples, another extra length scale was required to fit the scattering profile. This was due to agglomeration of nanoparticles or formation of non-spherical anisotropic particles. To account for the scattering contribution from such inhomegeneities, which is predominant only at very small q regime, a third term similar to that of equation 2 was added to equation 1 for fitting the whole scattering profile in a simpler way. In addition, the scattering profiles for the nanorod sample (A1) in both the ionic form were fitted using the form factor of cylinder [Pedersen 1997]. A lognormal distribution for the radius polydispersity was assumed. Radius distribution and length of the nanorods was estimated by fitting the scattering data with the model. For cylindrical nanostructures of radius ‘R’ and length ‘L’, the term ‘P_{NS}’ (form factor) of the equation is expresses as:

$$P_{NS}(q) = \int_0^{\pi/2} \left[\frac{2J_1(qR\sin(\alpha))}{qR\sin(\alpha)} \frac{\sin(qL\cos(\alpha)/2)}{(qL\cos(\alpha)/2)} \right]^2 \sin(\alpha) d\alpha \tag{6}$$

Where $J_1(x)$ represents the Bessel function of first order. The integration over 0 to $\pi/2$ takes care of all possible orientation of the cylinders.

3. Results and Discussion

Figure 3.4a and 3.4b shows the SAXS profile of pure Nafion 117 samples in Na^+ form equilibrated with formamide and ascorbic acid (0.1 mol L^{-1}) solution respectively. The peak seen at higher q value (q ~ 1.7 nm^{-1}) in Figure 3.4b is characteristic of water clusters in Nafion 117 [Mauritz and Moore 2004]. As seen in Figure 3.4a, the peak disappears for the membrane sample equilibrated with formamide. This is because formamide swells the PTFE backbone of the membrane and destroys the water clusters network of the membrane. The SAXS profile clearly shows the distinctly different morphology or local environment of the membrane, when reduction of Ag^+ is carried out with formamide and ascorbic acid solution respectively. The reduction with formamide has been carried out with fully Ag^+ loaded membrane samples as only 8-16 % of Ag^+ ions occupying ion-exchange sites are finally locked in the membrane as nanoparticles [Kumar et al. 2010]. Due to swelling of the membrane, bulk of the nanoparticles is released from the membrane to bulk formamide solution. Temperature has been used as a variable parameter during formamide reduction to vary reduction rates.

The selection of ascorbic acid has been based on the following considerations: (i) it is water soluble, (ii) room temperature reduction is possible, (iii) it can enter in the ionomer matrix as neutral molecules unlike BH_4^- reductant that are excluded from the cation-exchange membrane due to Donnan exclusion of anions [Sachdeva et al. 2006], (iv) the water clusters network morphology of pristine Nafion is preserved during reduction with ascorbic acid, see Figure 3.4b. Thus, ascorbic acid is expected to reduce the Ag^+ ions in water clusters domain of the ionomer matrix. The reduction with ascorbic acid has been carried out using membrane samples containing 25%, 10% and 2 % of ion-exchange sites occupied by Ag^+ ions. The ascorbic acid reduction of membrane samples having more than 25% ion-exchange sites occupied by Ag^+ ions lead to metallization.

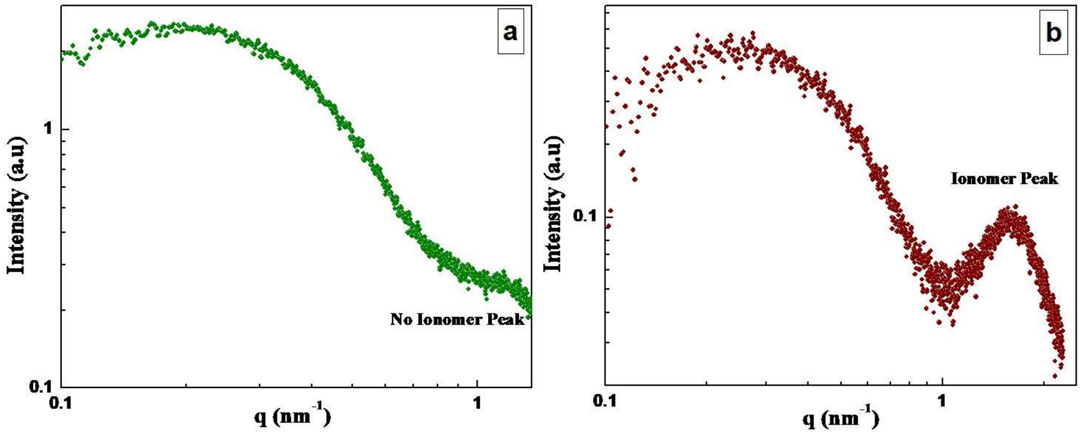

Figure 3.4. SAXS profiles of (a) formamide (65 °C) and (b) ascorbic acid (27 °C) treated Nafion 117 samples.

3.1. Chemical Reactions Involved in the Reduction of Silver Ions

3.1.1. Reduction of Ag^+ by Formamide

Mechanism of reduction of silver ions using N,N-dimethyl formamide and formamide as a reducing solvent have been discussed by Pastoriza-Santos and Liz. Marzan [1999, 2000, 2002] and Sarkar et al. [2005]. There are various possible routes for the oxidation of formamide by production of NH_3, CO_2, and H_2 gases [Yu et al. 1990]. Sarkar et al. [2005] have observed from GC measurement the evolution of CO_2 on addition of silver salt in formamide. Based on the observation of evolution of NH_3 and CO_2, Scheme 3.1 has been proposed for reduction of Ag^+ ion by formamide.

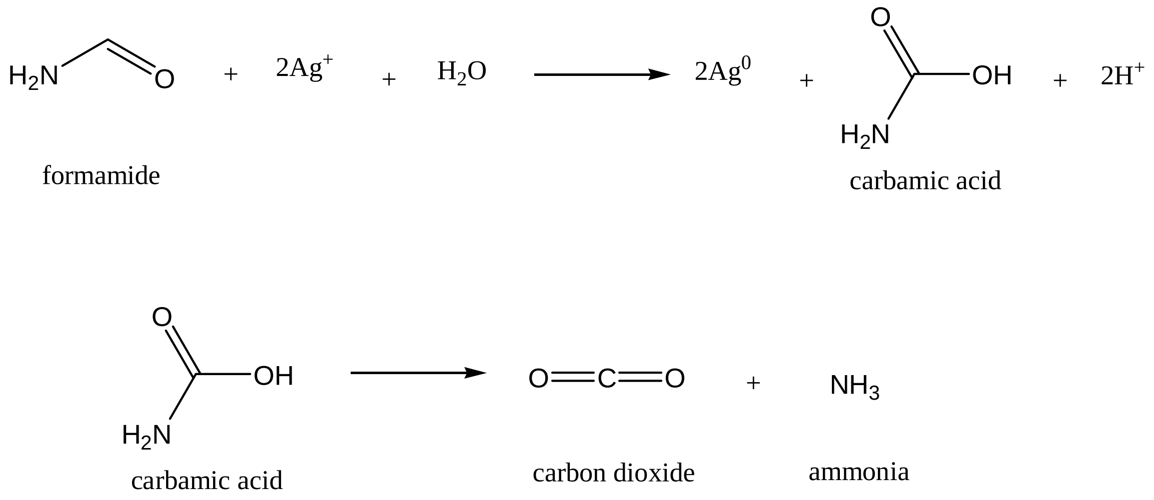

Scheme 3.1. Chemical reactions involved during the reduction of silver ions with formamide.

It is noteworthy that the evolution of CO_2 gas does not take place during reduction of silver ions by dimethyl formamide (DMF) at room temperature [Pastoriza-Santos and Liz. Marzan 1999, 2000, 2002].

3.1.2. Reduction of Ag^+ by Ascorbic Acid

Ascorbic acid is a water soluble dibasic acid with an enediol group built into a five membered heterocyclic lactone ring. It behaves as a vinylogous carboxylic acid because of its conjugated structure with involvement of the lone electron pair on the hydroxyl group, the double bond of the ring structure, and the carbonyl double bond. The L-ascorbic acid structure consists of two asymmetric carbon atoms. The hydroxyl proton located at the end of the vinyl group is extraordinarily acidic compared to a common alcoholic hydroxyl group due to the extra stability of the conjugate base of the ascorbic acid by two major resonance structures. It is known that the mono-protonated form of the ascorbic acid (HA^-) is the species which is primarily responsible for reduction of metal ions during nanoparticles synthesis [Jomova and Valko 2011.; Mushran et al. 1974].

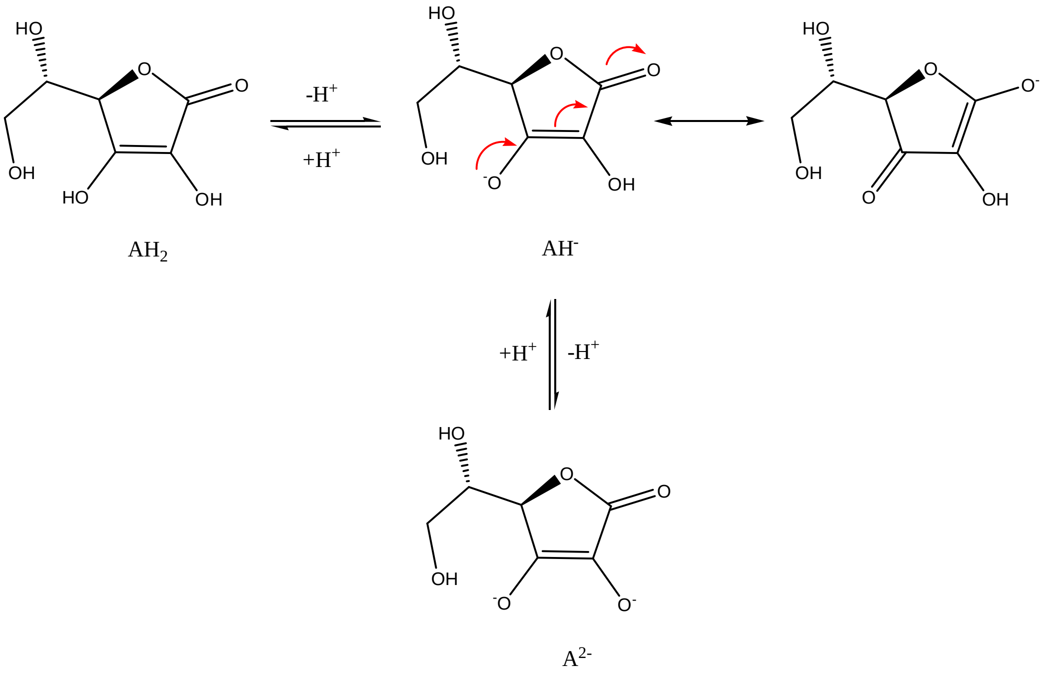

Scheme 3.2. Resonance structures in the conjugate bases of L-ascorbic acid. H_2A, HA^- and A^{2-} represents the neutral, mono-protonated and deprotonated form of ascorbic acid.

The pH of the L-ascorbic acid solution in the present experiment has been measured to be 2.63. At this low pH, ascorbic acid is expected to be present as neutral molecule (H_2A) and a small fraction will be present as ascorbate anion (HA^-) ($pK_a = 4.26$). The reduction of Ag^+ ions by ascorbic acid follows first order kinetics with respect to ascorbic acid and silver ion concentrations, together with an inverse first-order dependence on H^+ ions concentration

[Mushran et al. 1974]. S.P. Mushran et al. [1974] have monitored the progress of the reaction between ascorbic acid and silver ions and have proposed the stoichiometric equation for the reduction of silver ions with ascorbic acid (H_2A) as shown in Scheme 3.3. The mechanism involves the interaction of Ag^+ ions with the ascorbate anions (HA^-), which is the slowest step, resulting in the formation of a free radical ($HA^\cdot$), attacked by a second silver ion to form dehydroascorbic acid (A). Because of the proton release, the reduction potential of the system is pH dependent.

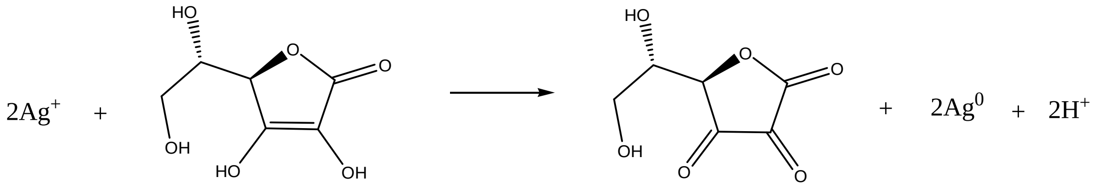

ascorbic acid

dehydroascorbic acid

Scheme 3.3. Stoichiometric equation for the reduction of silver ions by L-ascorbic acid.

3.2. Shapes and Spatial Distributions of Nanostructures

3.2.1. Formamide Reduced Samples (AFT65, AFT50 & AFT40)

Spherical silver nanostructures have been produced uniformly throughout the membrane matrix by formamide reduction at different temperature. The representative TEM image of cross-section of a formamide reduced membrane sample is shown in Figure 3.5. The size of the nanostructures has been found to increase with increase in temperature.

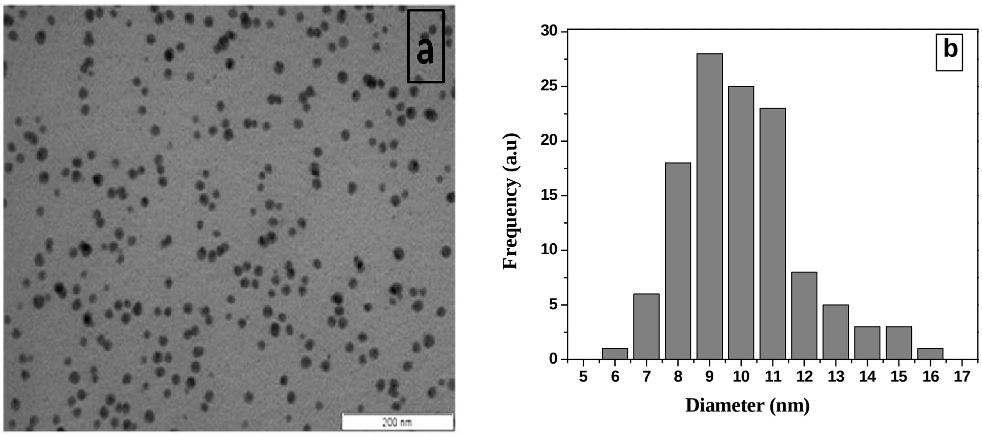

Figure 3.5. Representative TEM image of cross-section of membrane showing spatial distribution of silver nanospheres produced in sample AFT65 after post reduction neutralization with Na^+ ions (a), and corresponding size distribution histogram (b).

During formamide reduction, ~80% of the silver seeds formed in formamide swelled matrix is lost from the membrane. The seeds that are retained in the matrix grow to form bigger nanosphere. Because of uniform distribution of the reductant (formamide) in the membrane, the nucleation of AgNPs occurs uniformly in the membrane matrix; resulting in homogeneous spatial distribution of the nanoparticles in the membrane matrix. However, micro-inhomogeneity in spatial distribution of Ag nanoparticles has been observed in TEM image shown in Figure 3.5. This has been attributed to high density fluorocarbon domains that did not contain significant number of ionic clusters. It is noteworthy that the water clusters network is regenerated after equilibration of formamide reduced sample in salt solution as indicated by SAXS analyses.

The SAXS profiles for the formamide reduced samples named AFT65, AFT50 and AFT40 after post reduction neutralization with Na^+ and Cs^+ ions are shown in Figure 3.6a and Figure 3.6b, respectively. SAXS profile for pristine Nafion in the respective ionic form (Unmod) is also given to show the changes in SAXS profile after incorporation of nanostructure in the membrane matrix. The ionomer peak near q value of 1 nm^{-1} appears in all the Na$^+$ form of membrane due to scattering from the water clusters. The peak around q ~ 0.4 nm^{-1} is associated with the fluorocarbon matrix region of unmodified Nafion matrix and the embedded silver nanostructures along with fluorocarbon structures in Nafion nanocomposites. The variation in position and intensity of the scattering maxima at ionomer peaks indicated dimensional changes of the spherical water clusters. For Cs$^+$ loaded samples, the ionomer peak is much weaker due to lesser hydration of the membrane in Cs$^+$ form.

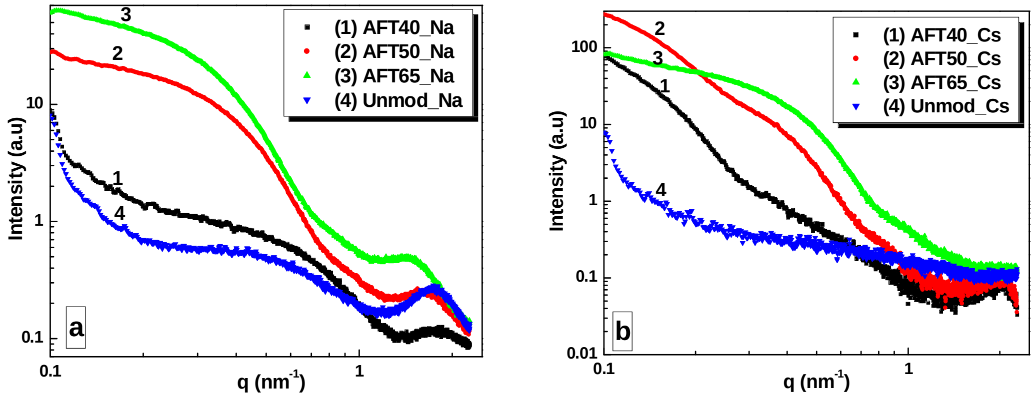

Figure 3.6. SAXS profiles for formamide reduced samples in Na$^+$ (a) and Cs$^+$ (b) counterionic forms, obtained after post reduction neutralization.

It can be seen from Figure 3.6 that the SAXS pattern strongly depends upon ionic form of the membrane. The size distribution profiles for both Ag nanostructures and water cluster in Nafion matrix has been obtained from the fitting of the SAXS profile with appropriate model as described in Section 2.3.2. Figure 3.7 shows the size distribution profiles for spherical Ag nanoparticles in Nafion matrix in Na^+ and Cs^+ counterionic forms. The comparison of size distribution profile obtained by SAXS analyses (plot 3 of Figure 3.7) with TEM histogram of size distribution for the same sample (Figure 3.5b) shows reasonable good agreement. This indicates that SAXS profiles can be used for identifying changes in size dispersions of the nanoparticles if assumption for the shape factor is valid.

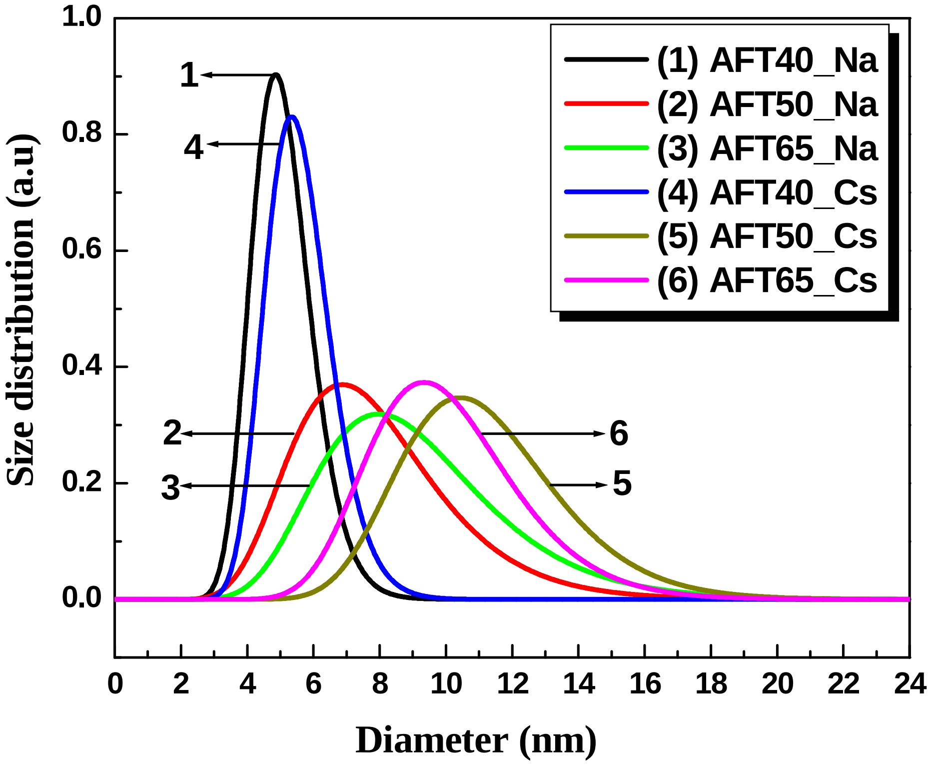

Figure 3.7. Size distributions of spherical Ag nanoparticles in formamide reduced Nafion samples obtained from analyses of SAXS profiles in Na^+ and Cs^+ post reduction neutralized forms.

From the size distribution plots of Na^+ neutralized samples, it is seen that mean size and size dispersion of the spherical Ag nanoparticles increases with increase in temperature during formamide reduction. Thus, lower temperature is preferable for formation of smaller spherical nanoparticles with narrower size dispersion. The size and size dispersion of nanoparticles in the samples post neutralized with Cs^+ ions shifts to higher mean size, indicating further reorganization of Ag nanostructures. There is no significant difference in the size distributions of Ag nanoparticles obtained from SAXS profiles of AFT50 and AFT65 samples in Cs^+ neutralized form.

In order to study the membrane morphology, the water clusters size distributions in the nanocomposite samples having Na^+ and Cs^+ ionic forms has been compared with that in the pristine samples, see Figure 3.8. In the Na^+ neutralized samples, the mean diameters and size dispersions of water clusters increase with increase in the mean size of spherical Ag nanostructures. As can be seen from Figure 3.8a, the mean diameter of water clusters follows the trend AFT65>AFT50>AFT40 and lies in the range of 2 to 4 nm. The mean size of water clusters in the unmodified Nafion in Na^+ form lies in between AFT65 and AFT50. The water cluster size distribution for the Cs^+ neutralized samples shows no significant difference in mean sizes of water clusters. The mean size distributions of water clusters in pristine and nanostructures embedded samples almost match in Cs^+ neutralized forms.

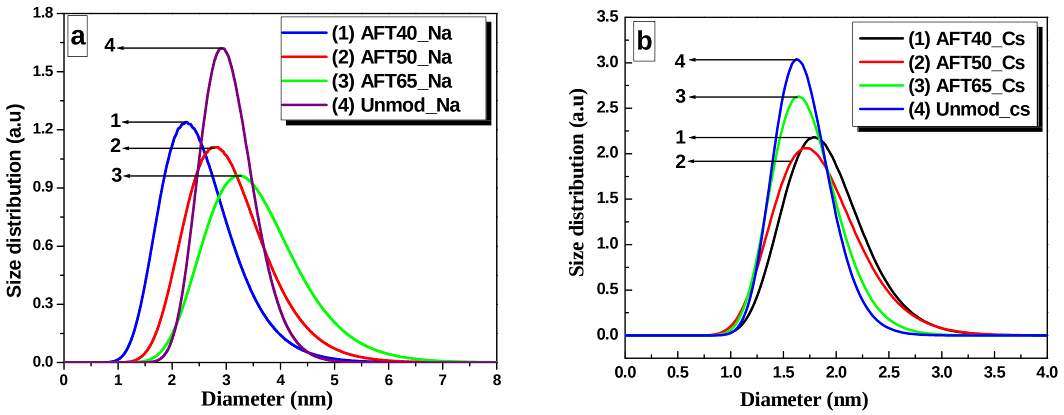

Figure 3.8. Water cluster size distribution plots for formamide reduced samples followed by post reduction neutralization with Na^+ ions (a) and Cs^+ ions (b).

3.2.2. Ascorbic Acid Reduced Samples (A1, A2 & A3)

The representative TEM images showing shapes and spatial distributions of ascorbic acid reduced sample (A1) formed using sample containing 25% Ag^+ ions in ion-exchange sites (IES) are given in Figure 3.9. It is seen from the figure that silver nanorods are formed. This is unusual as water clusters (reverse micelle) in the ionomer matrix are expected to be sites for growth of spherical Ag nanoparticles of size comparable to size of the water cluster. At surface, metallization is seen due to high reduction rate, which can be removed by gentle scrubbing of surface. Hollow cylinders are formed just below the surface as shown in Figure 3.9a. However, needle-like Ag nanorods are seen to be uniformly formed at interior of the ionomer matrix. The formation of hollow cylinders may be due to defects in matrix near the surface.

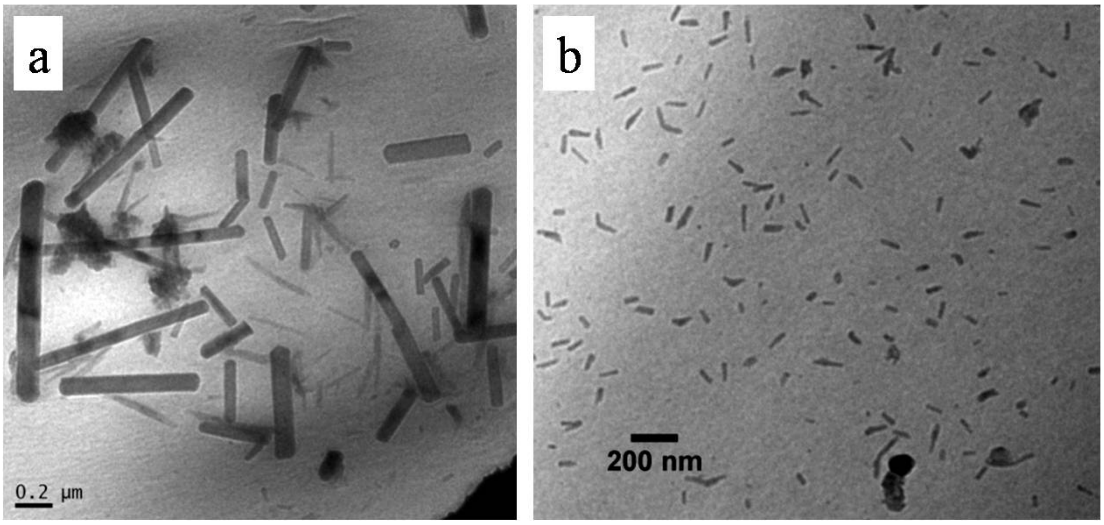

Figure 3.9. TEM images showing shapes and spatial distributions of Ag nano-cylinders near surface (a), and nano-rods across thickness (b) of the ionomer nanocomposite prepared by ascorbic acid reduction of the ionomer sample loaded with 25% of Ag^+ ions.

In sample containing 10% Ag^+ ions in ion-exchange sites (A2), the sponge like bigger Ag nanostructures are formed instead of nanorods (Figure 3.10). These bigger nanostructures appear to be embedded in localized area of PTFE matrix. These nanostructures have a central dense region surrounded by clustering of spherical nanoparticles.

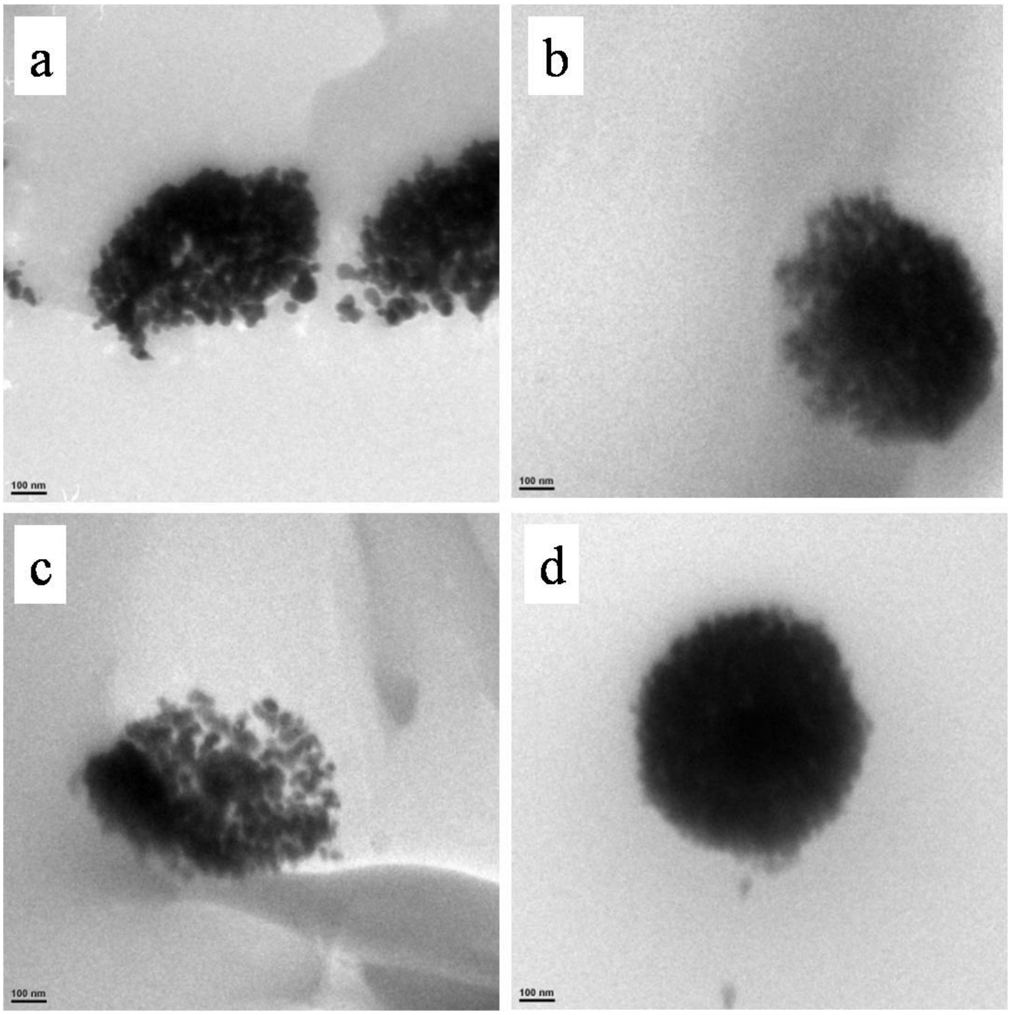

Figure 3.10. TEM images of cross-section of ionomer nanocomposite (A2) showing clustering of nanoparticles to nanosponge like big nanostructures at surface (a) as well as interior matrix (b-d). The samples were prepared by ascorbic acid reduction of the ionomer sample loaded with 10% of Ag^+ ions followed by neutralization with Na^+ ions. The length of the scale bars as shown in the images is 100 nm.

TEM images of ascorbic acid reduced membrane samples initially loaded with 2% Ag^+ ions are given in Figure 3.11 which clearly shows the formation of clusters of nanoparticles during reduction with ascorbic acid. It appears in this case that the nanoparticles remain separately or occasionally formed cluster. It can be seen that separate nanoparticles have diameter range of 4-5 nm, which matches well with the diameter of water clusters in Nafion.

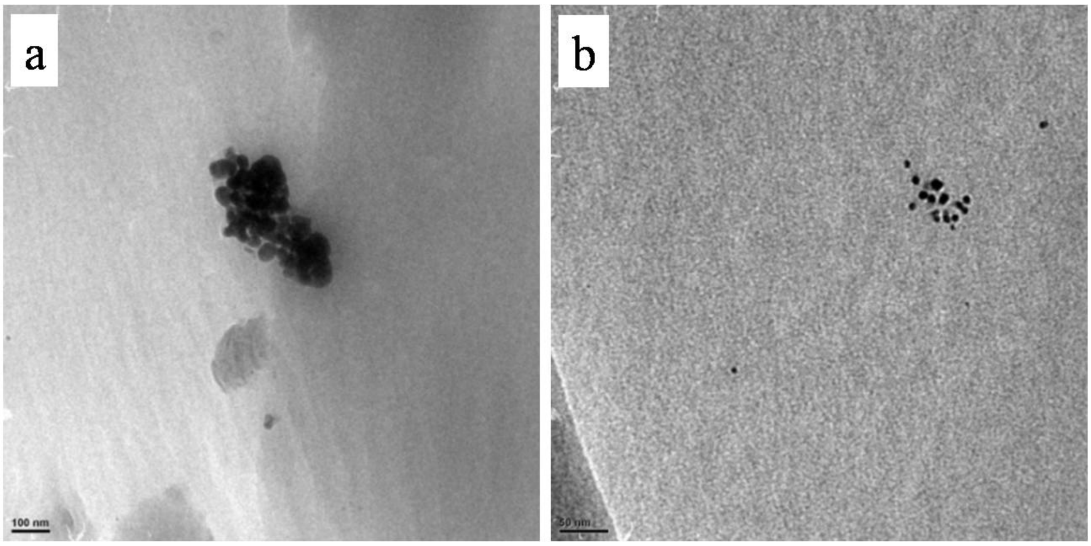

Figure 3.11. TEM images of cross-section of nanocomposite (A3) showing formation of nanoparticle clusters in ionomer matrix. The nanocomposite samples were prepared by ascorbic acid reduction of ionomer sample loaded with 2% of Ag^+ ions followed by neutralization with Na^+ ions. The scale bars as shown in the images are 100 nm (a) and 50 nm (b).

The SAXS profiles of ascorbic acid reduced samples A1, A2 and A3 after post reduction neutralization with Na^+ and Cs^+ ions are compared in Figure 3.12 with the SAXS profiles of pristine Nafion in respective ionic forms.

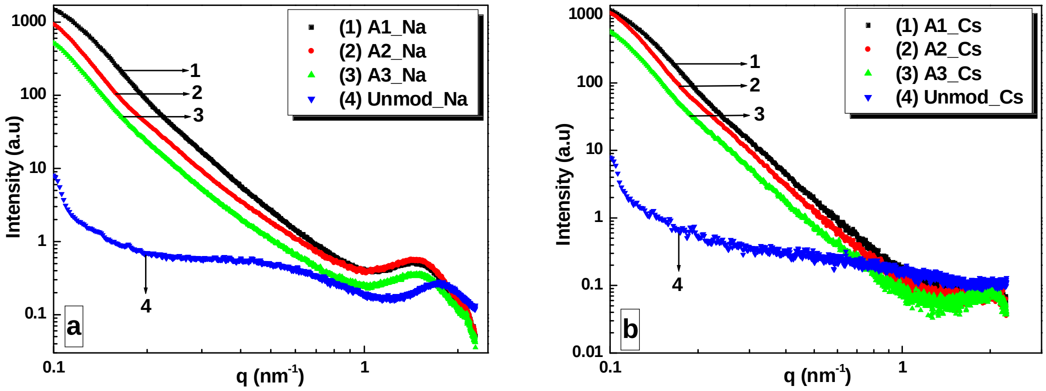

Figure 3.12. SAXS profiles for ascorbic acid reduced samples after post reduction neutralization with Na^+ (a) and Cs^+ (b) ions.

The SAXS profiles of ascorbic acid reduced samples are significantly different from formamide reduced samples. Appearance of a new, relatively more intense scattering maximum at lower q region especially at $q < 0.2$ nm^{-1}, corroborated the existence of extra length scale in the system as observed in the TEM images. This extra length scale has been attributed to the presence of relatively large rod like nanostructures in A1 sample and large nanosponge and nanoclusters in A2 and A3 samples. The size dispersion in cross-sectional diameter of nanostructures in the A1, A2 and A3 samples having Na^+ and Cs^+ ionic forms have been obtained by fitting profiles as described in Section 2.3.2.

The diameter and length distributions of Ag nanorods in the A1 samples obtained by SAXS analyses are compared with TEM size histogram in Figure 3.13. It is seen from the plots that there is reasonably good agreement between distribution profiles obtained from SAXS analyses with TEM histograms. As SAXS size distribution profiles represent bulk distributions, the nanorods having mean diameter ≈ 8 nm and mean length ≈ 40 nm are formed in bulk matrix. It is also seen from SAXS distribution profiles that dimensions of the nanorods are not affected by change in ionic form of Nafion matrix.

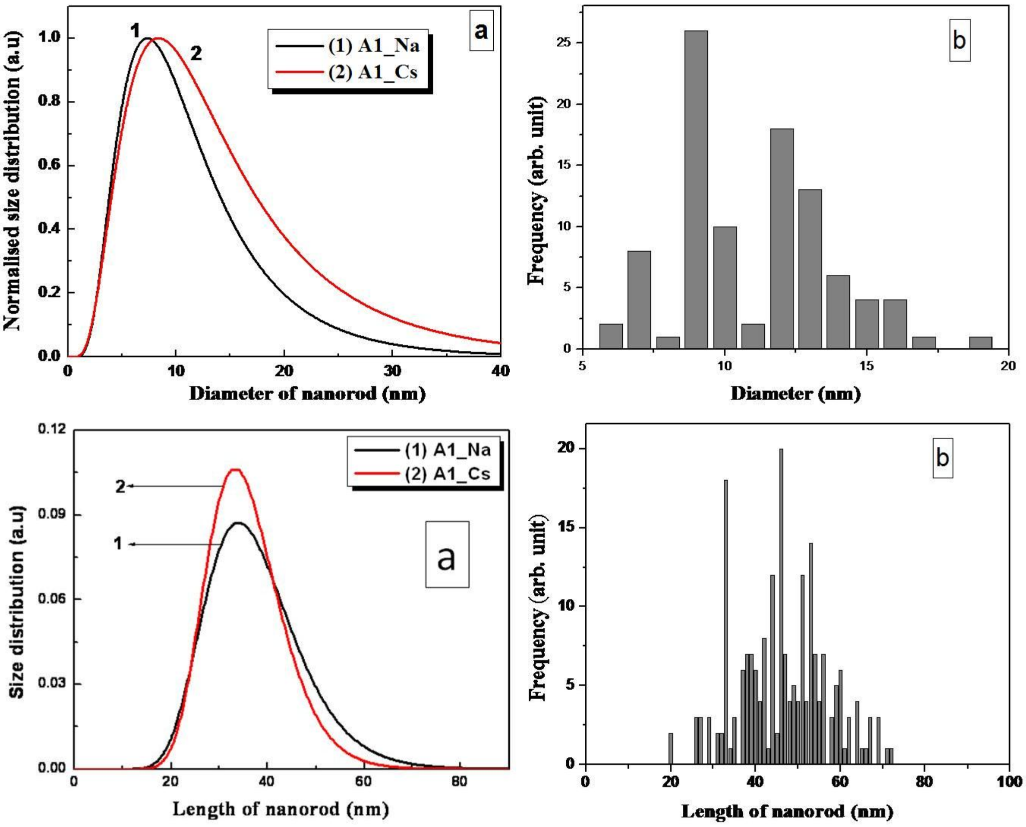

Figure 3.13. Comparison of diameter and length distributions of nanorods in A1 samples obtained by SAXS analyses (a) with TEM histograms (b).

The size distributions of nanorods given in Figure 3.13 have been obtained by fitting SAXS profiles with form factor of sphere. To ensure validity of size distributions given in Figure 3.13, the SAXS profiles for the sample A1 (nanorods) in two different counterionic form (Na^+ and Cs^+) have also been analyzed using the form factor of cylinder. In this case, simultaneous determination of lognormal distribution for both the diameter and the length of the nanorods is ambiguous. Thus, the better way to analyze profile is by assuming one parameter as monodisperse (eg. length of the nanorod) and then determining the lognormal distribution of the other parameter (eg. diameter of the nanorod). During fitting the SAXS profiles, the length has been assumed to be monodispersed with size 30 nm and the scattering profiles have been fitted using form factor of cylinder by varying the three parameters representing number density, polydispersity index and the median of the distribution of nanorod diameter. It is seen from Figure 3.14 that diameter distribution of nanorods obtained by fitting scattering profiles using form factor of cylinder did not show significant difference with that shown in Figure 3.13 using form factor for sphere.

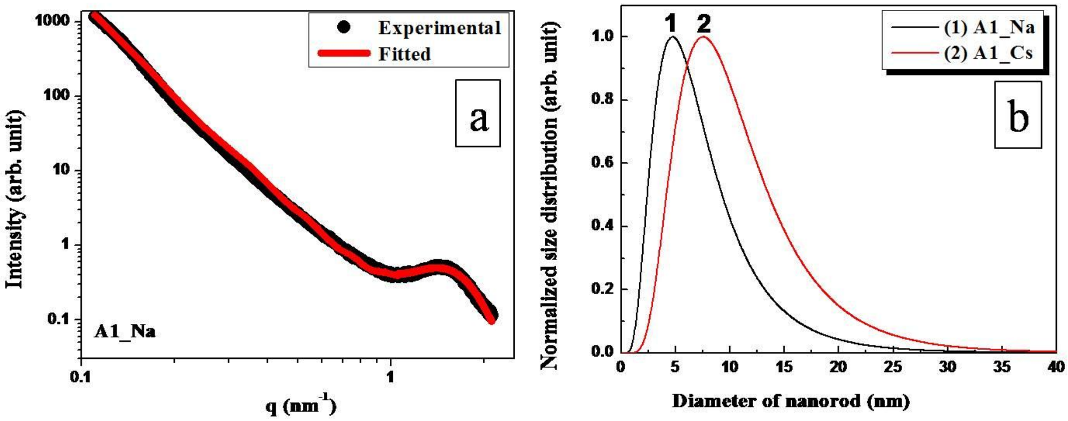

Figure 3.14. Comparison of experimental SAXS profile of sample A1 (in Na$^+$ form) with that fitted with form factor of cylinder (a), and diameter distributions of nanorods in membrane samples having Na$^+$ and Cs$^+$ ionic forms (b).

The diameter distributions of nanoparticles aggregated as nanosponges and nanoclusters in the samples A2 and A3 having different ionic forms are given in Figure 3.15. It is seen from Figure 3.15 that the nanoparticles size distributions drastically changed with change in

Na^+ to Cs^+ counterionic form of the membrane. Water content in Nafion matrix is highly dependent on its counterionic form i.e. water contents in Na^+ and Cs^+ forms of Nafion-117 are 17.2 wt.% and 8.2 wt.%, respectively [Goswami et al. 2001]. In Na^+ form, the nanoparticles having mean diameter 8-10 nm are formed in both A2 and A3 sample (SAXS data). However, TEM images (Figure 3.10 and 3.11) show the formation of nanosponge (A2) or nanoclusters (A3). Therefore, the sponge like structures appears as clusters of smaller nanoparticles as obtained from SAXS. This mean size of nanoparticles is greater than size of the water clusters but similar to diameters of nanorods (A1) and nanoprticles in formamide reduced samples. Thus, all nanostructures appear to be formed from Ag seeds (small particles and clusters) ejected from water clusters into surrounding low density domains. When water content is reduced in the Cs^+ form, the nanoparticles agglomerated due to strain caused by shrinking of surrounding low density fluorocarbon matrix on reduction of the water content. Thus, the size of agglomerated particles increases considerably. It is to be noted that the size distributions given in Figure 3.15 are only for nanostructures having sizes less than 100 nm. The bigger nanostructures (>>100nm) are also seen in TEM images of the samples A2 and A3, which have not been detected by SAXS.

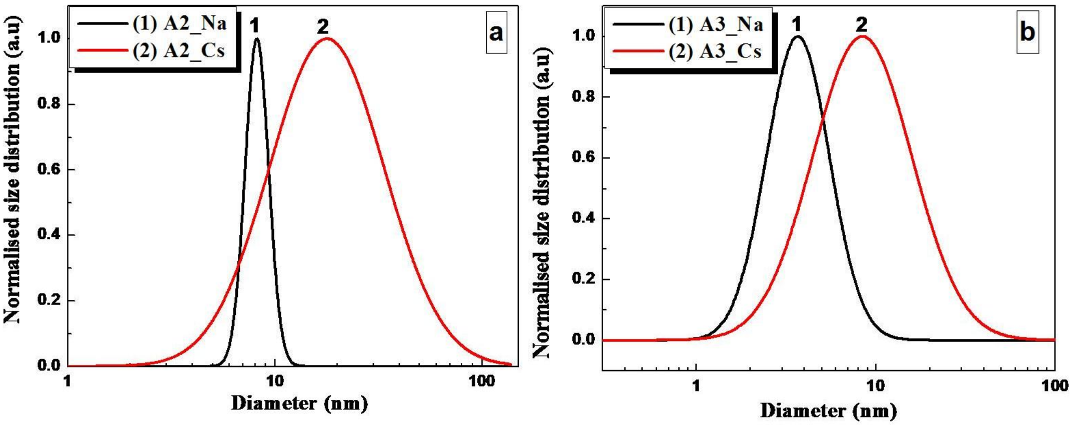

Figure 3.15. Ag nanostructures size distributions of the ascorbic acid reduced samples A2 (a) and A3 (b) obtained by SAXS analyses. The samples were converted to Na^+ and Cs^+ ionic forms after reduction.

The water cluster size distribution plots of ascorbic acid reduced samples after post reduction neutralization with Na^+ and Cs^+ ions are given in Figure 3.16a and 3.16b, respectively. It is seen from Figure 3.16 that there is no significant changes in mean size of the spherical water clusters in all three A1, A2 and A3 samples in same ionic (Na^+/Cs^+) form. Because of comparatively large size of incorporated Ag nanostructures, the mean size and polydispersity of water clusters in the nanoparticles embedded membranes is increased with respect to pristine membrane (unmodified) in Na^+ ionic form. There is not significant change in mean radii of water clusters of the nanoparticles loaded membranes in Cs^+ ionic from as shown in Figure 3.16b. However, larger dispersion of size of water clusters in the nanoparticles loaded samples clearly suggested agglomeration of water clusters to some extent.

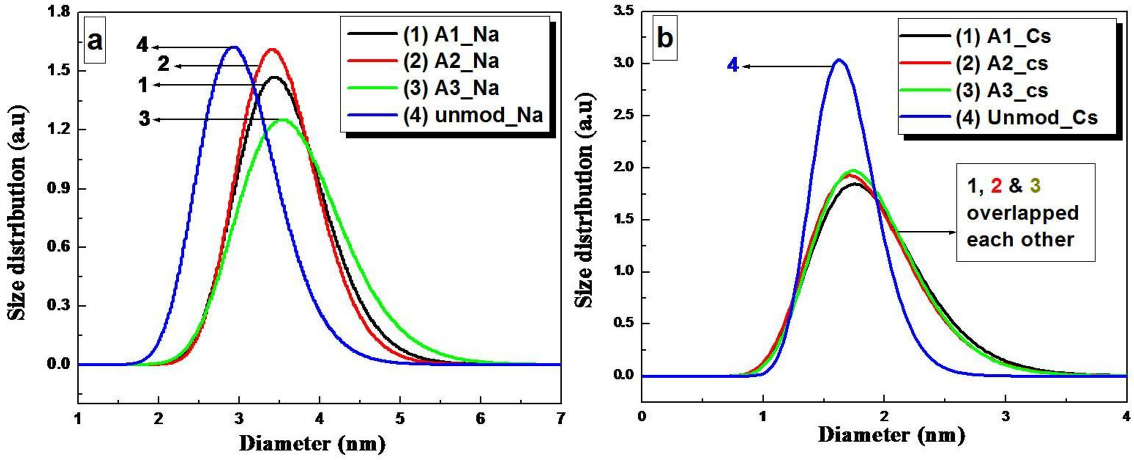

Figure 3.16. Water cluster size distribution plots for ascorbic acid reduced samples in Na^+ (a) and Cs^+ (b) ionic forms.

4. Conclusions

The results of the present studies show that local conditions during reduction and subsequent reorganizations of matrix influence the shape, size dispersion and spatial distribution of Ag nanostructures formed in Nafion 117 membrane. The monodisperse spherical nanoparticles (5 nm) are formed in the membrane by formamide reduction at 45 °C. The shape, size and distribution of Ag nanostructures formed by ascorbic acid reduction have been found to be highly dependent on the extent of initial loading of Ag^+ ions in Nafion matrix. Above a critical concentration of Ag^+ ions, one dimensional growth in form of the nanorods having ~8 nm diameter and varying length have been observed. At lower concentration of Ag^+ ions, the Ag seeds (atoms or clusters) agglomerates in localized zones resulting in formation of big sponge like nanostructures. Due to absence of chemical crosslinking in Nafion membrane, the membrane matrix is able to reorganize to attain original water clusters network in a given counterionic form. However, the water clusters network in matrix is modified significantly after incorporation of bigger Ag nanoparticles and nanorods.

Chapter 4

Mechanism of Growth of Silver Nanoparticles by Ascorbic Acid Reduction in Cation-exchange Membrane with Subsecond Time Resolution

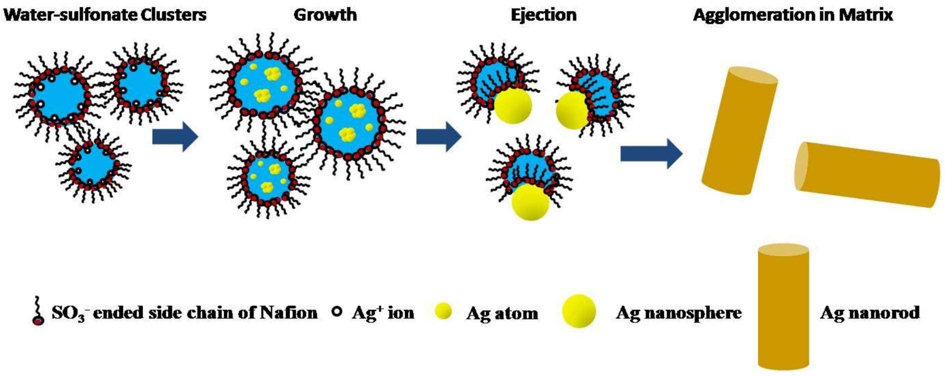

1. Introduction

As highlighted in Chapter 1, the metal nanoparticles embedded in polymer membranes are of high technological importance for a variety of advance applications such as water purification, catalytic applications, chemical sensors, actuators, fuel cell, water splitting, sequestering of ions, substrates for surface enhanced Raman scattering etc [Shahinpore et al. 1998.; Kim and Shahinpore 2003.; Shahinpore and Kim 2005.; Volkov et al. 2013.; Zhu et al. 2010.; Sel et al. 2011.; Sanchez et al. 2005.; Corma and Garcia 2008.; wang et al. 2003.; Hirano et al. 2011.; Wirtz et al. 2002.; Duan et al. 2009.; Santoro et al. 2014]. The physical architecture and chemical composition of the membrane as well as shape, size and spatial distribution of the nanoparticles play an important role in the successful application of a nanocomposite membrane designed for a specific purpose. Understanding the growth mechanism that governs the size, shape and spatial distribution of the nanoparticles is therefore crucial to prepare tailor-made membrane nanoparticles composite for a given application. It has been demonstrated in Chapter 3 that the reduction of silver ions with L-ascorbic acid produces silver nanoparticles of various shapes and sizes (one dimensional nanorods, nanosponge, and nanoclusters) under different experimental conditions, and the size of the nanoparticles are much bigger in comparison to the reverse micellar spherical water clusters in Nafion. This shows that, the assumption that the water clusters in Nafion act as a template for nanoparticle formation is not strictly valid. The mechanism of growth of nanoparticles in Nafion membrane may depends on many unknown matrix parameters.

Formation of metal nanoparticles in Nafion membrane involves loading of desired precursor metal ions and their in-situ reduction. Transmission electron microscopy (TEM) in combination with a small angle X-ray scattering is ideal for studying nanostructures embedded in the solid matrices [Giovanetti et al. 2012]. Campi et al. [2010, 2011] have studied the early stages of silver particles formation in a polymer solution by in situ time resolved small angle X-ray scattering. They have observed that the time evolution of spatial correlations between primary particles and the dynamic fractal geometry of the polymer-Ag matrix play an important role in the aggregation mechanism and the morphology of forming nanostructures in solution. It has been observed in study on Ag nanoparticles formation by borohydride reduction that coalescence is a fundamental growth principle if the monomer-supplying chemical reaction is faster than the actual particle formation [Polte et al. 2012]. Though literature exists on growth kinetics of nanoparticles in solution, there are limited studies on the topic in nanoconfined media where both nanoconfinement and restricted diffusion of reactant can significantly affect the growth process. The conditions of in situ reduction of metal ions in Nafion membrane are quite different as the monomer-supplying chemical reaction may be limiting step due to slow diffusion of the reductant. Hence, the mechanism of formation of metal nanoparticles in a membrane cannot be correlated with that involved in aqueous medium. The formation of metal nanoparticles in a membrane is affected by diffusion of ions/reductant, extent of precursor ions occupying ion-exchange sites, temperature, nature of the reductant and solvent, and local physical conditions [Kumar et al. 2010.; Kumar et al. 2010.; Patra et al. 2013.; Patra et al. 2014]. It is most likely that the initial growth of metal nanoparticles occurs in the nanoconfined hydrophilic ionic clusters (popularly known as water clusters) of Nafion. However, formation of the nanoparticles having size and shape different than the water clusters in Nafion is not understood. There are limited studies on the time dependent growth of nanoparticles in a Nafion matrix due to the inherent difficulty involved in such study. TEM in combination with time resolved SAXS can provide valuable information of the nanoparticle growth mechanism.

The objective of the present work is to investigate the mechanism behind the formation of metal nanoparticles in Nafion membrane. The early growth kinetics of silver nanoparticles by ascorbic acid reduction in Nafion 117 membrane has been studied by time resolved in situ SAXS using synchrotron radiation with a time resolution of 50 ms. Ascorbic acid has been chosen because of its interesting role as a weak reductant for growth of metal nanoparticles with various aspect ratios [Suber and Plunkett 2010]. A plausible mechanism for Ag nanoparticles growth confined in the water clusters has been elucidated. The time resolved information of nanoparticles growth obtained in the present work holds promise for controlled synthesis of silver nanoparticles in Nafion membrane with tunable size, shape and spatial distribution.

2. Experimental Section

2.1. Materials and Methods

Nafion-117 cation-exchange membrane with an equivalent weight of 1100 g/SO_3H was purchased from Ion Power Inc. Analytical reagent grade chemicals $AgNO_3$, $NaNO_3$ and L-ascorbic acid were purchased from BDH (Poole, England). De-ionised (DI) water (18 MΩ cm^{-1}) was used throughout the experiment for preparing solutions. Nafion-117 membrane was pre-conditioned by following standard treatments as described elsewhere [Goswami et al. 2001], and cut into 2 x 2 cm^2 piece. Ag^+ ions were loaded in the matrix by equilibrating with 0.5 mol L^{-1} $AgNO_3$ solution for 30 min with continuous stirring. The fully Ag^+ loaded ionomer samples were equilibrated with 0.25 mol L^{-1} $NaNO_3$ solution under stirring condition for 30 s to prepare a sample having 25 % Ag^+ loading. The time required for preparing sample having the desired load of Ag^+ ions was decided based on study by Sachdeva et al. [2006]. Fully Ag^+ loaded samples were not considered for this study to avoid any possibility of metallization due to the high silver content.

2.2. Nanoparticle Synthesis

Following the procedure reported previously [Chapter 3], two small pieces of Nafion films (2 x 2 cm^2) of which 25 % of the ion-exchange sites are loaded with Ag^+ ions were reduced with 0.1 mol L^{-1} ascorbic acid solution at room temperature for 60 s and 300 s respectively. Thin metallization of silver appeared on the membrane surface, which could be easily removed by soft rubbing with wet tissue paper. The prepared samples were then subjected to TEM characterization.

2.2.1. TEM Characterization

Transmission electron microscopy (TEM) was carried out on cross-sections of the prepared nanocomposite membrane samples. Prior to microscopy, the samples were equilibrated with 0.25 mol L^{-1} $NaNO_3$ solution to remove any unreduced Ag^+ ions. The nanocomposite films were sectioned under cryogenic environment in a Leica ultramicrotome to 70 nm thickness. The sections were collected on 200 mesh formvar and carbon coated Cu grids. The grids were examined in an FEI Technai G2 electron microscope at IIT Bombay, at 120 keV without any external treatment.

2.2.2. Temporal Evolution of AgNPs: In-situ Time Resolved SAXS Study Using Synchrotron Radiation

The SAXS experiments were carried out at the P03/MiNaXS beamline at PETRA-III, DESY, Hamburg, Germany [Buffet et al. 2012.; Santoro et al. 2014]. The wavelength of incident micro-focused X-ray beam was 0.957 Å and the beam size was 32 μm (H) × 23 μm (V). A 2-dimensional Pilatus 300K (Dectris Ltd., Switzerland) detector was used to record the scattering patterns. The sample to detector distance was 3.3 meter. A flow reactor cell made of Perspex® equipped with Kapton® windows was used as a sample holder. Nafion 117 membrane piece (2 x 2 cm^2), preconditioned and loaded with Ag^+ ions (25 % Ag^+ loading) was placed in the sample holder containing a small opening for the injection of reducing solution (ascorbic acid). Ascorbic acid (0.1 mol L^{-1}) solution was fed through an injection syringe with a rate of 0.2 mL / 5 s to sample holder ensuring the alignment of ascorbic acid drops to the beam. A schematic of the experimental setup is shown in Figure 4.1. The reaction started at room temperature. A maximum time resolution of 50 ms has been achieved with reasonable statistics in the scattering profiles. Ten consecutive profiles were averaged for further analysis to improve the statistics of the scattering data.

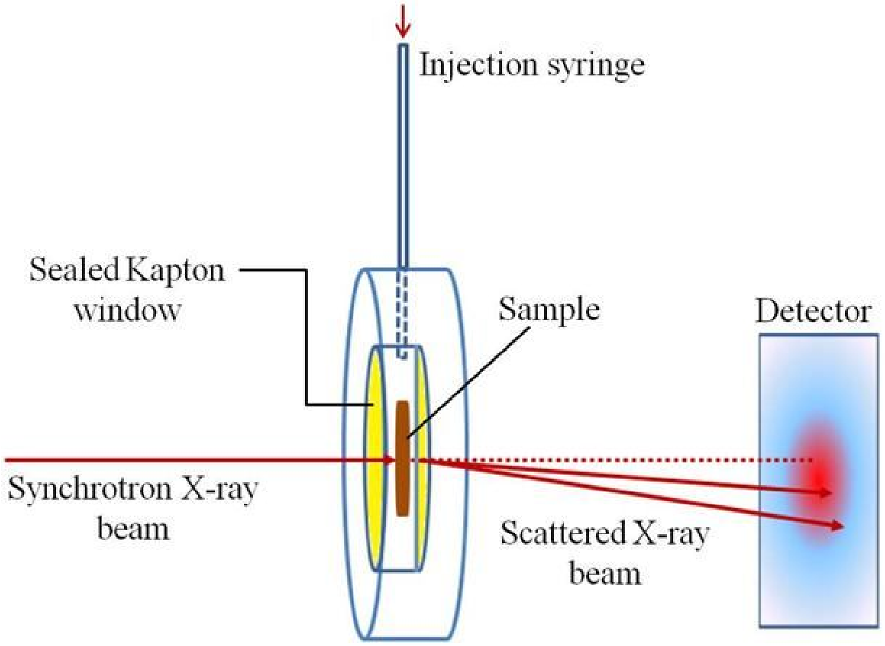

Figure 4.1. Schematic diagram of the experimental setup for in situ SAXS experiment.

SAXS analysis: The scattering patterns, recorded on a two-dimensional Pilatus detector (Pilatus 300K), have been converted to one-dimensional scattering profiles to obtain the scattering vector (q) dependence of the scattering intensities by azimuthal integration. The scattering contribution of the pristine ionomer matrix (Ag^+ loaded) has been subtracted from each scattering curve of the ascorbic acid treated Nafion (silver nanoparticles embedded). The size dispersion of the formed silver nanoparticles has been analysed based on non-linear least square fitting of the recorded scattering curve considering polydisperse spherical particle model which is supported by transmission electron microscopy. For such a case, the scattering intensity I(q) may be approximated as,

$$I_1(q) = I_{NS}(q) = \left(\int_0^\infty P_{NS}(q,R) R^6 D_{NS}(R) dR \right) \tag{1}$$

where, $P_{NS}(q,R)$ represents the form factor of a nanostructure. $D_{NS}(R)$ represents the nanostructure size distribution and R the particle radius. For spherical nanostructures of radius R, the form factor is analytically solvable presenting the following expression.

$$P_{NS}(q,R) = 9 \frac{(\sin(qR) - qR\cos(qR))^2}{(qR)^6} \tag{2}$$

In the present case, standard lognormal distribution of following type

$$D_{NS}(R) = \frac{1}{\sqrt{2\pi\sigma^2 R^2}} \exp\left[-\frac{[\ln(R/R_0)^2]}{2\sigma^2} \right] \tag{3}$$

was considered for the size distribution, where R_0 represents the median radius and σ represents the polydispersity index of the distribution.

3. Results and Discussion

Time resolved SAXS using synchrotron radiation is well suited to follow the in-situ formation of nanoparticles (number density) and their kinetics of growth (size) with millisecond time resolution. Krumrey et al. [2011] has recently reviewed the utility of synchrotron radiation-based X-ray reflection and scattering techniques in dimensional nanometrology. The temporal evolution of radial averaged SAXS profiles and corresponding increase in median diameter of nanoparticles as a function of time are shown in Figure 4.2. It is seen that the SAXS patterns (Figure 4.2a) evolves continuously with time revealing the in-situ growth of silver nanoparticles. However, the median diameter observed form the SAXS profile at the earliest time is 2.6 nm as shown in Figure 4.2b. The particles are likely to be formed by means of monomer addition after a discrete nucleation period. Takesue et al. [2011] have shown that in aqueous medium the first full-shell clusters Ag_{13} (size 0.7 nm) are involved in growth of silver nanoparticles. They have observed the Ag_{13} clusters with time resolution of 0.18 ms in their in situ experiment. Hence, the nucleation and initial growth may be too fast to be observed with the achieved time resolution of 50 ms in the present work. Though the very early stages of growth can not be resolved, the present study is the first of its kind showing that the evolution of nanoparticle size in a nanoconfined medium (polymer membrane) is an inherently much slower process than the one observed in bulk solution.

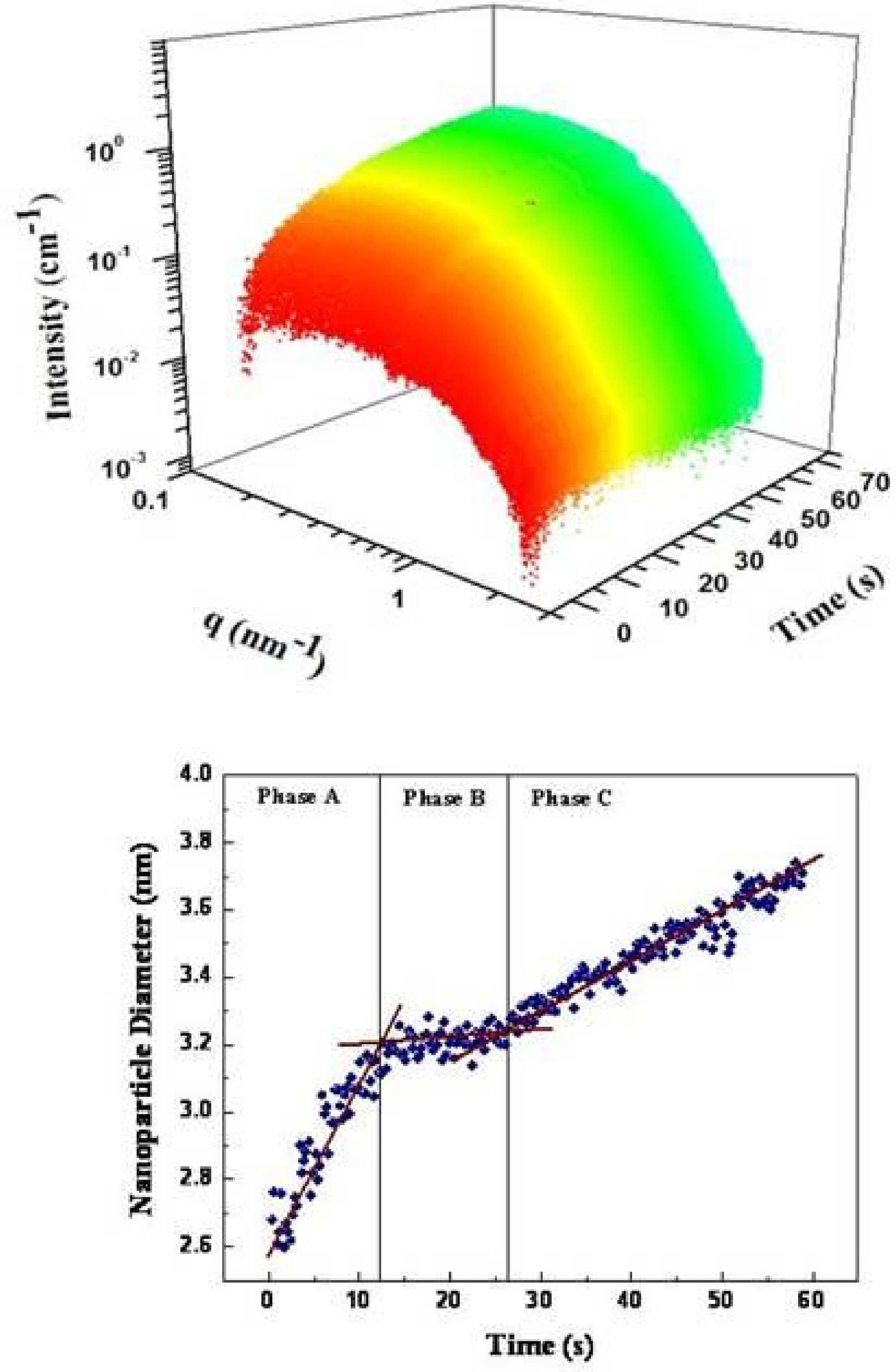

Figure 4.2. In-situ time resolved SAXS profiles during the formation and growth of silver nanoparticles by ascorbic acid reduction in Nafion-117 membrane (a), and corresponding evolution of median diameter of silver nanoparticles (b) as a function of reduction time.

It has been previously reported that the process of nucleation and growth of the silver nanoparticles in aqueous medium is complete in very short reaction time of 6 ms [Takesue et al. 2011]. In Figure 4.2b it is clearly seen that the growth of the silver nanoparticles continues for a longer period of time, revealing that the growth mechanism inside the nanodomains of a Nafion membrane is different from that of bulk. The figure shows the growth profile of silver nanoparticles can be divided into three distinct phases. The phase A shows a fast growth of nanoparticles as evidenced by higher slope. The rate of the nanoparticles growth reaches a plateau in about 12 s (Phase B). The further growth is noticed after a lag time of about 14 s, and thereafter progresses with slower rate (Phase C).

Mechanism of growth: Figure 4.3 gives the particles size distributions as a function of reduction time as obtained from SAXS analysis. The initial particle size distribution curve is almost symmetric ranging from 1.2 nm to 5 nm (standard deviation = 0.63). The nanoparticles with such size distribution profile could be accommodated in the reverse micellar hydrophilic clusters (water clusters) of the membrane. With progress of time, the size distribution curves broaden and became more asymmetric i.e. left side remained at 1.2 nm but right side of the curve shifts systematically from 5 nm to 8 nm (standard deviation = 1.13). This is possible only when there is continuous birth of new seeds to compensate for the particles undergoing growth (shifted to right side). It is noteworthy that, the particle size distribution curves start from 1.2 nm in all cases, that is the size of second full-shell Ag_{55} cluster [Amano et al. 2009.; Harb et al. 2010]. After 10 s, the particle size distribution curve stretches beyond 5 nm sizes that cannot be accommodated in the ~5 nm water clusters and must have started to be ejected from them. The ejection of nanoparticles from the water clusters has been corroborated by the existence of the ionomer peak at higher scattering vector (q) regime in the SAXS profiles of silver nanoparticles embedded Nafion-117 [Figure 3.6 and Figure 3.12]. The median diameter increased slowly from 2.6 to 3.2 nm. Thereafter, the increase in diameter of nanoparticles became considerably slower.

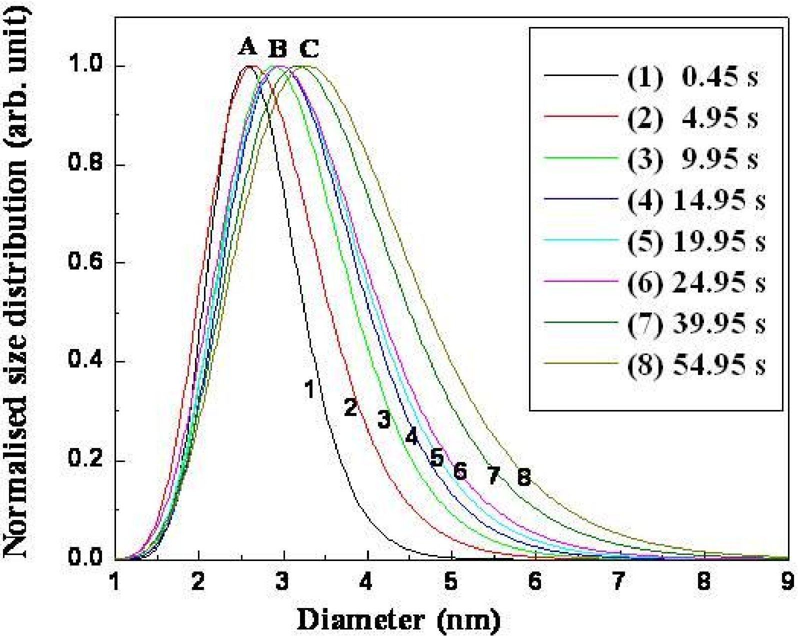

Figure 4.3. Temporal evolution of AgNPs size distributions deduced from SAXS profiles.

The variation of the number density (particles cm^{-3}) of silver nanoparticles during the reduction process has been deduced from the time resolved SAXS profiles, and given in Figure 4.4. It is seen that the particle number density increased continuously till ~ 25 s. This suggests that the birth of new particles is sustained even in the phase B (see Figure 4.2b) where median diameter growth shows a plateau. In addition, there is a change in the slope of the particle number density at 2-3 s indicating slowing down of the birth rate of new particles. Initial fast birth rate could be attributed to ascorbic acid reduction at the surface layer of the membrane. After 25 s, the number density profile decreased slowly in phase C indicating a significant decrease in the birth rate and disappearance of nanoparticles due to agglomeration to form bigger AgNPs ejected to the adjoining PTFE matrix.

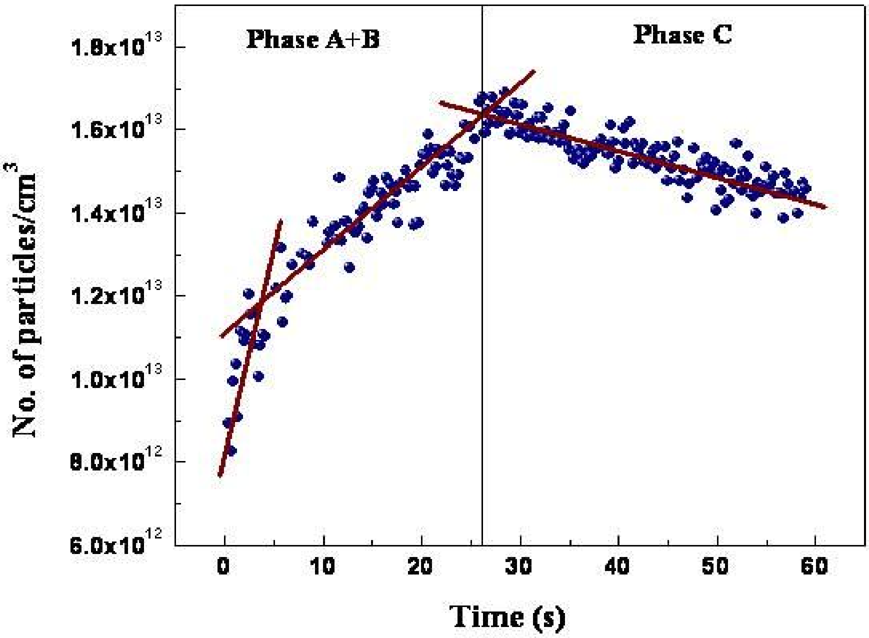

Figure 4.4. Time dependence of the number density (particles cm^{-3}) of AgNPs during in situ reduction.

TEM analysis of samples prepared in the same conditions has been carried out. Figure 4.5 presents the TEM image of the membrane cross-section after reduction for 60 s and the respective nanoparticle size distribution histogram. Formation of uniformly distributed ~3 nm silver nanoparticles is observed. The results obtained in the SAXS experiment (Figure 4.3) are in reasonably good agreement with TEM analysis (Figure 4.5).

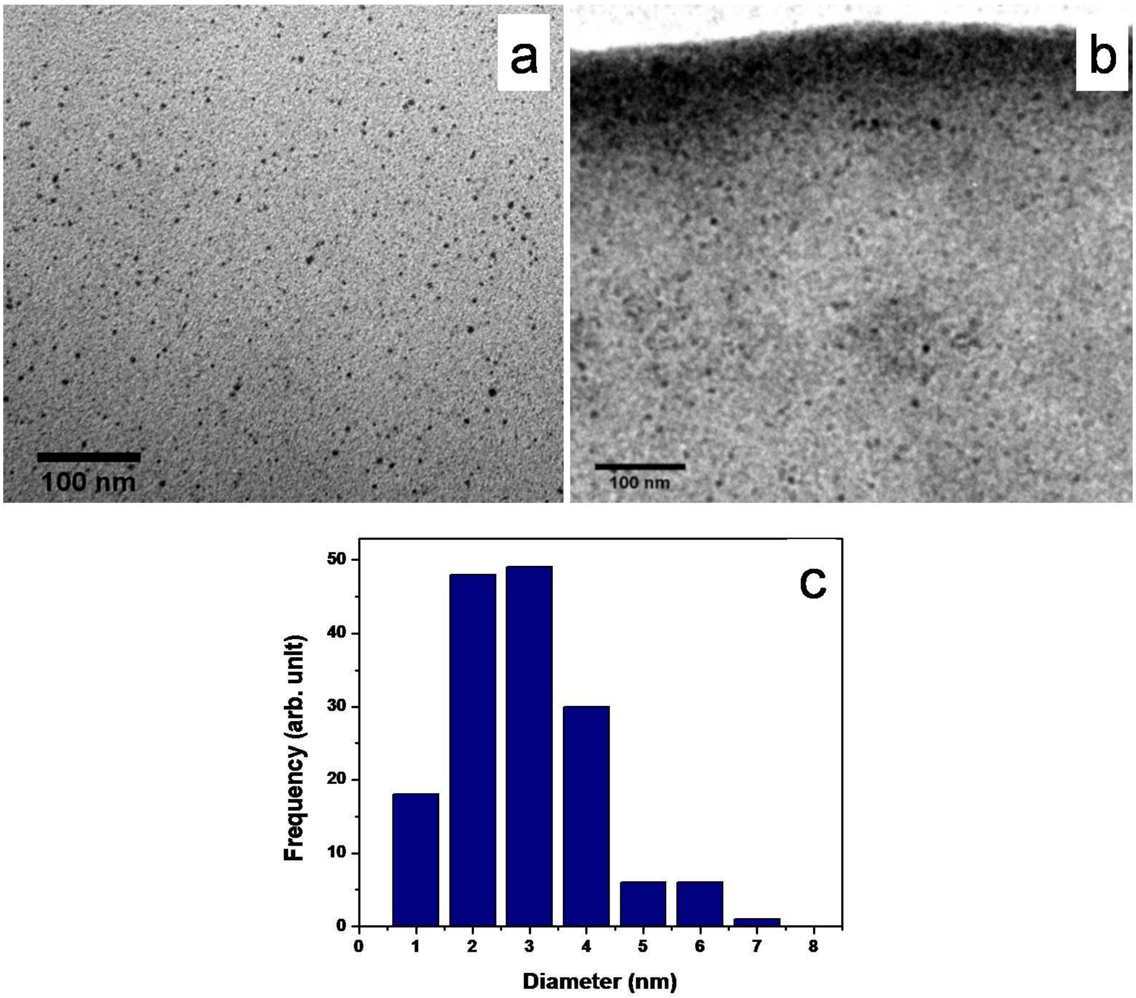

Figure 4.5. TEM image of cross section of Ag$^+$ loaded Nafion-117 membrane subjected to reduction with L-ascorbic acid for 60 s in bulk (a) and in surface (b) and size distribution histogram of silver nanoparticles as obtained from the TEM images analysis (c).

The nanoparticles produced at 60 s of chemical reduction possess significant size dispersion with mean diameter of ~3 nm. The wider size distribution of nanoparticles in SAXS analysis data in comparison to TEM analysis data can be attributed to the contribution of bigger particles formed on the matrix surface to the size distribution profiles extracted from the SAXS experiments, as the characterization based on scattering technique probe larger fraction (both interior and surface) of the samples. The mean diameter and the low degree of polydispersity of the formed nanoparticles exactly mimicking the water-sulfonate clusters (3-5 nm) in Nafion-117 membrane, provide clear evidences for the existence of such hydrophilic clusters in Nafion and their templating activity.

It has been described in Chapter 3 that extending the reduction time upto 5 min under similar experimental conditions led to the formation of nanorods [Patra et al. 2013]. The study of spatial distribution of such nanostructures using TEM characterisation across the thickness of membrane has been demonstrated in Chapter 3. Figure 4.6 represents the TEM image of a sample after 5 min of reduction, showing the formation of uniformly distributed nanorods (~8 nm diameter and ~40 nm length) across the membrane thickness. It is clear from the Figure 4.5a and 4.6 that, the particle number density (number of particles per unit area of the membrane) decreases significantly from 1 min (Figure 4.5a) to 5 min (Figure 4.6) of reduction process. This fact suggests that the smaller ~3 nm particles formed at 1 min of reduction are the building block units for the formation of bigger nanorods (~40 nm length) by sacrificial self-agglomeration in a preferential direction leading to the formation of 1-D nanostructures (nanorods) in the surrounding PTFE matrix. The unidirectional self-agglomeration may be a combination of (i) templating effect of the membrane and (ii) precursor concentration in the membrane.

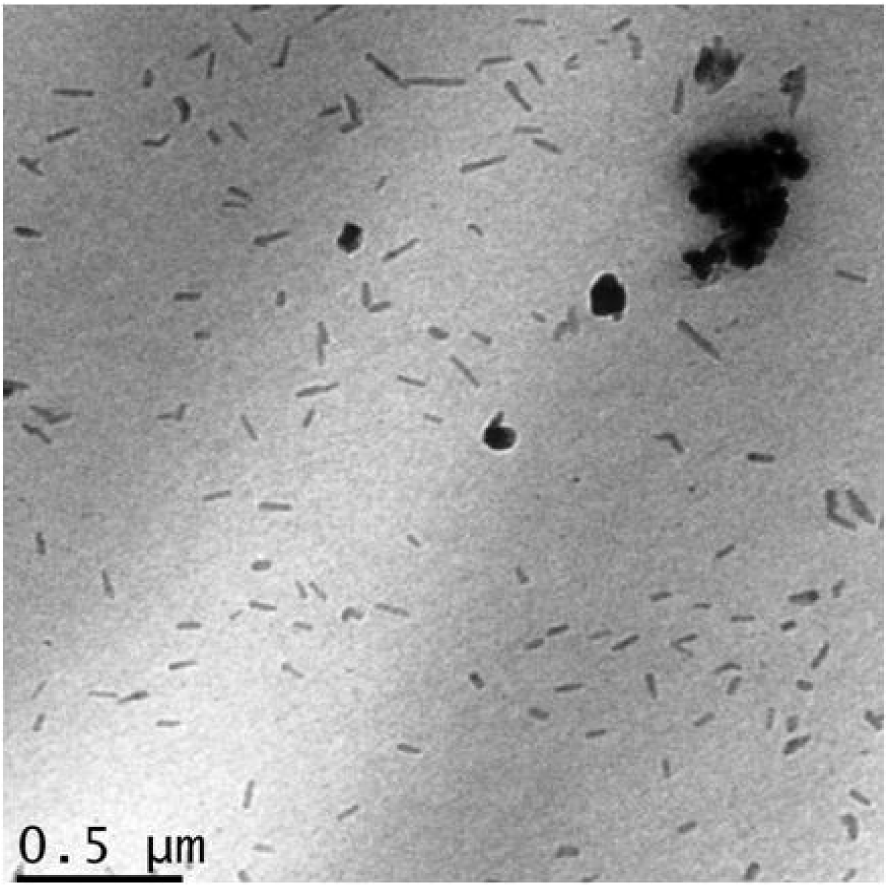

Figure 4.6. TEM image showing the spatial distribution of silver nanorods across thickness of the membrane subjected to reduction with ascorbic acid for 5 min.

4. Conclusions

It has been demonstrated that early growth of spherical silver nanoparticles with size of ~ 3 nm takes place in the water-sulfonate clusters of Nafion-117 membrane by room temperature L-ascorbic acid reduction. The whole process can be divided into three stages: a rapid initial formation and growth followed by, a saturation of the nanoparticles size with continuous increase in number density, and a further slow increase in nanoparticles size and decrease in number density. Further growth by sacrificial self-agglomeration takes place after ejection of nanoparticles from water-sulfonate clusters leading to formation of cylindrical nanostructures (nanorods) with bigger sizes. This study demonstrated the possibility for controlled synthesis of silver nanoparticles in Nafion-117 membrane with different shapes and sizes. The analytical tool employed in the present work can also be used for the study of growth mechanism of other metal nanoparticle (Au, Pt, Pd etc.) in polymer matrix.

Chapter 5

Synthesis and Mechanism of Formation of Silver Nanoparticles by Redox Decomposition of Silver Citrate Complex in Nanoscale Confinement

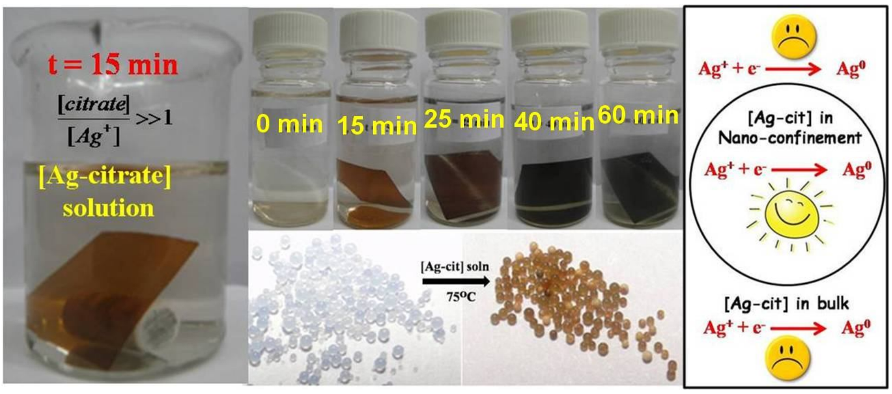

1. Introduction

The conventional process of metal nanoparticles synthesis in ion-exchange membranes involve the loading of the desired metal ions in the membrane by ion-exchange followed by chemical reduction using a suitable chemical agent. Synthesis of silver nanoparticles by such methodology has been described in detail in the previous two chapters. Various reducing agents like borohydride, formamide, ascorbic acid have been extensively used for the synthesis of metal nanoparticles in ion-exchange matrices [Kumar et al. 2010.; Patra et al. 2013.; Patra et al. 2014]. Though the process is simple, it is not general for all kind of metal-ionomer systems. Thus synthesis of silver nanoparticles in the anion exchange membrane and in the neutral polymer is difficult. So is the case for gold nanoparticles in cation exchange membrane. There is a need for a relatively simpler and generalized synthetic strategy which can be applicable for a wide class of metal-polymer systems.

There exists literature where it has been shown that spatial confinement in nanoscale can significantly alter the chemical equilibrium and kinetics. Thompson has shown that solvent nanoconfinement mostly affects the chemical reactions that are strongly coupled to the solvent, typically electron and proton transfer reactions [Thompson et al. 2002]. Polak and Rubinovich [2011] have predicted that a reaction involving a small number of molecules in an entirely segregated nanoscale domain can lead to shift in the position of equilibrium toward products side via reactant-product reduced mixing. Most recently the same group has demonstrated that the DNA hybridization in nanoconfinement is significantly favored over the same reaction occurring in bulk media with the same reactant concentrations [Rubinovich and Polak 2013]. The current literature status and the present understanding on the concept of “nanoconfinement effect” have been discussed in detail in Chapter 8. Though different types of reactions have been explored in a variety of confined media, no special attention has been paid on the role of nanodomains of the membranes or resins as a confined nanoreactor. Also, least attention has been paid on redox reactions in spatial confinement. With this in view attempt has been made to explore the role of nanoconfinement in facilitating the reduction of metal ion precursors in ion-exchange membranes and resins for the synthesis of metal nanoparticles. Appropriate selection of a metal-reductant system which is highly stable in bulk but may enter into the confined nanodomains of all kind of matrices (cationic, anionic & neutral) is highly crucial to observe the effect of nanoconfinement.

In this work, a simple and general methodology for synthesis of silver nanopaticles (AgNPs) in confined nanodomains of ion-exchange membranes and porous polymer resin beads has been explored taking tri-sodium citrate as a complexing reductant. Experiments have been carried out with both anion exchange (Selemion-AMV), cation exchange (Nafion-117) ionomer membranes, and with neutral nanoporous amberlite XAD-4 beads as well as with nanoporous silica gel particles as the host matrices. These matrices can serve as a host where reactions can be carried out in their nanopores or nano water clusters of dimension 4-10 nm. Citrate reduction of silver ions has been chosen in the present study because of absence of reduction in the bulk solution under the condition of $[\text{citrate}/\text{Ag}^+] >> 1$, providing opportunity to study the effect of nanoconfinement in the redox reaction. Also the slow kinetics of formation of AgNPs in the ionomer matrices (in minutes to hour scale) gives opportunity to study the time dependent growth mechanism using laboratory based characterization techniques. The real-time monitoring of the growth of AgNPs in ion-exchange matrices has been done using time resolved SAXS measurements and *in-situ* radiotracer study. The shape and spatial distribution of the nanoparticles have been observed by transmission electron microscopy (TEM). The temporal evolution of particle size and the size distributions of the AgNPs in the course of the experiments have been explored. The detailed mechanism of growth of nanoparticles has been proposed based on the experimental data. The first experimental observation on the intrinsic role of nanoconfinement in solid matrices in facilitating the chemical reduction during the synthesis of metal nanoparticles has been demonstrated.

2. Experimental Section

2.1. Materials and Methods

The anion exchange membrane Selemion AMV and the cation exchange membrane Nafion-117 (with an equivalent weight of 1100 g/SO_3H) were obtained from Asahi Glass Co., Japan and Ion Power Inc., respectively. The Amberlite XAD-4 resin beads and the silica gel particles (63-200 μm) used in the present study were purchased from Sigma-Aldrich. Silver nitrate ($AgNO_3$) salt and tri-sodium citrate were purchased from BDH, Poole, England. De-ionized water, 18 MΩ cm^{-1}, purified by model Quantum^{TM} from Millipore, Mumbai, India was used throughout the entire work.

2.1.1. Description of Host Matrices

The anion exchange membrane Selemion AMV, the cation exchange membrane Nafion 117, the neutral nanoporous polymer resin beads Amberlite XAD-4 and nanoporous silica gel particles (SiO_2) have been used as the host matrix for nanoparticle synthesis in the present study. The exact chemical structure of Selemion AMV is unknown. Based on the studies by Le et al [2009], Gao et al [2008], and Giffin et al [2012], the AMV ionomer is likely to be a blend of poly (vinyl chloride) (PVC) and a copolymer synthesized from styrene, chloromethylstyrene, and divinylbenzene. Further, the copolymer is functionalized by the introduction of an ammonium-based ion exchange group. Figure 5.1 gives the possible arrangement of functional groups in Selemion AMV ionomer. The chemical structure of Nafion 117 is given in Chapter 3 (Figure 3.1). The Amberlite XAD-4 spherical beads used in the present work are based on highly crosslinked macroreticular polystyrene (av. pore diameter of 10 nm). The chemical structure of XAD-4 resin is given in Figure 5.2. The silica gel (SiO_2) particles (63-200 μm) used in the present study is of average pore size 4 nm and ~0.68 cm^3g^{-1} pore volume.

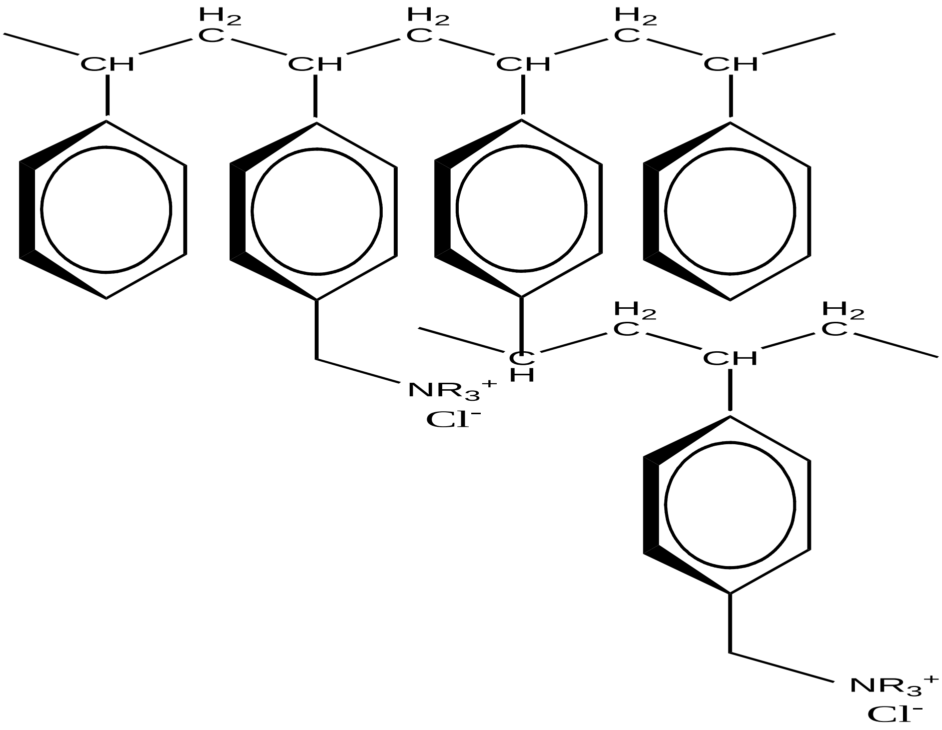

Figure 5.1. Possible arrangement of functional groups in Selemion AMV ionomer.

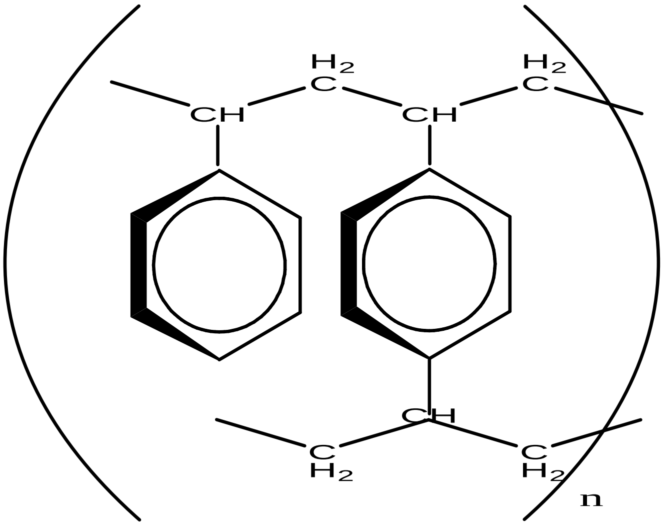

Figure 5.2. Chemical structure of amberlite XAD-4 resin.

2.1.2. Nanoparticle Synthesis

The ion-exchange membranes were cut into a few 2 x 2 cm^2 pieces. The Selemion AMV membranes (available commercially in Cl^- form) were equilibrated with 0.25 mol L^{-1} $NaNO_3$ solutions for ~24 h ensuring exchange of all the Cl^- ions in the matrix with NO_3^-. The complete exchange was confirmed by the absence of white precipitate of AgCl by immersing the membrane in $AgNO_3$ solutions. Nafion pieces were conditioned by conventional treatments described elsewhere and neutralized with Na^+ ions [Goswami et al. 2001]. Nanoporous amberlite XAD-4 microbeads were soaked overnight in methanol and washed thoroughly with 2 mol L^{-1} HNO_3 and water to remove any chemical impurities. Aqueous solution of silver citrate complex was prepared by dissolving 0.02 g of $AgNO_3$ salt into 25 mL aqueous solution of 0.2 mol L^{-1} tri-sodium citrate. A local white precipitate was noticed immediately, which re-dissolved on stirring.

Membrane pieces as well as the porous polymer beads (XAD-4) were treated separately with silver citrate solution at 75 °C under stirring condition. Constant temperature was maintained using a water bath. The experimental setup is shown schematically in Figure 5.3. The membrane pieces and the polymer beads in the silver citrate solution slowly turned to yellow to light brown to dark brown colour. There was no colour change in the solution. This indicated selective formation of AgNPs in the polymeric matrices. In order to follow the growth of nanoparticles, a number of AgNPs containing ionomer membranes were prepared by carrying out the reduction for various periods of time.

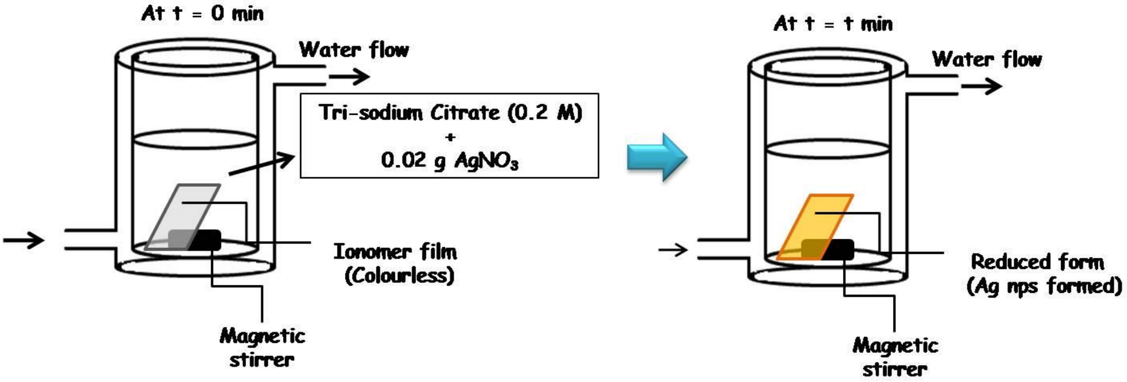

Figure 5.3. Schematic representation of the experimental set-up for the synthesis of AgNPs in ion-exchange membranes.

2.2. Nanoparticle Characterization

2.2.1. Microscopy

The AgNPs containing membrane samples were sectioned across the thickness in Leica ultramicrotome to 70 nm thickness under cryogenic environment, and picked on 200 mesh

Cu grids for the transmission electron microscopy (TEM). The TEM was carried out using an FEI Technai G2 electron microscope at 120 keV without any external treatment of the sample.

Field emission scanning electron microscopy (FE-SEM) was carried out for the surface and the interior of a AgNP incorporated polystyrene bead sample. In order to observe the interior of beads, the spherical beads were grinded carefully with SiC sandpaper followed by polishing with diamond suspensions. Finally the beads were made conductive by gold coating prior to microscopy.

2.2.2. Small Angle X-ray Scattering

Small angle X-ray scattering experiments were performed using a laboratory based SAXS instrument with CuK_{α} as probing radiation. Radial averaged scattering intensity (I(q)) was obtained within a wave vector transfer ($q=4\pi \sin(\theta)/\lambda$, where λ is the wavelength and 2θ is the scattering angle) range ~0.1 nm^{-1} to 2.5 nm^{-1}. The scattering contribution of the respective pristine ionomer matrix was subtracted from each scattering curve of the AgNPs embedded ionomer samples. The substracted SAXS spectra represent the scattering from nanoparticles only. This is the difference between the present analysis and that given in Chapter 3. So the structure factor (S_{WC}) due to water cluster is not considered in equation 2. Taking guidance from TEM images, the SAXS profiles were fitted to either unimodal or bimodal size distributions. As the scattering space and the real space are connected by Fourier transform, the information about the smaller length scale (silver seeds) is primarily manifested at relatively higher q region. Similarly, the scattering signal at lower q region is primarily due to the bigger nanoparticles. Thus, in order to analyze the present scattering data, the following model was adopted.

Total scattering intensity I(q) may be represented as

$$I(q) = C_1 I_1(q) + C_2 I_2(q) \tag{1}$$

where the first term corresponds to the scattering behavior of the bigger nanoparticles and the second term corresponds to the scattering from the smaller silver seeds. C_1 and C_2 are proportional to the respective number densities. Polydisperse spherical particle model is adopted to fit the recorded profiles. The model is supported by transmission electron microscopy. According to this model, $I_1(q)$ or $I_2(q)$ may be approximated as:

$$I_{NP}(q) = \left(\int_0^\infty P_{NP}(q,R) R^6 D_{NP}(R) dR \right) \tag{2}$$

where $P_{NP}(q,R)$ represents the form factor of a nanoparticle. For spherical nanoparticle of radius R,

$$P_{NP}(q,R) = 9 \frac{(\sin(qR) - qR\cos(qR))^2}{(qR)^6} \tag{3}$$

$D_{NP}(R)$ represents the nanoparticle size distribution, i.e., $D_{NP}(R)dR$ indicates the probability of having size between R to R+dR. In the present case standard lognormal distribution is considered, as given by the following equation.

$$D_{NP}(R) = \frac{1}{\sqrt{2\pi\sigma^2 R^2}} \exp\left[- \frac{\left[\ln(R/R_0)^2\right]}{2\sigma^2} \right] \tag{4}$$

R_0 represents the median radius and σ represents the polydispersity index of the distribution being obtained by fitting the SAXS profiles.

2.3. Radiotracer Technique

Time resolved accumulation of silver in the ionomer matrices was monitored by tagging Ag^+ ions with $^{110m}Ag^+$ radiotracer. The radiotracer kinetics experiments were performed in three different sets. In the first set of experiments, a pre-conditioned small piece of Nafion (2 x 2 cm^2) was equilibrated with 0.5 mol L^{-1} $AgNO_3$ solution for 30 min under stirring condition for the complete exchange of Na^+ ions with the Ag^+ ions. Based on the work by Sachdeva et al. [2006], the equilibration period of 30 min was chosen to ensure the complete exchange with Ag^+ ions in the Nafion sample. The Ag^+ loaded Nafion sample was equilibrated with radiotracer $^{110m}Ag^+$ (obtained from BRIT, Mumbai, India) and the activity was measured in a well type NaI (Tl) detector using 4K multichannel analyser. The radiotracer tagged sample was reduced with 0.2 mol L^{-1} tri-sodium citrate solution at 75 ^oC. During the chemical reduction, the sample was taken out from the reaction solution at regular time intervals, and the radioactivity was measured.

In the second set of experiments, 0.02 g of silver nitrate salt was added into 25 mL aqueous solution of tri-sodium citrate (0.2 mol L^{-1}). The silver ions were tagged with $^{110m}Ag^+$ radiotracers. A Selemion membrane (2 x 2 cm^2) in NO_3^- form and a pre-conditioned Nafion membrane (2 x 2 cm^2) in Na^+ form were immersed separately into the silver-citrate solution (Section 2.1) and kept at 75 ^oC under stirring condition. The radioactivity in the membranes was measured at a regular time interval. In order to account for the unreduced silver present in a typical membrane, both the membranes at the final stage (highest reaction time) of the experiment were equilibrated with 0.25 mol L^{-1} aqueous solution of $NaNO_3$ in stirring condition for 24 h and the radioactivity in the membrane was measured further to quantify the loss of ^{110m}Ag activity (unreduced silver) from the membrane. The (Ag^+/Ag^0) ratio was obtained from the the ratio of activity lost from a typical membrane to the residual activity in the same membrane after equilibration with $NaNO_3$.

In the third set of experiments, a pre-AgNP incorporated Nafion membrane, prepared by borohydride reduction, was taken for investigation. For this purpose, first a fully Ag^+ loaded Nafion membrane (Nafion membrane equilibrated for 30 min with 0.5 mol L^{-1} $AgNO_3$ salt solutions) was immersed in 20 mL of 0.25 mol L^{-1} $NaNO_3$ solutions for 60 s, so that 2% Ag^+ remained in the membrane. The time required for preparing the Nafion membrane having a desired extent of loading of Ag^+ ions was fixed based on experimental information given in the publication of Sachdeva et al. [2006]. The membrane was reduced with 20 mL 0.1 mol L^{-1} $NaBH_4$ (BDH, Poole, England) solution at room temperature for 15 s. The membrane immediately turned dark brown colour, indicating the formation of AgNPs in the matrix. Any unreduced Ag^+ was removed from the matrix by equilibrating the membrane with 0.25 mol L^{-1} $NaNO_3$ salt solutions. The AgNPs incorporated membrane was further treated with radiolabelled silver citrate complex solution (0.2 mol L^{-1}) at 75 ^oC and the kinetics of radioactivity uptake was followed by in-situ monitoring of ^{110m}Ag activity in the membrane.

Precautions: The experiments with radiotracer have been carried out in fume hood with good ventilation and with necessary protective clothing.

3. Results and Discussion

Solution of silver citrate complex with citrate/Ag^+ >> 1 has been found to be an attractive system for synthesis of silver nanoparticles in the confined nanodomains of the ion-exchange membranes. The first set of radiotracer experiment with $^{110m}Ag^+$ loaded Nafion membrane shows the role of high citrate concentration in this novel synthesis. It has been seen that almost 100% of the radiotracer comes out of the matrix within 30 min of treating the membrane in citrate solution without formation of any nanoparticles as shown by the sharp fall in tracer activity in the membrane (Figure 5.4). It has been observed that there is no formation of AgNPs in the membrane during this stage.

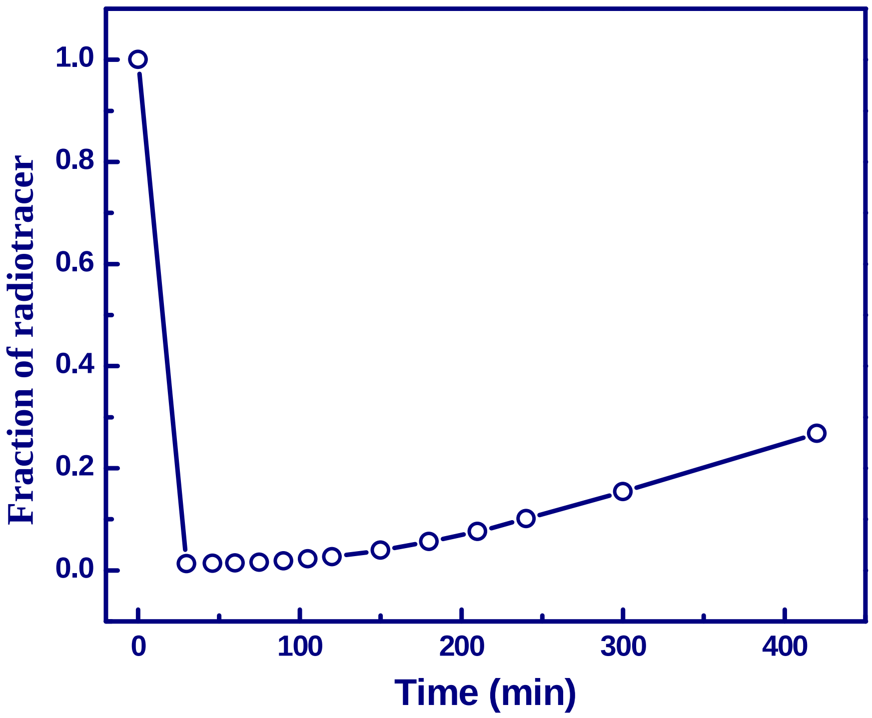

Figure 5.4. Time profile of Ag activity in Nafion matrix during the chemical reduction process at 75 ^{o}C. The solid line through the points is an eye guide.

The initial decrease in tracer activity indicates the exchange of the Ag^+ ions in the membrane with the Na^+ ions of tri-sodium citrate. This is due to higher concentration and selectivity of Na^+ towards the ionomer. With further progress of time, it has been observed that the radioactivity slowly reverses back into the ionomer matrix as shown by the rising part of Figure 5.4. This is accompanied by the formation of silver nanoparticles as indicated by the change in colour of the membrane from colourless to yellow to light brown to dark brown. However, no colour typical of Ag-nanoparticles appears in the aqueous citrate solution during the entire process indicating absence of reduction in the bulk. Citrate is a versatile chemical, widely used by various researchers in synthesis of metal nanoparticles, for its multiple roles as reductant, as well as complexant for the Ag^+ ions and stabilizers of AgNPs depending on the situation [Pillai and Kamat 2004.; Dong et al. 2009.; Henglein and Giersig. 1999.; Rivas et al. 2001]. Citrate ion ($C_6H_5O_7^{3-}$) forms silver citrate salt ($Ag_3C_6H_5O_7$) with Ag^+ ion, which is a white substance having very limited solubility in aqueous media [Djokic 2008]. The silver citrate/citric acid solution has been widely investigated by Djokic [2008], who has observed that the minimally soluble silver citrate complex dissolves in excess citric acid solution due to the formation of silver citrate complexes of a general formula $[Ag_3(C_6H_5O_7)_{n+1}]^{3n-}$. The other two probable water soluble silver citrate complex species can be $[Ag_2C_6H_5O_7]^-$ and $[AgC_6H_5O_7]^{2-}$. The superior stability of such silver citrate complexes has been reported by Djokic [2008] under the condition when the concentration of Ag^+ ion is less than 15 g L^{-1} and the concentration of citric acid is more than 3 mol L^{-1}. In the present case, the minimally soluble $Ag_3C_6H_5O_7$ salt gets dissolved by probable formation of soluble $[Ag_3(C_6H_5O_7)_{n+1}]^{3n-}$ ion. The possibility of formation of such an ionic species is due to the presence of far excess citrate ions in comparison to Ag^+ ions. Formation of AgNPs in membrane indicates such stable anionic species eventually diffuses into the hydrophilic domain of the membrane, where it undergoes reduction, facilitated by the nanoconfinement effect. Based on this assumption, experiments have been carried out in anion exchange membrane Selemion AMV and in cation exchange membrane Nafion 117, with [Ag-citrate] complex solution as starting material, without prior loading of Ag^+ ions into the membrane. The anion exchange membrane Selemion AMV has been chosen since it would allow it's counterion to be freely exchanged with the negatively charged silver-citrate complex. This would permit high equilibrium concentration of the complex in the membrane. The rate of colour change due to the formation of silver nanoparticles has been found to be faster in anion-exchange Selemion AMV than in cation-exchange Nafion 117. It is worthwhile to mention that, though the reactions in the present study have been carried out at 75 ^{O}C, the reduction of Ag^+ has been found to take place in both the membranes even at room temperature but at a much slower rate. This shows the excellent role of nanoconfinement in softening the reduction conditions.

3.1. Formation of Nanoparticles in Anion-exchange Membrane

Selemion AMV membrane has fixed positive charge sites and exchangeable anions. It has crosslinked polymer matrix without any periodic water domains leading to higher network elasticity (rigidity). Figure 5.5 gives the TEM images of thin sections across the thickness of Selemion AMV sample at different time of reduction along with the respective size distribution profiles of formed nanoparticles.

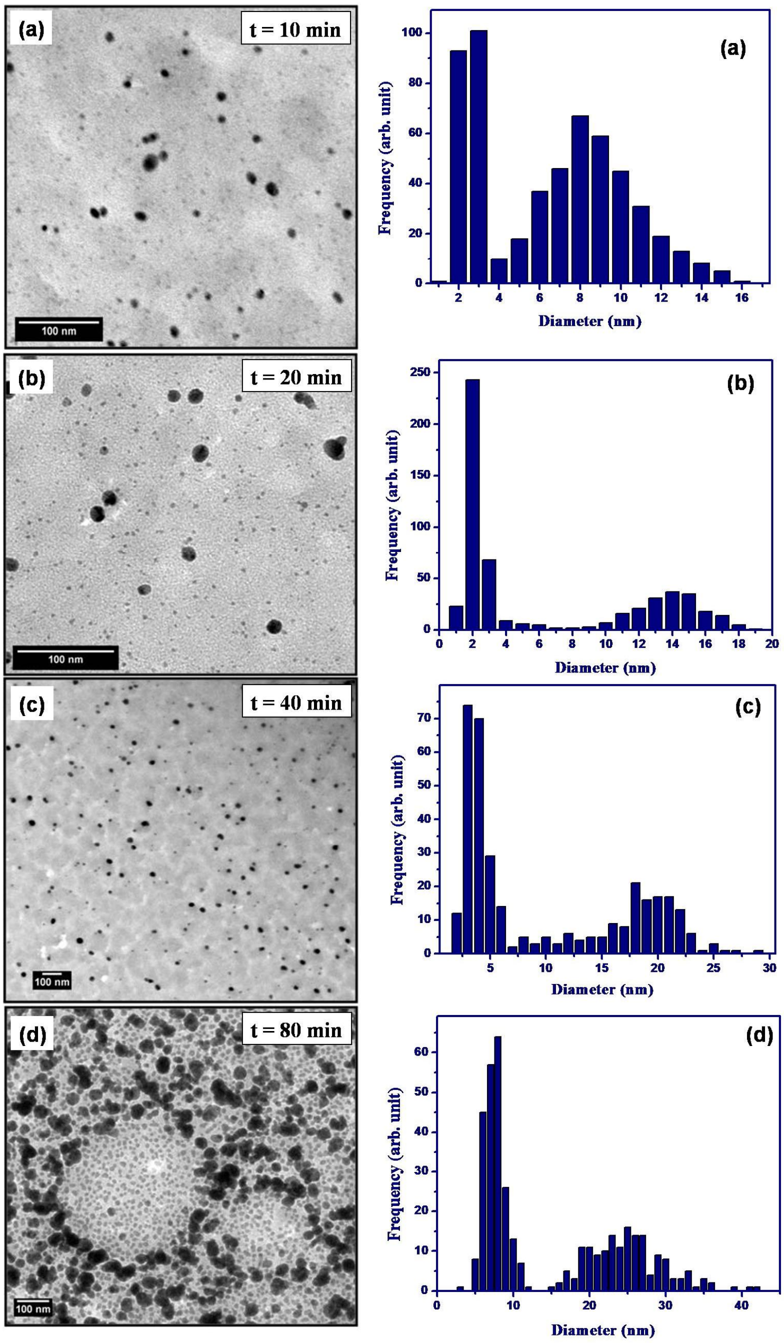

Figure 5.5. TEM images along the thickness of the Selemion AMV membrane and respective size distribution profiles of formed nanoparticles after 10 min (a), 20 min (b), 40 min (c) and 80 min (d) of reduction.

It can be seen that, spherical nanoparticles with bimodal size distribution have been formed. From the size distribution profiles, it is seen that there is a constant population of smaller AgNPs (silver seeds) along with the continuously growing particles throughout the reaction time scale. The constant population of the tiny seeds can be attributed to the steady supply of silver-citrate complexes into the ionomer matrix from the silver citrate solution, which gets reduced more favorably in the matrix.

The radial averaged SAXS profiles for different periods of reduction in Selemion membrane matrix have been analyzed to obtain the size distribution of the nanoparticles and the time dependence of the peak diameter and relative number density (n_t/n_5) as shown in Figure 5.6a-c. The SAXS profiles have been fitted to unimodal or bimodal distributions, taking guidance from TEM images. In the case of bimodal size distributions, the parameters pertaining to the distribution of larger size particles have been used to reconstruct the Figure 5.6b and 5.6c. The plots of size distribution for smaller silver seeds (in the samples with bimodal distributions) have been avoided in Figure 5.6b, as it would overlap with the data corresponding to earlier stages of the reaction (lower time scale). It is seen that the nanoparticle formation process involves two steps: (1) continuous birth of monomers (smaller seeds) and (2) their growth into bigger size particles. From Figure 5.6b and 5.6c it is seen that there is a rapid rise in the peak diameter (mode of the distribution) after ~10 min of reduction, and thereafter it remains constant. This shows the coalescence of smaller particles into bigger particles after ~10 min of reduction.

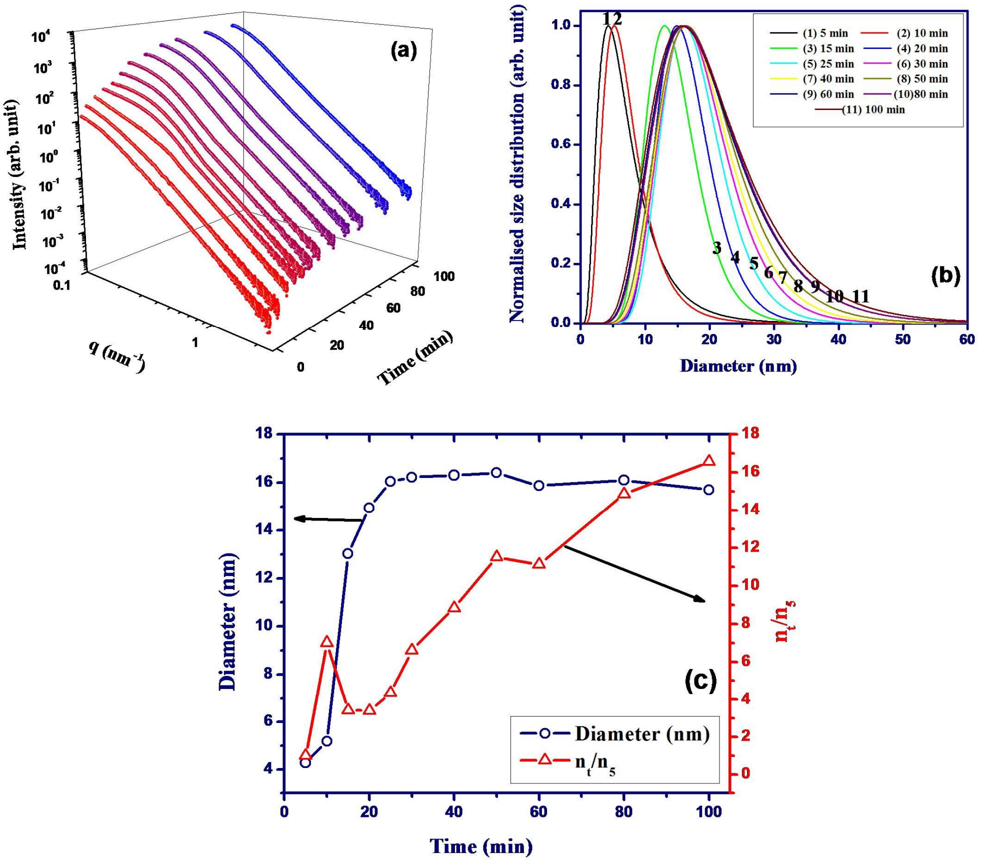

Figure 5.6. Radial averaged SAXS profiles at different reduction time (a), the size distribution of the nanoparticles obtained from SAXS analyses (b) and the time dependence of the peak diameter and the relative number density (n_t/n_5) (c) in Selemion AMV matrix. The term 'n_t' and 'n_5' represents the number density of the nanoparticles at time t and 5 min respectively. Solid lines through the points are eye guide.

The critical peak diameter of the particles as obtained from SAXS shows saturation at ~16 nm. However, the TEM image analyses show the growth of the nanoparticles into bigger sizes (> 16 nm). The SAXS analyses in Figure 5.6b show the broadening of size distribution profiles for bigger nanoparticles to higher diameter beyond 20 min, though the peak diameter does not change (Figure 5.6b & c). The phenomenon of sudden jump in particle size has been reflected in the relative number density plot as shown in Figure 5.6c. It can be seen that, during the period of 10 to 15 min, there is a sudden drop in relative number density due to self-agglomeration of nanoparticles. However from 25 min onwards, the relative number density of the particles increases continuously without break. The increase in relative number density after 25 min may be attributed to the scattering contribution of the growing seeds (> 5 nm, as seen in TEM images at higher time) into the scattering intensity at lower scattering vector (q) regime. Practically in such situations, the two zones for particles and seeds (as described in the experimental section, 2.2.2) do not remain distinct; rather they may overlap with each other to some extent. However, it is very difficult to resolve the individual scattering contributions from larger seeds and particles during the SAXS analyses for such cases.

3.2. Formation of Nanoparticles in Cation-exchange Membrane

Nafion-117 membrane is a ionomer having negative fixed charged sites (SO_3^-) and exchangeable cations. The matrix of Nafion has well organized water domains in the form of network of 3-5 nm water clusters, and has lower network elasticity (soft matrix) due to the absence of crosslinking. Figure 5.7 gives the TEM images of thin sections across the thickness of Nafion 117 sample at different time of reduction along with the respective size distribution profiles of formed nanoparticles.

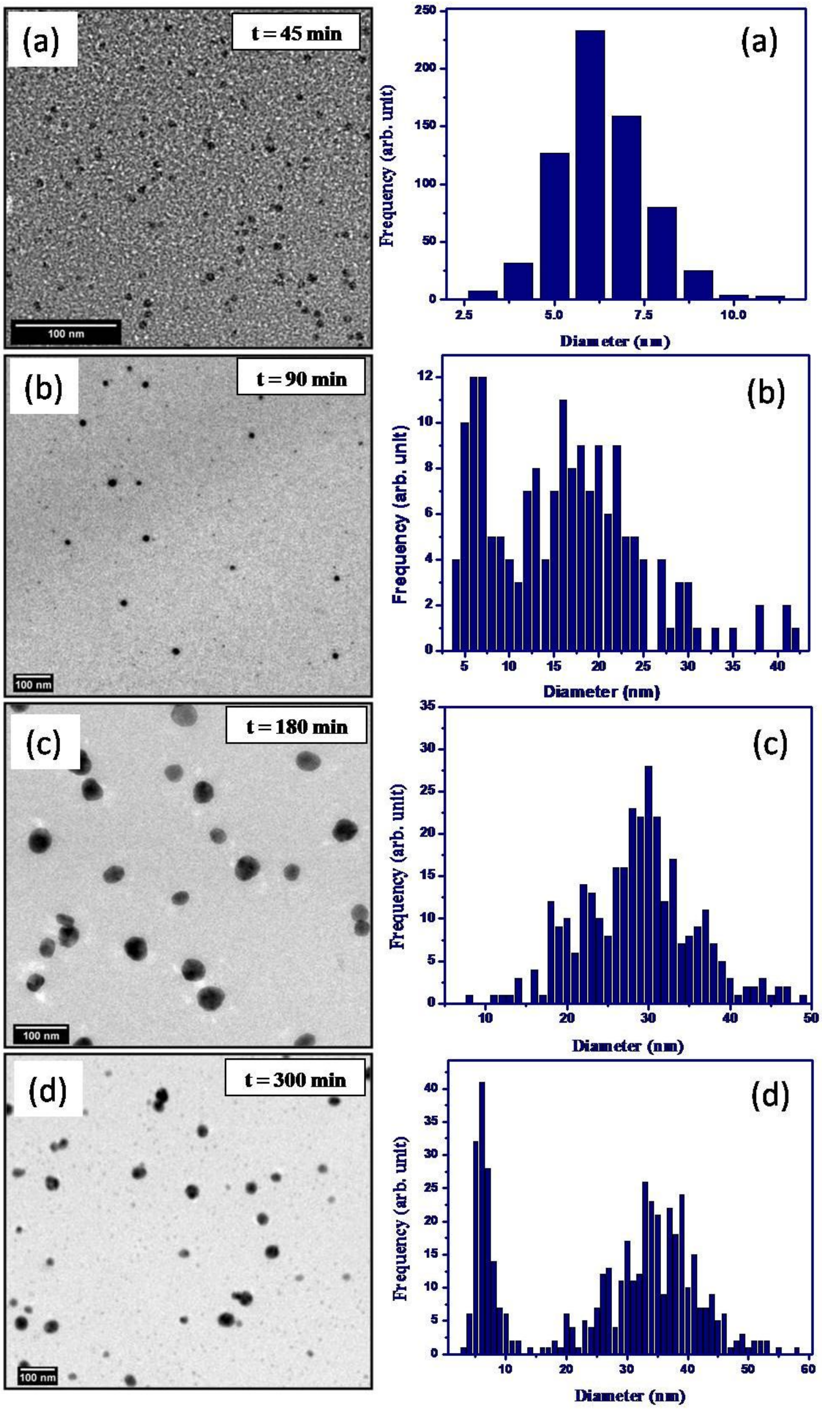

Figure 5.7. TEM images along the thickness of the Nafion 177 membrane and respective size distribution profiles of formed nanoparticles after 45 min (a), 90 min (b), 180 min (c) and 300 min (d) of reaction.

It is interesting to observe that silver particles are formed in a significant number uniformly across the thickness of the membrane though negatively charged ions are not easy to penetrate the cation-exchange matrix of Nafion-117, which has very high permselectivity for cations. Formation of AgNPs in Nafion membrane in the present experimental conditions thus indicates that the anionic species of silver citrate slowly diffuses into the hydrophilic domain of the membrane through leakage, where it undergoes reduction, facilitated by the nanoconfinement effect. It seems to suggest that this synthetic route can be used for both cation and anion-exchange matrices.

Figure 5.8 gives the evolution of radial averaged SAXS profiles during the growth of AgNPs in Nafion 117 matrix (a), the size distribution of nanoparticles obtained from SAXS analyses (b) and the time dependence of peak diameter and relative number density (n_t/n_{30}) (c). The procedure followed to reconstruct the SAXS data corresponding to the unimodal and bimodal size distribution in Nafion (Figure 5.8b and 5.8c) is similar to that used for Selemion (as discussed in Section 3.1).

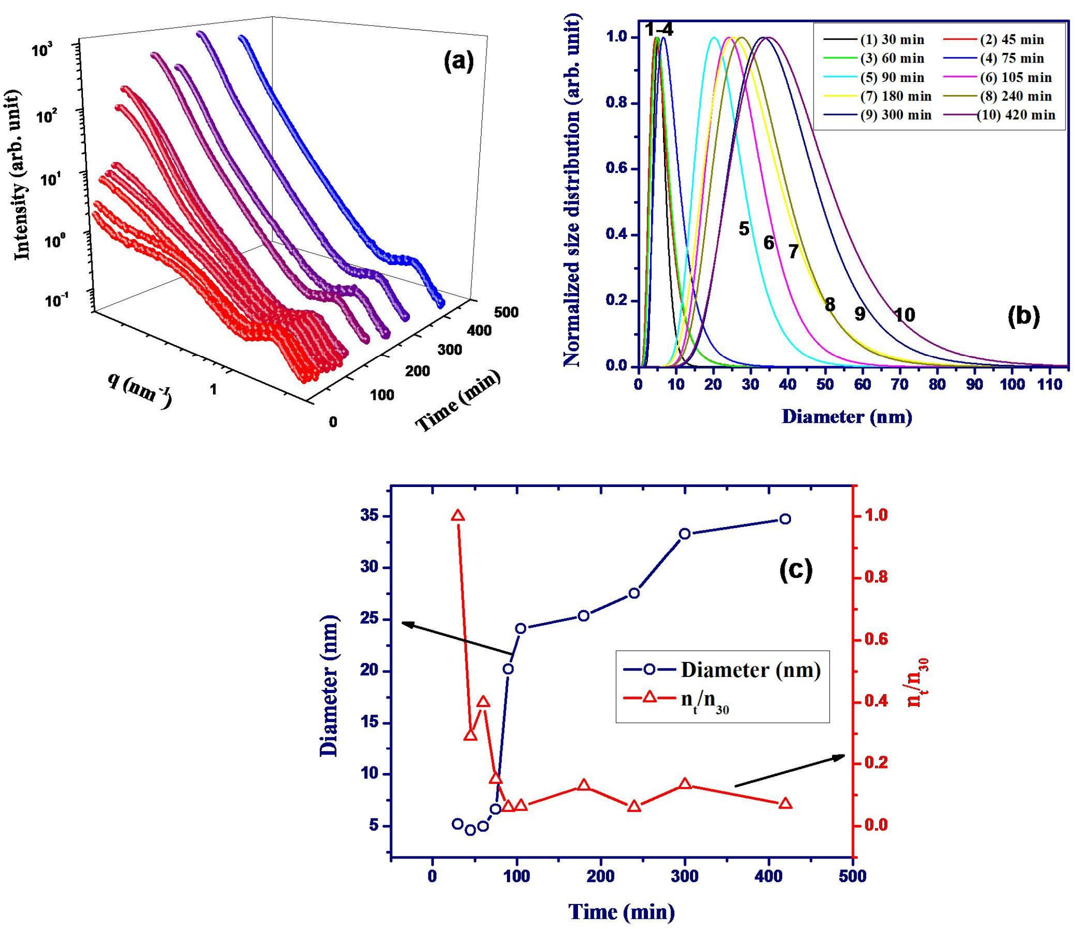

Figure 5.8. Radial averaged SAXS profiles at different reduction time (a), the size distribution of the growing nanoparticles obtained from SAXS analyses (b) and the time dependence of the peak diameter and the relative number density (n_t/n_{30}) (c) in Nafion 117 matrix. The term 'n_t' and 'n_{30}' represents the number density of the nanoparticles at time t and 30 min respectively. Solid lines through the points are eye guide.

It is seen that the reaction is much slower in Nafion in comparison to Selemion matrix. The clean peak at higher q regime (~1.7 nm^{-1}) of the SAXS profiles given in Figure 5.8a is attributed to scattering from correlated hydrophilic ionic clusters in Nafion 117 [Mauritz and Moore 2004]. The appearance of the characteristic ionomer peak of Nafion 117 at high q regime at all time scale suggests that, while nanoparticles grow in the hydrophilic domain of the ionomer, the ionic clusters always reorganize themselves to attain the original physical structure in the matrix. From the size distribution profiles obtained from TEM analysis, it is seen that, the continuously evolving ~5 nm seeds are the building blocks for the growth of AgNPs in Nafion matrix. From Figure 5.8b & c it is evident that the growth process in Nafion matrix mainly comprises of two steps. The first one is similar to Selemion, i.e. initial slow growth followed by a rapid growth to attain saturation of peak diameter at about 105 min. The critical peak diameter of the particles at the saturation is ~25 nm in Nafion. The difference in growth of the AgNPs in Nafion compared to Selemion is further slow growth followed by final saturation of peak diameter at 300 min of reduction, resulting in the final size of ~35 nm. This may be attributed to lower network elasticity due to absence of crosslinking in Nafion as compared to Selemion, which allows the ionomer matrix to expand freely and accommodate bigger nanoparticles. The time dependence of the relative number density of the nanoparticles is shown in Figure 5.8c. It can be seen that, from 30 min to 105 min of reduction, there is a significant fall in the relative number density accompanied by a rapid jump in particle size. After 105 min, the relative number density of the particles almost saturates. After 105 min, the continuously fed silver species in Nafion is consumed in the slow increase in particle diameter, keeping the relative number density of the particles almost unchanged, as seen from Figure 5.8c. In the TEM analysis in Figure 5.7c (180 min), the smaller seeds (5 nm) are not observed. This corroborates the slow growth stage (105-300 min) of the AgNPs in Nafion matrix at the expense of the continuously evolving smaller seeds. After the size of the nanoparticles gets saturated finally at 300 min, the smaller seeds re-appear as seen in the TEM image and size distribution histogram as given in Figure 5.7d.

3.3. Mechanism of Formation of Nanoparticles in Ion-exchange Membranes

The possible mechanism of formation of AgNPs in ionomer membranes has been elucidated mainly based on the results obtained from the time resolved SAXS, and radiotracer experiments. SAXS has been used to follow the kinetics because of its high brilliance for analyzing very large number of particles (large volume of the membrane) and thus producing results with good statistics. The spatial distribution of the AgNPs has been inferred from the TEM data, which shows the AgNPs have been formed uniformly throughout the matrix in all cases. Qualitative support for the proposed mechanism has also been obtained from the TEM results, particularly the concept of steady production of tiny silver seeds. However, for comparison purpose, the peak diameter of the growing AgNPs obtained from the SAXS and TEM data at different time of reduction are given in Table 5.1. It is seen from the Table that there is a good agreement between SAXS and TEM results for all the cases except one case where particle number density is very high (Selemion at 80 min of reduction) as is stated earlier in Section 3.1. Due to very high particle number density and very small interparticle distance in this sample, the smaller AgNPs possibly could agglomerate slowly during the time lag between SAXS and TEM experiments. However, this doesn’t alter the proposed growth mechanism, as the kinetics of growth saturates at 25 min of reduction (Figure 5.6c). It is also to be noted that in Nafion, as the overall particle density is low throughout the process, the AgNPs have good stability even after 300 min of reduction.

Table 5.1. Peak diameter of the growing AgNPs in different matrices and their relative number density.

Host matrix	Time of reduction (min)	SAXS data	TEM data	Relative number density of AgNPs (obtained from SAXS analysis)	
		[a]Peak diameter (nm)	[a]Peak diameter (nm)		
Selemion AMV	10	5.2	7.9	7.00	(N_t/N_5)
	20	14.9	14.0	3.39	
	40	16.3	17.8	8.83	
	80	16.1	24.2	14.84	
Nafion 117	45	5.0	6.2	0.29	(N_t/N_{30})
	90	20.2	17.6	0.06	
	180	25.3	28.6	0.12	
	300	33.3	34.9	0.13	

[a]Peak diameter represents the mode of the distribution.

N_t represents the particle number density at time t min in a given matrix.

N_5 and N_{30} represent the particle number density at time 5 min in Selemion and at time 30 min in Nafion matrix respectively.

The particle number density and size of the particles are found to depend on the type of ion exchanger used i.e., physical structure of the ion-exchange matrix. The rate of formation of

AgNPs in ionomer matrices is mainly determined by two factors viz. (i) equilibrium concentration of the anionic [Ag-citrate] species in the ionomer matrix, and (ii) the rate of reduction. The second factor is almost same for both the cases assuming the water nanodomains as host for nanoparticle precursors. The first process varies with the ionic nature of the ionomer. The difference in the growth rate in two different ionomer matrices (anion exchange and cation exchange) suggests the first one as the rate determining process. Nafion, being a cation exchange membrane, would exclude negatively charged species by Donnan exclusion, while Selemion, being an anion exchange membrane would favour the anionic species. Thus, equilibrium concentration of the negatively charged species will be much higher (determined by concentration of fixed charge) in anion exchange matrix compared to cation exchange matrix. Thus the rate of reduction in cation exchange matrix is expected to be slower as observed. Therefore, Ag content in Selemion is considerably higher than that in Nafion at a given reaction time. The particle number density is lesser in Nafion due to lower number of monomer produced by reduction of precursor [Ag-citrate] species. In case of Selemion, the particles number density is higher due to a higher equilibrium concentration of [Ag-citrate] species. However, the particles do not grow to bigger sizes due to steric hindrance caused by the crosslinking. This leads to higher number density of AgNPs (~16 nm) in Selemion.

3.3.1. Mechanism of Nucleation

The rate of Ag^+ reduction by citrate is very slow at room temperature. In the case of high citrate concentration ($[citrate]/[Ag^+] >> 1$), the reaction is extremely slow even at higher temperature (75 ^{O}C) because of higher stability of silver citrate complexes. Our results show the reduction takes place in the ion-exchange membranes under the same reaction conditions. This shows that the nanodomains of water in the hydrophilic ion exchange membranes act as nanoreactors, facilitating the reduction of silver citrate complex. The redox decomposition of silver citrate complexes may take place via thermal oxidation of citrate in the confined nanospace through the Scheme 5.1. The nanoconfinement may be facilitating the electron transfer to Ag^+ ions.

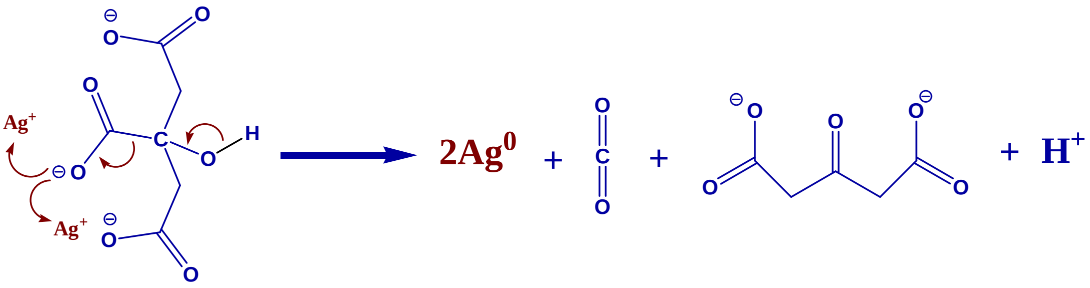

Scheme 5.1. Proposed mechanism of redox decomposition of silver citrate complex in the nanoconfinement of ionomer matrices at 75 ^{O}C.

The formed Ag^0 atoms in the confined space come together to form thermodynamically stable Ag clusters. However, these stages could not be investigated in the present study because of not having faster time scale measurements. As the initial induction of Ag^+ to Ag^0 is a slow process in this case, the growth process is also very slow in the beginning as directly observed from the SAXS data.

3.3.2. Mechanism of Growth

The combined radiotracer and SAXS experiments reveal the growth of the nanoparticles in the ionomer matrices as a combination of continuous reduction of silver ions on the nanoparticle surfaces and a sudden coalescence of nanoparticles at a critical number density. Figure 5.9a gives the profile for silver loading per unit area (mg cm^{-2}) of Selemion AMV membrane from [^{110m}Ag-citrate] complex solution (2nd set of radiotracer experiment). Figure 5.9b gives the profiles for silver loading per unit area (mg cm^{-2}) of Nafion 117 matrix without (2nd experiment) and with (3rd experiment) silver seeds (pre seeded by $NaBH_4$ reduction) during chemical reduction from [^{110m}Ag-citrate] complex solution. It is seen that, the rate of loading of silver in Selemion AMV is significantly higher (~0.9 mg cm^{-2} in 130 min) than in Nafion 117 (~0.2 mg cm^{-2} in 300 min), corroborating the diffusion of negatively charged [Ag-citrate] species into the ionomer matrices. The values of (Ag^+/Ag^0) obtained at the highest reaction time (Section 2.3) have been found to be 7.6 x 10^{-3} in Selemion and 0.23 in Nafion, showing very small fraction of loaded silver remains unreduced in Selemion while it is about 20% in Nafion.

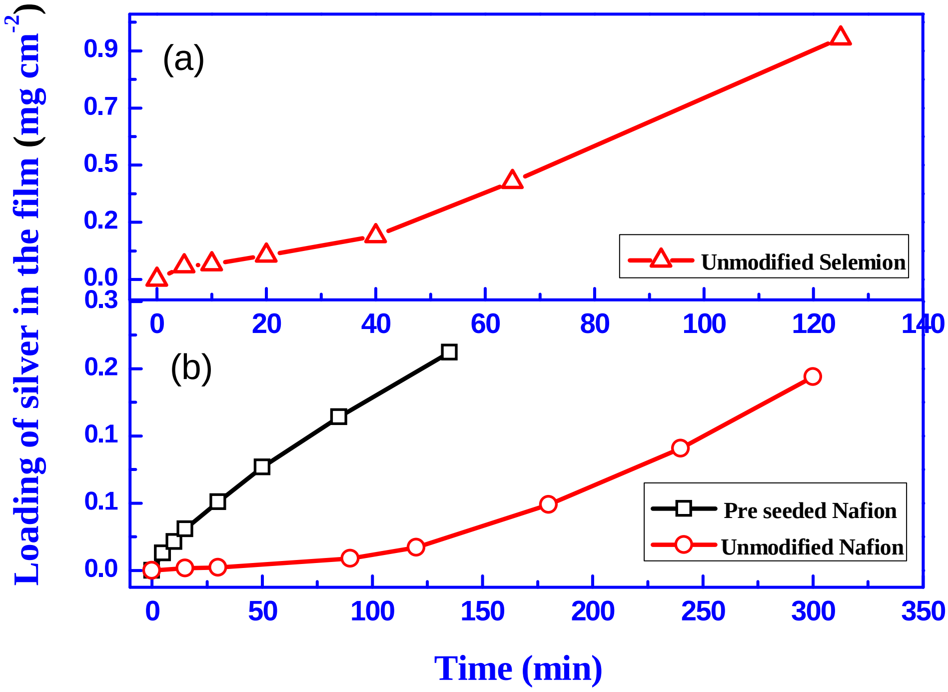

Figure 5.9. Time dependence of the silver loading per unit area of (a) Selemion AMV membrane and (b) Nafion 117 membrane with and without silver seeds during the synthesis as obtained from radiotracer experiment. For pre-seeded Nafion membrane, mass given excludes the mass of pre-loaded silver seeds.

It is to be noted that, in both type of unmodified ionomer membrane, the kinetics of silver loading is very slow in the beginning followed by rapid increase beyond a critical time (Figure 5.9). The critical time correlates well with the time at which jump in peak diameter is observed from SAXS study (Figure 5.6c and 5.8c). As stated earlier, this shows the coalescence of the nanoparticles into bigger size beyond a critical number density. Beyond the critical time (size), the nanoparticles probably lose their mobility and settle on the polymer matrix surfaces (due to their bulky size) and acts as site for further auto-reduction of the [Ag-citrate] species on their surface via thermal oxidation of citrate on the nanoparticle surface. The reduction process also seems to be faster as seen in the rapid growth in silver uptake profiles (Figure 5.9). The concept of photo-oxidation of citrate on silver nanoparticles and the photocatalytic growth of colloidal silver particles by auto-reduction have been discussed by Redmond et al. [2007]. The reduction of Ag^+ in the early stages (before the critical time) is less favorable due to the absence of AgNPs (at $t = 0$ min) or the presence of smaller AgNPs (at $t <$ critical time). In order to prove this conjecture, the silver uptake experiment has been carried out with pre-AgNPs loaded Nafion matrix using ^{110m}Ag radiotracer. The silver loading profile in the pre-AgNPs loaded Nafion matrix is shown in Figure 5.9b. It is seen that the initial slow step disappeared in the pre-AgNPs loaded Nafion membrane. This shows the key role of the pre-loaded AgNPs in facilitating the auto-reduction of silver ions on the nanoparticles surface. This observation confirms the proposed mechanism of growth of the nanoparticles. The schematic of the auto-reduction mechanism on the nanoparticles surface is given in Scheme 5.2. It is shown that the auto-reduction mechanism comprises two steps: (i) the thermal oxidation of citrate on the AgNP surface followed by donation of two electrons to the metal particles and (ii) reduction of metal ions on the nanoparticles surface (isotropically) by electron transfer.

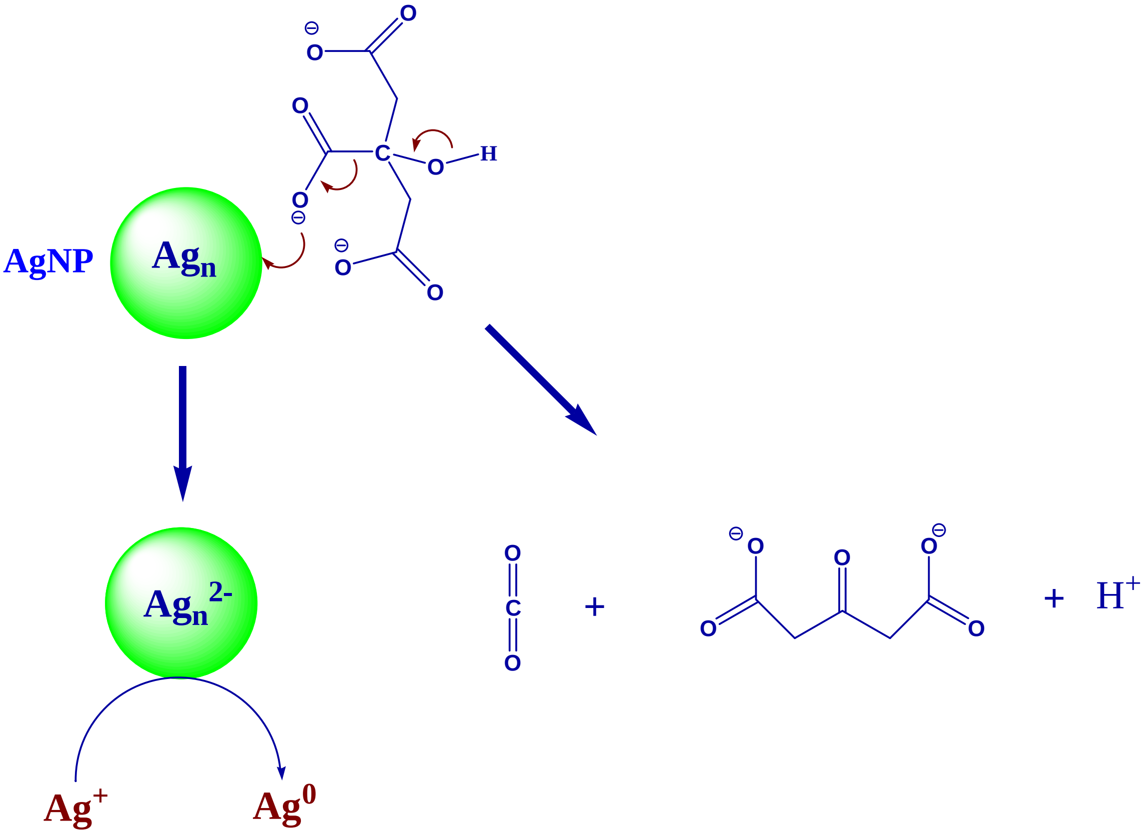

Scheme 5.2. Mechanism of the thermal oxidation of citrate on AgNP and the autoreduction of Ag^+ on AgNP surface at high temperature.

The auto-reductive pathway is a parallel process with the initial induction process, which is responsible for the birth of new silver seeds. This is directly evidenced from the TEM images at different time scale, where it can be seen that the tiny particles of silver always exists throughout the reaction time scale. Another parallel growth mechanism involved in this process is the coalescence of the growing nanoparticles at a critical size and critical number density, beyond which the individual existence of the particles becomes difficult.

The proposed nanoparticle growth mechanism in the ion-exchange membranes has been shown schematically in Scheme 5.3.

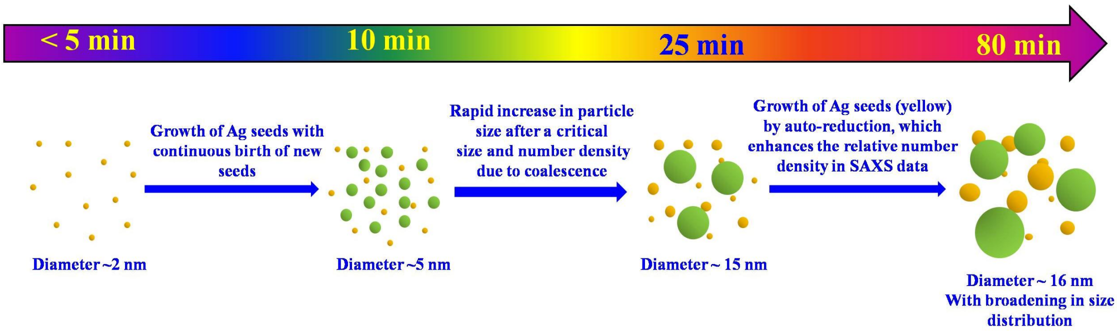

Mechanism of growth of AgNPs in Selemion AMV

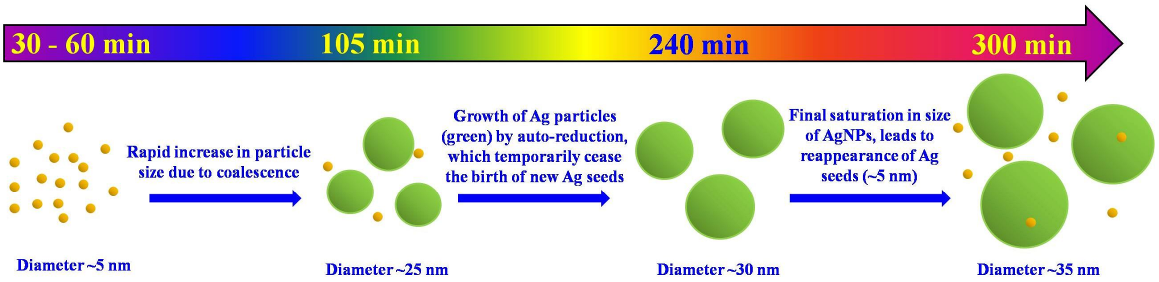

Mechanism of growth of AgNPs in Nafion 117

Scheme 5.3. Proposed mechanism of nanoparticles growth in both Selemion and Nafion membrane by citrate complex route. The bimodal particle distribution has been schematized in a combination of yellow (silver seeds) and green (silver particles) spheres for clarity.

3.4. Formation of AgNPs in Neutral Nanoporous Beads

In order to confirm that the reduction of [Ag-citrate] complex is facilitated by the nanoconfinement effect, not by the nature of the matrix, the developed method for synthesis of silver nanoparticles has been tried in neutral nanoporous Amberlite XAD-4 beads. The colourless transparent beads turned to characteristic golden yellow colour of AgNP in short period under the similar reaction conditions used for synthesis of AgNPs in ion-exchange membranes. The digital photograph of the XAD beads before and after the reaction is given in Figure 5.10. This observation confirms the nanoconfinement effect plays the key role for reduction.

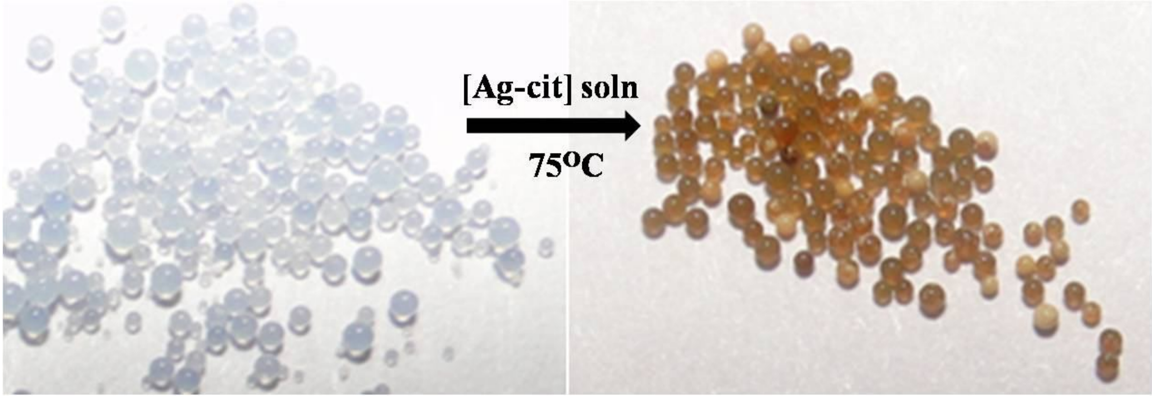

Figure 5.10. Digital photograph of the XAD-4 beads before and after treatment with [Ag-citrate] solution at 75 ^{O}C for 210 min.

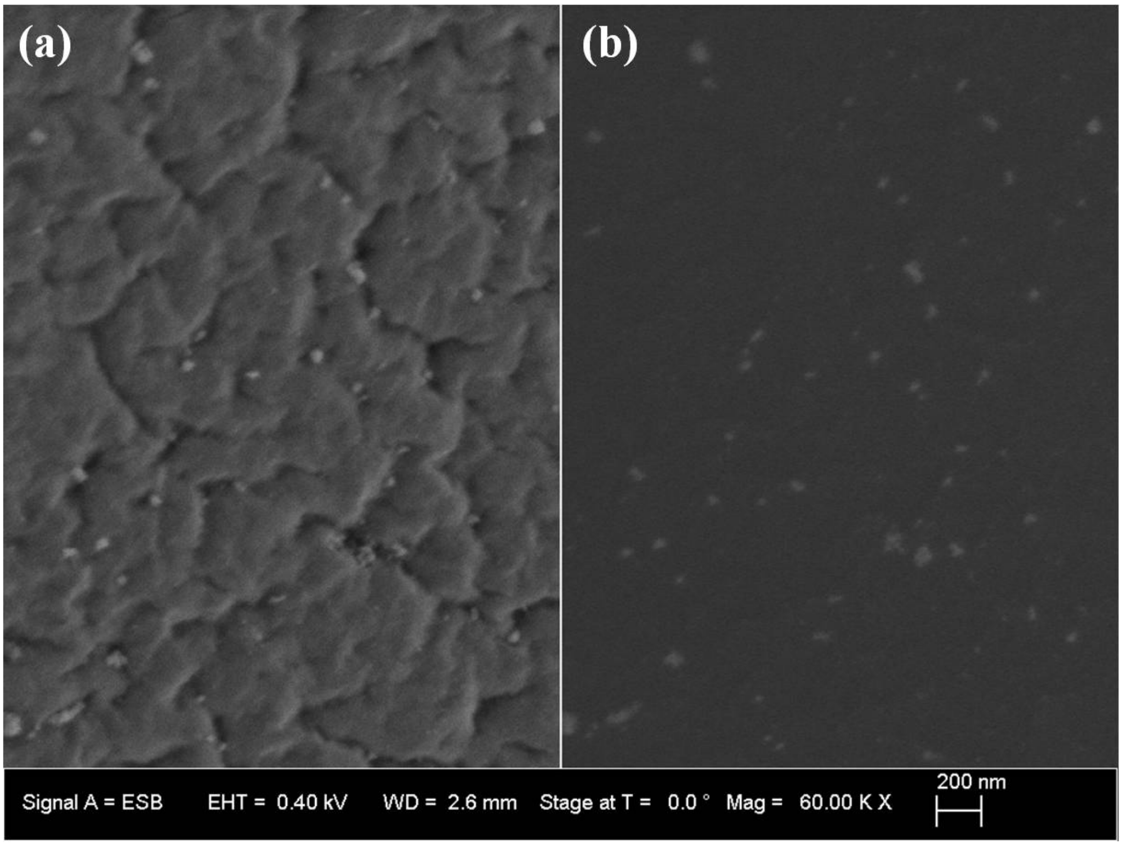

Figure 5.11. FE-SEM images of the surface of a AgNP incorporated XAD-4 bead in secondary electrons imaging mode for surface topography (a) and backscattered electron imaging mode for elemental mapping (b). White dots represent the silver nanoparticles.

Figure 5.11 shows the FE-SEM image of the surface of the beads after treatment with [Ag-citrate] solutions, where the AgNPs can be clearly seen. It is clearly seen from the topographic image of AgNPs incorporated XAD-4 bead that the AgNPs (~40 nm) have selectively formed near the nanoscale crevices (pores), not on the flat surface of the beads. The formation of larger amount of AgNPs has been observed in the interior pores of the beads as can be seen from Figure 5.12. This corroborates the proposed concept of nanoconfinement effect on the course of the reduction reactions.

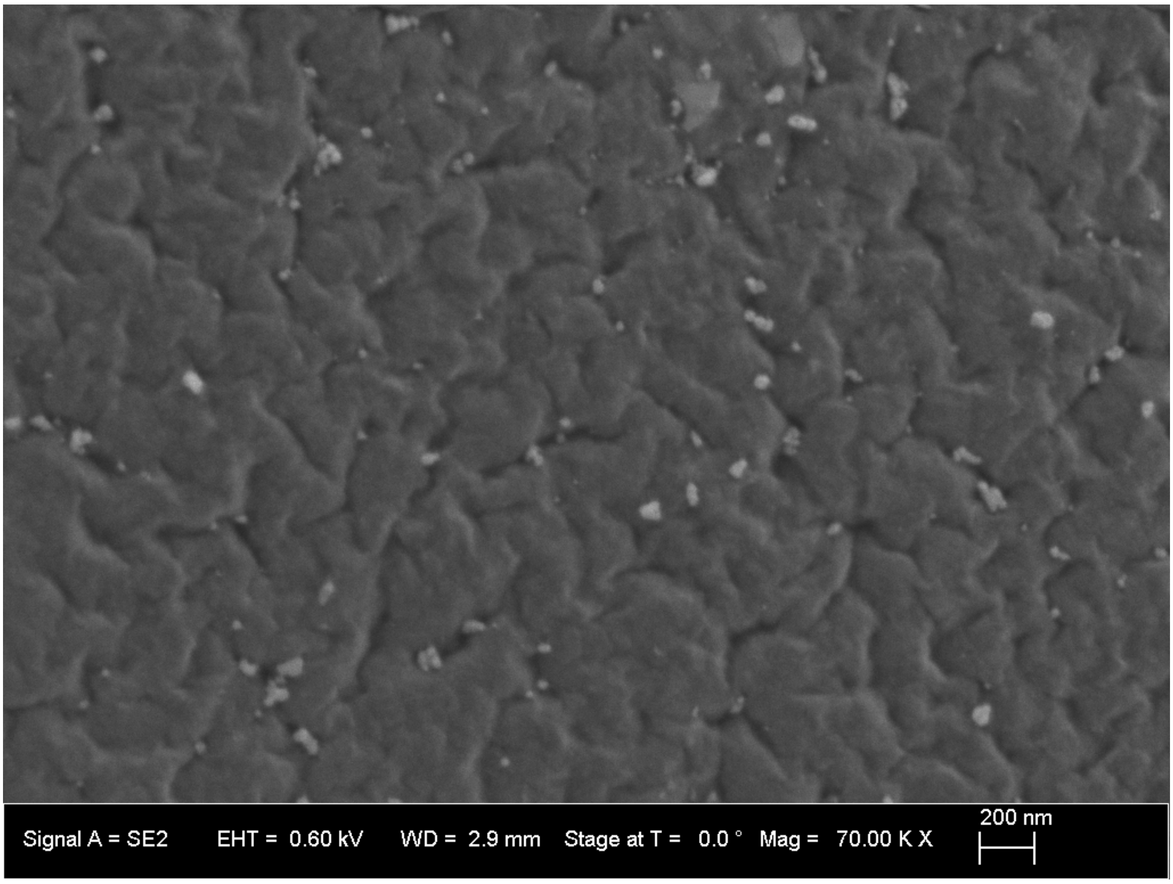

Figure 5.12. FE-SEM images of the interior of a AgNP incorporated XAD-4 bead in secondary electrons imaging mode for surface topography. White dots represent the silver nanoparticles (AgNPs).

3.5. Formation of AgNPs in Silica Gel Particles

The method has been extended further using the nanoporous silica gel particles having 4 nm pores as host matrix. As shown in Figure 5.13 AgNPs are formed by nanoconfinement facilitated auto-reduction of silver-citrate complex in nanopores of the silica matrix, which further shows that the nanoconfinement effect is matrix independent.

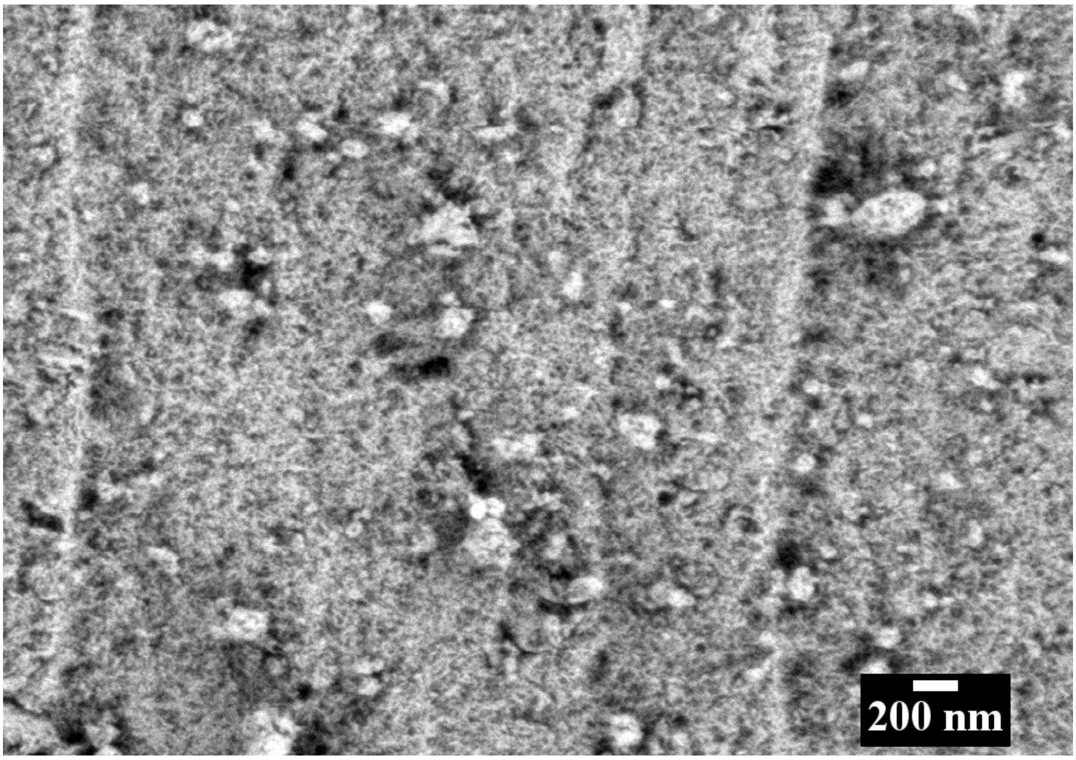

Figure 5.13. FE-SEM image showing distribution of Ag nanoparticles (brighter spots) in nanoporous silica matrix.

4. Conclusions

Redox decomposition of silver citrate complex has been found to be a promising route for selectively incorporating silver nanostructures in ion-exchange membranes, neutral nanoporous resin beads as well as in nanoporous silica gel particles. The slower kinetics of nanoparticle growth provides better control in tuning the size of the nanoparticles by carrying out reaction efficiently for a desired time period. The difference in the growth rate of the AgNPs in two different types of ion-exchange membranes is due to the difference in equilibrium concentration of the negatively charged [Ag-citrate] species in different membranes. The observation of constant population of smaller silver seeds corroborates the mechanism of continuous feeding of silver species from solution into the matrix by diffusion of silver-citrate complexes. The growth of nanoparticles is assisted by both autocatalytic reductions of Ag^+ ions on the nanoparticles surface by thermal oxidation of citrate and the interparticle coalescence. There is a critical size (~5 nm) and a critical relative number density of the nanoparticles in the membranes, beyond which they suddenly collapse into bigger nanoparticles, resulting in rapid rise in the diameter of the particles. The confined nanospace in a matrix has been found to facilitate the citrate reduction of Ag^+ ions for the formation of AgNPs, which otherwise does not take place in bulk solution.

Chapter 6

Synthesis of Noble Metal Nanoparticles by Polyol Reduction: Role of Nanoconfinement in Softening the Reaction Conditions

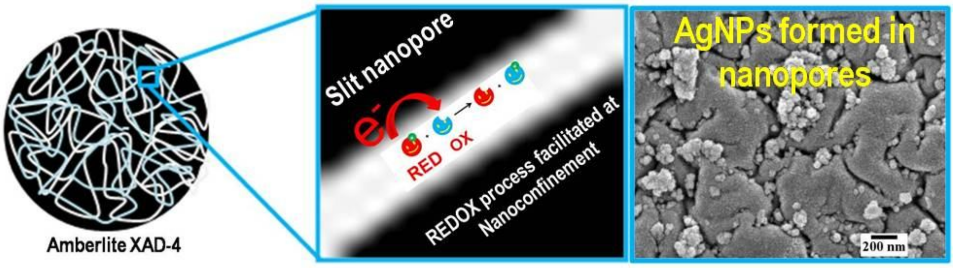

1. Introduction

Polyol reduction process is a well established method for production of the metal nanoparticles with different aspect ratio. Generally, this process requires refluxing of a solution containing precursor ions, ethylene glycol (or other polyols) and suitable capping agent at temperature of 160 ^{o}C or more under nitrogen/argon atmosphere [Ayyappan et al. 1996.; Chen et al. 2008.; Cho et al. 2013.; Sun et al. 2002.; Kasuya et al. 2010.; Yin et al. 2012]. In the previous chapter, it has been shown that, the nanoscale confinement or compartmentalisation of the metal ions and the reductant molecules (or the metal ion-reductant stable complex) in the porous matrices play a key role in driving the chemical reaction towards the forward direction. The results also show the porous materials or polymers facilitate chemical reactions which are not merely the surface effect as the results do not depend on the chemical nature of the pore surface. Thus cation exchange membrane, anion exchange membrane or neutral XAD-4 beads can all enhance the rate of redox decomposition of silver citrate complex to form AgNPs.

Therefore, attempt has been made to further explore the effect of confinement on different types of redox reactions, which are commonly used for synthesis of noble metal nanoparticles in solution. The reactions performed in this chapter belong to the categories which in general are not feasible under ambient condition. Such redox reactions include polyol reduction of noble metal ions to form noble metal nanoparticles, borohydride reduction of Pt ions to form Pt nanoparticles etc. Attempt has been made to perform those reactions at ambient condition (room temperature or at a temperature lower than it usually demands). In the present work, nanoporous amberlite XAD-4 beads have been used as the host matrix for the synthesis of silver, gold and platinum nanoparticles.

2. Experimental Section

2.1. Materials and Methods

The Amberlite XAD-4 spherical beads used in the present work were purchased from Sigma-Aldrich. These beads are made from highly crosslinked macroreticular polystyrene (av. pore size of 10 nm). The distribution of pore size as obtained from FE-SEM characterization is given in Figure 6.1. Silver nitrate ($AgNO_3$) with purity 99.9 % Ag, chloroplatinic acid (H_2PtCl_6) with purity 40 % Pt, and sodium borohydride ($NaBH_4$) were purchased from S.D. Fine Chem Ltd. Chloroauric acid ($HAuCl_4$) with purity 50% Au was purchased from Pravat Chemicals, India. Deionised water, 18 MΩ/cm, purified by model Quantum^{TM} from Millipore, Mumbai, India was used throughout the study. The commercially obtained XAD-4 beads were preconditioned following the procedure as described in Chapter 5.

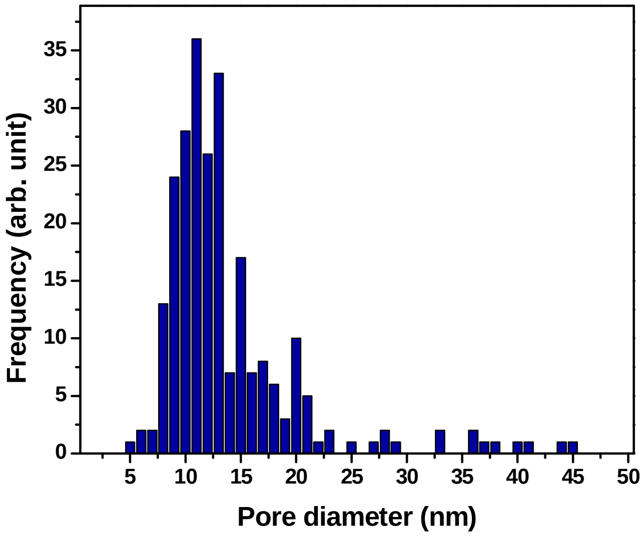

Figure 6.1. Pore size distribution of Amberlite XAD-4 beads as obtained from FE-SEM images.

2.1.1. Synthesis of Metal Nanoparticles at Ambient Conditions

2.1.1.1. Reduction of Noble Metal Ions With Ethylene Glycol (EG) at Ambient Temperature

For the synthesis of different noble metal nanoparticles (i) 20 mg of $AgNO_3$, (ii) 47.3 mg of $HAuCl_4$ and (iii) 58.4 mg of $H_2PtCl_6.xH_2O$ were dissolved in 10 mL of deionised water (18 MΩ/cm, purified by model Quantum^{TM} from Millipore, Mumbai, India) separately in three different beakers. To each of the precursor solution 10 mL of ethylene glycol (EG) was added. The final concentration of precursor ions in each system was 6 mM. In each of the beakers 1.5 g of preconditioned XAD-4 beads were added. The solutions were kept in dark for 48 h under stirring condition (300 rpm) at room temperature and atmospheric pressure. Faint colours characteristic of the respective metal nanoparticles appeared in the XAD-4 beads with time. It is worthy to mention that no colour typical of noble metal nanoparticles was observed in the bulk solutions. For gold, there was initially a light yellow colur in the bulk solution due to the presence of unreduced $AuCl^{4-}$ ions, whereas with time the solution turned colourless. Finally, the beads were filtered out, washed thoroughly with deionised water and dried. FE-SEM characterisation of the beads was done in order to see the formation of noble metal nanoparticles. The EG reduction of H_2PtCl_6 was carried out also in higher temperature (80 ^{o}C) keeping all other parameters constant in order to see the temperature dependence of the reaction rate. In that case, the reaction was continued for 6 h. The constant temperature was maintained using a water bath.

2.1.2.2. Reduction of $PtCl_6^{2-}$ with Sodium Borohydride ($NaBH_4$) at 80 ^{o}C

20 mg of $H_2PtCl_6.xH_2O$ was mixed with 20 mL freshly prepared aqueous solution of sodium borohydride (0.2 mol L^{-1}) at room temperature. 2 g of preconditioned XAD-4 beads

were added into it. The mixed solution was then kept at 80 °C for 6 h under continuous stirring (300 rpm). The colour of the beads changed quickly from colourless to gray with time. On the other hand the bulk solution remained almost colourless even after 6 h of reduction, showing the slow reduction at bulk.

2.2. Characterization of Nanoparticles

2.2.1. Field Emission Scanning Electron Microscopy

Field emission scanning electron microscopy (FE-SEM) was carried out for the surface of the XAD-4 beads with and without noble metal nanoparticles. For some of the samples FE-SEM was done for the interior of the beads. In order to observe the interior, the spherical beads were ground carefully with SiC sandpaper followed by polishing with diamond suspensions. Finally the beads were made conductive by gold coating prior to microscopy.

3. Results and Discussion

The present work reports the first effort to carry out the polyol reduction of noble metal ions at room temperature by physically imposing nanoscale confinement on the reaction media with the help of nanoporous matrices. It has been observed that, during equilibration of XAD-4 beads in aqueous solution of precursor ions (Ag^+, $AuCl_4^-$, $PtCl_6^{2-}$) and ethylene glycol (EG) at room temperature (25 °C), the colour of the beads changes to a characteristic colour of nanoparticles as shown in the representative images given in Figure 6.2. However, no colour typical of noble metal nanoparticles has been observed in the equilibrating solution, showing absence of reduction in bulk (Figure 6.2b). Scheme 6.1 gives the chemical reactions involved in ethylene glycol reduction of metal ions.

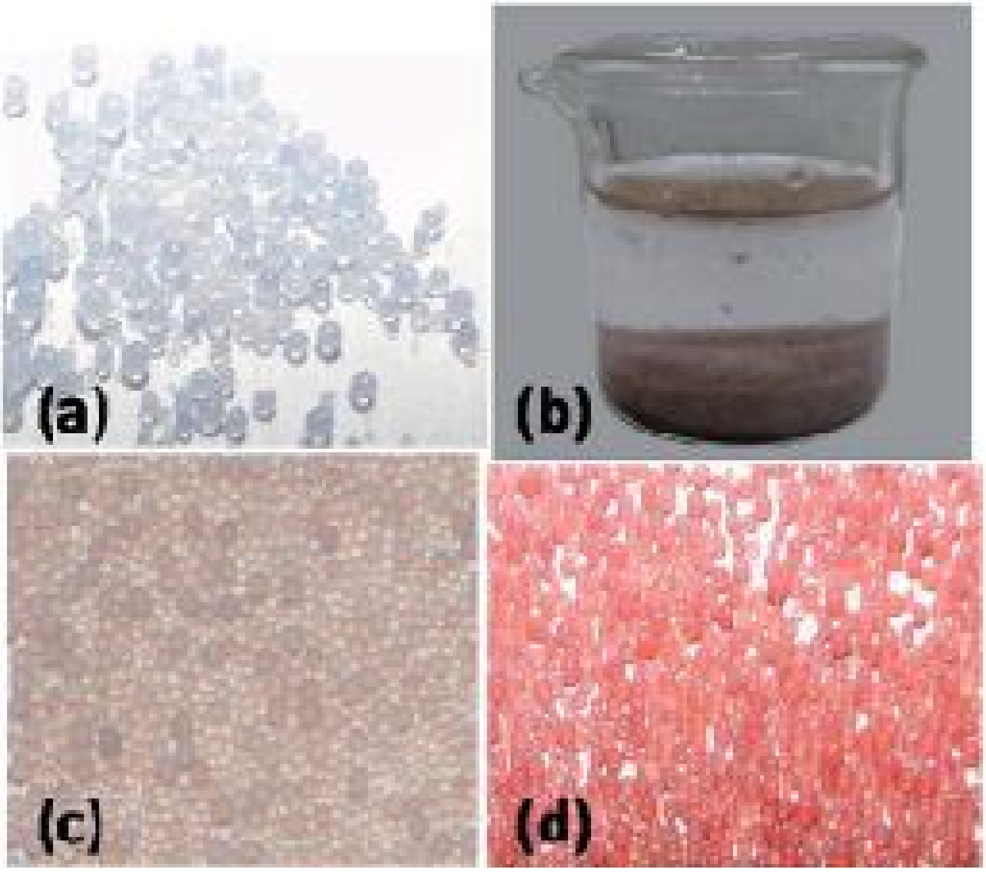

Figure 6.2. Digital photograph of blank XAD-4 beads (a), XAD-4 beads equilibrated with aqueous solution of $HAuCl_4$ and EG for 48 h, the colour in the beads is due to formation of AuNPs (b), XAD-4 beads containing AgNPs (c), XAD-4 beads containing AuNPs (d).

$$2HOCH_2\text{-}CH_2OH \longrightarrow 2CH_3CHO + 2H_2O$$

$$2CH_3CHO + M^{n+} \longrightarrow CH_3CO\text{-}COCH_3 + M + nH^+$$

Scheme 6.1. Chemical reactions involved for the ethylene glycol reduction of metal ions.

Figure 6.3 gives the FE-SEM image of the surface of a XAD-4 resin bead. The nanoscale slit/channel like porous network is clearly seen in the image. It is clearly evident from the FE-SEM images given in Figure 6.4 that the clusters of nanoparticles are seen near the nanoscale crevices in the matrix. This suggests that nanoconfinement facilitates the polyol reduction process at room temperature that is not observed in bulk solution under the same reaction condition. It is interesting to note that the used solution containing precursor ions in EG can be stored and reused for forming nanoparticles in the beads.

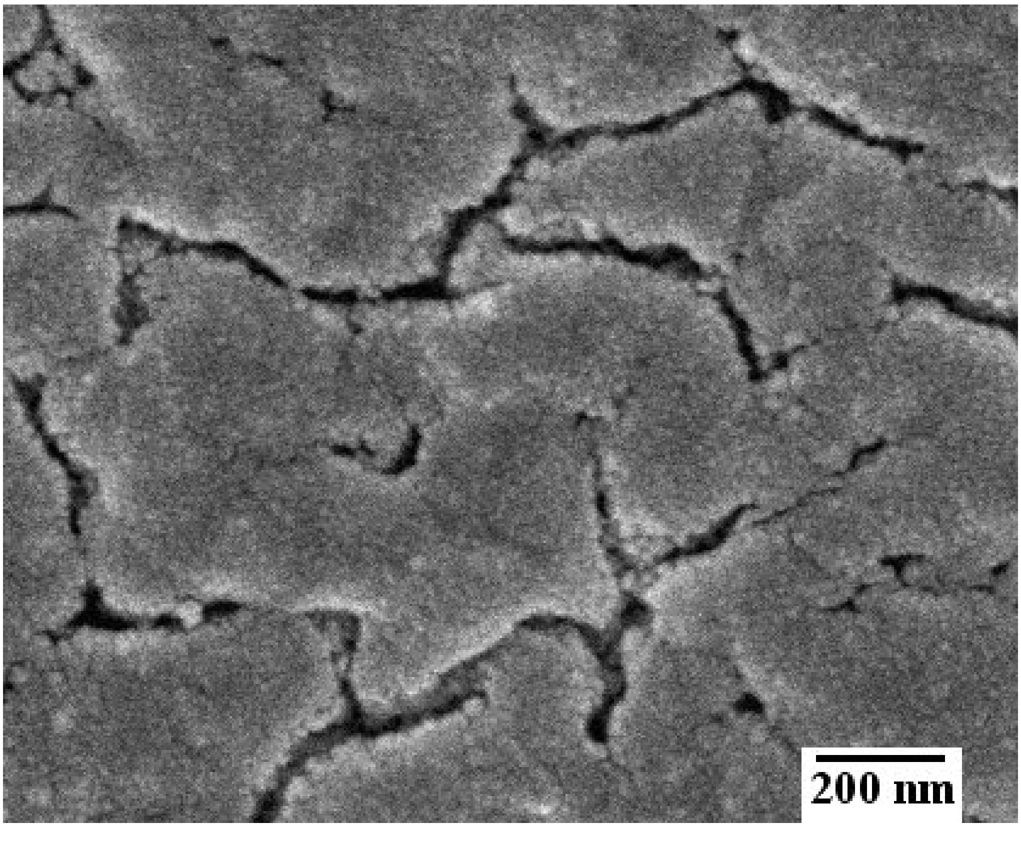

Figure 6.3. FE-SEM image of the surface of the XAD-4 bead showing blank matrix.

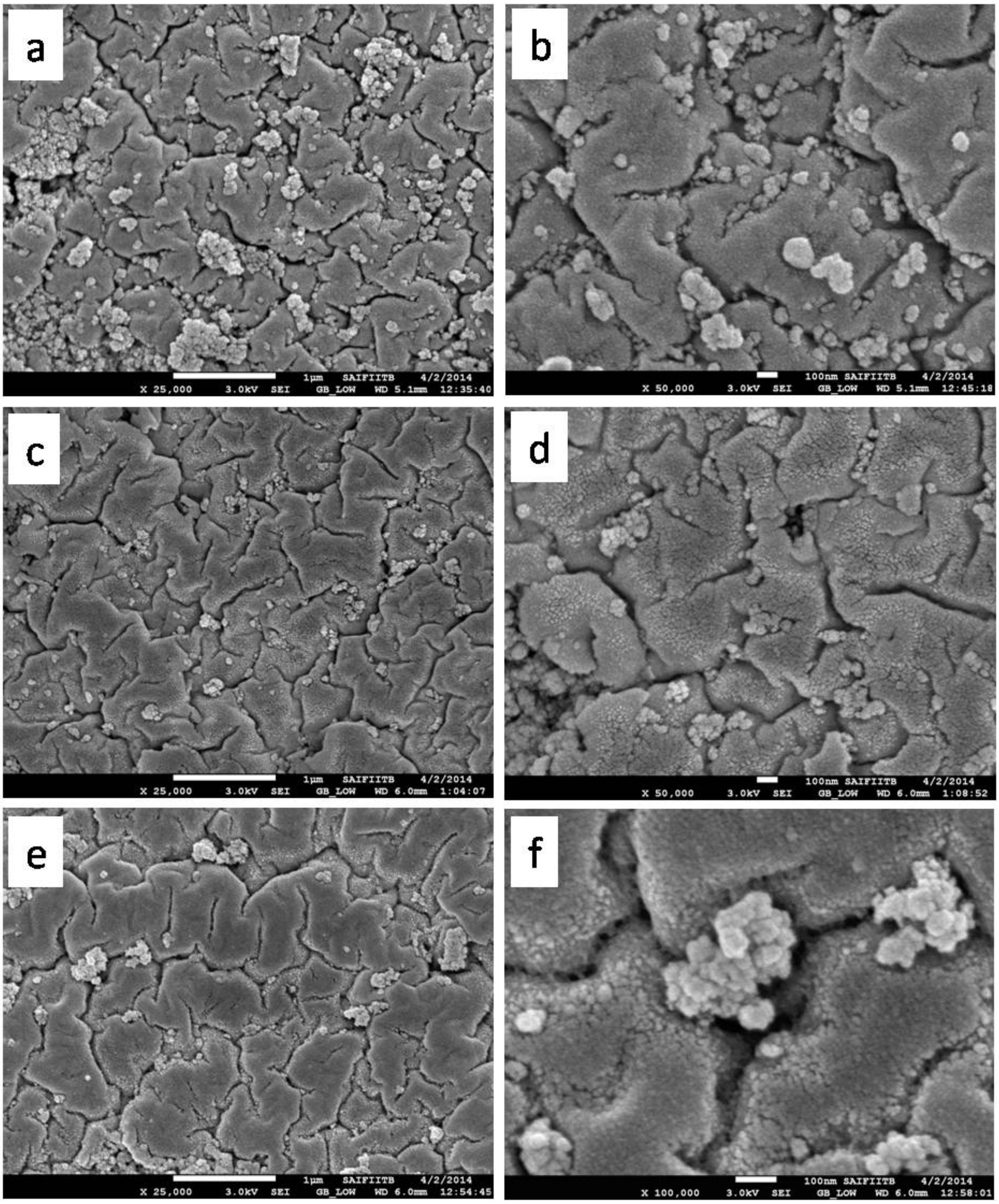

Figure 6.4. FE-SEM images (secondary electrons mode) at different magnifications of the surface of a XAD-4 bead after treating with an aqueous solution of EG and $AgNO_3$ (a and b), EG and $AuCl_4^-$ (c and d), EG and $PtCl_6^{2-}$ (e and f). Clusters of bright spherical objects near the nanoscale crevices represent the respective metal nanoparticles as produced.

It is seen from the FE-SEM image given in Figure 6.5a that the clusters of small spherical Pt nanoparticles are formed after nanoconfined reduction of $PtCl_6^{2-}$ by EG at room temperature. On increasing temperature to 80 °C, the bigger sized Pt nanostructures are formed in 6 h as shown in Figure 6.5b. This may be attributed to faster reduction kinetics as well as agglomeration of monomer and smaller nanoparticles. The nanoconfined reduction of $PtCl_6^{2-}$ ions was also carried out using BH_4^- ions at 80 °C for 6 h. In this case, uniformly distributed smaller Pt nanoparticles are formed (Figure 6.5c). It should be noted that both EG and BH_4^- do not reduce $PtCl_6^{2-}$ ions even at 80 °C significantly in aqueous solution. Appreciable reduction of Pt ions by BH_4^- has been observed by Song et al. [2007] and Pal et al. [2009] in nanosized soft templates. Though the authors have not mentioned, the results show possible effect of nanoconfinement in facilitating the reduction.

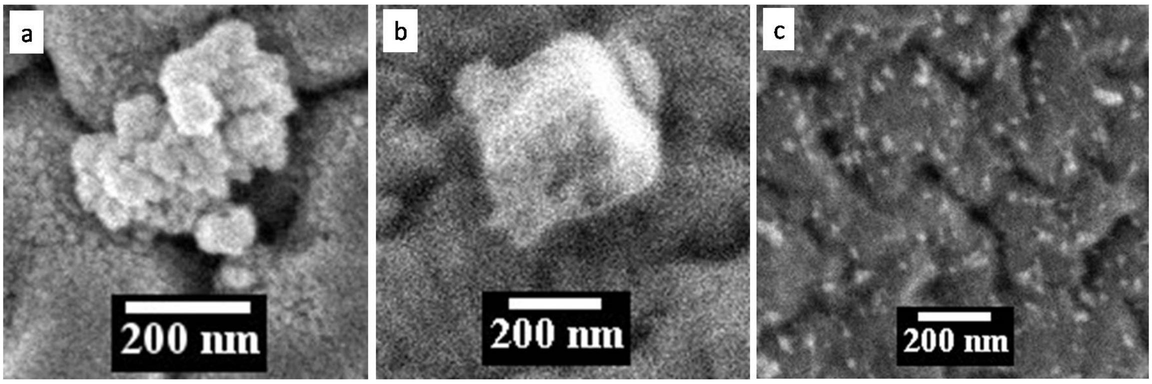

Figure 6.5. FE-SEM images showing distributions of Pt nanoparticles in XAD-4 beads after nanoconfined reduction of $PtCl_6^{2-}$ ions with EG at 25 °C (a), EG at 80 °C, (b) and BH_4^- at 80 °C (c).

4. Conclusions

Polyol reduction of noble metal ions have been found to occur at room temperature, which otherwise doesn’t takes place in bulk solution under identical condition. The redox reactions are thus remarkably facilitated in nanoconfined spaces. The selective reduction in nanoconfined spaces provides a soft synthetic route for preparing a variety of noble metal nanoparticles stabilized in polymer matrices using an appropriate combination of reductant and precursor ions.

Chapter 7

Catalytic Performances of Silver Nanoparticles in Nanoscale Confinement

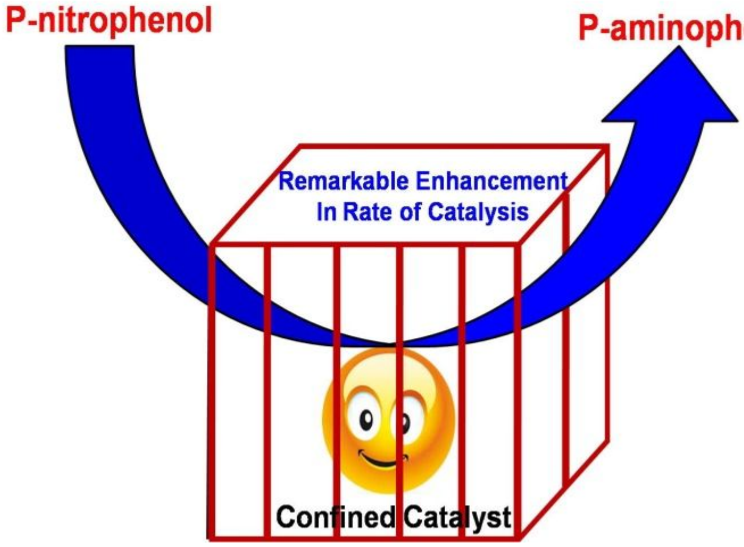

1. Introduction

Earlier chapters describe the synthesis and mechanistic aspects of noble metal nanoparticles in confined nanodomains of polymer matrices. The role of such matrices in providing excellent stability to the formed nanoparticles has also been shown. The synthetic routes include both direct in-situ reductions of metal ions with a reducing agent as well as the nanoconfinement driven reduction approach. The role of nanoconfined morphology of the polymer matrices in facilitating the synthesis of nanoparticles via chemical routes has been discussed. The present chapter reports on the catalytic performances of metal nanoparticles confined in porous polymer matrices. The nanosized reaction vessels in the ion-exchange membranes and XAD-4 resins which offer unique nanoconfinement effect on a chemical reaction, are best suited for their use as catalytic nanoreactor when subnanometer metal particles are encapsulated within their pores. The synergetic size effect and the confinement effect in such catalytic nanoreactors hold strong promises for enhanced catalytic activity.

Catalysis in nanoscale confinement has become an exotic research topic during past few years [Johnson 2014.; Chamberlain et al. 2014.; Pan and Bao 2011.; Chen et al. 2007.; Guo et al. 2010.; Chen et al. 2008.; Xiao et al. 2015.; Rance et al. 2013.; Cotanda et al. 2012.; Sanlés-Sobrido et al. 2012.; Leenders et al. 2015.; Saha et al. 2014.; Chen et al. 2013.; Song et al. 2015]. It has been shown that the solid catalytic nanoreactors, where the catalytic motif is confined in a nanoporous host matrix, show unique properties when catalyzing reactions under pseudohomogeneous conditions and exhibit more activity than just a solid supported catalyst [Johnson 2014]. These hybrid materials are popularly named as yolk-shell, core-shell, nanorattle, or ship-in-a-bottle nanoreactors, which consists of catalytic metal nanoparticles confined within nanoscale domains of organic or inorganic materials. Various kinds of catalytic reactions have been studied in nanoreactors, however the diffusion rate of the reactants through the encapsulating shells is an additional parameter involved. This problem may be overcome by preparing metal nanoparticles in thin porous ion-exchange polymer membranes or nanoporous polymer resin beads. Metal nanoparticles hosted in such matrices are good candidates as a catalytic nanoreactor for use in heterogeneous catalysis because of high thermal, chemical and mechanical stability and good contact of the reactants with the nanoparticle surfaces by the way of diffusion through hydrophilic channels. Also the polymer (membranes or resins) based catalyst offers an advantage over nanoparticles dispersed in aqueous medium as they can be easily separated from the reaction media after the completion of the reaction.

The nanoparticles used in the present work have been synthesised with proper size control in commercially available Nafion-117 membrane (by ascorbic acid reduction as discussed in chapter 4), in Amberlite XAD-4 resin beads (by polyol process as discussed in Chapter 6), and in a tailor-made pore filled anion exchange membrane (by citrate reduction route as discussed in Chapter 5). The catalytic activities of spherical silver nanoparticles stabilized in Nafion 117 membrane have been studied for borohydride (BH_4^-) reduction of methylene blue. The catalytic performance of silver nanoparticles hosted in Amberlite XAD-4 beads and in the tailor-made pore filled anion exchange membrane has been studied using BH_4^-

reduction of para nitrophenol (PNP) to para aminophenol (PAP) as a model reaction [Pradhan et al. 2001]. Attempt has been made to discern the role of nanoconfinement vis-à-vis size effect of the nanoparticles on the catalytic activity. In order to see the effect of nanoconfinement only on reaction rate, the same reaction has been studied in presence of nanoporous XAD-4 resin beads as well as in the nanoconfined domain of AEM without any nanoparticles. The first experimental evidence of the nanoconfinement driven room temperature BH_4^- reduction of para nitrophenol (PNP) to para aminophenol (PAP) has been reported.

2. Experimental

Synthesis of silver nanoparticles hosted in Nafion 117 membrane and in Amberlite XAD-4 resin beads and their morphological characterization has been carried out following the method given in detail in Chapter 4 and Chapter 6 respectively. In this chapter, the synthesis and characterisation of a tailor made anion exchange membrane (AEM) based catalytic nanoreactor (silver nanoparticles confined in nanoporous AEM) is described.

2.1. Materials and Reagents

The host polypropylene membrane (AccurelR PPIE) with 0.1 µm pore size was purchased from Membrana GmbH, Germany. The chemical reagents (3-acrylamido propyl) trimethyl ammonium chloride (APMC), (3-acryloxy propyl) trimethoxy silane (APTMS), ethylene glycol dimethacrylate (EDGM), α-α’-dimethoxy-α-phenyl acetophenone (DMPA), silver nitrate, tri-sodium citrate, methylene blue, para nitrophenol, and sodium borohydride were purchased from Sigma Aldrich.

2.2. Preparation of Catalytic Nanoreactor

The preparation of catalytic nanoreactor in the present work is a two step process, which includes: (i) the synthesis of nanoporous host anion exchange membrane (AEM) and (ii) the incorporation of silver nanoparticles within its matrix.

2.2.1. Synthesis of Anion Exchange Membrane (AEM)

The anion exchange membrane (AEM) was synthesized by pore filling of the commercially available porous polypropylene as a base membrane [Yang et al. 2011.; Pandey et al. 2003]. The monomers APMC and APTMS taken in 1:1 mol proportion were dissolved in dimethyl formamide (DMF) solvent. The cross-linker EGDM (10 mol%) and UV-initiator DMPA (1 wt.%) were added in this polymerizing solution. In order to fill its pores, the polypropylene membrane, cut into a 5x5 cm^2 piece, was soaked in such solution for 12 h. After removing the excess of polymerizing solution, the membrane piece was exposed to UV light (365 nm) for 20 min to prepare the pore filled anion exchange membrane. Finally the pore-filled membrane was washed with hot DMF and water to remove any soluble components. The percentage of monomer grafting was found to be 100% by weight.

2.2.2. Synthesis of Silver Nanoparticles of Different Sizes in the AEM

The silver nanoparticles (AgNPs) were synthesized using redox decomposition of anionic silver citrate complex in the confined nanospaces of the AEM, using the same protocol as described in Chapter 5. Briefly silver citrate complex solution (citrate/Ag^+)>>1 was prepared by dissolving 20 mg of $AgNO_3$ salt in 20 mL of aqueous solution of tri-sodium citrate (0.2 mol L^{-1}). The AEM was dipped into this solution at 75 ^oC under stirring condition for 10, 20, 40 and 60 min respectively.

AgNPs were formed in the confined nanospaces of the membrane. The size of the nanoparticles were 17, 20, 30 and 61 nm median diameters as determined from small angle X-ray scattering (SAXS) experiment.

2.3. Characterization of the Nanoreactor

2.3.1. Field Emission Scanning Electron Microscopy and Energy Dispersive X-ray Spectroscopy

Field emission scanning electron microscopy (FE-SEM) was performed for the AEM hosted AgNPs. Prior to microscopy, the membranes were coated with gold to make them conducting. In order to exchange the Cl^- ions of APMC with I^- ions, the AEM was equilibrated with potassium iodide (KI) solution prior to EDS study. I^- was chosen because of its high Z value, which improves the contrast of the ion-exchange sites with respect to the matrix.

2.3.2. Small Angle X-ray Scattering

SAXS experiments were performed in a laboratory based SAXS instrument using CuK_α as probing radiation. Radial averaging of the raw experimental data was done to obtain the scattering intensity (I(q)) within a wave vector transfer ($q=4\pi \, Sin(\theta)/\lambda$, where λ represents the wavelength and 2θ represents the scattering angle) range ~0.1 nm^{-1} to 2.5 nm^{-1}. The scattering contribution of the pristine AEM was subtracted from each scattering curve of the silver nanoparticles loaded AEM (Ag@AEM). In order to fit the background subtracted scattering profiles, polydisperse spherical particle model was adopted. The model was supported by field emission scanning electron microscopy (FE-SEM) data. Unlike the earlier chapters, the SAXS analysis in the present work has been carried out by fitting the entire scattering profile with a single model.

The scattering intensity $I_{NP}(q)$ is represented as

$$I_{NP}(q) = \left(\int_0^\infty P_{NP}(q,R) R^6 D_{NP}(R) dR \right) \tag{1}$$

where the term $P_{NP}(q,R)$ represents the form factor of the nanoparticle. For spherical nanoparticle of radius R,

$$P_{NP}(q,R) = 9 \frac{(\sin(qR) - qR\cos(qR))^2}{(qR)^6} \tag{2}$$

$D_{NP}(R)$ represents the size distribution of the nanoparticles, i.e., $D_{NP}(R)dR$ indicates the probability of having size between R to R+dR. In the present case standard lognormal distribution is considered, as given by the following equation.

$$D_{NP}(R) = \frac{1}{\sqrt{2\pi\sigma^2 R^2}} \exp\left[-\frac{\left[\ln(R/R_0)^2\right]}{2\sigma^2} \right] \tag{3}$$

R_0 denotes the median radius and σ denotes the polydispersity index of the distribution being obtained by fitting the SAXS profiles.

2.3.3. Quantification of Silver in the Polymer Host Matrices

2.3.3.1. Radiotracer Technique

Time resolved loading of silver in AEM matrices (mg cm^{-2}) was monitored by tagging Ag^+ ions with $^{110m}Ag^+$ radiotracer. 20 mg of $AgNO_3$ salt was dissolved in 20 mL of aqueous solution of tri-sodium citrate (0.2 mol L^{-1}). The silver ions in the solution were tagged with radioactivity by adding trace quantity of $^{110m}Ag^+$

radiotracer (obtained from BRIT, Mumbai, India). An AEM (2 x 2 cm^2) in NO_3^- form was immersed into the radioactivity tagged silver citrate solution at 75 °C under stirring condition. During the reduction process, the AEM was taken out from the solution at regular time intervals and the ^{110m}Ag radioactivity in the films was measured in a well type NaI(Tl) detector using 4K multichannel analyser. Since known mass of silver was tagged with measured quantity of radioactivity in the beginning of the experiment, the measured activity in a typical film at any given reaction time could be easily converted into the mass of silver loaded.

After a given period of reduction, the membrane was equilibrated with 0.25 mol L^{-1} $NaNO_3$ solution for 24 h under stirring condition to remove any unreduced $^{110m}Ag^+$ ions from the membrane. The residual activity in the membrane was measured using a NaI(Tl) detector. The ratio of ^{110m}Ag activity lost from the membrane to the residual activity in the same membrane gives the ratio of unreduced to reduced silver in the membrane.

Precaution: The handling of radiotracer during the experiment was done in a fume hood with good ventilation and with proper protective clothing.

2.3.3.2. Inductively Coupled Plasma Atomic Emission Spectroscopy Technique

For this purpose known mass of Ag@XAD beads were dissolved in concentrated nitric acid, evaporated to dryness under a IR lamp, and further dissolved in measured volume of water. The sample was then subjected for inductively coupled plasma atomic emission spectroscopy (ICP-AES) characterization. The mass of silver accumulated per unit mass of the XAD-4 beads was obtained.

2.4. Catalytic Study

The progress of the catalytic reactions was monitored in-situ using ultraviolet-visible spectroscopy. For this purpose, the reactions were performed in a quartz cell with a path length of 1 cm. A small piece of catalytic membrane with measured area or a fixed mass of catalytic polymer beads was inserted without obstructing the path of light in the quartz cell filled with reaction solution, placed in a portable UV-VIS spectrometer (K-MAC, South Korea). The UV-VIS absorption spectra were recorded at a fixed time interval in the scanning range of 200-700 nm at room temperature (25 ^{o}C) with continuous stirring of the reaction solution with a stirring rate of 300 rpm. This was achieved by placing the spectrophotometer on a stir plate and adding a micro-stir bar into the reaction solution. The kinetics of the reaction was monitored by measuring the time resolved change in absorbance at wavelength of absorption maxima (λ_{max}), characteristics of the reactant. Figure 7.1 gives the digital photograph of the spectrometer setup used throughout the study.

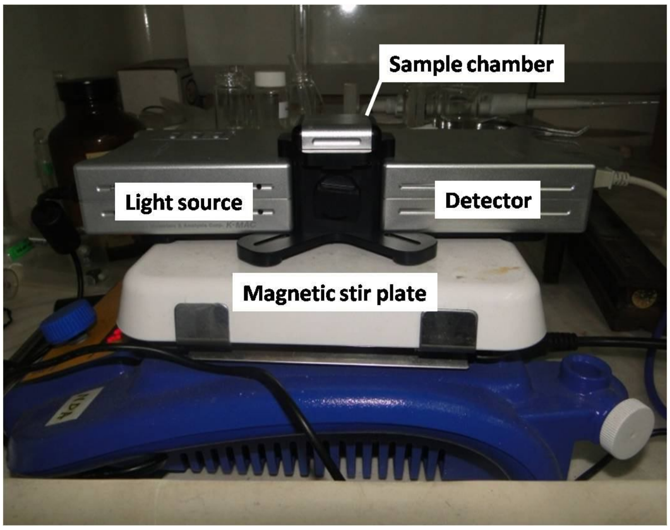

Figure 7.1. Digital photograph of the portable UV-VIS spectrometer system (K-MAC, Korea) used in the present study.

2.4.1. Reduction of Methylene Blue

Room temperature borohydride (BH_4^-) reduction of a model dye methylene blue (MB) was studied using the silver nanoparticles embedded Nafion 117 membranes as solid phase catalyst (as prepared in Chapter 4). A 1 x 2 cm^2 piece of nanocomposite membrane was used as catalyst. Typically, the composition of reaction solution was 100 μL of 0.2 mmol L^{-1} MB + 1800 μL water + 200 μL 0.2 mol L^{-1} of freshly prepared $NaBH_4$.

2.4.2. Reduction of Para Nitrophenol

Room temperature borohydride reduction of para nitrophenol (PNP) to para aminophenol (PAP) was used as model reaction for the catalytic investigation of silver nanoparticles confined in the nanopores of XAD-4 resin beads as well as in the anion exchange membrane (AEM). For each kinetic measurement, 100 μl of PNP solution (2 mM) was taken in the cell, followed by addition of 1.8 mL of deionised water. A small piece of Ag@AEM composite membrane (1 X 2 cm^2) was used as catalyst. Finally 200 μl of freshly prepared $NaBH_4$ solution (0.1 mol L^{-1}) was added into the reaction solution. The colour of the solution was changed from light-yellow to yellow-green with addition of $NaBH_4$. The cell was immediately placed in the portable UV-VIS spectrophotometer (K-MAC, Korea) and the absorption spectra were recorded at 1 min time interval in the scanning range of 200-700 nm at room temperature (25 ^oC).

3. Results and Discussion

The metal nanoparticles hosted in ion-exchange membranes or XAD resin beads act as nanoreactor because of their unique morphology. In all the systems the catalytic nanoparticles are confined in nanopores or nanoconfinement of the membrane or resins where the reaction takes place.

3.1. Catalytic Activity of Silver Nanoparticles Hosted in Nafion 117 Membrane

The silver nanoparticles formed by the reduction of Ag^+-loaded Nafion 117 by ascorbic acid (Chapter 4) for 1 min (nanosphere) and 5 min (nanorods) respectively have been used to study their redox catalytic activities for room temperature borohydride reduction of a model dye methylene blue (MB). The choice of these two Ag-Nafion samples is based on the size of the AgNPs formed. Spherical AgNPs with size ~3 nm are formed after 1 min as described above, and 5 min reduction lead to a formation of bigger nanostructures with sizes larger than 10 nm (spherical or rod) as shown in Figure 7.2.

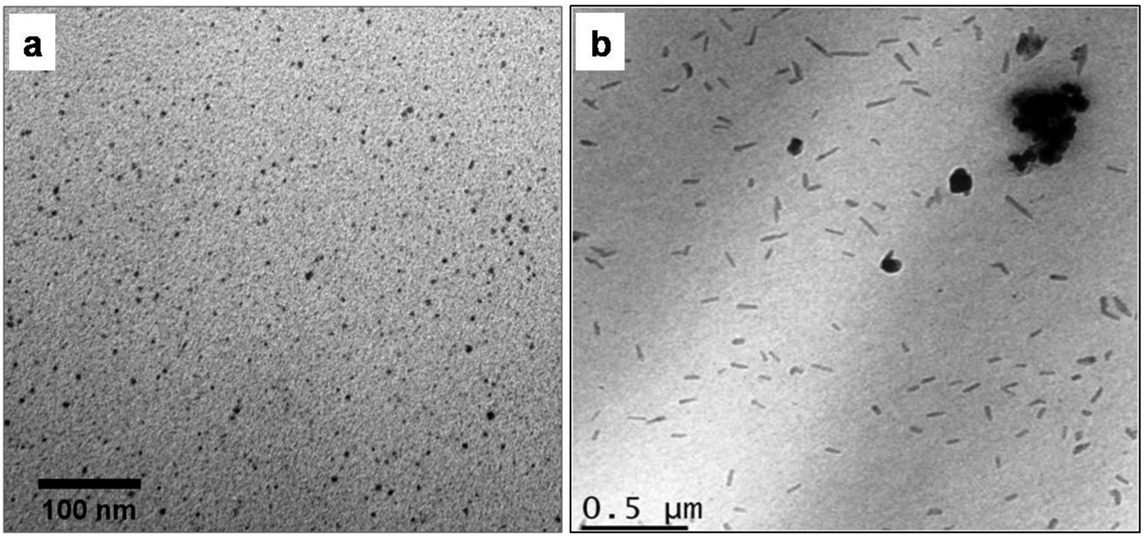

Figure 7.2. TEM images showing spatial distribution of AgNPs across thickness of the membrane subjected to reduction with ascorbic acid for 1 min (a) and 5 min (b).

The two factors that may be responsible for the catalytic activity of the silver nanoparticles are: the size/shape of the particles and their accessibility to reactants MB and BH_4^- ions.

The Ag nanoparticles mediate electron transfer after sorptions of MB and BH_4^- on its surface. Figure 7.3a gives the representative time resolved UV-VIS absorption spectrum of MB undergoing catalytic reduction in presence of the silver nanosphere embedded catalyst membrane. The gradual decrease of the peak intensity at 665 nm with time shows the decrease in MB concentration in bulk solution. This is due to the sorption of MB by the membrane, which is a diffusive process and the catalytic reduction of MB. Curves (i) and (ii) in Figure 7.3b represent the rate of decrease of MB concentration in presence of the reducing agent (BH_4^-) for the sample with silver nanospheres and silver nanorods respectively. The curve (iii) represents the rate of decrease of MB concentration in the solution due to its diffusion into the silver nanosphere loaded membrane in absence of BH_4. Methylene blue (MB) being a cationic dye, it can diffuse in the Nafion membrane through ion-exchange process. For AgNPs loaded membranes, initially the curves (i), (ii) and (iii) are superimposing, indicating absence of catalytic reduction of MB during the period (lag phase). The decrease in MB concentration during this lag phase is therefore attributed to the diffusion of MB into the membrane. However, beyond the lag phase the catalytic reduction of MB is a parallel process, resulting in an increased slope of the curves. The catalytic reduction of MB with BH_4^- follows pseudo-first-order kinetics described by:

$$\ln(A_t/A_0) = - kt \tag{4}$$

where A_0 and A_t are the initial absorbance and the absorbance at time t, respectively, and k is the catalytic reduction rate constant.

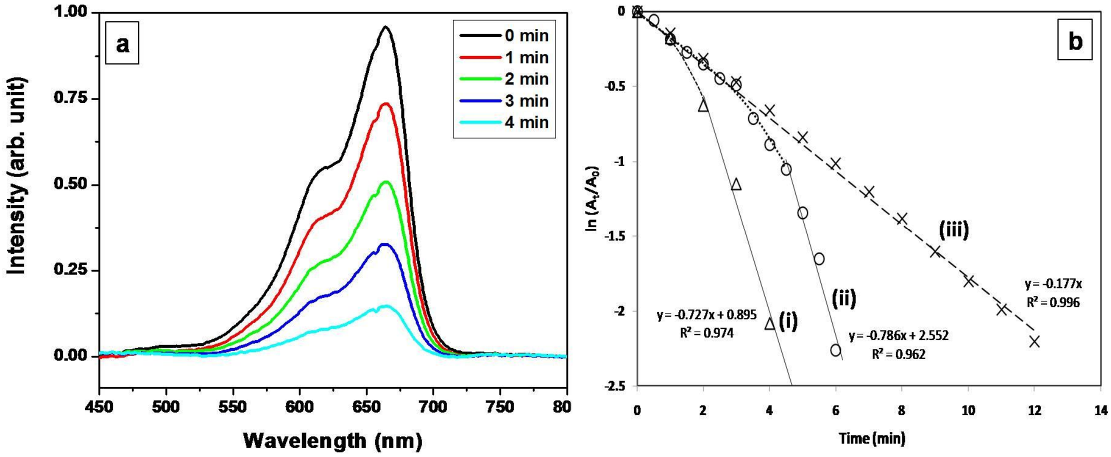

Figure 7.3. Successive UV-VIS spectra of catalytic reduction of MB by $NaBH_4$ in the presence of silver nanospheres (1 min reduction) embedded Nafion-117 membrane (a), and Variation of logarithm of A_t/A_0 as a function of reduction time in the presence of AgNPs loaded membrane samples formed by ascorbic acid reduction for 1 min (Δ) and 5 min (O) (b). The dashed line plot (X) shows the variation of A_t/A_0 with time in absence of the reducing agents (only because of diffusion of MB in AgNPs (1 min) embedded Nafion). A_t and A_0 represent absorbance of 665 nm at time t and initial time, respectively.

Solid lines in curve (i) and (ii) give the linear fit of the data points after lag time. Similarly the dashed line in curve (iii) represents the linear fit of the data points as obtained from the experiment without reducing agent. For curve (i) and (ii), the values of k from the slopes of linear portion of curves are found to be nearly same (0.727 min^{-1} and 0.786 min^{-1} respectively), indicating same rate of reduction. This is probably due to reduction occurring at the surface of the membrane under identical chemical environment making the rate constants similar. The difference in lag time may be due to difference in depassivation time in the two samples which may be due to difference in surface number density/morphology of the nanoparticles in the two samples.

3.2. Catalytic Activity of Silver Nanoparticles Hosted in XAD-4 Resin Beads

These XAD-4 resin beads hosted nanoparticles formed by ethylene glycol (EG) reduction at room temperature (Chapter 6) have been tested for catalytic borohydride reduction of PNP to PAP. As seen from Figure 7.4, the reduction of 4-nitrophenolate anions to PAP leads to decrease in absorbance at 400 nm, and increase in absorbance at 300 nm.

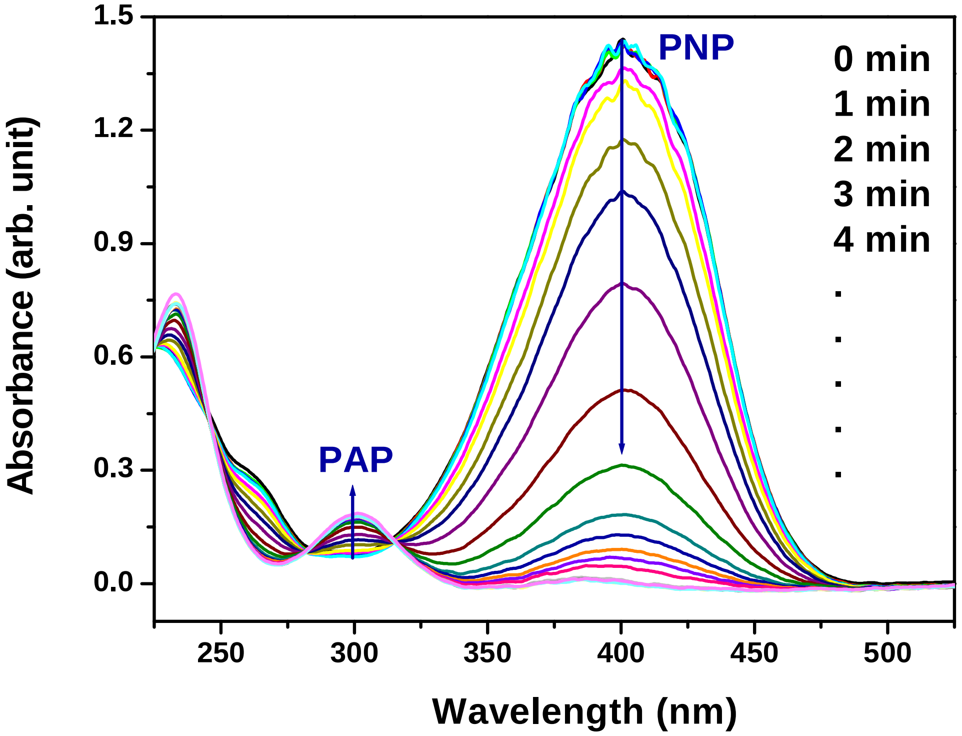

Figure 7.4. UV-Vis spectra obtained as a function of time during reduction of para-nitrophenolate anions (PNP) to para-aminophenol (PAP) with BH_4^- ions in presence of XAD-4 beads containing silver nanoparticles.

It is reported in the literature that the reduction of PNP to PAP in excess of $NaBH_4$ follows pseudo-first-order kinetics [Gangula et al. 2011.; Liu et al. 2013.; Tang et al. 2010.; Rashid et al. 2007.; Jana et al. 2006.; Pozun et al. 2013]. Figure 7.5 shows the variation of $\ln(A_t/A_0)$ as a function of time. It is seen that, after a certain lag time, $\ln(A_t/A_0)$ varies linearly with t indicating that the reduction of PNP with BH_4^- ions in the presence of AgNPs embedded XAD-4 beads follow pseudo-first-order kinetics. As reduction proceeds, the slope changes suddenly indicating onset of unprecedented acceleration in the rate of reduction by "nanoconfinement effect". The delay in observing "nanoconfinement effect" may be associated to steady state diffusion of reactants in the interconnected nanopores containing AgNPs to augment the reduction process occurring at the exterior matrix.

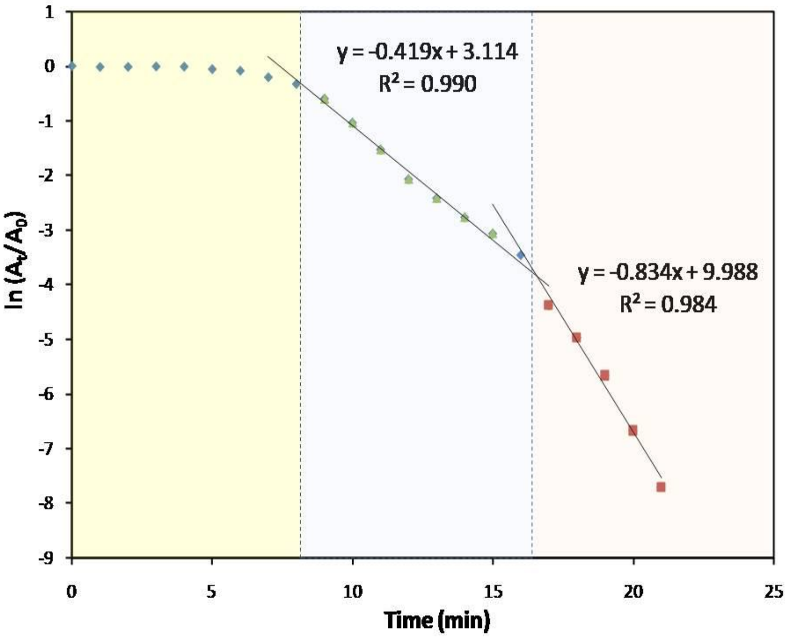

Figure 7.5. Variation of logarithm of A_t/A_0 as a function of time during reduction of PNP to PAP in presence of poly(styrene) beads containing Ag nanoparticles. A_t and A_o represents absorbance of 400 nm at time t and initial, respectively.

The rate constant k, calculated from the first slope of linear portions of the curve given in Figure 7.5, has been found to be 6.98x10^{-3} s^{-1} with an activity parameter κ = 489.13 $s^{-1}g^{-1}$ (rate constant per unit mass of silver). The silver loading has been determined by ICP-AES technique and has been found to be 0.143 mg per g of XAD beads. Jana et al. [2006] have studied the catalytic activity of AgNPs, embedded in cationic polystyrene beads (SERALITE-SRA-400). They have reported the rate constant k = 5.27 x 10^{-3} s^{-1}. The activity parameter κ (rate constant per unit mass of Ag) in their case has been found to be 107.5 $s^{-1}g^{-1}$, which is higher than unconfined AgNPs systems in aqueous solution [Gangula et al. 2011.; Liu et al. 2013; Tang et al. 2010.; Rashid et al. 2007]. The value of activity parameter (κ) obtained with silver nanoparticles embedded in nanopores of the XAD-4 beads is significantly higher than values reported by Jana et al. [2006]. The final value of k obtained from second slope is found to be 13.9x10^{-3} s^{-1} with an activity parameter of 974.07 $s^{-1}g^{-1}$. This is remarkable considering the fact that the reduction rate in the present case involves diffusion of PNP in XAD-4 matrix. This seems to suggest that nanoconfinment may also be enhancing Ag catalyzed reduction of PNP in the nanopores of XAD-4 beads. It is noteworthy that, the higher value of activity parameter (κ) in the work reported by Jana et al. [2006] in comparison to unconfined AgNPs may also be attributed to the possible confinement effect by the porous resin beads, which has not been reported by them.

3.3. Catalytic Activity of Silver Nanoparticles Hosted in Pore Filled Tailor-made Anion Exchange Membrane (AEM)

3.3.1. Synthesis and Characterization of Silver Nanoparticles in AEM

The prepared AEM used in the present work also acts as a nanoreactor and provides nanoconfinement effect because of its crosslinked, nanoporous gel type morphology, similar to a hydrogel-filled membrane [Yang et al. 2011]. Figure 7.6a and 7.6b gives the FE-SEM images of host polypropylene membrane before and after pore filling. Though the membrane surfaces appears to be dense in FE-SEM images (Figure 7.6b), the uniform distribution of I^- ions (can be seen in the EDS mapping of an iodide ions loaded AEM, Figure 7.6c, d & e) shows the ion-exchange sites are accessible to the ions in solution. This corroborates the interconnecting porous architecture (gel type network) of the pore filled membrane. The fibrous macroporous morphology of the membrane interior can be seen in FE-SEM image (Figure 7.6b). As seen from the FE-SEM images, the gel type dense morphology appears only in the membrane surface which serves as the nanoreactor.

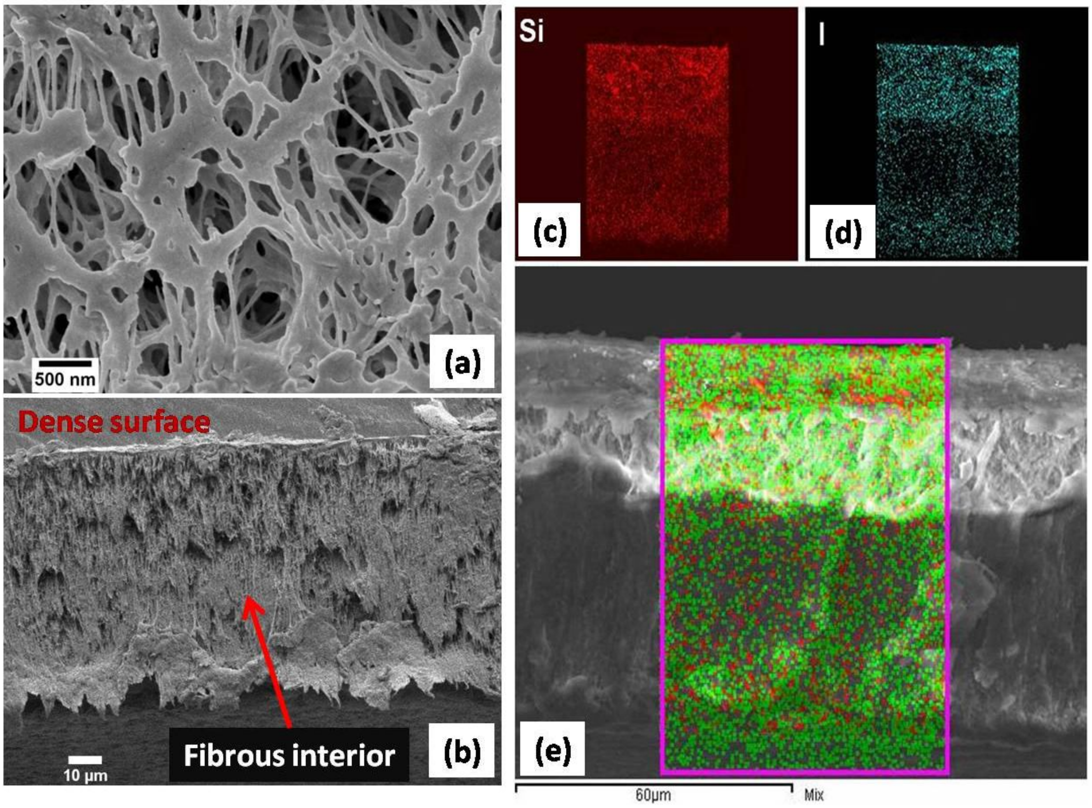

Figure 7.6. FE-SEM image of the surface of a pristine polypropylene membrane (a), the pore filled AEM with dense surface and fibrous interior (b), EDS mapping showing the spatial distribution of (3-acryloxy propyl) trimethoxy silane (c), (3-acrylamido propyl) trimethyl ammonium iodide (d), and combined distribution of both Si and I (e) across the membrane thickness. Red dots and green dots represent Si and I respectively.

The nanoporous gel type morphology of the membrane surface led to the redox decomposition of silver citrate complex, resulting in the formation of nanoparticles selectively on membrane surfaces (Figure 7.7).

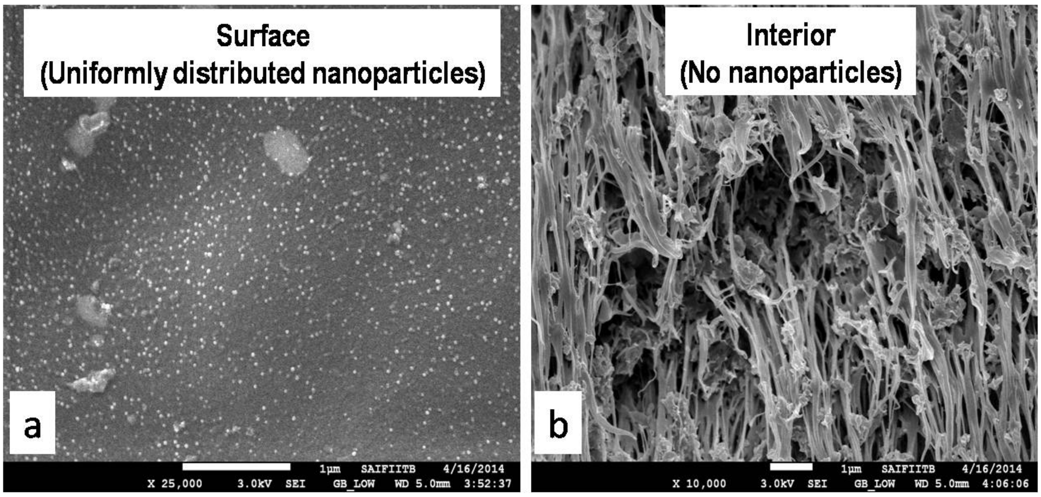

Figure 7.7. FE-SEM images of surface (a) and interior (b) of Ag@AEM composite membrane after 20 min of reduction.

The mechanism of nanoparticle formation by this method involves continuous supply of anionic silver citrate complex from bulk solution to the membrane by diffusion followed by its reduction in the nanopores of the AEM, facilitated by “nanoconfinement effect”. The detailed mechanism of formation of silver nanoparticles in commertially available ion-exchange membranes Nafion 117 and Selemion AMV using this method has been described in Chapter 5. The growth mechanism of nanoparticles involves continuous auto-reduction of the silver ions on existing nanoparticles surfaces and agglomeration of the nanoparticles after a critical number density. In order to prepare silver nanoparticles (AgNPs) of varying size, in the present work, the reduction time has been varied from 5 min to 60 min. The resulting size and size dispersions of the AgNPs produced have been obtained from the analysis of SAXS data. The same has been further confirmed from the FE-SEM results. Figure 7.8 shows the time resolved radial averaged SAXS profiles during the growth of AgNPs in AEM (a), the size distribution of the AgNPs obtained from SAXS analyses (b), and the time dependence of the peak diameter and relative number density (n_t/n_5) (c). The results on evolution of AgNPs size with time show that the present method of synthesis allows to produce nanoparticles of controlled size by varying the time of reduction.

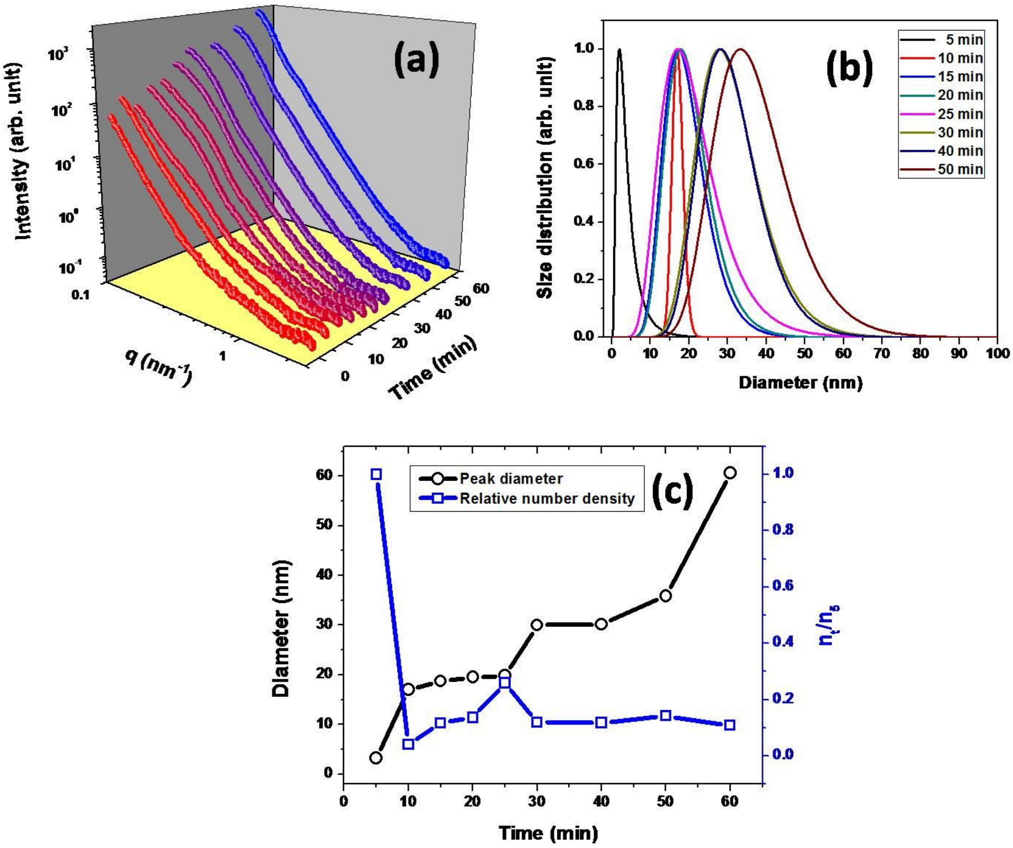

Figure 7.8. Radial averaged SAXS profiles at different reduction time (a), the size distribution of the nanoparticles obtained from SAXS analyses (b), and the time dependence of the peak diameter and the relative number density (n_t/n_5) of the nanoparticles(c). n_t and n_5 represent the number density of the particles at time t and 5 min, respectively. Solid lines connecting the points are eye guide.

It is seen from Figure 7.8c that the size of the AgNPs initially remains constant at ~20 nm during 10 – 25 min of reduction period. SAXS data show that AgNPs with median diameter of 61 nm have been formed after reduction of 60 min. Figure 7.8b shows that the polydispersity increases with progress of the reaction. Figure 7.9 gives the FE-SEM images of AgNPs formed after 20 min (a), 40 min (b) and 60 min (c) of reduction and the corresponding size distribution profiles (d) as obtained from the FE-SEM images. It can be seen that the size and size distribution of the AgNPs obtained from SAXS analyses are in good agreement with the FE-SEM data. Figure 7.10 gives the variation of silver loading per unit area of the AEM (mg cm^{-2}) with increase in reduction time as obtained from the radiotracer study. It has been observed that a negligible fraction of loaded silver remains unreduced in the AEM at any period of reaction, indicating the silver loading (mg cm^{-2}) data as plotted in Figure 7.10 correspond to the mass of silver nanoparticles only.

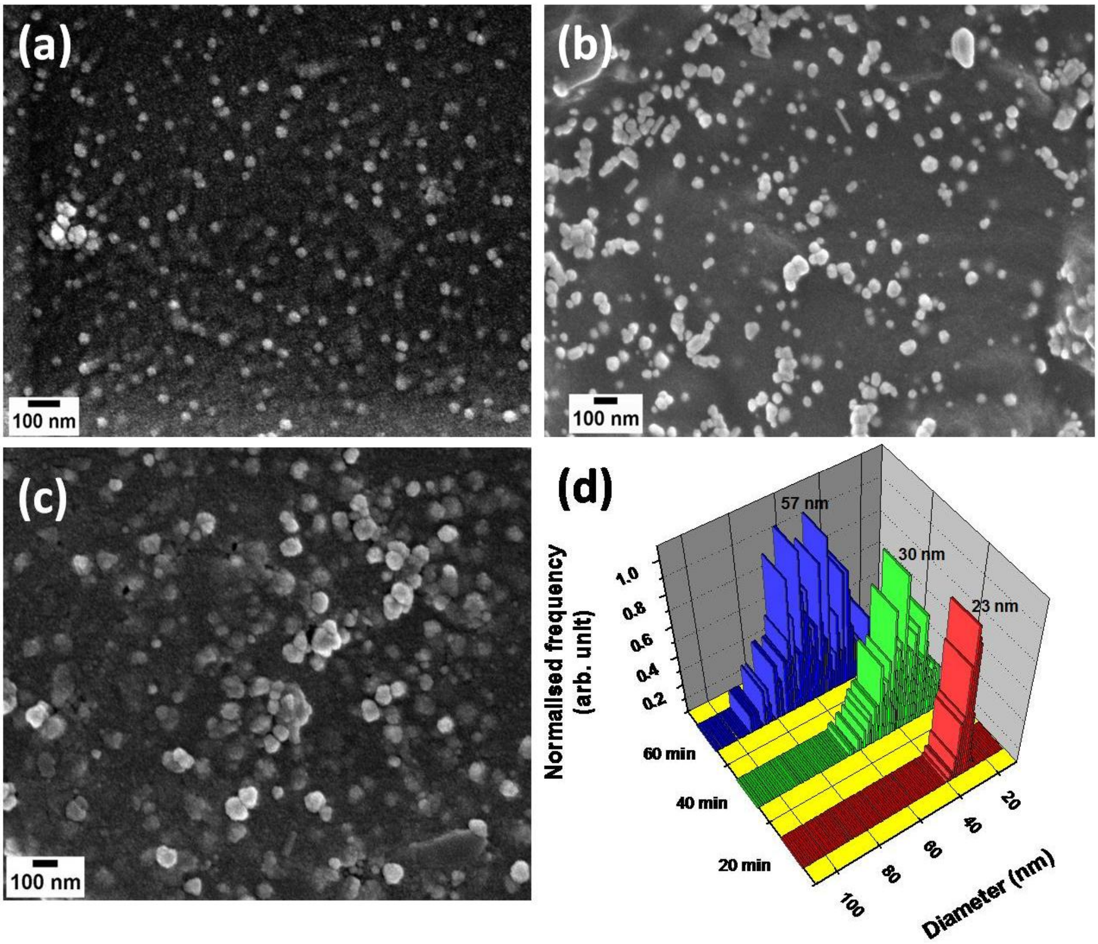

Figure 7.9. FE-SEM images of Ag@AEM composite after 20 min reduction (a), 40 min reduction (b), 60 min reduction (c) and respective size distribution profile of the nanoparticles (d).

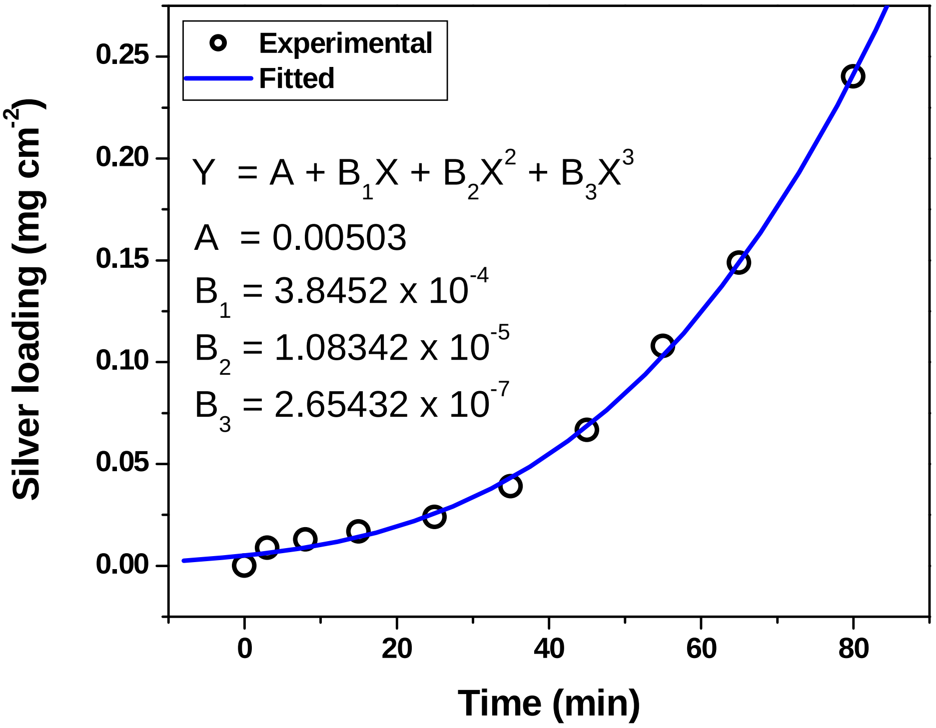

Figure 7.10. Time dependent profile of silver loading per unit area of AEM (mg cm^{-2}) during redox decomposition of silver-citrate complex.

3.3.2. Catalytic Activity of Silver Nanoparticles (Ag@AEM) for Borohydride Reduction of Para Nitrophenol

Four Ag@AEM composite membranes have been chosen for catalytic study with nanoparticles size of about 17, 20, 30, and 61 nm. Figure 7.11 gives the time resolved UV-VIS absorption spectra for the first catalytic cycle of para nitrophenol reduction in presence of four different catalyst membranes containing AgNPs of different size distribution. Figure 7.12 gives the variation of logarithm of (A_t/A_0) with time during the first catalytic cycle of para nitrophenol (PNP) reduction. In all cases, $\ln(A_t/A_0)$ decreases linearly with time (except an initial induction period), which shows that the reduction of PNP with excess of BH_4^- follows pseudo first order kinetics. The slope of each of the plots after the induction period gives the apparent rate constants of that reaction.

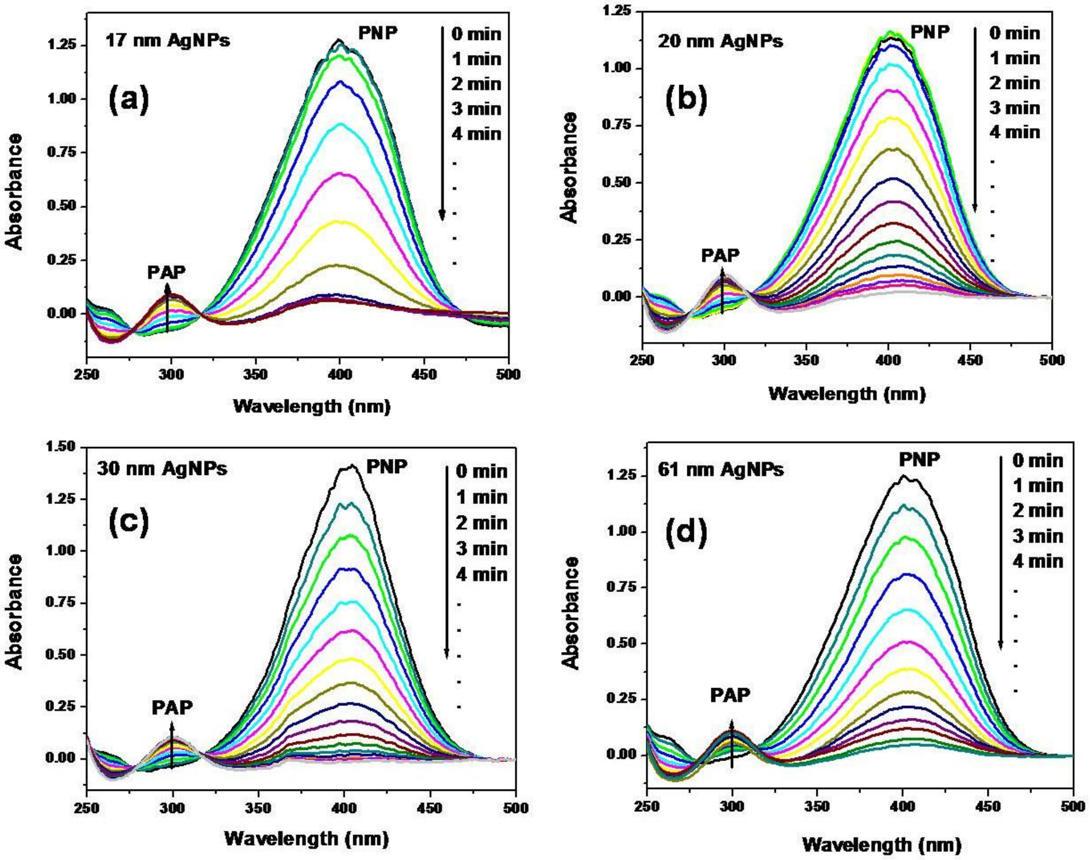

Figure 7.11. Time resolved UV-VIS absorption spectra for the catalytic reduction of para nitrophenol (PNP) with four different catalyst membranes containing AgNPs of median diameter (SAXS data) 17 nm (a), 20 nm (b), 30 nm (c) and 61 nm (d).

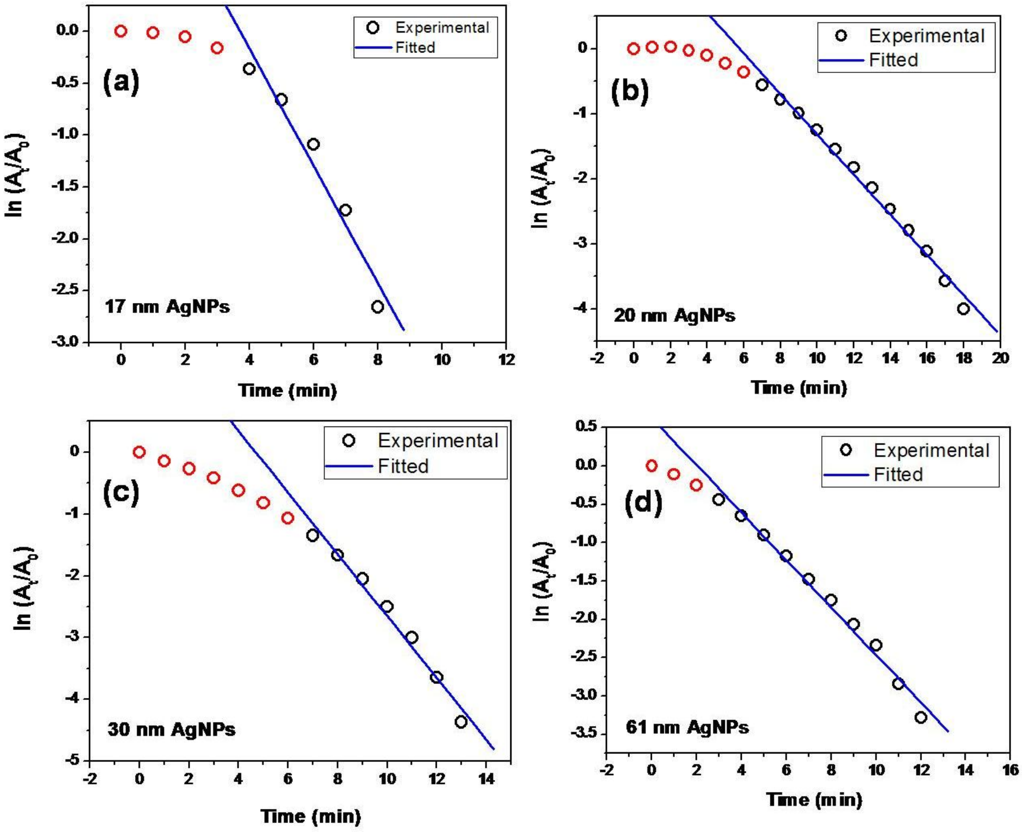

Figure 7.12. Variation of logarithm of (A_t/A_0) with time during the catalytic reduction of para nitrophenol (PNP) with four different catalyst membrane containing AgNPs of median diameter (SAXS data) 17 nm (a), 20 nm (b), 30 nm (c) and 61 nm (d).

Since the slope (rate constant) of the linear fit of $\ln(A_t/A_0)$ vs. t plot depends on the silver loading in the membranes, therefore it can’t be used directly for the comparison of size dependence of nanoparticles. Therefore the slopes (rate constants) have been normalized with mass of silver loaded (g) in respective membrane pieces to get mass normalized rate constant, termed as activity parameter (κ. $s^{-1}g^{-1}$). In order to see the size (diameter) dependence of the activity parameter, ln[κ. $s^{-1}g^{-1}$] has been plotted with 1/d (where d = diameter in nm) as shown in Figure 7.13a. The linearly increasing trend can be explained as the effect of increasing surface area [Fu et al. 2014]. The reusability of the catalyst membranes has been tested by using each membrane for 21 catalytic cycles. Figure 7.13b gives the variation of activity parameter ($s^{-1}g^{-1}$) with number of catalytic cycles for four different catalyst membranes. It can be seen that the catalytic activity remains almost constant upto 21st reuse, showing remarkably high reusability of the prepared catalysts.

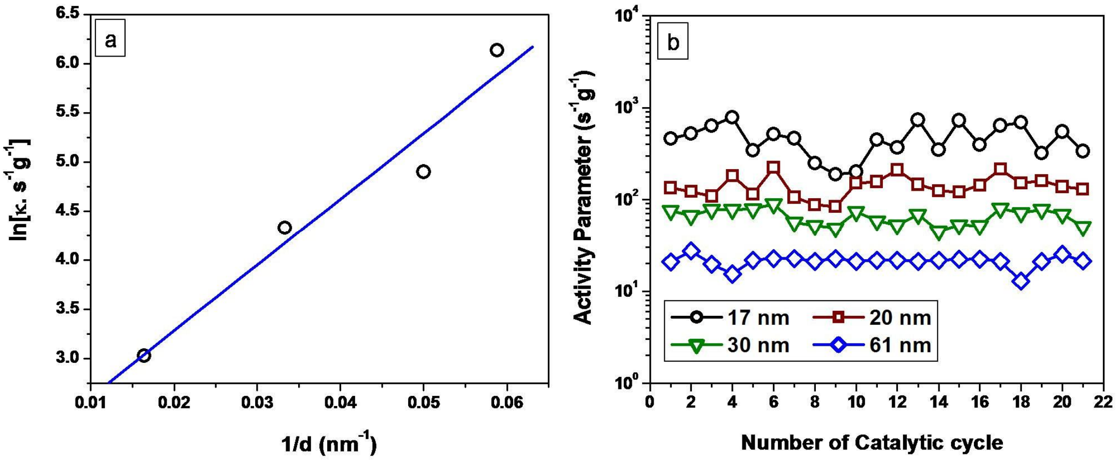

Figure 7.13. The plot of logarithm of activity parameter with inverse of diameter (a), and the variation of activity parameter ($s^{-1}g^{-1}$) with number of catalytic cycles for four different catalyst membranes (b).

3.4. Comparison of the Catalytic Activity of Spatially Confined Silver Nanoparticles with Unconfined Silver Nanoparticles

Comparison of the catalytic activity of the present nanoreactors (Ag@XAD-4 and Ag@AEM) with silver nanoparticles of nearly identical dimensions and similar surface property (same capping material) in aqueous solution shows that the activity parameter (κ) obtained using the present catalysts are significantly higher (see Table 7.1). The order of magnitude enhanced activity ($s^{-1}g^{-1}$) of confined nanoparticles shows that there is additional factor other than the effect of capping agent or the effect of particle sizes/concentration that are involved in accelerating the reaction rate. A plausible cause can be nanoconfinement effect, which accelerates the reaction kinetics. Appreciable enhancement of catalytic activity ($s^{-1}g^{-1}$) for BH_4^- reduction of para nitrophenol using solid mesoporous materials confined silver nanoparticles (citrate capped) has also been observed by Naik et al [2011, 2012]. Though the authors have not mentioned, the results show possible effect of nanoconfinement in enhancing the reaction rate constant in their case also.

Table 7.1. Comparison of rate constant (*k*) and activity parameter (κ) of different AgNPs catalysts during reduction of PNP with $NaBH_4$ at room temperature.

Spherical Nanoparticles (NPs)		Capping agent	d (nm)	k (s^{-1})	κ (s^{-1} g^{-1})	ref
Un-confined NPs	AgNPs	Citrate	10	3.64×10^{-4}	0.09	Rashid and Mandal 2007
	AgNPs	Oleylamine	9.6 11.3	2.1×10^{-3} 1.6×10^{-3}	2.00 1.52	Liu et al. 2013
Confined NPs	AgNPs confined in SBA-15	Citrate	7	1.77×10^{-3}	^{a}39.40	Naik et al. 2011
	AgNPs confined in γ-Al_2O_3	Citrate	10	5.00×10^{-3}	^{a}166.67	Naik et al. 2012
	AgNPs confined in XAD-4	Ethylene glycol	40	13.9×10^{-3}	^{a}974.07	Present work
	AgNPs confined in AEM	Citrate	17 20 30 61	9.42×10^{-3} 5.16×10^{-3} 8.32×10^{-3} 5.16×10^{-3}	^{a}460.50 ^{a}134.52 ^{a}75.97 ^{a}20.74	

[a]rate constant per unit mass of silver only. d = average diameter of nanoparticles.

3.5. Possible Origin of the "Lag Phase"

The occurrence of a lag phase in the metal nanoparticles catalyzed redox reaction has been observed by many researchers [Gangula et al. 2011.; Pozun et al. 2013.; Vidhu and Philip 2014.; Suvith and Philip 2014]. However, a clear understanding has not emerged. A possible explanation has been given by Pradhan et al. [2002] and Ray et al. [2013] in terms of passivation of metal nanoparticles in aqueous environment, which reduces their catalytic activity. On addition of BH_4^-, the nanoparticles are depassivated, restoring their catalytic activity. The lag time has been attributed to the depassivation phase, when no reduction occurs. After the lag time, the catalytic reduction takes place, increasing the rate of disappearance of substrate in the bulk solution. They have shown that, with increase in the catalyst concentration, such lag phase is reduced. Zhou et al. [2010] explained the origin of such lag phase due to surface restructuring of metal nanoparticles. In the present work, both the effect of passivation as discussed by Pradhan et al. [2002] and Ray et al. [2013], effect of surface restructuring as discussed by Zhou et al. [2010] and the diffusion of reactants (both MB and BH_4^-) into the membrane/resin beads may considerably influence the reaction kinetics. The Ag@Nafion catalyst consists of fixed anionic charge sites, and it will expel the negatively charged BH_4^- ions by Donnan exclusion. So the catalytic reduction is expected to occur largely on the membrane surface. Since the metal particles on the membrane surface are exposed to atmosphere, their surfaces will be passivated which leads to the appearance of a lag phase. In presence of borohydride, the catalytic activity of the nanoparticles is slowly restored, and the catalytic reduction of the organic substrate on the membrane surface starts, which leads to the rapid increase in the slope of ln (A_t/A_0) vs. t plot. However, for Ag@XAD and Ag@AEM catalysts, the diffusion of the reactants is also a considerable factor in addition to passivation.

3.6. Catalytic Activity of XAD-4 Beads and AEM without Metal Nanoparticles: Evidence of Pure Nanoconfinement Effect

The synthesis of silver nanoparticles in the pores of commercially available ion-exchange membranes (Chapter 5) and XAD-4 resins (Chapter 6), as well as in tailor made pore filled AEM (in the present Chapter) clearly shows the reactions are driven by nanoconfinement effect as they do not occur in the bulk solution. Similarly, enhanced catalytic activity of XAD beads and AEM hosted silver nanoparticles relative to bare nanoparticles in solution also points to the possible effect of nanoconfinement. In order to support this observation, experiments have been carried out with blank XAD-4 beads and blank AEM for the borohydride reduction of PNP. Figure 7.14 shows the in-situ time resolved UV-Vis spectrophotometric data for reduction of PNP in presence of blank XAD-4 resin beads and blank AEM. The successive decrease in the absorption peak at 400 nm (due to para nitrophenolate anion) and appearance of a new peak at 300 nm (para aminophenolate anion) confirms the occurrence of the reduction reaction without any AgNPs.

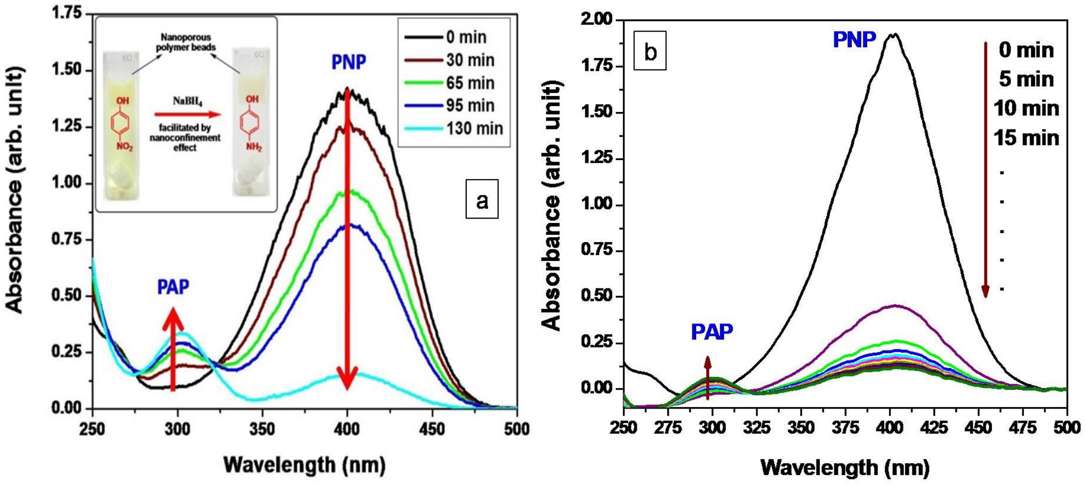

Figure 7.14. Time resolved UV-Vis absorption spectra during the room temperature BH_4^- reduction of para nitrophenol (PNP) to para aminophenol (PAP) in presence of blank nanoporous XAD-4 beads (a) and blank AEM (b) without nanoparticles. Inset in Figure 7.14a shows the digital photograph of the cuvette at start (yellow solution of PNP) and at end (colourless solution of PAP) of the reaction.

Similar spectrophotometric result for the control experiment (in absence of blank AEM or XAD beads) can be seen in Figure 7.15. The figure shows there is negligible change in the absorption spectrum even after 48 hr, indicating absence of reduction in the bulk.

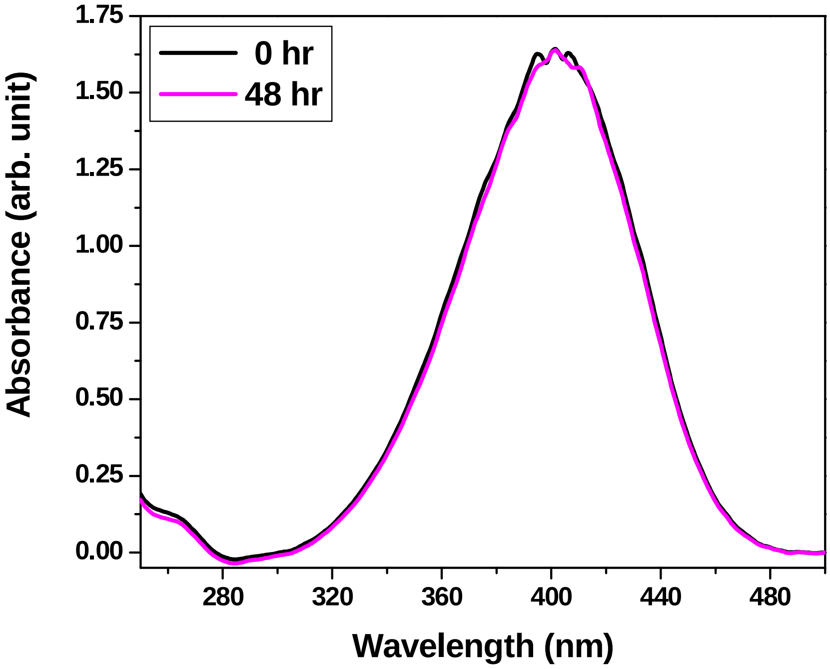

Figure 7.15. The UV-Vis absorption spectra of PNP in solution containing excess of $NaBH_4$ at different time period.

This is the first report showing the room temperature borohydride reduction of para nitrophenol taking place by only imposing spatial confinement of the reactants in the nanodomains of the resin/membrane. However, the rate of reduction is slower than the nanoparticle loaded resin/membrane. The synergy of catalytic effect of nanoparticles as well as nanoconfinement may be responsible for the exceptionally high activity parameters ($s^{-1}g^{-1}$). However, it is difficult to disentangle the two effects.

4. Conclusions

The rate of catalytic reaction using silver nanoparticles as catalyst has been found to be significantly enhanced in nanoconfined environment in comparison to the unconfined case. This is attributed to nanoconfinement effect in metal nanoparticle catalyzed reaction in the host matrices having nanoscale domain where reaction can take place. The AEM confined silver nanoparticles have been found to be highly reusable (tested upto 21st catalytic cycle). The effect of nanoconfinement in facilitating chemical reaction is clearly manifested in the PNP reduction by BH_4^- in presence of nanoporous XAD-4 resin beads and AEM without any catalyst.

Chapter 8

Effect of Nanoscale confinement on Chemical Reactions: Entropic Origin of Nanoconfinement Effect

Molecules in Jail

1. Introduction

As described in the previous chapters, materials confined at the atomic scale exhibit unusual properties due to nanoconfinement effect. Study of chemical reactions in nanoscale spatial confinement has thus been a fascinating topic of research in recent years. Spatial confinement at nanoscale can be visualized as the division of a given volume into many small compartments of molecular dimensions by adiabatic walls. On spatial confinement the reaction equilibrium switches to microcanonical ensemble situation from the classical canonical ensemble situation, as a reaction occurring in bulk solution. Though there is a lack of clear understanding, several explanations has been put forward in the literature for the nanoconfinement effect on chemical reactions equilibrium. These include surface effect, change in solvent structure in nanodomain, pore size selectivity, increased density inside pore due to higher pressure, reactant product reduced mixing, system size dependent entropy variation etc [Turner et al. 2001.; Turner et al. 2002.; Thomas et al. 2003.; Santiso et al. 2005.; Shon and Cohen 2012.; Polak and Rubinovich 2008.; Polak and Rubinovich 2011.; Rubinovich and Polak 2013.; Nielsen et al. 2010.; Thompson 2002.; Li and Thompson 2005.; Hill 2001]. In Chapter 5 and 6, it is demonstrated that nanoconfinement in commercial ion-exchange membranes and neutral XAD-4 resin beads significantly favours various types of redox reactions, which includes synthesis of inorganic nanoparticles under mild conditions. Lorenz et al. [2014] have also reported the electron transfer rate enhancement during reduction of $[Co(dipic)_2]^-$ (dipic = dipicolinato) complexes with ascorbic acid in a nanoscale reverse micellar waterpool. Many organic reactions like borohydride reduction of esters, organic coupling reactions, degradation of phenol have been found to be facilitated in reverse micelles, and in organic supramolecules having nanocavities [Das et al. 2004.; Padma et al. 2013.; Zhao et al. 2010.; Masson et al. 2012.; Assaf and Nau 2015]. It is of general interest to explore different types of reaction, driven by nanoconfinement. Relatively fewer inorganic redox reactions have been studied so far under nanoconfinement conditions and there is a need of detail investigation on the effect of confinement on metal nanoparticles catalyzed redox reactions.

The results in Chapter 7 shows that the concept of nanoreactor goes beyond the host-guest chemistry as observed in the cavities of dendrimers/curcubit or size selective zeolites. The observation of the special effect at nanoconfinement (as demonstrated in Chapter 5, 6 and 7) show that the chemistry at the nanodomains of porous materials or polymers are not merely the surface effect as the results do not depend on whether the pore surface is neutral, positively charged (cation exchange membrane) or negatively charged (anion exchange membrane). Thomas et al. [2003] and Shon and Cohen [2012] performed excellent experiments to see the effect of occupancy of reactant molecules in the nanometer size pores under the condition when the pore dimension is less than the average separation distance between the reactant molecules in the bulk. Effect of pore surface on the outcome of the reaction has been carefully eliminated in their experiments. It has been shown by Thomas et al. [2003] that the dimerization of pyrene takes place only when the pore occupancy exceeds a threshold value when there is a finite probability of at least two pyrene molecules being present in a pore. This requires a concentration in the bulk solution greater than a threshold value. Similarly Shon and Cohen [2012] has shown that the dimerization of single-stranded DNA (ssDNA) is favoured inside the dimples on a substrate and the thermodynamic equilibrium condition is not obeyed due to fluctuation in the population when only a few molecules occupy the dimples. They attributed it to the fact that, the local concentration of reactant molecules in the occupied pores are very high, thereby affecting the equilibrium compared to that in the bulk. They have also shown that the rate is also increased due to the higher local concentration in confinement. Polak and Rubinovich attributed this nanoconfinement effect as being due to reduced mixing of the reactant and product state [Polak and Rubinovich 2008.; Polak and Rubinovich 2011.; Rubinovich and Polak 2013].

In the present work, effect of pore occupancy on the catalytic reduction rate of PNP under nanoconfinement condition has been studied. Pore occupancy has been varied by varying the bulk reactant concentration. Silver nanoparticles loaded XAD-4 nanoporous beads have been used as catalyst. Taking cue from the published theoretical work, the dependence of rate constant on the concentration of bulk solution under the condition of single molecule occupancy in the pores has been attributed to entropic effect.

2. Experimental

2.1. Materials and Reagents

Silver nanoparticles loaded XAD-4 beads were used as catalytic nanoreactor in the present study. The preparation of silver nanoparticles in the nanoporous host XAD-4 resins by citrate reduction method was discussed in Chapter 5. Para nitrophenol and sodium borohydride were purchased from Sigma Aldrich.

2.2. Catalytic Study

The effect of average pore occupancy of the reactant molecules (PNP) on the rate of catalysis using Ag@XAD-4 catalytic nanoreactor was studied by varying the bulk PNP concentration. Kinetic measurements were done taking 50, 75, 100, 125, 150, 175, and 200 μl of PNP solution (2 mM) in a cell followed by addition of deionised water upto a total volume of 1.8 mL. 0.2 g of Ag@XAD beads were added in each case. Finally 200 μl of freshly prepared $NaBH_4$ solution (0.1 mol L^{-1}) was added into the cell. Control experiments were also performed using unconfined AgNPs as catalyst for the same reaction under varying bulk reactant concentration. For this purpose, two types of AgNPs were synthesised by borohydride reduction of silver salt using PVP and SDS independently as stabilizers. The synthesis was accomplished as follows:

(i) PVP stabilized AgNPs: 5 mg of $AgNO_3$ salt and 0.5 g of polyvinylpyrolidone (PVP) were dissolved in 70 mL water. The mixture was kept in stirring condition at ice cold temperature. A freshly prepared solution of sodium borohydride (0.1 mol L^{-1}) was added drop by drop into the reaction mixture and stirring was continued for 1 hour. The reduction of all the Ag^+ ions was ensured by adding excess of $NaBH_4$ solution into the reaction mixture.

(ii) SDS stabilized AgNPs: The synthesis of SDS stabilized silver nanoparticles was accomplished following a procedure given by Song et al. [2009]. In brief, 50 mL of 0.001 mol L^{-1} $AgNO_3$ solution was prepared by dissolving the required amount of $AgNO_3$ in distilled water. Aqueous solution of sodium borohydride ($NaBH_4$) with concentration of 0.004 moles L^{-1} was also prepared by dissolving $NaBH_4$ and SDS in 50 ml distilled water for half an hour together in ice cold temperature. The SDS/$AgNO_3$ weight ratio of 20 was fixed. Silver nanoparticles were synthesized by adding the $AgNO_3$ solution drop wise into the $NaBH_4$ solution with SDS slowly. After complete addition, the mixed solutions were stirred for 1 hour more in ice cold condition.

The nanoparticles of both types had strong surface plasmon absorption at ~400 nm (Figure 8.1). The SDS stabilized and PVP stabilized nanoparticles were characterized independently using dynamic light scattering technique and were found to have an average diameter of 23.7 nm and 25 nm respectively. The particle size distribution as obtained from DLS study is given in Figure 8.2.

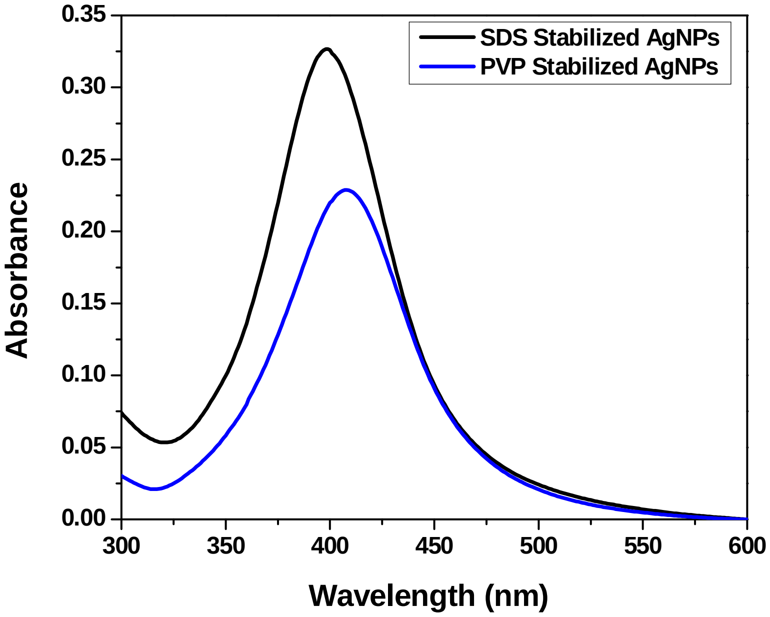

Figure 8.1. UV-VIS absorption spectrum of SDS and PVP stabilized unconfined silver nanoparticles prepared by BH_4^- reduction.

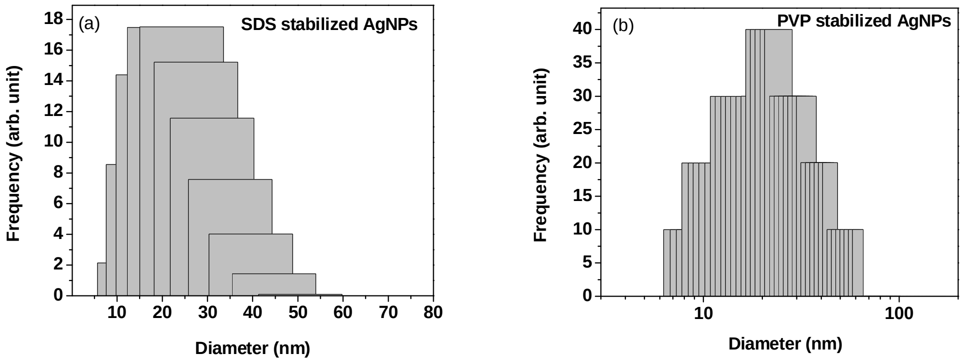

Figure 8.2. Size distribution of SDS stabilized (a) and PVP stabilized (b) unconfined silver nanoparticles prepared by BH_4^- reduction as obtained from DLS study.

For the catalysis experiments, 50, 75, 100, 150, 200 μl of PNP solution (2 mM) were taken in a cell followed by addition of deionised water upto a total volume of 2 mL. 200 μl of freshly prepared $NaBH_4$ solution (0.1 mol L^{-1}) was added into the cell. Finally 100 μl of AgNPs solution was added into the cell. The kinetic measurements were carried out using a UV-VIS spectrometer.

3. Results and Discussion

Figure 8.3 shows the FE-SEM image of the Ag@XAD nanoreactor. It can be seen that spherical silver nanoparticles are positioned near the nanoscale pores/crevices of the resin bead. The average pore diameter in XAD-4 beads is 10 nm (assuming spherical pore for simplicity). Bulk concentration has been varied to reach the average occupancy much less than one (assuming ideal compartmentalization when pores are not connected). For example, we consider the bulk solution is 0.1 millimoles L^{-1} with respect to PNP. Assuming the pores of the XAD-4 beads are filled with same concentration of PNP solution, a typical spherical pore of diameter 10 nm can accommodate on the average only 0.031 PNP molecules, which essentially means in real sense that on the average 100 pores are occupied by 3 PNP molecules, keeping the rest of the pores empty. Because of statistical distributions, out of 100 equivalent pores, one single pore may contain all the three molecules (least probability), or two molecules (moderate probability), or one molecule (high probability) or no molecules (highest probability). Thus the effective concentration of the reactant molecule in the occupied pore (nanoconfined subvolume) is much higher in comparison to its bulk concentration.

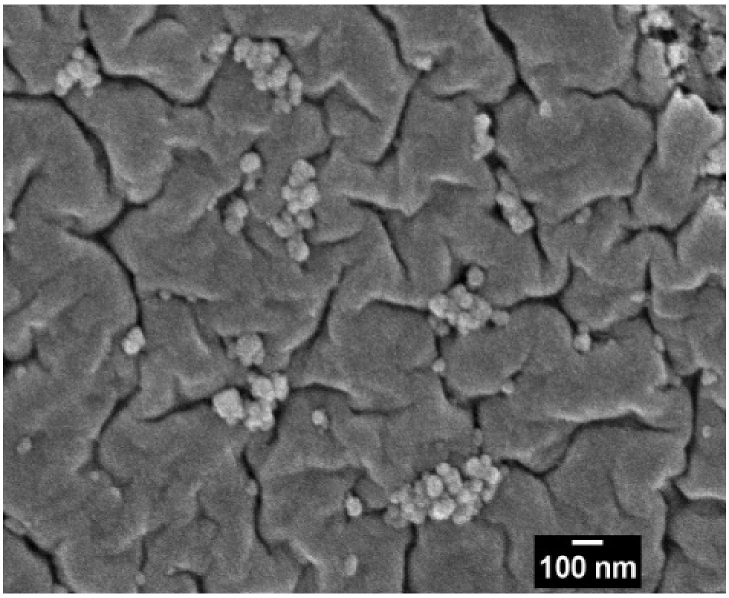

Figure 8.3. FESEM image of the Ag@XAD nanoreactor. White spots represents silver nanoparticles.

Figure 8.4 gives the dependence of the reduction rate on the bulk PNP concentration for silver nanoparticle catalysed PNP reduction in the nanopores of XAD-4 beads. The slope of the falling part of the curves gradually decreases with increasing PNP concentration, showing slower reaction rate. Figure 8.5 shows the variation of normalized rate constant as a function of bulk reactant (PNP) concentration using both unconfined and confined AgNPs as catalyst. For the case of confined nanoparticles catalyst (Ag@XAD-4 beads), the respective average pore occupancy of PNP molecules is given in inset.

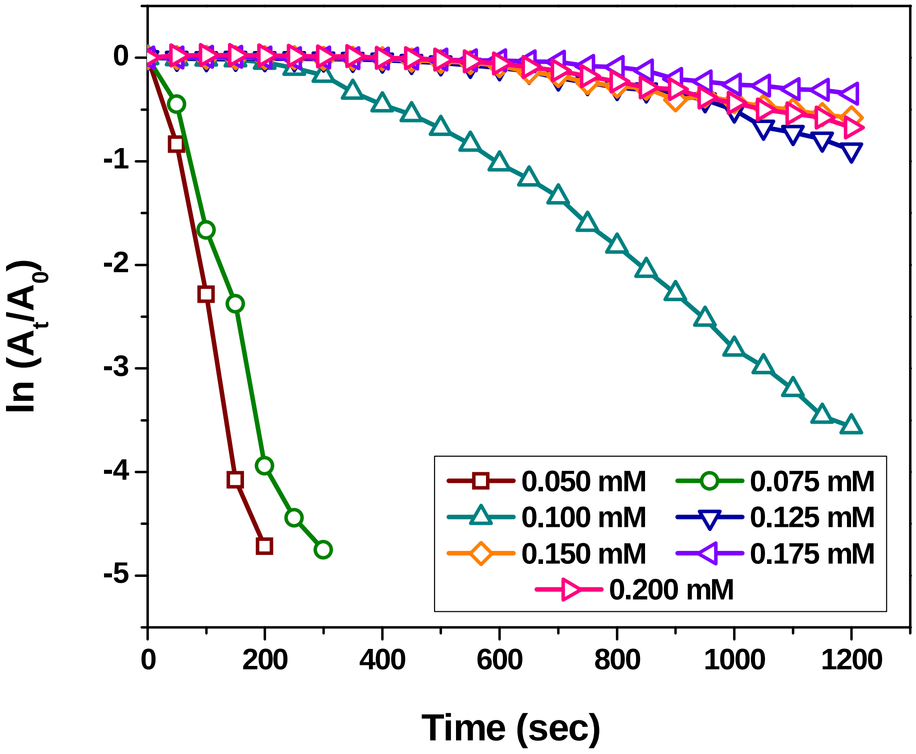

Figure 8.4. Variation of logarithm of (A_t/A_0) with time at λ = 400 nm during catalytic reduction of para nitrophenol (PNP) with variable initial concentration of PNP using AgNPs@XAD-4 catalyst. Solid lines connecting the points are eye guide.

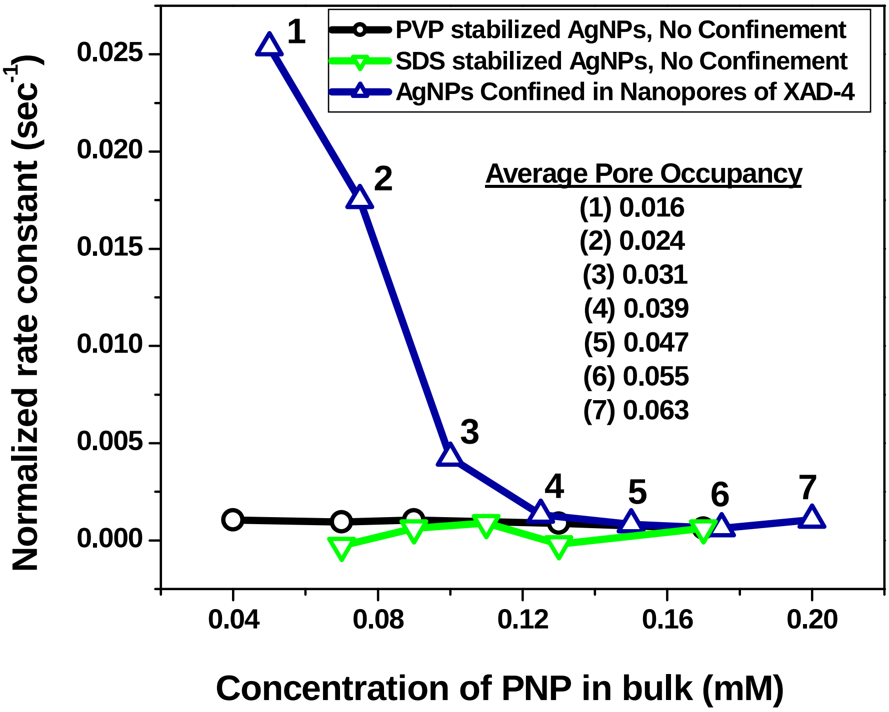

Figure 8.5. Variation of normalized rate constant (sec^{-1}) with bulk PNP concentration (mM) during room temperature BH_4^- reduction of PNP using PVP and SDS stabilized bare AgNPs (control experiment) and spatially confined AgNPs in XAD-4 beads as catalyst. Solid lines connecting the points are eye guide.

It can be clearly seen that the rate of reaction rapidly falls with increase in the average number of reactant molecules per pore (average pore occupancy) before a plateau is reached. Since the silver nanoparticles are deposited on the pore surfaces, the situation is similar to heterogeneous catalysis. Thus the role of surface interaction on the rate constant cannot be ruled out. However, as the results show, the effect of pore occupancy by reactant molecules clearly influence the reaction rate constant significantly, the effect being more prominent when the average pore occupancy decreases. This can be attributed to the fact that at lower value of average pore occupancy the average distance between the reactant molecules are so large in the porous network that the occupancy of a pore doesn't increase during the chemical reaction due to molecular diffusion of reactants from neighbouring pores, i.e the condition of "single molecule" experiment (perfect compartmentalization) is achieved. Therefore if we consider only one molecule in a pore, the system contains either reactant or product molecule at a particular time (assuming no supply of reactant molecules from the interconnected pore). In such a situation, equilibrium is highly shifted toward the product side because of absence of reactant product mixed microstate [Polak and Rubinovich 2008]. This essentially enhances the rate constant for the reaction. At higher reactant concentration, each pore will contain larger number of reactant molecules, thereby making the situation similar to that exists in bulk when both reactant and product molecules are homogeneously distributed. The decrease in rate constant with increase in bulk reactant concentration cannot be explained as being due to the saturation of active sites of the nanoparticles at higher reactant concentration as the range of working concentration in the present work is too low (maximum average pore occupancy = 0.063) to saturate the active sites of nanoparticles.

This has been further confirmed by the results of control experiments (unconfined AgNPs catalysis). The average diameter of the SDS and PVP stabilized nanoparticles as prepared in the present work are 23.7 nm and 25 nm respectively as obtained from DLS study (Figure 8.2). The nanoparticles concentration has been kept constant during the study. The rate constants as obtained from the control experiments (unconfined nanoparticles) as a function of different PNP concentration have been normalized with the rate constant of confined nanoparticles at higher PNP concentration and plotted in Figure 8.5. The normalized rate constants as obtained from the control experiments are found to be independent of PNP concentration. This clearly shows the effect of compartmentalisation and the pore occupancy on the reaction kinetics, which can be considered as distinct nanoconfinement effect on reaction rate.

4. Conclusions

Silver nanoparticles catalyzed room temperature borohydride reduction of para nitrophenol (PNP) has been used as a model reaction to study the influence of spatial confinement on a redox chemical reaction. Silver nanoparticles hosted in nanoporous XAD-4 resin beads have been used as nanoreactor. Although the confinement conditions were not ideal (perfect adiabatic separation of individual species) in the present system due to the presence of interconnecting slit pores, it could be shown that the kinetics of catalytic reduction is altered by the spatial confinement in XAD bead, which, in addition, depends strongly on the pore occupancy. When the pore volume is smaller than the mean volume per molecule in bulk, the condition of single molecular occupancy reaches and the effective concentration of the molecules in the occupied pores become very high. At lower bulk concenration of PNP molecules, the average separation distance between two PNP molecules exceeds the pore dimension and the condition for “single molecule” experiment is achieved in the pores. This shifts the equilibrium towards product side due to reduced molecular mixing of reactant and product state, resulting in remarkably high rate constant (s^{-1})/activity parameter ($s^{-1}g^{-1}$).

Chapter 9

Summary and future scopes

The work presented in this thesis has been aimed at exploring some novel routes for the synthesis of noble metal nanoparticles in solid polymer matrices, understanding their mechanism of formation and catalytic activity. Ion-exchange membranes and neutral polymeric resins have mostly been used as the host matrices for nanoparticle synthesis. The synthesis of nanoparticles has been accomplished by two approaches: (i) the direct in-situ reduction of metal ions in the polymeric host and (ii) nanoconfinement driven reduction of metal ions in the polymeric host. Advanced characterization techniques like small angle X-ray scattering (SAXS) and electron microscopy have been frequently used for the study of nanoparticle morphology as well as their time resolved formation and growth. ^{110m}Ag radiotracer has been employed as a marker for obtaining the time resolved information on the formation of silver nanoparticles in different membranes for the first time. Special emphasis has been given on understanding the role of nanoscale confinement of the host matrices on facilitating the chemistry of nanoparticle synthesis as well as the chemistry of nanoparticles mediated catalysis. Experiments have been carried out to investigate the possible origin of the so called “Nanoconfinement Effect” and have been explained in terms of reduced molecular mixing of the reactant and product states. The study sought to get answer of some of the fundamental questions like, (i) how to control the size and shape of metal nanoparticles stabilized in polymer matrices? (ii) how metal nanoparticles can be chemically impregnated into nanoporous polymer matrices at ambient condition irrespective of the chemical nature of the matrix, and (iii) how such nanoporous polymer-metal nanoparticles composites can acts as catalytic nanoreactor with enhanced activity.

1. Summary of the Present Study and Major Conclusions

The present investigation has been focused on three aspects : (i) Chemical synthesis of noble metal nanoparticles in polymer matrices, (ii) mechanism of formation of the metal nanoparticles in polymer matrices, and (iii) catalytic applications of the metal nanoparticles hosted in polymer matrices. The major findings of the individual parts as obtained from the entire study have been summarized below.

(i) Chemical Synthesis of Metal Nanoparticles in Polymer Matrices: The present thesis describes the chemical synthesis of noble metal nanoparticles (mostly silver) in ion-exchange membranes and neutral resins. It has been observed that the local environment in the membranes changes depending upon the nature of the reducing agents, temperature as well as extent of the loading of silver ions. This in turn dictates the final size and shape of the nanoparticles formed. During formamide reduction the host membrane Nafion 117 loses its water cluster network due to high degree of swelling. In this reduction, spherical nanoparticles have been formed uniformly throughout the matrix. The size of the nanoparticles has been varied by varying the temperature. However, ascorbic acid reduction, where the membrane morphology remains unaffected, produces silver nanoparticles with various size and shapes such as nanorods, nanosponge and nanoclusters depending upon the extent of loading of silver ions in the membrane.

Apart from the direct reduction routes, another new approach has been adopted for the first time for metal nanoparticle synthesis in polymer matrices. This involves nanoconfinement driven reduction of metal ions selectively in the pores or confined nanodomains of the polymer matrices under ambient condition, when the identical reaction doesn’t occurs at bulk. Based on this approach, two novel methods have been developed for the synthesis of nanoparticles. The first one involves the synthesis of silver nanoparticles in the nanoscale confinement of ion-exchange membranes, neutral resins as well as in mesoporous silica gel particles by nanoconfinement driven redox decomposition of highly stable silver citrate complex. The second method describes the room temperature polyol reduction of noble metal ions (silver, gold, and platinum) in the nanoscale confinement of neutral polystyrene resin beads, which otherwise requires refluxing condition in bulk. The methods of nanoparticle synthesis developed in the present study are unique in a sense that they can be applied for the synthesis of metal nanoparticles in any matrices having nanoscale morphology, irrespective of its chemical nature. This is the first report showing the excellent role of nanoconfinement in facilitating the chemistry of nanoparticle synthesis, which otherwise doesn't takes place at bulk or may require vigorous reaction conditions.

(ii) Mechanism of Formation of Metal Nanoparticles in Polymer Matrices: Time resolved small angle X-ray scattering (SAXS) technique has been used as the primary tool for the mechanistic investigation on the growth of nanoparticles in polymer matrices. Synchrotron based X-ray source has been used for fast time scale measurements (milliseconds time resolution). Laboratory based X-ray source have been used for the reactions which are slow. The results obtained from the analysis of SAXS data has always been supplemented by the results of electron microscopy (TEM/FE-SEM). However, due to better statistics, results of SAXS analysis have exclusively been used to elucidate the mechanism. ^{110m}Ag radiotracer has also been used to obtain the information of time resolved accumulation of silver nanoparticles in the membrane (mg cm^{-2}). Ag/Ag^{+} ratio in the membrane at any given period of reduction has also been obtained by this technique. Mechanism of formation of silver nanoparticles in polymer matrices by direct reduction route using L-ascorbic acid as reductant as well as by nanoconfinement driven reduction using tri-sodium citrate have been studied.

The mechanism of formation of silver nanoparticles (~3 nm) by direct reduction of silver ions by L-ascorbic acid in the water clusters of Nafion membranes has been found to be a three stages process. These include a rapid initial growth in size followed by a saturation of size of the nanoparticles, and a further slow increase in nanoparticles size. The mechanism of nanoparticle growth in case of nanoconfinement driven redox decomposition of silver citrate complex in anion exchange membrane Selemion AMV and in cation exchange membrane Nafion 117 has been explored using laboratory based SAXS experiments. The growth mechanism has been explained in terms of both autocatalytic reductions of Ag^+ ions on the nanoparticles surface by thermal oxidation of citrate and the interparticle coalescence at a critical number density. Similar time resolved SAXS measurements, carried out during the synthesis of silver nanoparticle in a tailormade pore filled anion exchange membrane (AEM), have been used to tune the size of the nanoparticles by controlling the time of reduction.

(iii) Catalytic Applications of the Metal Nanoparticles Hosted in Polymer Matrices: The last part of the thesis discusses possible catalytic applications of the metal polymer hybrid nanoreactors formed by stabilizing silver nanoparticles in nanoporous polymer matrices. The study is focused on the effect of confinement on the catalysis. Two different redox reactions: (i) BH_4^- reduction of methylene blue (MB), and (ii) BH_4^- reduction of para nitrophenol (PNP) have been used as model reactions for the study of catalysis. The catalytic nanoreactors have been found to show significantly higher catalytic activity in comparison to unconfined silver nanoparticles of identical dimensions and similar surface properties, which shows a distinct nanoconfinement effect.

Attempt has been made to explore the possible origin of enhancement of the rate of catalytic reaction using spatially confined silver nanoparticles. The results of experiments with variable average pore occupancy of the reactant molecules show that the catalytic rate constant is highly occupancy dependent, when the average reactant occupancy per pore is much less than one. This has been attributed as single molecular event, which shifts the equilibrium to the product side due to reduced molecular mixing of the reactant and product states, which essentially accelerate the kinetics.

2. Future Scopes

Though enough literature exists on the synthesis, mechanism of formation and catalytic applications of metal nanoparticles of various aspect ratios in solution, the issues have been only occasionally touched for the polymer hosted metal nanoparticles. For metal nanoparticles synthesis in polymer membranes or resins, the understanding of the fundamental parameters on the nanoparticle growth process has remained a black box. The present thesis opens up a new avenue of future nanochemistry research. As discussed earlier, the subject of the present research is in its very early developmental stage in terms of understanding and knowledge. Future studies may include development of route of synthesis of other metal nanoparticles using the advantage of nanoconfinement effect. The nucleation stages during nanoparticle growth in polymer matrices can be explored with SAXS experiments with still better time resolution, which will provide better control over size and shape of the metal nanoparticles. Further work may be carried out on the catalytic nanoreactors for many other types of reactions.

Bibliography

A

Aiken, J.D., III; Lin, Y.; Finke, R.G. *J. Mol. Catal. A: Chem.***1996**, *114*, 29-51.

Alonso, A.; Shafir, A.; Macanas, J.; Vallribera, A.; Munoz, M.; Muraviev, D.N. *Catalysis Today* **2012**, *193*, 200– 206.

Amano, C.; Niina, H.; Mikami, Y. *J. Mol. Struct.: THEOCHEM* **2009**, *904*, 64-68.

Amiens, C.; De Caro, D.; Chaudret, B.; Bradley, J. S.; Mazel, R.; Roucau, C. *J. Am. Chem. Soc.* **1993**, *115*, 11638-11939.

Arnikar, H.J. Isotopes in the Atomic Age, Wiley, New York, **1989.**

Assaf, K.I.; Nau, W.M. Chem. Soc. Rev., **2015**, *44*, 394-418.

Ayyappan, S.; Subbanna, G.N.; Gopalan, R.S.; Rao, C.N.R. *Solid State Ionics* **1996**, *84*, 271-281.

B

Ball, P. *Nature* **2000**, *408*, 904.

Baruah, B.; Gabriel, G. J.; Akbashev, M. J.; Booher, M. E. *Langmuir* **2013**, *29*, 4225−4234.

Beers, K.M.; HallinanJr, D.T.; Wang, X.; Pople, J.A.; Balsara, N.P. *Macromolecules* **2011**, *44*, 8866-8870.

Behrens, S.; Unger, E.; Wu, J.; Habicht, W.; Dinjus, E. *MRS Online Proc. Libr.* **2004**, *818*, null−null.

Berne, B.J.; Pecora, R. Dynamic Light Scattering: With Applications to Chemistry, Biology, and Physics, Dover Publications; Unabridged edition, August, **2000**, ISBN-13: 978-0486411552.

Buffet, A.; Rothkirch, A.; Dohrmann, R.; Korstgens, V.; Kashem, M.M.A.; Perlich, J.; Herzog, G.; Schwartzkopf, M.; Gehrke, R.; Muller-Buschbaum, P.; Roth, S.V.; *J. Synchr. Radiation.* **2012**, *19*, 647-653.

C

Cademartiri, L.; Ozin, G.A. Concepts of Nanochemistry, Copyright © **2009** WILEY-VCH Verlag GmbH & Co. KGaA, Weinheim ISBN: 978-3-527-32626-6.

Campi, G.; Mari, A.; Amenitsch, H.; Pifferi, A.; Cannas, C.; Suber, L. *Nanoscale* **2010**, *2*, 2447-2455.

Campi, G.; Pifferi, A.; Mari, A.; Amenitsch, H.; Cannas, C.; Suber, L. *J. Nanopart. Res.* **2011**, *13*, 3107-3112.

Cha, D.Y, Parravano, G. *J. Catal.* **1970**, *18*, 200–211.

Chamberlain, T.W.; Earley, J.H.; Anderson, D.P.; Khlobystov, A.N.; Bourne, R.A. *Chem. Commun.* **2014**, *50*, 5200-5202.

Chekin, F.; Ghasemi, S. *Bull. Mater. Sci.* **2014**, *37*, 1433–1437.

Chen, C.; Wang, L.; Yu, H.; Jiang, G.; Yang, Q.; Zhoua, J.; Xiang, W.; Zhang, *J. Materials Chemistry and Physics*, **2008**, *107*, 13–17.

Chen, S.; Kimura, K. *J. Phys. Chem. B* **2001**, *105*, 5397-5403.

Chen, W.; Pan, X.; Bao, X. *J. Am. Chem. Soc.* **2007**, *129*, 7421-7426.

Chen, X.; Schröder, J.; Hauschild, S.; Rosenfeldt, S.; Dulle, M.; Förster, S. *Langmuir* **2015**, *31*, 11678−11691.

Chen, Y.; Wang, Q.; Wang, T. *Dalton Trans.*, **2013**, *42*, 13940–13947.

Chen, W.; Fan, Z.; Pan, X.; Bao, X. *J. Am. Chem. Soc.* **2008**, *130*, 9414-9419.

Cho, S.J.; Suri, A.; Mei, X.; Ouyang. J.; *RSC Adv*., **2013**, *3*, 1201–1209.

Clinton, W.J. Remarks at the California Institute of Technology, Public Papers, January 1-June 26, p. 96, **2000**.

Colby, R.; Hulleman, J.; Padalkar, S.; Rochet, J. C.; Stanciu, L. A. *J. Nanosci. Nanotechnol.* **2008**, *8*, 973−978.

Corma, A.; Garcia, H. *Chem. Soc. Rev*. **2008**, *37*, 2096-2126.

Cotanda, P.; Petzetakis, N.; O'Reilly, R.K. *MRS Communications* **2012**, *2*, 119-126.

D

Das, D.; Roy, S.; Das, P.K. *Org. Lett.*, **2004**, *6*, 4133-4136.

Dassenoy, F.; Philippot, K.; Ould Ely, T.; Amiens, C.; Lecante, P.; Snoeck, E.; Mosset, A.; Casanove, M. J.; Chaudret, B. *New J. Chem.* **1998**, *22*, 703-712.

Díaz, D.J.; Bohn, P.W. "Nanochemistry." Chemistry: Foundations and Applications. **2004**. Encyclopedia.com. 20 Jul. 2015 <http://www.encyclopedia.com>.

Djokic, S. Hindawi Publishing Corporation. *Bioinorg. Chem. Appl.* **2008**, 436458 (7 pages) doi:10.1155/2008/436458.

Domenech, B.; Munoz, M.; Muraviev, D.N.; Macanas, *J. Chem. Commun*., **2014**, *50*, 4693-4695.

Dong, X.; Ji, X.; Wu, H.; Zhao, L.; Li, J.; Yang, W. *J. Phys. Chem. C.* **2009,** *113,* 6573–6576.

Duan, J.L.; Cornelius, T.W.; Liu, J.; Karim, S.; Yao, H.J.; Picht, O.; Rauber, M.; Müller, S.; Neumann, R. *J. Phys. Chem. C* **2009**, *113*, 13583-13587.

Duteil, A.; Schmid, G.; Meyer-Zaika, W. *J. Chem. Soc., Chem.Commun*. **1995**, 31.

E

Elliott, J.A.; Wu, D.; Paddison, S.J.; Moore, R.B. *Soft Matter.* **2011**, *7*, 6820-6827.

Esumi, K., Miyamoto, K., Yoshimura, T. *J. Colloid Interface Sci.*, **2002**, *254*, 402-405.

Esumi, K.; Isono, R.; Yoshimura, T. *Langmuir* **2004**, *20*, 237–243.

Esumi, K.; Miyamoto, K.; Yoshimura, T. *J. Colloid Interface Sci.* **2002**, *254*, 402–405.

Evans, D.F.; Wennerstrom, H. The Colloidal Domain, 2nd ed.; Wiley-VCH: New York, **1999**.

F

Friedlander, G.; Kennedy, J.W.; Macius, E.S.; Miller, J.M. Nuclear and Radiochemistry, John Willey & Sons, Inc. **1981**.

Fu, Q-S.; Xue, Y-Q.; Cui, Z-X.; Wang, M-F. Hindawi Publishing Corporation, Journal of Nanomaterials, **2014**, Article ID 856489, 8 pages http://dx.doi.org/10.1155/2014/856489.

Fujimura, M.; Hashimoto, R.; Kawai, H. *Macromolecules* **1982**, *15*, 136-144.

Fujimura, M.; Hashimoto, T.; Kawai, H. *Macromolecules* **1981**, *14*, 1309-1315.

G

Galvagno, S.; Parravano, G. *J. Catal.* **1978**, *55*, 178–190.

Gangula, A.; Podila, R.; Ramakrishna, M.; Karanam, L.; Janardhana, C.; Rao, A.M. *Langmuir*, **2011**, *27*, 15268-15274.

Gao, F.; Weiland, L. M.; Kitchin. *J. Proc. SPIE* **2008**, *6929*, 69290M/69291−69290M/69296.

Gebel, G. *Polymer* **2000**, *41*, 5829-5838.

Gebel, G.; Moore, R.B. *Macromolecules* **2000**, *33*, 4850-4855.

Ghosh, S.K., Mandal, M., Kundu, S., Nath, S., Pal, T. *Appl. Catal., A*, **2004**, *268*, 61-66.

Ghosh, S.K.; Kundu, S.; Mandal, M.; Pal, T. *Langmuir* **2002**, *18*, 8756–8760.

Ghosh, S.K.; Mandal, M.; Kundu, S.; Nath, S.; Pal, T. *Appl. Catal. A* **2004**, *268*, 61–66.

Gierke, T.D.; Munn, G.E.; Wilson, F.C. *ACS Symposium Series* No. 180; American Chemical Society: Washington, DC, **1982**, 195-216.

Gierke, T.D.; Munn, G.E.; Wilson, F.C. *J. Polym. Sci., Polym. Phys.* **1981**, *19*, 1687-1704.

Giffin, G.A.; Lavina, S.; Pace, G.; Noto, V.D. *J. Phys. Chem. C* **2012**, *116*, 23965−23973.

Gilham, R.J.J.; Brown, R.J.C. The characterisation of nanoparticles, amc technical briefs, Analytical Methods Committee, AMCTB 48, December 2010, Royal Society of Chemistry **2010**, ISSN 1757- 5958.

Giovanetti, L.J.; Ramallo-López, J.M.; Foxe, M.; Jones, L.C.; Koebel, M.M.; Somorjai, G.A.; Craievich, A.F.; Salmeron, M.B.; Requejo, F.G. *Small* **2012**, *8*, 468–473.

Glatter, O.; Kratky, O. Small angle X-ray scattering, Academic press INC. (London) Ltd. **1982**.

Goettmanna, F.; Sanchez, C. *J. Mater. Chem.*, **2007**, *17*, 24–30.

Goldstein, J.; Newbury, D.E.; Joy, D.C.; Lyman, C.E.; Echlin, P.; Lifshin, E.; Sawyer, L.; Michael, J.R. Scanning Electron Microscopy and X-ray Microanalysis, Springer; 3rd Corrected ed. **2003**.

Goswami, A.; Acharya, A.; Pandey, A.K. *J. Phys. Chem. B.* **2001**,*105*, 9196-9201.

Guinier, A.; Fournet, G.; Walker, B. C.; Yudowith, L. K. *“Small Angle Scattering of X-Rays”* Wiley, New York. **1955**.

Guo, S.; Pan, X.; Gao, H.; Yang, Z.; Zhao, J.; Bao, X. *Chemistry* **2010**, *16*, 5379-5284.

H

Hall, S. R.; Collins, A. M.; Wood, N. J.; Ogasawara, W.; Morad, M.; Miedziak, P. J.; Sankar, M.; Knight, D. W.; Hutchings, G. J. *RSC Advances* **2012**, *2*, 2217−2220.

Hammer, B. *Top. Catal.* **2006**, *37*, 3−16.

Hammer, B.; Morikawa, Y.; Nørskov, J.K. *Phys. Rev. Lett.* **1996**, *76*, 2141− 2144.

Hammer, B.; Nørskov, J.K. *Nature* **1995**, *376*, 238−240.

Hammer, B.; Nørskov, J.K. *Surf. Sci.* **1995**, *343*, 211−220.

Hammer, B.; Nørskov, J.K. *Surf. Sci.* **1996**, *359*, 306.

Harada, M.; Tamura, N.; Takenaka, M. *J. Phys. Chem. C* **2011**, *115*, 14081–14092.

Harb, M.; Rabilloud, F.; Simon, D. *Phys. Chem. Chem. Phys.* **2010**, *12*, 4246-4254.

Haruta, M. *Catal. Today* **1997**, *36*, 153–166.

Haruta, M. *Faraday Discuss.* **2011**, *152*, 11–32.

Haruta, M.; Kobayashi, T.; Sano, H.; Yamada, N. *Chem. Lett.* **1987**, *16,* 405–406.

Haruta, M.; Yamada, N.; Kobayashi, T.; Iijima, S. *J. Catal.* **1989**, *115*, 301–309.

Hasegawa, T.; Strunskus, T.; Zaporotjenko, V.; Faupel, F.; Mizuhata, M. *ECS Transactions* **2012**, *41*, 9-18.

Haubold, H.-G.; Vad, Th.; Jungbluth, H.; Hiller, P. *Electrochim. Acta* **2001**, *46*, 1559-1563.

Hayakawa, K., Yoshimura, T., Esumi, K. *Langmuir*, **2003**, *19*, 5517-5521.

Heitner-Wirguin, C. *J. Memb. Sci.* **1996**, *120*, 1-33.

Henglein, A.; Giersig, M. *J. Phys. Chem. B.* **1999,** *103,* 9533-9539.

Hill, T. L. *Nano Lett.* **2001**,*1*, 273-275.

Hirano, L. A.; Escote, M. T.; Martins-Filho, L. S.; Mantovani, G. L.; Scuracchio, C. H. *Artificial Organs* **2011**, *35*, 478-483.

Hsu, W.Y.; Gierke, T.D. *J. Membr. Sci.* **1983**, *13*, 307-326.

Hsu, W.Y.; Gierke, T.D. *Macromolecules* **1982**, *15*, 101-105.

Hunter, R.J. Foundations of Colloid Science; Oxford University Press: New York, **1987**; Vol. 1, p 316.

I

Iwahori, K.; Yamashita, I. *J. Cluster Sci.* **2007**, *18*, 358−370.

J

Jana, N.R.; Gearheart, L.; Murphy, C.J. *J. Phys. Chem. B* **2001,** *105*, 4065-4067.

Jana, N.R.; Pal, T. *Langmuir* **1999**, *15*, 3458–3463.

Jana, N.R.; Sau, T.K.; Pal, T. *J. Phys. Chem. B* **1999**, *103*, 115–121.

Jana, N.R.; Wang, Z.L.; Pal, T. *Langmuir* **2000**, *16*, 2457-2463.

Jana, S.; Dutta, B.; Bera, R.; Koner, S. *Inorganic Chemistry* **2008**, *47*, 5512-5520.

Jana, S.; Ghosh, S.K.; Nath, S.; Pande, S.; Praharaj, S.; Panigrahi, S.; Basu, S.; Endo, T.; Pal, T. *Applied Catalysis A: General* **2006**, *313*, 41–48.

Jana, S.; Ghosh, S.K.; Nath, S.; Pande, S.; Praharaj, S.; Panigrahi, S.; Basu, S.; Endo, T.; Pal, T. *Applied Catalysis A: General*, **2006**, *313*, 41-48.

Jeon, S. –H.; Xu, P.; Zhang, B.; Mack, N. H.; Tsai, H.; Chiang, L. Y.; Wang, H. –L. *J. Mater. Chem*. **2011**, *21*, 2550-2554.

Johnson, R. *Nature Chemistry* **2014**, 6, 5.

Jomova, K.; Valko, M. *Toxicology* **2011**, 283, 65.

K

Kasuya, R.; Balachandran, J.; Itoh, T.; Matsumoto, T. Abstract No. C4.10. **2010**, Abstract Viewer. San Francisco, CA: Materials Research Society

Kim, K.J.; Shahinpoor, M. *Smart Mater. Struct.* **2003**, *12*, 65–79.

Knoll, G.F. Radiation Detection and Measurement, John Wiley & Sons, Inc. **1979**.

Kresge, C.T.; Leonowlcz, M.E.; Roth, W.J.; Vartuli, J.C.; Beck, J.S. *Nature* **1992**, *359*, 710-712.

Kreuer, K.D. *J. Membr. Sci.* **2001**, *185*, 29-39.

Krumrey, M.; Gleber, G.; Scholze, F.; Wernecke, *J. Meas. Sci. Technol.* **2011**, *22*, 094032 (6pp).

Kumar, R.; Pandey, A. K.; Dhara, S.; Misra, N. L.; Ramagiri, S. V.; Bellare, J. R.; Goswami, A. *J. Membr. Sci.* **2010**, *352*, 247-254.

Kumar, R.; Pandey, A.K.; Das, S.; Dhara, S.; Misra, N.L.; Shukla, R.; Tyagi, A.K.; Ramagiri, S.V.; Bellare, J.R.; Goswami, A. *Chem. Commun.* **2010**, *46*, 6371-6373.

Kumar, R.; Pandey, A.K.; Dhara, S.; Misra, N.L.; Ramagiri, S.V.; Bellare, J.R.; Goswami, A. *J. Membr. Sci.* **2010**, *352*, 247-254.

Kuo, J. Electron Microscopy: Methods and Protocols, Springer Science & Business Media, **2007**.

Kusoglu, A.; Modestino, M. A.; Hexemer, A.; Segalman, R. A.; Weber, A.Z. *ACS Macro Lett.* **2012**, *1*, 33-36.

L

L'Annunziata Michael F., Handbook of Radioactivity Analysis, 2nd Edition, Academic Press, California, **2003.**

LaMer, V.K. *Ind. Eng. Chem.* **1952**, *44*, 1270-1277.

LaMer, V.K.; Dinegar, R.H. *J. Am. Chem. Soc.* **1950**, *72*, 4847-4854.

Le, X.T.; Bui, T.H.; Viel, P.; Berthelot, T.; Palacin, S. *J. Membr. Sci.* **2009**, *34*0, 133-140.

Lee, E.M.; Thomas, R.K.; Burgess, A.N.; Barnes, D.J.; Soper, A.K.; Rennie, A.R. *Macromolecules* **1992**, *25*, 3106-3109.

Leenders, S.H.A.M.; Gramage-Doria, R.; Bruin, B.de.; Reek. J.N.H. *Chem. Soc. Rev.*, **2015**, *44*, 433-448.

Lehmani, A.; Durand-Vidal, S.; Turq, P. *J. Appl. Polym. Sci.* **1998**, *68*, 503-508.

Li, S.; Thompson, W.H. *J. Phys. Chem. B* **2005,** *109*, 4941-4946.

Lifshitz, I.; Slyozov, V. *J. Phys. Chem. Solids.* **1961**, *19*, 35-50.

Lihitkar, N.B.; Abyaneh, M.K.; Samuel, V.; Pasricha, R.; Gosavi, S.W.; Kulkarni, S.K. *J Colloid Interface Sci.* **2007**, *314*, 310-316.

Lin, Y.; Finke, R.G. *J. Am. Chem. Soc.* **1994**, *116*, 8335-8353.

Liu, Y.; Zhang, Y.; Ding, H.; Xu, S.; Li, M.; Kong, F.; Luo, Y.; Li, G. *J. Mater. Chem. A*, **2013**, *1*, 3362-3371.

Lopez, N.; Nørskov, J.K. *J. Am. Chem. Soc*. **2002**, *124*, 11262–11263.

Lorenz, B.B.; Crans, D.C.; Johnson, M.D. *Eur. J. Inorg. Chem.* **2014**, *2014*, 4537-4540.

Lu, L.; Kobayashi, A.; Tawa, K.; Ozaki, Y. *Chem. Mater.* **2006,** *18*, 4894-4901.

M

MacKnight, W.J.; Taggart, W.P.; Stein, R.S. *J. Polym. Sci., Polym. Symp.* **1974**, *45*, 113-128.

MacMillan, B.; Sharp, A.R.; Armstrong, R.L. *Polymer* **1999**, *40*, 2471-2480.

Makosch, M. A dissertation submitted to the ETH Zurich for the degree of Dr. sc. ETH Zürich. **2012**, Diss. ETH No. 20844.

Masson, E.; Ling, X.; Joseph, R.; Kyeremeh-Mensah, L.; Lu, X. *RSC Adv*. **2012**, *2*, 1213-1247.

Mauritz, K.A.; Moore, R.B. *Chem. Rev*. **2004**, *104*, 4535-4585.

McLean, R.S.; Doyle, M.; Saner, B.B. *Macromolecules* **2000**, *33*, 6541-6550.

Mistry, M.K.; Choudhury, N.R.; Dutta, N.K.; Knott, R. *Langmuir* **2010**, *26*, 19073-19083.

Mohan, Y. M.; Premkumar, T.; Lee, K.; Geckeler, K. E. *Macromol. Rapid Commun*. **2006**, *27*, 1346-1354.

Mushran, S.P.; Agrawal, M.C.; Mehrotra, R.M.; Sanehi, R. *J. Chem. Soc., Dalton Trans*. **1974**, 1460–1462, DOI: 10.1039/DT9740001460.

N

Naik, B.; Hazra, S.; Prasad, V.S.; Ghosh, N.N. *Catalysis Communications* **2011**, *12*, 1104–1108.

Naik, B.; Prasad, V.S.; Ghosh, N.N. *Powder Technology*, **2012**, *232*, 1–6.

Napper, D.H. Polymeric Stabilization of Colloidal Dispersions; Academic Press: London, **1983**.

Newns, D.M. *Phys. Rev.* **1969**, *178*, 1123−1135.

Nielsen, L.P.; Besenbacher, F.; Stensgaard, I.; Laegsgaard, E.; Engdahl, C.; Stoltze, P.; Jacobsen, K.W.; Nørskov, J.K. *Phys. Rev. Lett.* **1993**, *71*, 754-757.

Nielsen, T. K.; Bosenberg, U.; Gosalawit, R.; Dornheim, M.; Cerenius, Y.; Besenbacher, F.; Jensen, T. R. *ACS Nano* **2010**, *4*, 3903-3908.

Nielsen, T.K.; Bosenberg, U.; Gosalawit, R.; Dornheim, M.; Cerenius, Y.; Besenbacher, F.; Jensen, T.R. *ACS Nano* **2010**, *4*, 3903-3908.

O

Ostwald, W.Z. *Phys. Chem.* **1900**, *34*, 495-503.

Ozin, G.A. *Adv. Mater.* **1992**, *4*, 612-649.

Ozin, G.A.; Arsenault, A.C. Nanochemistry, A chemical approach to nanomaterials, **2008**, RSC Publishing, ISBN: 978-1-84755-895-4.

Ozin, G.A.; Chomski, E.; Khushalani, D.; Maclachlan, M.J. *Curr. Opin. Colloid Interface Sci.* **1998**, *3*, 181-193.

P

Padma, M.; Shyamala, P.; Satyanarayana, A.; Subba Rao, P.V.; Mathew, A. *Indian Journal of Chemistry*. **2013**, *52A*, 221-225.

Pal, A.; Shah, S.; Belochapkine, S.; Tanner, D.; Magner, E.; Devi, S. *Colloids and Surfaces A: Physicochem. Eng. Aspects*, **2009**, *337*, 205–207.

Pan, X.; Bao, X. *Acc. Chem. Res*. **2011**, *44*, 553-562.

Panáček, A.; Prucek, R.; Hrbáč, J.; Nevečná, T.; Šteffková, J.; Zbořil, R.; Kvítek, L. *Chem. Mater.*, **2014**, *26*, 1332–1339.

Pandey, A.K.; Goswami, A.; Sen, D.; Mazumder, S.; Childs, R.F. *J. Mem. Sci.* **2003**, *217*, 117-130.

Papp, S.; Szucs, A.; Dekany, I. *Solid State Ionics* **2001**, *141-142*, 169-176.

Pastoriza-Santos, I.; Liz-Marzan, L.M. *Langmui*r **1999**, *15*, 948-951.

Pastoriza-Santos, I.; Liz-Marzan, L.M. *Langmui*r **2000**, *18*, 2888-2894.

Pastoriza-Santos, I.; Liz-Marzan, L.M. *Nano Lett.* **2002**, *2,* 903-905.

Patra, S.; Pandey, A.K.; Sen, D.; Ramagiri, S.V.; Bellare, J.R.; Mazumder, S.; Goswami, A. *Langmuir,* **2014***, 30,* 2460–2469.

Patra, S.; Sen, D.; Pandey, A. K.; Agarwal, C.; Ramagiri, S. V.; Bellare, J. R.; Mazumder, S.; Goswami, A. *J. Phys. Chem. C.* **2013,** *17*, 12026–12037.

Pedersen, J.S. *Adv. Colloid Interface Sci.* **1997**, *70*, 171-210.

Pedersen, J.S. *J. Appl. Cryst. Sci.* **1994**, *7,* 595-608.

Perala, S.R.K.; Kumar, S. *Langmuir* **2013**, *29*, 9863−9873.

Pillai, Z.S.; Kamat, P.V. *J. Phys. Chem. B.* **2004,** *108,* 945-951.

Polak, M.; Rubinovich, L. *Nano Lett.* **2008**, *8*, 3543−3547.

Polak, M.; Rubinovich, L. *Phys. Chem. Chem. Phys.* **2011**, *13*, 16728−16734.

Polte, J.; Ahner, T.T.; Delissen, F.; Sokolov, S.; Emmerling, F.; Thunemann, A.F.; Kraehnert, R. *J. Am. Chem. Soc*. **2010**, *132*, 1296–1301.

Polte, J.; Erler, R.; Thunemann, A.F.; Emmerlinga, F.; Kraehnert, R. Chem. Commun. **2010**, *46*, 9209–9211.

Polte, J.; Tuaev, X.; Wuithschick, M.; Fischer, A.; Thuenemann, A.F.; Rademann, K.; Kraehnert, R.; Emmerling, F. *ACS Nano* **2012**, *6*, 5791-5802.

Pozun, Z.D.; Rodenbusch, S.E.; Keller, E.; Tran, K.; Tang, W.; Stevenson, K.J.; Henkelman, G. *J. Phys. Chem. C* **2013**, *117*, 7598−7604.

Pradhan, N., Pal, A., Pal, T. *Colloid Surf. B,* **2002**, *196*, 247-257.

Pradhan, N.; Pal, A.; Pal, T. *Langmuir* **2001**, *17*, 1800–1802.

Prorod G. *Small-Angle X-ray Scattering*. Kratky, O. and Glatter, O. editors. Academic Press London, **1982**.

Q

Qin, Y.; Ji, X.; Jing, J.; Liu, H.; Wu, H.; Yang, W. *Coll. Surf. A: Physicochem. Eng. Aspects* **2010**, *372*, 172-176.

R

Ramaraj, R. *J. Chem. Sci.* **2006**, *118*, 593-600.

Rance, G.A.; Solomonsz, W.A.; Khlobystov, A.N. *Chem. Commun.* **2013**, *49*, 1067-1069.

Rashid, M.H.; Mandal, T.K. *J. Phys. Chem. C,* **2007**, *111*, 16750–16760.

Ray, C.; Dutta, S.; Sarkar, S.; Sahoo, R.; Roy, A.; Pal. T. *RSC Advances,* **2013**, *3*, 24313-24320.

Redmond, P. L.; Wu, X.; Brus, L. *J. Phys. Chem. C* **2007,** *111*, 8942-8947.

Reimer, L.; Kohl, H. Transmission Electron Microscopy: Physics of Image Formation, Springer; 5th ed. **2008**.

Reiss, H.J. *Chem. Phys.* **1951**, *19*, 482-487.

Richards, V.N.; Rath, N.P.; Buhro, W.E. *Chem. Mater.* **2010**, *22*, 3556–3567.

Rivas, L.; Sanchez-Cortes, S.; Garcı´a-Ramos, J. V.; Morcillo, G. *Langmuir* **2001,** *17*, 574-577.

Roche, E.J.; Stein, R.S.; Russell, T.P.; MacKnight, W.J. *J. Polym. Sci., Polym. Phys. Ed*. **1980**, *18*, 1497-1512.

Rodriguez, A.; Amiens, C.; Chaudret, B.; Casanove, M.J.; Lecante, P.; Bradley, J.S. *Chem. Mater*. **1996**, *8*, 1978-1986.

Roduner, E. *Chem. Soc. Rev*., **2006**, *35*, 583–592.

Roduner, E. Nanoscopic materials: size dependent phenomenon, 2005, RSC Publishing, ISBN-10: 0-85404-857-X, ISBN-13: 978-0-85404-857-1

Rollet, A. L.; Diat, O.; Gebel, G. *J. Phys. Chem. B* **2004**, *108*, 1130–1136.

Rollet, A.-L.; Diat, O.; Gebel, G. *J. Phys. Chem. B* **2002**, *106*, 3033-3036.

Rollet, A.-L.; Gebel, G.; Simonin, J.-P, Turq, P. *J. Polym. Sci., Polym. Phys.* **2001**, *39*, 548-558.

Rollins, H.W.; Lin, F.; Johnson, J.; Ma, J- J.; Liu, J- T.; Tu, M- H.; DesMarteau, D.D.; Sun, Y-P. *Langmuir* **2000**, *16*, 8031-8036.

Roucoux, A.; Schulz, J.; Patin, H. *Chem. Rev*. **2002,** *102*, 3757-3778.

Rubatat, A.L. Rollet, G. Gebel and O. Diat. *Macromolecules* **2002**, *35*, 4050–4055.

Rubatat, L. Gebel, G. and Diat, O. *Macromolecules* **2004**, *37*, 7772–7783.

Rubinovich, L.; Polak, M. *Nano Lett.* **2013**, *13*, 2247−2251.

Ruth, T.J. *Rep. Prog. Phys*. **2009**, *72*, 016701.

S

Sabir, T.S.; Rowland, L.K.; Milligan, J.R.; Yan, D.; Aruni, A.W.; Chen, Q.; Boskovic, D.S.; Kurti, R.S.; Perry, C.C. *Langmuir* **2013**, *29*, 3903-3911.

Sabir, T.S.; Yan, D.; Milligan, J.R.; Aruni, A.W.; Nick, K.E.; Ramon, R.H.; Hughes, J.A.; Chen, Q.; Kurti, R.S.; Perry, C.C. *J. Phys. Chem. C* **2012**, *116*, 4431-4441.

Sachdeva, A.; Sodaye, S.; Pandey, A.K.; Goswami, A. *Anal. Chem.* **2006**, *78*, 7169-7174.

Saha, J.; Mitra, A.; Dandapat, A.; De, G. *Dalton Trans*., **2014**, *43*, 5221-5229.

Sanchez, C.; Julian, B.; Belleville, P.; Popall, M. *J. Mater. Chem.* **2005**, *15*, 3559-3592.

Sanlés-Sobrido, M.; Pérez-Lorenzo, M.; Rodríguez-González, B.; Salgueiriño, V.; Correa-Duarte, M.A. *Angew. Chem. Int. Ed*. **2012**, *51*, 3976.

Santiso, E.E.; George, A.M.; Sliwinska-Bartkowiak, M.; Nardelli, M.B.; Gubbins, K.E. *Adsorption*, **2005**, *11*, 349-354.

Santoro, G.; Buffet, A.; Döhrmann, R.; Yu, S.; Körstgens, V.; Müller-Buschbaum, P.; Gedde, U.; Hedenqvuist, M.; Roth, S.V. *Rev. Sci. Instrum.* **2014**, *85*, 043901.

Santoro, G.; Yu, S.; Schwartzkopf, M.; Zhang, P.; Vayalil, S.K.; Risch, J.F.H.; Rübhausen, M.A.; Hernández, M.; Domingo, C.; Roth, S.V. *Appl. Phys. Lett* **2014**, *104*, 243107.

Sarkar, A.; Kapoor, S.; Mukherjee, T. *J. Phys. Chem. B* **2005,** *109*, 7698-7704.

Sau, T.K.; Pal, A.; Pal, T. *J. Phys. Chem. B* **2001**, *105*, 9266–9272.

Schmid, G.; Emde, S.; Maihack, V.; Meyer-Zaika, W.; Peschel, S. *J. Mol. Catal. A: Chem.* **1996**, *107*, 95-104.

Schmid, G.; Maihack, V.; Lantermann, F.; Peschel, S. *J. Chem.Soc., Dalton Trans.* **1996**, 589.

Schmid, G.; Morun, B.; Malm, J.O. *Angew. Chem., Int. Ed. Engl.* **1989**, *28*, 778-780.

Schmid, G.; Pfeil, R.; Boese, R.; Bandermann, F.; Meyers, S.; Calis, G. H. M.; Van Der Velden, J. W. A. *Chem. Ber.* **1981**, *114*, 3634-3642.

Schmidt-Rohr, K.; Chen, Q. *Nature Mater.* **2008**, *7*, 75-83.

Schwank, J.; Galvagno, S.; Parravano, G. *J. Catal.* **1980**, *63*, 415-424.

Sel, O.; Azais, T.; Maréchal, M.; Gébel, G.; Laberty-Robert, C.; Sanchez, C. *Chem. Asian J.* **2011**, *6*, 2992-3000.

Selvaraju, T.; Ramaraj, R. *Pramana- J. Phys.* **2005**, *65*, 713-722.

Selvaraju, T.; Sivagami, S.; Thangavel, S.; Ramaraj, R. *Bull. Mater. Sci.* **2008**, *31*, 487-494.

Shah, D.; Kaur, H. *Journal of Molecular Catalysis A: Chemical* **2014**, *38*, 70-76.

Shahinpoor, M.; Bar-Cohen, Y.; Simpson, J.O.; J. Smith. Smart Mater. Struct. **1998**, *7*, R15-R30.

Shahinpoor, M.; Kim, K.J. *Smart Mater. Struct.* **2005**, *14*, 197–214.

Shchukin, D.G.; Sukhorukov, G.B. *Adv. Mater*. **2004**, *16*, 671-682.

Shine, H.J., Mallory, H.E. *J. Org. Chem.*, **1962**, 27, 2390-2391.

Shon, M.J.; Cohen, A.E. *J. Am. Chem. Soc.* **2012**, *134*, 14618-14623.

Simo, A.; Polte, J.; Pfänder, N.; Vainio, U.; Emmerling, F.; Rademann, K. *J. Am. Chem. Soc.* **2012**, *134*, 18824−18833.

Singha, D.; Barman, N.; Sahu, K. *Journal of Colloid and Interface Science* **2014**, *413*, 37-42.

Skoog, D.A.; Holler, F.J.; Crouch, S.R. Principals of instrumental analysis, Brooks Cole; 6 edition, **2006**.

Sodaye, S.; Agarwal, C.; Goswami, A. *J. Mem. Sci.* **2008**. *314*, 221–225.

Sohn, L.L. *Nature* **1998**, *394*, 131-132.

Song, K.; Liu, P.; Wang, J.; Pang, L.; Chen, J.; Hussain, I.; Tan, B.; Li, T. *Dalton Trans*., **2015**, *44*, 13906–13913.

Song, K.C.; Lee, S.M.; Park, T.S.; Lee, B.S. *Korean J. Chem. Eng*., **2009**, *26*, 153-155.

Song, Y.; Garcia, R.M.; Dorin, R.M.; Wang, H.; Qiu, Y.; Coker, E.N.; Steen, W.A.; Miller, J.E.; Shelnutt, J.A. *Nano Lett*., **2007**, *7*, 3650-3655.

Starkweather, Jr, H.W. *Macromolecules* **1982**, *15*, 320-323.

Steinigeweg, D.; Schlucker, S. *Chem. Commun*. **2012**, *48*, 8682-8684.

Suber, L.; Plunkett, W.R. *Nanoscale* **2010**, *2*, 128-133.

Sun, K.; Qiu, J.; Liu, J.; Miao, Y. *J. Mater. Sci.* **2009**, *44*, 754–758.

Sun, Y.; Gates, B.; Mayers, B.; Xia, Y. *Nano Lett.,* **2002**, 2, 165-168.

Sun, Y.-P.; Atorngitjawat, P.; Lin, Y.; Liu, P.; Pathak, P.; Bandara, J.; Elgin, D.; Zhang, M. *J. Membr. Sci.* **2004**, *245*, 211-217.

Suvith, V.S.; Philip, D. *Spectrochimica Acta Part A: Molecular and Biomolecular Spectroscopy*, **2014**, *118*, 526–532.

T

Takahashi, Y.; Yukita, W.; Chatterjee, M.; Suzuki, T.M. *Reactive & Functional Polymers* **2008**, *68*, 1476–1482.

Takesue, M.; Tomura, T.; Yamada, M.; Hata, K.; Kuwamoto, S.; Yonezawa, T. *J. Am. Chem. Soc.* **2011**, *133*, 14164–14167.

Tanakaa, T.; Ohyamab, J.; Teramuraa, K.; Hitomic, Y. *Catalysis Today* **2012**, *183*, 108– 118.

Tang, S.; Vongehr, S.; Meng, X. *J. Mater. Chem.*, **2010**, *20*, 5436-5445.

Tant, M.R.; Mauritz, K.A.; Wilkes, G. L. *Ionomers: Synthesis, Structure, Properties and Applications*; Blackie Academic & Professional, Glasgow, **1997**.

Tersoff, J. *Nature* **2001**, *412*, 135.

Thanh, N.T.K.; Maclean, N.; Mahiddine, S. *Chem. Rev.* **2014**, *114*, 7610−7630.

Thanh, N.T.K.; Maclean, N.; Mahiddine, S. *Chem. Rev.* **2014**, *114*, 7610−7630.

Thomas, A.; Polarz , S.; Antonietti, M. *J. Phys. Chem. B* **2003**, *107*, 5081-5087.

Thompson, W.H. *J. Chem. Phys.* **2002**, *117*, 6618-6628.

Turner, C.H.; Brennan, J.K.; Johnson, J.K.; Gubbins, K.E. *J. Chem. Phys.*, **2002**, *116*, 2138-2148.

Turner, C.H.; Johnson, J.K.; Gubbins, K.E. *J. Chem. Phys*., **2001**, *114*, 1851-1859.

U

Unruh, K.M.; Huber, T.E.; Huber, C.A. *Phys. Rev. B: Condens. Matter*, **1993**, *48*, 9021-9027.

V

Vidhu, V.K.; Philip, D. *Micron*, **2014**, *56*, 54-62.

Vijayaraghavan, K.; Nalini, S.P.K. *Biotechnol. J.* **2010**, *5*, 1098-1110.

Volkov, V.V.; Kravchenko, T.A.; Roldughin, V.I. *Russ. Chem. Rev.* **2013**, *82*, 465-482.

W

Wagner, C.; Bunsenges, B. *Phys. Chem.* **1961**, *65*, 581.

Wang, F.; Richards, V.N.; Shields, S.P.; Buhro, W.E. *Chem. Mater.* **2014**, *26*, 5−21.

Wang, J.; Musameh, M.; Lin, Y. *J. Am. Chem. Soc.* **2003**, *125*, 2408-2409.

Watzky, M.A.; Finke, R.G. *Chem. Mater.* **1997**, *9*, 3083-3095.

Whitesides, G. *Technol. Rev*. **1998**, *101*, 84-86.

Wirtz, M.; Parker, M.; Kobayashi, Y.; Martin, C.R. *Chem. Eur. J.* **2002**, *8*, 3572-3578.

Wu, Z.; Yang, S.; Wu, W. Nanoscale, **2016**, *8*, 1237–1259.

Wuithschick, M.; Paul, B.; Bienert, R.; Sarfraz, A.; Vainio, U.; Sztucki, M.; Kraehnert, R.; Strasser, P.; Rademann, K.; Emmerling, F.; Polte, *J. Chem. Mater.* **2013**, *25*, 4679-4689.

X

Xia, Y.; Yang, H.; Campbell, C.T. *Acc. Chem. Res.* **2013**, 46, 1671-1672.

Xiao, J.; Pan, X.; Guo, S.; Ren, P.; Bao, X. *J. Am. Chem. Soc*. **2015**, *137*, 477-482.

Xing, S.; Xu, H.; Chen, J.; Shi, G.; Jin, L. *J. Electroanal. Chem.* **2011**, *652*, 60-65.

Xue, T.; Trent, J. S.; Osseo-Asare, K. *J. Membr. Sci.* **1989**, *45*, 261-271.

Y

Yang, Q.; Adrus, N.; Tomickiab, F.; Ulbricht, M. *J. Mater. Chem.*, **2011**, *21*, 2783–281.

Yin, J.; Wang, J.; Li, M.; Jin, C.; Zhang, T. *Chem. Mater*., **2012**, *24*, 2645−2654.

Yu, J.Y.; Schreiner, S.; Vaska, L. *Inorg. Chim. Acta* **1990**, *170*, 145-147.

Z

Zhang, H., Li, X., Chen, G. *J. Mater. Chem.*, **2009**, *19*, 8223-8231.

Zhao, S.; Sun, C.; Wang, L.; Xu, X.; Wang, X. *Dalton Trans*., **2010**, *39*, 5087–5090.

Zhou, X.; Xu, W.; Liu, G.; Panda, D.; Chen, P.; *J. Am. Chem. Soc.*, **2010**, *132*, 138-146.

Zhu, G.; Liu, Y.; Xu, Z.; Jiang, T.; Zhang, C.; Li, X.; Qi, G. *ChemPhysChem* **2010**, *11*, 2432-2437.

Zhu, M.; Wang, C.; Meng, D.; Diao, G. *J. Mater. Chem. A* **2013**, *1*, 2118-2125 and references therein.